



**CATARINA
FERREIRA DOS
SANTOS**

**Síntese e funcionalização de nanopartículas de
Hidroxiapatite**

**Synthesis and functionalization of Hydroxyapatite
nanoparticles**



**CATARINA
FERREIRA DOS
SANTOS**

**Síntese e funcionalização de nanopartículas de
Hidroxiapatite**

**Synthesis and functionalization of Hydroxyapatite
nanoparticles**

Dissertação apresentada à Universidade de Aveiro para cumprimento dos requisitos necessários à obtenção do grau de doutor em Ciência e Engenharia de Materiais, realizada sob a orientação científica da Doutora Maria Elizabete Jorge Vieira Costa, Professora Auxiliar e da Doutora Maria Margarida Tavares Almeida, Professora Auxiliar, ambas do Departamento de Engenharia Cerâmica e do Vidro da Universidade de Aveiro.

Dissertation presented to the University of Aveiro to obtain the Doctor degree in Materials Science and Engineering, under scientific supervision of Dr. Maria Elizabete Jorge Vieira Costa, Auxiliary Professor and Dr. Maria Margarida Tavares Almeida, Auxiliary Professor, both of the Department of Ceramic and Glass Engineering of the University of Aveiro.

Apoio financeiro da FCT e do FSE no âmbito do III Quadro Comunitário de Apoio.

o júri

Presidente

Prof. Doutor Carlos Fernandes da Silva
Professor Catedrático da Universidade de Aveiro

Prof. Doutor Rui Luis Reis
Professor Catedrático da Escola de Engenharia da Universidade do Minho

Prof. Doutora Maria Filomena Rabaça Roque Botelho
Professora Catedrática da Faculdade de Medicina da Universidade de Coimbra

Prof. Doutor Ralf-Peter Franke
Full Professor, Biomaterials Department, University of UIm, Alemanha

Doutora Paula Alexandrina de Aguiar Pereira Marques
Investigador Auxiliar do Centro de Tecnologia Mecânica e Automação (TEMA) da Universidade de Aveiro

Prof. Doutora Maria Margarida Tavares Lopes de Almeida
Professora Auxiliar da Universidade de Aveiro

Prof. Doutora Maria Elizabete Jorge Vieira da Costa
Professora Auxiliar da Universidade de Aveiro

Agradecimentos

Não gostaria de terminar esta tese sem agradecer a todas aquelas pessoas que sem a sua ajuda, o seu contributo e a sua amizade a realização não teria sido possível. Existem muitas, às quais estarei sempre muito agradecida e por essa razão, agradeço do fundo do coração a todas as que me rodearam durante esta jornada e que de alguma forma contribuíram para o meu desenvolvimento e para a sua realização.

Para começar gostaria de gratular a minha orientadora Professora Elizabete Costa pelo seu incansável esforço em me transmitir o seu conhecimento e as suas sugestões, para que fosse possível enriquecer com tanto prestígio este documento com tão vasto conhecimento científico. Estou também muito agradecida à minha co-orientadora Professora Maria Margarida Almeida, porque sem o seu esforço e vontade pessoal não teria sido possível dar continuidade a este trabalho fora da Universidade de Aveiro. Ao Professor Ralf-Peter Franke que sempre acreditou nas minhas potencialidades e me incentivou a realizar este trabalho.

Queria também agradecer à Escola Superior de Tecnologia de Setúbal do Instituto Politécnico de Setúbal, em especial ao Departamento de Engenharia Mecânica, pelas facilidades disponibilizadas para que fosse exequível a concretização desta tese conjuntamente com o desempenho das funções de docência. Não podendo esquecer a sincera gratidão dada pela Coordenadora da área científica, a Professora Maria João Carmezim que sempre me apoiou de uma forma singular e especial ao longo dos últimos três anos.

Queria expressar a minha imensa gratidão ao Professor Mário Ferreira, pela sua enorme amabilidade e esforço para que fosse possível realizar grande parte do trabalho experimental no grupo de Electroquímica e Corrosão do Instituto Superior Técnico em Lisboa. Gostaria também de expressar os meus sinceros agradecimentos a todos os elementos do grupo de Electroquímica e Corrosão do Instituto Superior Técnico pelo caloroso acolhimento e por me terem apoiado quer institucionalmente quer pessoalmente ao longo desta caminhada.

Gostaria de expressar a minha inteira gratidão à Professora Maria Helena Fernandes do Laboratório de Farmacologia e Biocompatibilidade celular da Faculdade de Medicina Dentária da Universidade do Porto, pelo apoio científico, pelos seus importantes aconselhamentos pessoais e científicos bem como pelas suas sugestões.

Pretendo também agradecer ao Professor Pedro Gomes pela grande ajuda que me deu na realização experimental de uma parte muito importante desta tese como na discussão e decisão de novas experiências.

Não queria deixar de agradecer ao Professor João Bordado do Instituto Superior Técnico e a alguns elementos do seu grupo particularmente ao Professor Humberto, ao Engenheiro José Condeço, pelo seu empenho nas diversas tentativas que tiveram de realizarem para me ajudarem a encontrar algumas soluções para os meus problemas de HPLC, que tão bem controlam. Agradeço igualmente a Fundação para a Ciência e Tecnologia pelo suporte financeiro que me foi dado no primeiro ano de doutoramento através de uma bolsa de doutoramento (FCT, Ref da Bolsa SFRH/BD/48276/2008). Expresso também a minha gratidão a Universidade de Aveiro e ao Laboratório associado CICECO pelo suporte técnico.

Agradeço também aos meus amigos que de diversas formas me apoiaram e contribuíram para que os momentos de maior tensão e de stress fossem menores e menos intensos.

Estou também muito grata à minha família em especial aos meus pais (Alcides e Amelia), ao meu irmão (Rui) e a sua família (Nadine e Bruna) que durante estes anos me acompanharam nesta jornada sem perceberem muito bem quando e como seria o fim... Não quero igualmente, deixar de agradecer à família do meu marido Bruno (Gloria, Fernando, Cláudia, Paulo, Telma e Rodrigo) que me apoiaram e me ajudaram a levar esta tarefa até ao fim. Por fim, com muito carinho e de uma forma muito especial gostaria de agradecer ao Bruno, por fazer parte da minha vida e por ter participado neste “meu” desafio com uma enorme paciência e compreensão durante estes longos anos. Não poderia terminar sem deixar umas palavras para a minha filha Adriana, que embora seja pequena e ainda não compreenda a importância real deste desafio, gostaria que soubesse que para além de uma realização pessoal minha, muito do esforço realizado foi com o intuito de lhe proporcionar uma vida melhor e por esse motivo espero que me perdoe pelo tempo que não lhe dediquei nestes últimos anos e que tanto merecia.... A minha outra filha (Filipa) que ainda não conheço, mas que em breve espero conhecer.

palavras-chave

Partículas de hidroxiapatite, nanopartículas, ácido cítrico, síntese química a temperatura fisiológica e hidrotérmica, ouro, ácido fólico, citotoxicidade.

Resumo

Graças aos desenvolvimentos na área da síntese de nanomateriais e às potentes técnicas de caracterização à nanoescala conseguimos hoje visualizar uma nanopartícula (NP) como um dispositivo de elevado potencial terapêutico. A melhoria da sua efectividade terapêutica requer no entanto o aprofundamento e sistematização de conhecimentos, ainda muito incipientes, sobre toxicidade, selectividade, efeitos colaterais e sua dependência das próprias características físico-químicas da NP em análise. O presente trabalho, elegendo como alvo de estudo uma substância considerada biocompatível e não tóxica, a hidroxiapatite (Hap), pretende dar um contributo para esta área do conhecimento. Definiram-se como metas orientadoras deste trabalho (i) estudar a síntese de nanopartículas de Hap (Hap NP), e a modificação das características físico-químicas e morfológicas das mesmas através da manipulação das condições de síntese; (ii) estudar a funcionalização das Hap NP com nanoestruturas de ouro e com ácido fólico, para lhes conferir capacidades acrescidas de imagiologia e terapêuticas, particularmente interessantes em aplicações como o tratamento do cancro (iii) estudar a resposta celular a materiais nanométricos, com propriedades físico-químicas diversificadas.

No que se refere à síntese de Hap NP, compararam-se dois métodos de síntese química distintos, a precipitação química a temperatura fisiológica (WCS) e a síntese hidrotérmica (HS), em meios aditivados com ião citrato. A síntese WCS originou partículas de tamanho nanométrico, com uma morfologia de agulha, pouco cristalinas e elevada área superficial específica. A síntese HS à temperatura de 180°C permitiu obter partículas de dimensões também nanométricas mas com área específica inferior, com morfologia de bastonete prismático com secção recta hexagonal e elevada cristalinidade. Com o objectivo de aprofundar o papel de algumas variáveis experimentais na definição das características finais das partículas de hidroxiapatite, designadamente o papel do ião citrato (Cit), variou-se a razão molar [Cit/Ca] da solução reagente e o tempo de síntese. Demonstrou-se que o ião citrato e outras espécies químicas resultantes da sua decomposição nas condições térmicas (180°C) de síntese tem um papel preponderante na velocidade de nucleação e de crescimento dessas mesmas partículas e por conseguinte nas características físico-químicas das mesmas. Elevadas razões [Cit/Ca] originam partículas de dimensão micrométrica cuja morfologia é discutida no contexto do crescimento com agregação.

Com o objectivo de avaliar a citotoxicidade *in vitro* das nanopartículas sintetizadas procedeu-se à esterilização das mesmas. O método de esterilização escolhido foi a autoclavagem a 121° C. Avaliou-se o impacto do processo de esterilização nas características das partículas, verificando-se contrariamente às partículas WCS, que as partículas HS não sofrem alterações significativas de morfologia, o que se coaduna com as condições de síntese das mesmas, que são mais severas do que as de esterilização. As partículas WCS sofrem processos de dissolução e recristalização que se reflectem em alterações significativas de morfologia. Este estudo demonstrou que a etapa de esterilização de nanopartículas para aplicações biomédicas, por autoclavagem, pode alterar substancialmente as propriedades das mesmas, sendo pois criticamente importante caracterizar os materiais após esterilização. Os estudos citotxicológicos para dois tipos de partículas esterilizadas (HS_{ster} e WCS_{ster}) revelaram que ambas apresentam baixa toxicidade e possuem potencial para a modelação do comportamento de células osteoblásticas.

Tendo em vista a funcionalização da superfície das Hap NP para multifunções de diagnóstico e terapia exploraram-se condições experimentais que viabilizassem o acoplamento de nanopartículas de ouro à superfície das nanopartículas de Hidroxiapatite (Hap-AuNP). Tirando partido da presença de grupos carboxílicos adsorvidos na superfície das nanopartículas de Hap foi possível precipitar partículas nanométricas de ouro (1,5 a 2,5 nm) na superfície das mesmas adaptando o método descrito por Turkevich. No presente trabalho as nanopartículas de Hap funcionaram assim como um *template* redutor do ouro iónico de solução, propiciando localmente, na superfície das próprias nanopartículas de Hap, a sua redução a ouro metálico. A nucleação do ouro é assim contextualizada pelo papel redutor das espécies químicas adsorvidas, designadamente os grupos carboxílicos derivados de grupos citratos que presidiram à síntese das próprias nanopartículas de Hap. Estudou-se também a funcionalização das Hap NP com ácido fólico (FA), uma molécula biologicamente interessante por ser de fácil reconhecimento pelos receptores existentes em células cancerígenas. Os resultados confirmaram a ligação do ácido fólico à superfície das diferentes partículas produzidas HS e Hap-AuNPs. Graças às propriedades ópticas do ouro nanométrico (efeito plasmão) avaliadas por espectroscopia vis-UV e às potencialidades de hipertermia local por conversão fototérmica, as nanoestruturas Hap-AuNPs produzidas apresentam-se com elevado interesse enquanto nanodispositivos capazes de integrar funções de quimio e terapia térmica do cancro e imagiologia.

O estudo da resposta celular aos diversos materiais sintetizados no presente trabalho foi alvo de análise na tentativa de se caracterizar a toxicidade dos mesmos bem como avaliar o seu desempenho em aplicações terapêuticas. Demonstrou-se que as Hap NP não afectam a proliferação das células para concentrações até 500 $\mu\text{g/ml}$, observando-se um aumento na expressão genética da BMP-2 e da fosfatase alcalina. Verificou-se também que as Hap NP são susceptíveis de internalização por células osteoblásticas MG63, apresentando uma velocidade de dissolução intracelular relativamente reduzida. A resposta celular às Hap-AuNP confirmou a não citotoxicidade destas partículas e revelou que a presença do ouro na superfície das Hap NP aumenta a taxa proliferação celular, bem como a expressão de parâmetros osteogénicos. No seu conjunto os resultados sugerem que os vários tipos de partículas sintetizadas no presente estudo apresentam também comportamentos interessantes para aplicações em engenharia de tecido ósseo.

Keywords

Hydroxyapatite particles, nanoparticules, citric acid, chemical synthesis at physiological temperature and hydrothermal, gold, folic acid, *in vitro* test.

Abstract

Thanks to the last developments in the field of nanomaterials synthesis and to the powerful characterization techniques at the nanoscale, a nanoparticle (NP) can now be viewed as a device of high therapeutic potential. The improvement of its therapeutic effectiveness however still requires the deepening and systematization of important knowledge, still very incipient, on critical related issues including toxicity, selectivity, side effects and their own dependence on the physicochemical characteristics of the NP under analysis. The awareness of this need has framed the present work whose material target is a substance currently considered as biocompatible and nontoxic, hydroxyapatite (Hap), aiming to contribute to the referred pool of knowledge. The guiding goals of this work are here stated as: (i) to study the synthesis of nanoparticles Hap (Hap NP) for understanding the control of particle physico-chemical characteristics through the manipulation of its synthesis conditions, (ii) to study the functionalization of Hap NP with gold and with folic acid in order to impart both imaging and therapy abilities to the synthesized NP thus addressing their usefulness for particular applications related to the treatment of cancer, (iii) to examine the cellular response to nanosized materials having diverse physico-chemical properties.

For the study of Hap synthesis a hydrothermal synthesis (HS) technique assisted by citric acid additive was followed. The potential of citrate ion (Cit) for tailoring the synthesized particle morphology was exploited by varying the molar ratio [Cit:Ca] of the starting precursor solution. It was demonstrated that the citrate ion and/or other chemical species resulting from citrate decomposition at the used synthesis temperature (180°C) has a major role on nucleation and growth processes of the resulting Hap particles and on their final physico-chemical characteristics. Prismatic Hap particles with hexagonal cross section but with nanometric dimensions were obtained for a low [Cit:Ca] ratio while increasing ratios originated micrometer-sized particles composed by assembled fiber-like or sheet-like particles whose morphology may be discussed in the framework of an aggregation assisted growth. The evaluation of the biological performance of the produced nanometric Hap particles was the natural step in the present study. However, for the goal of comparing the impact of Hap NP morphology variations on cell response, a second chemical precipitation method (WCS) at physiological temperature and using the same additive was also adopted to produce thinner Hap NP. The physico-chemical characteristics of the two precipitated particles, i.e. HS and WCS Hap NP, were comparatively discussed, being found that thin needle-like particles of very high specific surface area (170 m²/g) are obtained from WCS as compared to the prismatic HS particles of lower specific surface area (55 m²/g) but of higher crystallinity. Moreover, as *in vitro* studies require sterilized materials, the particles were autoclaved at 121° C and the sterilization impact

on the particles properties was evaluated as well. Contrarily to WCS particles no significant changes are observed on HS morphology, consistently with the high synthesis temperature conditions for HS NP that exceed largely autoclaving condition. WCS particles undergo dissolution and recrystallization processes which are reflected on significant changes of WCS NP morphology. These results demonstrate that autoclaving sterilization may substantially alter the properties of NP intended for biomedical applications being thus critically important to characterize the materials after sterilization. The *in vitro* cytotoxicity studies on both type of sterilised particles (HS_{ster} and WCS_{ster}) revealed that they present low toxicity and have potential for the modulation of the osteoblastic cell behaviour.

The possibility of functionalizing Hap NP surface for multifunction purposes (diagnosis and therapy, for instance) was also exploited in the present work. Taking advantage from the presence of adsorbed carboxylic groups left by the synthesis process, HS NP surfaces could be used as a kind of template for gold precipitation, thus providing a new approach to Turkevich method for gold precipitation. Gold nanoparticles with an average diameter of 1.5 to 2.5 nm were effectively precipitated on HS nanoparticles facets as revealed by transmission electron microscopy (TEM). The reducing ability of the species adsorbed on HS surface including carboxylate compounds derived from citrate was thus confirmed as gold ions supplied by the neighbouring gold solution underwent a local reduction giving place to metallic gold spots and hence to nanostructured hydroxyapatite-gold nanoparticles (Hap-AuNPs). The functionalization of Hap NP with folic acid (FA), a molecule with high biological interest due to its easy recognition by the receptors on tumor cells, was also studied. The results confirmed the conjugation of FA to the surface of HS and Hap-AuNPs nanoparticles. Thanks to the optical properties of Hap-AuNPs imparted by the nanometric gold (plasmon effect) as confirmed by UV-vis spectroscopy and to the hyperthermia effect reported for metallic nanometric gold, the Hap-AuNPs here produced show a great potential as nanodevices able to integrate functions of chemical and thermal therapy for cancer and imaging. The cellular response to the various nanomaterials synthesized in this work was also analysed in an attempt to characterize their toxicity and to assess their biological performance aiming to identify potential therapeutic applications. It was demonstrated that Hap NP do not affect MG63 cell proliferation until concentrations up to 500 µg/ml, as indicated by BMP-2 and alkaline phosphatase expression. It was also found that Hap NP undergo internalization by MG63 osteoblast cells, suffering a relatively low intracellular dissolution rate.

The cellular response to Hap AuNPs confirmed their non-cytotoxicity while showing that the presence of gold at the surface of Hap NP increases the cell proliferation rate and the expression of osteogenic parameters. Altogether the *in vitro* results suggest that the behavior of the various types of particles synthesized in this study addresses a potential interest for applications in hard tissue engineering.

Ao meu marido Bruno

e às minhas filhas, Adriana e Filipa

TABLE OF CONTENTS

TABLE OF CONTENTS.....	i
LIST OF FIGURES	v
LIST OF TABLES	xii
GLOSSARY OF SYMBOLS.....	xiii
ABBREVIATIONS.....	xiv
Introduction.....	1
Background on hydroxyapatite nanoparticles synthesis and functionalization	7
1.1. Introduction.....	9
1.2. Hydroxyapatite (Hap): an overview	9
1.2.1. Hap as the main inorganic constituent of bone.....	9
1.2.2. Hydroxyapatite crystal structure issues	13
1.2.3. Synthesis methodologies of Hydroxyapatite nanoparticles.....	17
1.2.4. Hydroxyapatite particles: nucleation, growth and morphology.....	21
1.2.5. Citric acid and biological Hydroxyapatite particles.....	25
1.2.6. Influence of citric acid on Hap synthesis.....	29
1.2.7. <i>In vitro</i> and <i>in vivo</i> performance of Hydroxyapatite nanostructures	30
1.2.8. Biomedical applications of hydroxyapatite nanoparticles.....	35
1.2.8.1. Bone repair.....	35
1.2.8.2. Dental applications	35
1.2.8.3. Other applications	36
1.3. Noble metal nanoparticles and surface Plasmon resonance ...	38
1.3.1. Synthesis of gold nanoparticles methods	42
1.3.2. Applications of gold nanoparticles	49
1.3.2.1. Labelling and imaging	49
1.3.2.2. Clinical diagnostics and therapy.....	51
1.4. Folic acid conjugation.....	55

1.5. References	60
Materials processing and experimental techniques.....	73
2.1. Introduction.....	75
2.2. Hydroxyapatite particles synthesis	76
2.2.1. Hydrothermal Method (HS).....	76
2.2.2. Wet Chemical Method (WCS)	77
2.2.3. Sterilization procedure.....	78
2.3. Surface nano-functionalization of Hap nanoparticles	78
2.3.1. Gold nanoparticles	78
2.3.2. Folic acid molecule.....	79
2.3.3. Interaction of MG63 osteoblast-like cells with Hap-NPs	79
2.4. Hap-NPs characterization techniques	80
2.4.1. Physical characterization.....	80
2.4.1.1. X-Ray diffraction analysis.....	80
2.4.1.2. Differential thermal analysis and thermogravimetry.....	81
2.4.1.3. Specific Surface Area Analysis, Brunauer-Emmett-Teller (BET).....	81
2.4.2. Morphological characterization.....	83
2.4.2.1. Scanning electron microscopy	83
2.4.2.2. Transmission electron microscopy	84
2.4.2.3. Confocal Laser Scanning Microscope	85
2.4.3. Chemical characterization	86
2.4.3.1. Fourier transforms infrared spectroscopy.....	86
2.4.3.2. Zeta potential	89
2.4.3.3. Ultra Violet-Visible spectrophotometer (UV-Vis).....	91
2.4.3.4. Liquid Chromatography	94
2.4.4. Biological characterization.....	96
2.4.4.1. Cell Viability/proliferation	96
2.4.4.2. Immunofluorescent staining of F-actin cytoskeleton filaments and nuclei	97
2.4.4.3. Apoptosis	97
2.4.4.4. Gene expression by Reverse-Transcription Polymerase Chain Reaction (RT-PCR)	100
2.5. References	101

Citrate assisted synthesis of hydroxyapatite nano and micro crystals with different morphologies	105
3.1. Introduction.....	107
3.2. Synthesis of Hap particles	109
3.2.1. Effects of (Citrate:Calcium) ratio on Hap particle morphology	109
3.3. Morphology evolution with growth time	124
3.4. References	137
Viability and proliferation of MG-63 osteoblastic cells exposed to hydroxyapatite nanoparticles with different characteristics	141
4.1. Introduction.....	143
4.2. Comparing the characteristics of hydroxyapatite nanoparticles synthesized by hydrothermal (HS) and Wet Chemical Method (WCS)...	144
4.3. Sterilization process of HS and WCS nanoparticles.....	150
4.4. Interaction of Hap nanoparticles with osteoblastic cells after sterilization.....	153
4.4.1. Cell viability/proliferation.....	153
4.4.2. F-actin cytoskeleton organization	155
4.4.3. Apoptosis.....	157
4.4.4. Gene expression of osteoblastic proteins.....	158
4.4.5. Nano-Hap cell uptake	158
4.5. References	165
Functionalization of Hydroxyapatite nanostructures.....	171
5.1. Introduction.....	173
5.2. Precipitation of nanosized gold dots on hydroxyapatite nanoparticles facets.....	174
5.2.1. Crystal structure and microstructure.....	175
5.3. Gold precipitation and surface-characteristics of HS-AuNPs .	180

5.4.	Interaction of HS-AuNps with osteoblastic cells	185
5.5.	Hap and Hap-AuNPs nanoparticles functionalized with folic acid, a cell membrane receptor	194
5.5.1.	Synthesis of folic-acid conjugated HS and HS-AuNPs	194
5.6.	Interaction of HS-FA and HS-AuNPs-FA with osteoblastic cells	199
5.7.	References	202
	General Conclusion and Future Work	211
6.1.	References	217

CHAPTER 1

Figure 1.1 - Hierarchical multiscale structure of bone, showing the different hierarchical levels (adapted from ⁶).....	11
Figure 1.2 - A schematic model of apatite evolution via the conglutination of “bricks (Hap) and mortar (ACP)”. Under the control of biological components such as glycine and glutamate, the Hap subunits can be re-organized (adapted from ⁹).....	12
Figure 1.3 - Crystal structure of Hap showing its c-axis perpendicular to 3 a-axes lying at 120°C angles to each other (adapted from ³).....	15
Figure 1.4 - Crystal form of hydroxyapatite mineral (re-printed from ¹⁷).....	16
Figure 1.5 - SEM image of hydroxyapatite crystals, with different sizes and morphologies, (adapted from ⁵⁷).....	22
Figure 1.6 - Schematic representation of a nanoparticle formed from an inorganic nanocrystal with an organic/inorganic compound bonded to its surface (adapted from ⁵⁴)	23
Figure 1.7 - Schematic diagram of the nucleation and growth process showing the dependence of the Gibbs free energy (ΔG) on the crystal radius. Below a critical radius (r^*), reversible events leading to clusters formation take place; for $r > r^*$ the process becomes irreversible (source ⁵⁴).....	24
Figure 1.8 - Scheme of nanocrystal growth controlled by: (a) Ostwald ripening mechanism; (b-1 and b-2) oriented attachment mechanism.....	26
Figure 1.9 - Schematic representation of the influence of citrate in bone formation (adapted from ⁷⁰).....	28
Figure 1.10 - Schematic representation of citric acid molecule (adapt from ⁷²).	29
Figure 1.11 - A proposed biological evolution of cell-nanoceramics interface according to <i>in vivo</i> and <i>in vitro</i> experimental results ³⁶	33
Figure 1.12 - Schematic representation of a smart biomedical nanodevice.	39
Figure 1.13 - Scheme of the interaction of a metal nanosphere with light showing the displacement of the conduction electron charge cloud relative to the nuclei (adapted from ¹¹¹).....	40

Figure 1.14 - Tunable optical properties of gold nanoparticles by changing the particle aspect ratio. Gold nanoparticles of different aspect ratio exhibit different dimensions as seen by TEM (a, b), different SPR wavelength (c) and in different colour (d, e) adapted from ^{114,115}	41
Figure 1.15 - Shows the UV-vis absorption spectrum of colloidal gold nanorods solution. The absorption band at 520 nm is the transverse mode of the surface Plasmon absorption, while the longitudinal mode absorbs around 800 nm for the nanorods, adapted from ¹¹⁰	42
Figure 1.16 - Schematic illustration of metal nanoparticles preparation methods ¹¹⁸	44
Figure 1.17 - Schematic representation of equilibrium between gold species according to pH (adapted from ¹²²)	45
Figure 1.18 - Schematic representation of dicarboxy acetone aurous complex species (adapted from ¹²⁰)	46
Figure 1.19 - Formation mechanism of AuNPs with various particle sizes and shapes by chemical reduction method	49
Figure 1.20 - Schematic illustration of how large and small gold particles penetrate through blood vessels at tumor sites due to their disordered endothelial cells (adapted from ¹¹⁷)	53
Figure 1.21 - Wavelength range of the near-infrared (NIR) tissue transmission window (adapted from ¹¹⁷)	54
Figure 1.22 - Chemical structure of folic acid (adapted from ¹⁴¹)	58

CHAPTER 2

Figure 2.1 - a) Schematic diagram of the oven setup used to precipitate hydroxyapatite particles. b) Detail of the calcium/citrate solution inside of the Teflon vessel; c) thermal cycle used for precipitating Hap particles	79
Figure 2.2 - Image of the thermostatic water bath used in WCS precipitation	80
Figure 2.3 - Schematic representation of the pore geometry, present in a porous material (adapted from ¹¹)	84
Figure 2.4 - Schematic representation of IUPAC classification of sorption hysteresis loops (adapted from ^{11,12})	84

Figure 2.5 - A portion of the electromagnetic spectrum showing the relationship of the vibrational infrared to other types of radiation ²³	89
Figure 2.6 - Typical molecular vibrations of the molecules (adapted from ²³).....	90
Figure 2.7 - Main types of interaction between a carboxylate ligand and a cation (adapted from ²⁴).	90
Figure 2.8 - Schematic representation of the structure of the electric double layer ²⁵	92
Figure 2.9 - Electronic transition and UV-visible spectra in molecules (adapted from ²⁷) .	94
Figure 2.10 - Schematic diagram of an HPLC unit (re-printed from ³¹).....	96
Figure 2.11 - Schematic overview of a typical flow cytometer setup (adapted from ³⁸)..	101

CHAPTER 3

Figure 3.1 - XRD patterns of Hap particles synthesized by HS method under different (Cit:Ca) ratios, after 24 hours.....	112
Figure 3.2 - TEM and SEM micrographs of Hap particles synthesized from solutions with different (Cit:Ca) ratios: (a) 3:1; (b) 3.5:1; (c) 4:1 and (d) 7:1.....	113
Figure 3.3 - TEM images of Hap particles precipitated at 180°C after 24 H from solutions with different (Cit:Ca) molar ratios: 3:1 (a, b); 3,5:1 (c, d); 4:1 (e, f) and 7:1 (g, h). Images f) and g) are amplified views of particular sample regions identified by dotted circles on the images e) and g), respectively.....	116
Figure 3.4 - Nitrogen adsorption and desorption isotherms of Hap particles synthesized from solutions with different Cit:Ca ratios.....	118
Figure 3.5 - FTIR spectra of Hap particles synthesized from solutions with different Cit:Ca ratios at 180°C during 24 hours.....	119
Figure 3.6 - FTIR results corresponding to Hap particles synthesized from solutions with different Cit:Ca ratios at 180°C during 24 hours: magnification of the 1900-1200 cm ⁻¹ spectral region.....	120
Figure 3.7 - Different coordination modes of carboxylate ligands to a surface metal cation (adapted from ³¹).....	121
Figure 3.8 - HPLC chromatogram corresponding to citric acid when using acetic acid as internal standard.....	122

Figure 3.9 - HPLC chromatogram of the Hap particles prepared under different Cit:Ca molar ratios after being dissolved in a phosphoric acid solution.....	122
Figure 3.10 - (a) Thermogravimetric and (b) Differential thermal analyses plots of Hap nanoparticles precipitated from solutions containing different (Cit:Ca) ratios: 3:1, 3.5:1 and 4:1. The dotted circles 1, 2 and 3 identify the endo and exothermic effects that accompany the weight losses Δw_1 , Δw_2 and Δw_3 , respectively.....	125
Figure 3.11 - TEM images of Hap nanoparticles precipitated from solutions containing (Cit:Ca)= (3:1) after different times: (a) 5 min, (b) 30 min, (c) 45 min and (d) 60 min.....	127
Figure 3.12- N_2 adsorption–desorption isotherms of Hap nanoparticles precipitated from solutions containing (Cit:Ca)= (3:1) after different times: (a) 15 min, (b) 45 min and (c) 60 min.....	128
Figure 3.13 - X-ray spectra of Hap nanoparticles precipitated from solutions containing (Cit:Ca)= (3:1) after different times: (a) 15 min, (b) 45 min and (c) 60 min.....	129
Figure 3.14 - (a) FTIR spectra of Hap nanoparticles precipitated from solutions containing (Cit:Ca)= (3:1) after different times: 15 min, 45 min and 60 min ;(b) FTIR details of the 1200-1800 cm^{-1} spectral region.....	131
Figure 3.15 - (a) Thermogravimetric plots and (b) Differential thermal analyses plots of Hap nanoparticles precipitated from solutions containing (Cit:Ca)= (3:1) after different times: 15 min, 45 min and 60 min.....	133
Figure 3.16 - XRD patterns of Hap nanoparticles precipitated from solutions containing (Cit:Ca)= (7:1) after different times: 45 min (HS 7:1/45) and 60 min (HS 7:1/60).....	134
Figure 3.17 - SEM and TEM images of Hap particles precipitated from solutions with a (Cit:Ca) ratio of (7:1) and after different times: (a, b) 45 min and (c, d) 60 min.....	135
Figure 3.18 - FTIR spectra of Hap particles obtained from solutions with a (Cit:Ca) ratio of (7:1), at 180°C and after different synthesis times (—) 45 min, (—) 60 min and (—) 24 hours. Figure 3.18 (A) covers the wavenumbers range of 400 to 1200 cm^{-1} and figure 3.18 (B) covers the range from 1200 to 1800 cm^{-1}	136
Figure 3.19 - (a) Thermogravimetric analysis (TGA) plots of Hap nanoparticles precipitated from solutions containing (Cit:Ca) ratios of (3:1) and (7:1), after 60 min.....	138

CHAPTER 4

Figure 4.1 - X-ray diffraction patterns (DRX) of (a) WCS particles (b) HS particles as prepared; (c) WCS _{ster} after being sterilized and (d) HS _{ster} after being sterilized.....	147
Figure 4.2 - TEM images of nano-Hap synthesized by (a) Wet chemical method (WCS) method, (b) Hydrothermal (HS) method, (c) nano-Hap WCS after sterilization in autoclave (WCS _{ster}) and (d) nano-Hap HS after sterilization in autoclave (HS _{ster})	148
Figure 4.3 - pH dependence of zeta potential (ξ) for the (a) WCS nanoparticles (b) HS nanoparticles; for the (c) HS _{ster} sterilized and (d) WCS _{ster} sterilized.....	150
Figure 4.4 - FTIR spectra of (a) WCS particles (b) HS particles as prepared; amplified view of FTIR spectra in the range of 400-2000 cm ⁻¹ for (c) WCS and (d) HS.....	152
Figure 4.5 - FTIR spectra of sterilized (a) WCS _{ster} particles, (b) HS _{ster} particles; amplified FTIR area of (c) WCS _{ster} particles and (d) HS _{ster} particles.....	155
Figure 4.6 - Cell viability/proliferation of MG63 cell cultures exposed to (a) WCS _{ster} and (b) HS _{ster} nanoparticles, during 3 and 6 days for a nanoparticles concentration range between (50-5000µg/ml). *Significantly different from control.....	157
Figure 4.7 - CLSM images of MG63 cell cultures exposed to the WCS _{ster} and HS _{ster} nanoparticles, for a nanoparticles concentration of 500 µg/ml, during 3 and 6 days.....	158
Figure 4.8 - Rate of apoptosis of MG63 cell cultures exposed to WCSster and HSster nanoparticles during 3 days for the 50 and 500 µg/ml concentrations.....	159
Figure 4.9 - Gene expression of Collagen I, ALP, BMP-2 of MG63 cell cultures exposed to WCS _{ster} and HS _{ster} nanoparticles, 50 µg/ml and 500 µg/ml, for 3 days. RT-PCR, the PCR products were subjected to a densitometric analysis and normalized: to the corresponding GAPDH value. *Significantly different from control.....	160
Figure 4.10 - Representative TEM micrographs of MG63 cell cultures exposed to WCS _{ster} nanoparticles, 50 and 500 µg/ml, during different periods (3 hours, 24 hours and 3 days). The development of pseudopods surrounding adjacent nanoparticles is observed in A (3 hours, 50 µg/ml) and B (3 hours, 500 µg/ml), D (24 hours, 500 µg/ml) and E (3 days, 500 µg/ml), depict clusters of nanoparticles entrapped in endosomes. Apart the entrapped nanoparticles within endosomes, it can be also observed in C (24 hours, 50 µg/ml) cellular debris in intercellular space. A cell with early signals of apoptosis, such as the rounded	

shape, the cytoplasmic vacuolization and signs of blebs formation is shown in F (3 hours, 50 $\mu\text{g/ml}$).....162

Figure 4.11 - Representative TEM micrographs of MG63 cell cultures exposed to HS_{ster} nanoparticles, 50 and 500 $\mu\text{g/ml}$, during different periods (3 hours, 24 hours and 3 days). A (3 hours, 50 $\mu\text{g/ml}$) and B (3 days, 50 $\mu\text{g/ml}$) depict the development of pseudopods surrounding nanoparticles and in D (24 hours, 500 $\mu\text{g/ml}$), E (3 days, 50 $\mu\text{g/ml}$), and F (3 days, 500 $\mu\text{g/ml}$) it can be observed clusters of nanoparticles entrapped in endosomes. An apoptotic cell with a rounded shape, condensed chromatin at nuclear periphery, cytoplasmic vacuolization and signs of blebs formation is shown in C (24 hours, 500 $\mu\text{g/ml}$).....163

Figure 4.12 - High magnification TEM images of MG63 cell cultures exposed to WCS_{ster} and HS_{ster} nanoparticles, 500 $\mu\text{g/ml}$, for 24 hours. A and E show the close interaction of the nanoparticles with the cell membrane, and B and F the intracellular vesicles loaded with the particles. C and G, a high magnification of B and F, respectively, display the nanoparticles within the intracellular vesicles, showing signs of particle dissolution. D and H display the electron diffraction patterns of the internalized nanoparticles.....164

CHAPTER 5

Figure 5.1 - Images of HS particles (a) as synthesized at 180°C or after reacting with hydrogen tetrachloroaurate solution during (b) 5 min, (c) 10 min and (d) 20 min.....177

Figure 5.2 - X-ray diffraction patterns of hydroxyapatite particles (HS) as prepared (a), and after reacting with H₂AuCl₄ solution during (b) 5 min, (c) 10 min and (d) 20 min.....178

Figure 5.3 - TEM images of HS particles coupled with Au nanoparticles after different reaction times with H₂AuCl₄ solution: 5 min ((a) and (c)) and 20 min ((b) and (d)).....179

Figure 5.4 - UV-Visible spectra of as prepared HS nanoparticles (a) and of HS-AuNPs after a reaction time of 5 min (b), 10 min (c) and 20 min (d).....182

Figure 5.5 - A) FTIR spectra of HS and HS-AuNPs nanoparticles; (B) Spectra magnification in the region of 1200-1900 cm^{-1} for HS (a) and for HS-AuNPs after different times of gold precipitation : 5 min (b), 10 min (c) and 20 min (d).....185

Figure 5.6 - Zeta potential (ξ) as a function of pH for: (a) HS nanoparticles, (b) HS-AuNPs after 5 min of synthesis and (c) AuNPs after 20 min of synthesis.....186

Figure 5.7 - Cell viability/proliferation of MG63 cell cultures exposed to HS, HS-AuNPs and HS-AuNPs-FA nanoparticles, during 1, 3 and 7 days for a nanoparticles concentration range between (1-500 $\mu\text{g/ml}$).....	188
Figure 5.8 - CLSM images of MG63 cell cultures exposed to the HS and HS-AuNPs, for a nanoparticles range concentration of 1-500 $\mu\text{g/ml}$, during 1 day.....	190
Figure 5.9 - CLSM images of MG63 cell cultures exposed to the HS and HS-AuNPs, for a nanoparticles range concentration of 1-500 $\mu\text{g/ml}$, during 3 days.....	191
Figure 5.10 - CLSM images of MG63 cell cultures exposed to the HS and HS-AuNPs, for a nanoparticles range concentration of 1-500 $\mu\text{g/ml}$, during 7 days.....	192
Figure 5.11 - Gene expression of RUNX-2, Collagen I, ALP, OC and OPG of MG63 cell cultures exposed to HS, HS-AuNPs and HS-AuNPs-FA nanoparticles, 100 $\mu\text{g/ml}$, during three days. RT-PCR, the PCR products were subjected to a densitometric analysis and normalization to the corresponding GAPDH value.....	193
Fig.5.12 - Schematic representation of (a) HapNPs (HS) and (b) HapNPs with gold (HS-AuNPs), both functionalized with folic acid (FA).....	197
Figure 5.13 - TEM micrographs of HS (a); HS-FA (b); HS-AuNPs (c) and HS-AuNPs-FA (d).....	198
Figure 5.14 - FTIR spectra of (—) HS nanoparticles, (—) HS-FA nanoparticles, (—) HS-AuNPs-FA nanoparticles and (—) FA.....	199

LIST OF TABLES

CHAPTER 1

Table 1.1- calcium phosphate minerals biologically relevant (adapted from ^{3,13,14}).....	13
Table 1.2- Chronological data on nano-hydroxyapatite synthesis.....	17
Table 1.3- Synthesis methods of various CaP nanostructures. Advantages and disadvantages.....	19

CHAPTER 2

Table 2.1- Literature-reported carboxylate stretching bands for the main coordination types between a carboxylate ligand and a cation (adapted from ²⁴).....	91
Table 2.2- Zeta potential and associate stability.	93
Table 2.3- Various types and applications of HPLC	97
Table 2.4 – Primers used on RT-PCR analysis of MG63 cell cultures.....	103

CHAPTER 3

Table 3.1- Characteristics of Hap particles precipitated from solutions with different (Cit:Ca) ratios.....	111
Table 3.2- Identification of the samples precipitated under different (Cit:Ca) ratios and during different times.....	126

CHAPTER 4

Table 4.1 Properties of hydroxyapatite particles obtained by wet chemical precipitation (WCS and WCSster) and by hydrothermal synthesis (HS and HSster): particles as prepared (WCS and HS, respectively) and after being sterilized (WCSster and HSster, respectively).....	149
--	-----

GLOSSARY OF SYMBOLS

λ	Wavelength of incident wave
D	Crystallite size (Å)
K	SHape factor
B	Diffraction peak width at half height
b	Natural width of the instrument
r	Radius
ε_m	Dielectric constant of the surrounding/embedding medium
d_{hkl}	Spacing between the planes in the atomic lattice
n	is a numeral
A	Absorbance
ε	Absorption coefficient
b	path length
c	concentration
R	Reflectance
S	Scattering coefficient
ε_r	Real part of the material dielectric function
ε_i	Imaginary part of the material dielectric function
ν	frequency
ξ	Zeta potential
h	Planck's constant

ABBREVIATIONS

NPs	Nanoparticles
Hap	Hydroxyapatite
Hap-NPs	Hydroxyapatite Nanoparticles
FA	Folic acid
WCS	Wet Chemical Synthesis
HS	Hydrothermal synthesis
WSC _{ster}	Hap particles sterilized and prepared by Wet Chemical method
HS _{ster}	Hap particles sterilized and prepared by Hydrothermal method
DRX	Powder X-ray diffraction analysis
TEM	Transmission Electron Microscopy
HRTEM	High-resolution Transmission Electron Microscopy
SEM	Scanning Electron Microscopy
SAED	Selected Area Electron Diffraction
EDX	Energy dispersive X-ray analysis
EDTA	Ethylenediamine Tetraacetic Acid
CLSM	Confocal Laser Scanning Microscope
FTIR	Fourier Transform Infrared Spectroscopy
UV	Ultra violet
DL	Interfacial double layer
HPLC	High-performance liquid chromatography
AuNPs	Gold nanoparticles
Au	Gold
ECM	Extracellular matrix
FDA	Food and Drug Administration
CaP	Calcium Phosphates
OR	Ostwald ripening
LSW	Lifshitz, Slyozov and Wagner model
OA	Oriented attachment
BCP	Biphasic calcium phosphate

β -TCP	β -Tricalcium phosphate
CE	Conformite Europeenne
DNA	Deoxyribonucleic acid
RNA	Ribonucleic acid
SPR	Surface Plasmon Resonance
TOAB	Tetraoctylammonium bromide
CTAB	Cetyl trimethylammonium bromide
PEG	Polyethylene Glycol
SERS	Enhanced Raman Scattering
RDI	Recommended daily intake
PT	Pterin ring
PABA	p-aminobenzoic acid
Glu	glutamic acid
FA	Folic acid
FR	Folate receptor
MW	Molecular weight
Cit	citric acid
Ca	calcium nitrate
HS-AuNPs	hydroxyapatite gold nanoparticles
HS-AuNRs	hydroxyapatite gold nanorods
HS-AuNPs-FA	Hydroxyapatite gold nanoparticles functionalized with folic acid
HS-FA	Hydroxyapatite nanoparticles functionalized with folic acid
MTS	Tetrazolium compound (3-(4,5-dimethylthiazol-2-yl)-5-(3-carboxymethoxyphenyl)-2-(4-sulfophenyl)-2H-tetra-zolium)
ALP	Alkaline phosphatase
Col1	Collagen type I
BMP-2	Bone morphogenetic protein-2
GAPDH	Glycerolaldehyde-3-phosphate dehydrogenase
OC	Osteocalcin
OP	Osteonectin
OP	Osteopontin
OPG	Osteoprotegerin

Runx-2	Runt-related transcription factor 2
Cit:Ca	Citrate: calcium ratio
HL	Hysteresis loop
SSA	Specific surface area
BET	Multipoint Brunauer-Emmett-Teller isotherm
AFP	α -Fetoprotein
TCP	Tricalcium phosphate
ACP	Amorphous calcium phosphate
MCPM	Monocalcium phosphate monohydrate
DCPD	Dicalcium phosphate dehydrate
OCP	Octacalcium phosphate
Gly	Glycine
PALS	Phase analysis light-scattering
SBF	Synthetic body fluid
rf	Radio- frequency
CaO	Calcium oxide
NIR	Near to the infrared
R	Ratio
PBS	Phosphate buffer solution
RT-PCR	Reverse-Transcription polymerase chain reaction

Introduction

The precise architectural manipulation of nano or microcrystals with well-defined morphologies and tunable sizes remains a research focus and a challenging issue in the materials science field because it is well-known that the properties of the materials are closely interconnected with geometrical factors such as shape, dimensionality and size ¹. Consequently remarkable efforts have been dedicated to develop new fabrication methods of a range of high-quality inorganic nanoparticles. Furthermore, the emergence of novel nanoparticles (NPs) is expected to contribute as well to considerable improvements of bioanalytical measurements as to cause a substantial progress *in vitro* and *in vivo* diagnostics and therapies ².

Despite the remarkable therapeutic potential of nanoparticles in medicine, the fundamental information regarding the physico-chemical interaction between NPs and cells is still relatively limited. It is known that cellular uptake of nanoparticles is modulated by size, shape and effective surface charge and surface functionalization ². Depending on the nature of the NPs, cell membrane may exhibit different penetration and cytotoxic response. It is thus important to develop new NPs and to correlate their physicochemical properties with the cellular response for enlarging the pool of knowledge in this field.

Nowadays one of the major challenges related to NP is to combine therapeutic ability with a molecular imaging approach in order to provide coupled diagnosis and therapeutic functionalities to NP thus enhancing their biomedical usefulness. An ideal solution would imply the development of a simple system that could simultaneously present biocompatible properties and work as contrast agent allowing image enhancement by imaging techniques. Several metallic NPs such as gold are being exploited as contrast agent to achieve this goal. Moreover for certain applications like cancer treatment, nanometric sized noble metal particles may further enable the possibility of photothermal therapy which would reinforce the NP therapeutic potential.

The awareness of these demanding issues has framed the present work which is centred on a material target currently considered as biocompatible and nontoxic,

i.e. hydroxyapatite (Hap), aiming to contribute to the development of novel biomedical applications and to deepen its underlying scientific knowledge. This general objective will be guided by the following specific goals: (1) to study the synthesis of Hap nanoparticles (Hap NP) for understanding the dependence of nanoparticle physicochemical characteristics on its specific synthesis conditions, (2) to study the functionalization of Hap NP with gold and with folic acid in order to impart the possibility of both imaging and therapy abilities to the synthesized NP thus addressing their usefulness for particular applications related to the treatment of cancer and (3) to examine the cellular response to the synthesized nanosized materials having diverse physicochemical attributes.

Therefore, the first objective of this work will be pursued through the study of Hap particle size and shape evolutions under the variations of the experimental parameters of an hydrothermal synthesis method assisted by citrate ion (Cit). The understanding of this organic additive role as tailoring tool of the various nano and micro sized morphologies of the obtained Hap particles will be attempted. Furthermore, in order to access the effects of Hap nanoparticles (Hap NP) morphological features on the elicited biological response, Hap NP produced by two different methods hence displaying distinct attributes (size shape and crystallinity) will be also addressed either “as prepared” or after the sterilization step prior to *in vitro* studies.

The functionalization of Hap nanoparticles with nanometric metallic gold (Au^0) will be also exploited through a novel synthesis approach which revisits the classical Turkevich method for gold precipitation. The properties of the newly obtained nanostructured materials (Hap-NPs with Au) will be discussed envisaging potential applications of (Hap-NPs with Au) that might benefit from coupled therapeutic and contrasting properties. Finally the conjugation of the produced particles with a vitamine such as folic acid (FA) which is claimed as a tumour targeting moiety, is also studied. The functionalization studies are complemented by *in vitro* essays aiming to access the cytotoxicity and gene expression induced by the synthesized particles on MG63 osteoblastic cells.

The present thesis is organized in 5 chapters. Chapter 1 is dedicated to literature review aiming to bring up to date the reader with the state of the art. Literature review will cover the fundamental characteristics of Hap particles, its synthesis approaches and then Hap particles medical applications. Finally the advantages of the functionalization of Hap-NPs surface for diagnostic and therapeutic purposes will be also reviewed.

In chapter 2 the experimental procedures used for the synthesis of both Hap and Hap-Au nanoparticles and for particles functionalization with FA are detailed. The characterization techniques used throughout this work for accessing the various properties of the synthesized materials will be also introduced.

The following chapters will present, analyse and discuss the experimental results obtained in the work under analysis. The results regarding the hydrothermal synthesis of Hap nano and microparticles with a controllable size and morphology are discussed in chapter 3. Hap crystals properties including microstructure, crystalline phase and functional groups are comparatively judged for particles precipitated under different amounts of organic additive (Cit) and after different growth time. Chapter 4 discusses the interaction with cells of Hap-NPs with distinct morphology obtained by two different methods. Cell proliferation, alkaline phosphatase and genetic markers were used in the assessment of the cellular responses.

The functionalization of Hap-NPs is presented and discussed in the last chapter (chapter 5) in which gold precipitation on Hap surface and FA conjugation are focused. Metallic particles morphology analysis is based on transmission electron microscopy and UV spectroscopy and FA functionalization accessed by Fourier transforms infrared spectroscopy analyses. This chapter is complemented by *in vitro* studies which examine MG63 osteoblastic cells response to the different produced Hap nanoparticles.

The final chapter presents the main conclusions and suggest future work to complement the studies undertaken in this thesis as well.

Chapter 1

Background on hydroxyapatite nanoparticles synthesis and functionalization

1.1. Introduction

It is the objective of this chapter to provide an overall survey of the basic concepts and up-to-date literature results concerning the use of hydroxyapatite and functionalized hydroxyapatite nanoparticles for medical applications. It includes a brief description of the crystal structure and important properties of hydroxyapatite, and a review of the current methodologies of hydroxyapatite synthesis. Finally the applications of hydroxyapatite particles in various areas of medicine are also described.

Metallic nanoparticles in special gold are currently receiving a great attention, mainly due to their excellent optical, imaging and therapeutic properties. For that reason, they were considered as good candidates to be targeted on hydroxyapatite nanoparticles. The main characteristics, synthesis methods and applications of gold nanoparticles will be also surveyed.

Finally, in order to optimize the potentialities of hydroxyapatite nanoparticles for medical applications, the main properties of a recognized vitamine, folic acid, and its potential to be attached to hydroxyapatite nanoparticles will be addressed.

1.2. Hydroxyapatite (Hap): an overview

1.2.1. Hap as the main inorganic constituent of bone

Calcium phosphate, in particular hydroxyapatite (Hap), has a high potential for healthcare applications due to its high biocompatibility which reflects the fact of being the inorganic mineral of mammalian bone and teeth ^{3,4}.

Bone provides the basic mechanical support to the body by transferring forces that are involved in locomotion but has also other functions ³. It has now been established that bone not only acts as a reservoir for minerals, primarily calcium and phosphate related ones, which circulate through blood in supersaturated concentrations, but also stores growth factors, fatty acids, heavy metals, and other toxic elements, besides being further involved in blood buffering by controlled

release of alkaline salts ³. Bones also provide physical protection to vital internal organs and some bones also act as production plant of red and white blood cells ³. Bone performance comes not only from the synergetic combination of its mineral and organic components properties, but also from its hierarchical, superstructural organization ³. Figure 1.1 shows the hierarchical architecture of bone, detailing its different hierarchical levels. The shape of the bone as it is known macroscopically in our body is shown in the first picture (figure 1.1 (a)). A deeper analysis and depending on the bone position it is possible to observe the spongy and cortical bone (figure 1.1 (b)) which is composed by cylindrical structures called osteons. In the center osteons (figure 1.1 (c)) large blood vessels are found ^{3,5}. The cylindrical structures called of osteons are formed by fibril bundles that are organized in arrays of lamellar structures with thickness of 3–7 μm ⁶ (figure 1.1 (d) and (e)). These arrays are mineralized collagen fibrils, linked by a protein phase (figure 1.1 (f) and (g)). The mineral phase present in collagen fibrils is composed by hydroxyapatite nanoparticles (Hap-NPs) ^{3,5}. Hap-NPs are responsible for imparting appropriate compressive strength, so that collagen fibers, able to dissipate energy effectively, provide superior elastic properties, thus improving the brittleness of the Hap ³. In an effort to develop systems that promote the development of bone tissue, several groups have studied the effect of scaffolds based on a combination of natural bone with the information provided to cells by the extracellular matrix (ECM) and hydroxyapatite, showing that there is an improvement in the growth of osteoblasts adhesion and stimuli for the mineralization, compared to matrices without hydroxyapatite. In the most recent years, scaffolds containing hydroxyapatite particles with various shapes and sizes have been produced and their bioactivity investigated ⁷. It was found that a nanocomposite scaffold coated with needle-shaped hydroxyapatite particles showed the strongest osteoblast differentiation profile compared with round spherical shaped particles ⁷.

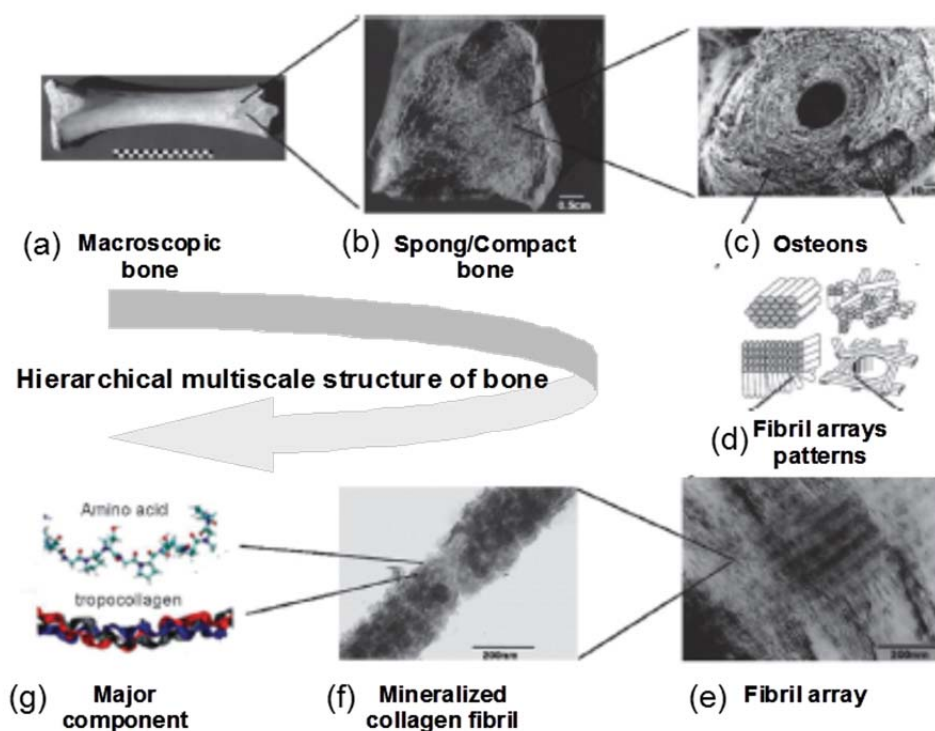


Figure 1.1- Hierarchical multiscale structure of bone, showing the different hierarchical levels (adapted from ⁶).

Biological mineralization (or biomineralization) is a process of *in vivo* formation of inorganic minerals. In the biomineralization processes, organized assemblies of organic macromolecules regulate nucleation, growth, morphology and assembly of inorganic crystals. Biologically calcium phosphates (biological apatite) formed *in vivo* under mild conditions are always nanodimensional and nanocrystalline. Two forms of Hap crystals can be distinguished in dentin and bone depending on their localization: extrafibrillar and intrafibrillar (figure 1.2) ³. According to many reports, at the nanostructural level, tiny plate-like crystals of biological apatite occur in bone within the discrete spaces of collagen fibrils and grow with a specific crystalline orientation along the *c* axis, which align roughly parallel to the longitudinal axis of the collagen fibrils ⁴. The apatite growth is somehow limited by the small intercollagenous spaces, which are approximately 50 nm in length, 25 nm in width and 2–3 nm thick ^{5,8}. Y. Cai et al. report a new model of “bricks and mortar” regarding the biological aggregation of apatite nanoparticles. According to their report an inorganic phase, amorphous calcium phosphate (ACP), acts as “mortar” to cement the crystallized “bricks” of nano-Hap. Meanwhile, biological

molecules control the nano-construction. For that is using Hap nanospheres as the building blocks, highly ordered enamel like and bone-like apatite are hierarchically constructed in the presence of glycine (Gly) and glutamate (Glu), respectively as observed in figure 1.2.

They also produce enamel-like apatites using bovine amelogenin. For that they use a concentration of 1.25 μM of amelogenin, and large enamel-like Hap mesocrystals were formed after 3 days, they observed that enamel-like apatites formation is about 20 times faster than with 10 μM glycine. This shows that this protein, a well-known effective modifier during *in vivo* tooth enamel formation, can dramatically accelerate the kinetics of nano-assembly and promote the formation of elongate apatite microstructures⁹.

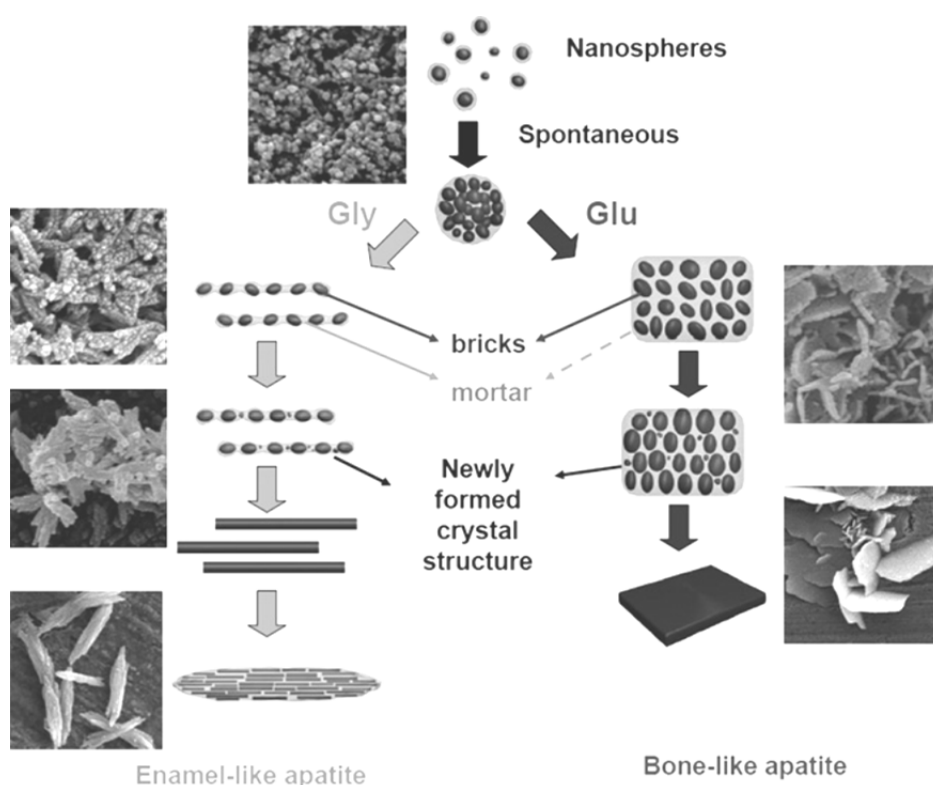


Figure 1.2- A schematic model of apatite evolution via the conglutination of “bricks (Hap) and mortar (ACP)”. Under the control of biological components such as glycine and glutamate, the Hap subunits can be re-organized (adapted from⁹).

1.2.2. Hydroxyapatite crystal structure issues

Owing to its chemical similarity to the calcium phosphate phase of human bone together with its biological performance, synthetic hydroxyapatite (Hap $\text{Ca}_{10}(\text{PO}_4)_6(\text{OH})_2$) has been recognized as an important bone substitute material in orthopaedics, dentistry and artificial implants. Moreover its biodegradation products, Ca^{2+} and PO_4^{3-} , are found in relatively high concentrations (about 1–5 mM) in the bloodstream¹⁰. Hap ceramics due to their natural occurrence, are classified as biocompatible and safe systems by the US food and drug administration (FDA)¹⁰ and are widely used in pharmaceutical technology^{11,12} being recommended by the World Health Organization and the European Pharmacopoeia¹⁰.

Calcium phosphate minerals can adopt numerous crystal structures depending on stoichiometry and conditions of formation and thus a number of other calcium phosphate minerals are known in addition to Hap (table 1.1) which details will not be analysed in this thesis.

Table 1.1- calcium phosphate minerals biologically relevant (adapted from^{3,13,14})

Mineral	Chemical formula	Ca/P ratio	Crystallographic characteristics	Solubility product (pK_{sp})
Monocalcium phosphate monohydrate (MCPM)	$\text{Ca}(\text{H}_2\text{PO}_4)_2\text{H}_2\text{O}$	0,5	Triclinic P1	Highly soluble
Dicalcium phosphate dehydrate (DCPD) (brushite)	$\text{CaHPO}_4\cdot\text{H}_2\text{O}$	1.0	Monoclinic C2/c	-6.4
Octacalcium phosphate (OCP)	$\text{Ca}_8\text{H}_2(\text{PO}_4)_6\cdot 5\text{H}_2\text{O}$	1.33	Triclinic P1	-46.9
Tricalcium phosphate (TCP)	α and β – $\text{Ca}_3(\text{PO}_4)_2$	1.5	β =rhombohedral R3c	-29.5
Hydroxyapatite (Hap)	$\text{Ca}_{10}(\text{PO}_4)_6(\text{OH})_2$	1.67	Hexagonal $\text{P6}_3/\text{m}$	-114.0
Fluoroapatite	$\text{Ca}_{10}(\text{PO}_4)_6\text{F}_2$	1.67	Hexagonal $\text{P6}_3/\text{m}$	-118.0

Hap is a mineral from the family of apatites, with general formula $\text{Ca}_{10}(\text{PO}_4)_6\text{X}_2$, where X is typically OH^- (hydroxyapatite Hap), F^- (fluorapatite), Cl^- (chlorapatite)¹⁵. In biological conditions, Hap can be subjected to an extensive substitution of ions. Thus human bone apatite is best described as $(\text{Ca},\text{Z})_{10}(\text{PO}_4,\text{Y})_6(\text{OH},\text{X})_2$, where $\text{Z} = \text{Na}^+$, Mg^{2+} , K^+ , Sr^{2+} , and so forth, $\text{Y} = \text{CO}_3^{2-}$, HPO_4^{2-} , and $\text{X} = \text{Cl}^-$, F^- ^{3,15}. In fact most of these impurities, except fluoride, contribute to the solubility increase of the resulting nonstoichiometric apatite. According to the literature, CO_3^{2-} is the most common impurity (3-8 wt %) in biological apatites, and the synthetic carbonated Hap is shown to have an improved bioactivity as compared with pure Hap, which has been attributed to the greater solubility of the carbonated phase³. The presence of CO_3^{2-} ions in the Hap crystal structure has also been shown to have a retarding effect on the crystal growth since it induces a reduction of symmetry, a decrease in the crystallite size and increased degree of distortion³.

The basic apatite crystal structure was published nearly simultaneously by Náray-Szabó and Mehmel in 1930¹⁵. The most frequently encountered structure of Hap belongs to a hexagonal system with $\text{P6}_3/\text{m}$ space group^{16,17} where the dimensions of the unit cell of the pure material were reported to range from $a=b= 9.398 \text{ \AA}$ to 9.438 \AA and $c= 6.868 \text{ \AA}$ to 6.887 \AA , with $\alpha=\beta= 90^\circ$ and $\gamma=120^\circ$ ¹⁸. A less common symmetry of Hap lattice is described by $\text{P2}_1/\text{b}$ space group within the monoclinic crystal system³. The two possible structural models of hydroxyapatite differ in the arrangement of the OH^- ions¹⁹. Furthermore, several substitution has an effect on the lattice parameters³. These changes in crystal lattice parameters are often correlated with changes in crystallinity, thermal stability, morphology, solubility and other physicochemical and biological properties of the material³. Biological Hap crystal surface is rarely smooth, and the reason is related to its biological application. The roughness of biological Hap, specially its surface irregularities, allow further adsorption of proteins and other biological molecules on its surface which benefits the biomineralization process³. Previous studies have shown that a rough surface improves the biocompatibility of the material and has a positive effect on inflammatory reactions, whereas the viability of monocytes seeded on flat surfaces tends to be far less³. Also, cells are constantly creating and

decomposing Hap in bone, and rougher surfaces provide conditions for an easier anchoring of cells.

The overall crystal structure of hydroxyapatite is indicated in figure 1.3. The optimized structure of hexagonal $P6_3$ Hap is characterized by two formula units per cell ($Z = 2$) and contains 44 atoms per unit cell ¹⁷. In the basal plane it is built up of a framework of PO_4 tetrahedra, where two oxygen atoms are located on a horizontal plane (with respect to the c-axis) and the other two are positioned on an axis parallel to the c-direction. Within the unit cell the PO_4 tetrahedra are situated in two layers, at a height of $\frac{1}{4}$ and $\frac{3}{4}$ of the unit cell respectively, and distributed in such a way that they form two types of channels perpendicular to the basal plane ¹⁶. The first type has a diameter of 2 Å and is occupied by calcium ions $Ca(I)$ where each unit cell contains two of these channels each containing two calcium ions, at heights of 0 and $\frac{1}{2}$ of the unit cell. The second type of channel (diameter 3-3,5 Å) has its walls formed by oxygen atoms and by $Ca(II)$ ions, located at heights of $\frac{1}{4}$ and $\frac{3}{4}$, which constitute two equilateral triangles perpendicular to the c-axis, offset from each other by a rotation of 60° . As a result, the overall shape of this second type of channel is hexagonal and it is here that the OH^- groups are located, although different anions (O, F, Cl) or impurities can be found in these channels as well ^{16,20}.

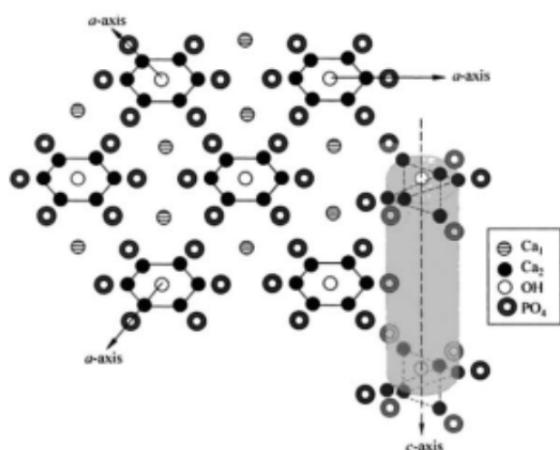


Figure 1.3- Crystal structure of Hap showing its c-axis perpendicular to 3 a-axes lying at 120° angles to each other (adapted from ³).

The Hap morphology usually is needle-like, as resulting from an oriented growth along the c-axis ¹⁷, which is thermodynamically favoured. The Hap crystal faces are responsible for the macroscopic crystal morphology as shown in Figure 1.4.

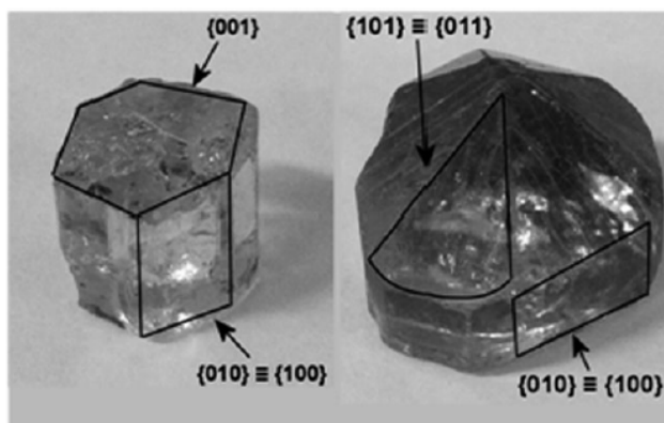


Figure 1.4- Crystal form of hydroxyapatite mineral (re-printed from ¹⁷).

It has been observed that during bio-mineralization of teeth hard tissues (dentine and enamel) crystal growth occurs mainly perpendicular to the (001) plane, i.e. along the c-axis ¹⁷. Still, these faces ((010) and (100)) appear during the uninhibited growth of the Hap crystal and determine a morphology transformation from needles to plates. It is clear that, because Hap crystals are elongated along the c direction in bones and during bio-mineralization of tooth hard tissue, the (100) plane is the most developed, being responsible for the interaction with molecule ¹⁷.

Nowadays several studies based on computational calculations have been carried out aiming to contribute for a better understanding of the interaction between molecules and the surface of minerals, including hydroxyapatite ^{18,20-23}. From these studies, it is possible to estimate which surface has a lower energy and which are the cleavage planes. Most of the works published refer the {0001}, {1010} and {1011} planes as hydroxyapatite cleavage plane based on experimental evidence that these faces act as the binding surface for many anionic species, including small molecules, polymers and anionically modified cell surfaces ^{18,20}. Considering the computational models developed by P.B. Ray et al. in 2002, and the experimental results obtained by W.A. Rachinger in 1982 it was

found that the cleavage plane for apatite is (100)^{21,24}. The presence of a cleavage plane is important, since the highest defect density is concentrated in that plane and it is possible to predict the growth of the hydroxyapatite particles along this cleavage plane.

1.2.3. Synthesis methodologies of Hydroxyapatite nanoparticles

Nanosized and nanocrystalline bioceramics clearly represent a promising class of orthopaedic and dental implant formulations as well as drug delivery systems with improved biological and biomechanical properties when compared with other class of materials. In general, nanostructured materials offer improved performances as compared to their larger sized counterparts due to their larger surface-to-volume ratios which turn them a kind of bridge between single molecules and bulk material systems⁵. Recently, numerous efforts have been devoted to the development of synthesis approaches of nanostructures able to ensure a close size and shape control. Chronological data regarding the synthesis of nanosized apatites are presented in Table 1.2^{5,25}. In general, the shape, size and specific surface area of the apatite nanoparticles appear to be very sensitive to both the reaction temperature and the reactant mode addition.

Table 1.2- Chronological data on nano-hydroxyapatite synthesis.

Year	Synthesis Process
1995	Synthesis of nanocrystalline hydroxyapatite (particle size ~20 nm) for the first time using calcium nitrate and ammonium hydrophosphate as precursors by solution spray dry method ²⁶
2000	Synthesis of biomimetic nano-sized Ca-hydroxyapatite powders (~50 nm) at 37°C and pH of 7.4 from calcium nitrate tetrahydrate and diammonium hydrogen phosphate salts in synthetic body fluid (SBF) using novel chemical precipitation technique ²⁵
2002	Preparation of nano-sized hydroxyapatite particles and hydroxyapatite/chitosan nano-composite ²⁷
2002	Direct precipitation from dilute calcium chloride and sodium phosphate solutions ²⁸
2003	Radio frequency (rf) plasma spray process employing fine spray dried (SD)

	Hap powders (average size $\sim 15\ \mu\text{m}$) as feedstock ²⁹
2003	Sol–gel process using equimolar solutions of $\text{Ca}(\text{NO}_3)_2 \cdot 4\text{H}_2\text{O}$ and $(\text{NH}_4)_2\text{HPO}_4$ dissolved in ethanol solvent ³⁰
2003	Chemical precipitation through aqueous solutions of calcium chloride and ammonium hydrogen phosphate ³¹
2003	Mechanochemical synthesis of nano-Hap and TCP powders using calcium hydrogen phosphate ($\text{CaHPO}_4 \cdot 2\text{H}_2\text{O}$) and calcium oxide (CaO) as starting materials ²⁵
2003	Synthesis of Hap nano-powders via sucrose-templated sol–gel method using calcium nitrate and ammonium hydrogen phosphate as precursor chemicals ³²
2004	Hydrolysis method by hydrolysis of dicalcium phosphate dihydrate ($\text{CaHPO}_4 \cdot 2\text{H}_2\text{O}$, DCPD) and CaCO_3 with 2.5 M NaOH (aq) ³³
2004	Citric acid sol–gel combustion process using calcium nitrate, diammonium hydrogen phosphate and citric acid ²⁵

The synthesis of calcium phosphate nanostructures where Hap-NPs are included, can be performed by using a wide variety of methods, such as: wet chemical precipitation^{34,35}, sol-gel processing⁵, co-precipitation, emulsion technique, hydrothermal process, mechanochemical method, ultrasonic technique, template method, microwave processing, emulsion hydrothermal combination, and microwave hydrothermal combination²⁵. Table 1.3 summarizes the synthesis methods of calcium phosphate (CaP) nanostructures as well as their own advantages and disadvantages³⁶. Using these methods, a variety of nanoscale calcium phosphate particles with different structures and morphologies have been synthesized, including needle-like, spherical, fibrous, mesoporous nanocrystals, nanorods, hollow nanospheres, layer nanostructures and flowers^{34,37-39}. In this thesis, a particular attention will be paid to two synthesis methods, the wet chemical method and the hydrothermal method. Both are relatively simple and low cost methods easy to be controlled.

Table 1.3- Synthesis methods of various CaP nanostructures. Advantages and disadvantages.

Synthesis methods	Nanocrystals morphological attributes	Advantages/Disadvantages
Sol-gel processing ^{30,40,41}	Aggregated nanocrystals	<p>The crystals with high purity and homogeneous components can be synthesized easily using simple experimental apparatus.</p> <p>Requires a high sintering temperature and is a time-consuming process.</p>
Co-precipitation ^{31,42}	Needle-like, spherical and rod-like nanocrystals	<p>Low-cost process allowing the easy synthesis of crystals possesses bone-like structures. The use of biomacromolecules allows controlling the particle aggregation.</p> <p>The products have low crystallinity and are easily aggregated.</p>
Emulsion technique ^{43,44}	Needle-like, spherical nanocrystals, nanorods and nanoplates	<p>The size and morphology of the products can be well controlled and the products exhibit low aggregation and narrow diameter distribution.</p> <p>Requires a high sintering temperature and is a time-consuming process. The reaction system is complex.</p>
Hydrothermal process ^{45,46}	Needle-like, spherical and fibrous nanocrystals and nanorods	<p>Particles have high cristalinity and purity and are well dispersed particle size and morphology can be well controlled.</p> <p>Time-consuming process.</p>
Mechanic-chemical method ⁴⁷	Fibrous and spherical nanostructures	<p>Simple and low cost method without high sintering temperature needs.</p> <p>Nanocrystals tend to aggregate. Special equipments are required</p>

Ultrasonic technique ³⁶	Needle-like and spherical nanocrystals	<p>The products have low aggregation and narrow diameter distribution; fast crystallization is obtained at low temperature.</p> <p>Needs special equipment and the yield is very low.</p>
Template method ^{48,49}	Nanorods, nanoplates, mesoporous and fibrous nanostructures, flowers and layer structures	<p>The structure, morphology, size and array of the products can be well controlled.</p> <p>Needs to employ template agents and high sintering temperature and is a time-consuming process; low yield.</p>
Microwave processing ^{36,50}	Rod, needle-like and flower structures	Needs special equipment and is difficult to apply to large-scale synthesis.
Emulsion-hydrothermal combination ^{51,52}	Spherical, rod, fibrous and strap-like structures	<p>The method avoids particle aggregation and growth and the final products have narrow diameter distribution; the size and shape of products can be well controlled under low temperature.</p> <p>Needs special apparatus and is a time-consuming process; the reaction system is complex and the yield is very low.</p>
Microwave-hydrothermal combination ⁵³	Needle-like and spherical crystals	<p>This method is fast and no high temperature is needed; The synthesized products have high crystallinity.</p> <p>Requires special apparatus and the yield is very low.</p>

1.2.4. Hydroxyapatite particles: nucleation, growth and morphology

In the last two decades, the study and development of nanomaterials including the chemical synthesis of inorganic nanocrystals has made remarkable progress. Chemical synthesis approach allows hydroxyapatite nanocrystals with different sizes and morphologies to be obtained, as shown in figure 1.5. Nanocrystals may not be merely objects of nanoscale dimensions. Rather, nanocrystals can be complex objects as illustrated in figure 1.6⁵⁴. As observed one of the inorganic nanocrystal constituents is a nanoparticle (with dimensions of 1 to 100 nm), with a single crystallographic domain. Moreover, due to their large proportion of surface to bulk atoms, nanocrystals present different types of organic and/or inorganic compounds or ions chemically or physically adsorbed. The presence of these adsorbed compounds may play an important role in their size and shape control, as well as in stabilizing and functionalizing the synthesized material⁵⁴⁻⁵⁶.

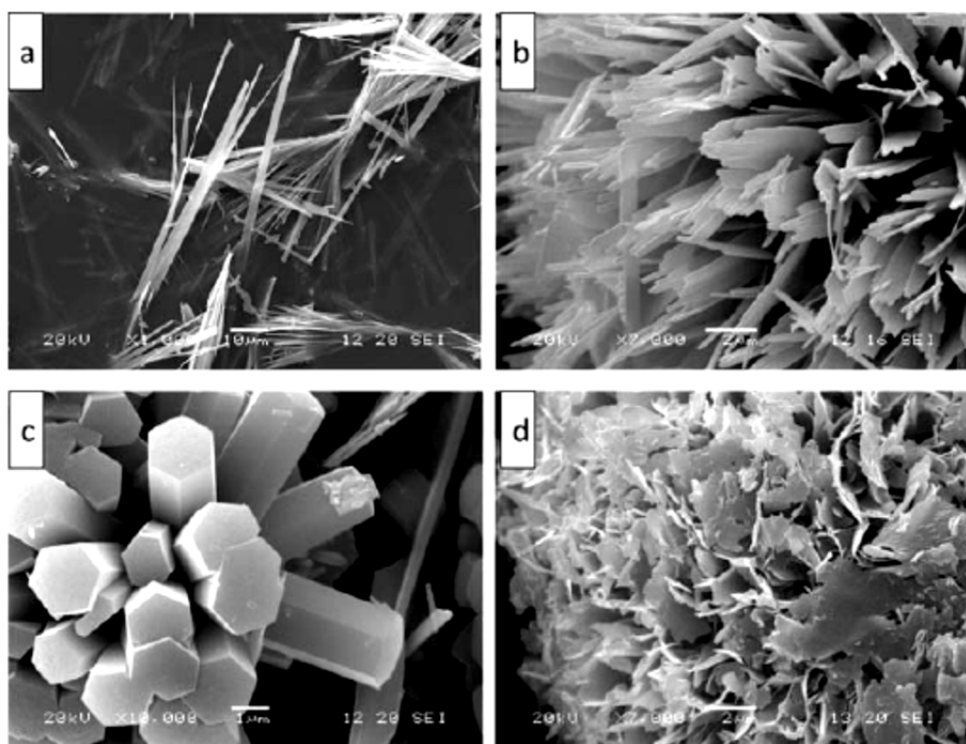


Figure 1.5- SEM image of hydroxyapatite crystals, with different sizes and morphologies, (adapted from⁵⁷).

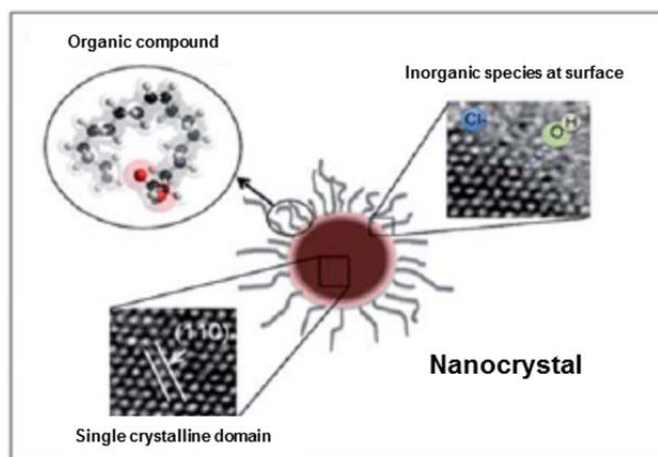


Figure 1.6- Schematic representation of a nanoparticle formed from an inorganic nanocrystal with an organic/inorganic compound bonded to its surface (adapted from ⁵⁴).

Another important point to be considered is the fact that during the genesis of nanocrystals, a phase-separation process takes place, which is generally described by a nucleation step followed by a growth process. According to the classical theory, nucleation can be described as the formation of “clusters” of chemical units (ions or molecules), i.e, the so-called critical nuclei, having such a critical size that a further unit addition causes its free energy to decrease. The Gibbs free energy curve depicted in figure 1.7 illustrates this process. The critical cluster formation may imply primary clusters formation (step 1) and cluster dimension increase (step 2) which are reversible events. When the critical size (r^*) is reached then a critical nucleus is formed and its natural growth will proceed (step 3) as it is a process accompanied by energy decrease being thus irreversible (thermodynamics condition). In many precipitation processes the use of stabilizers may help to control crystal size (step IV the figure 1.7) ⁵⁴.

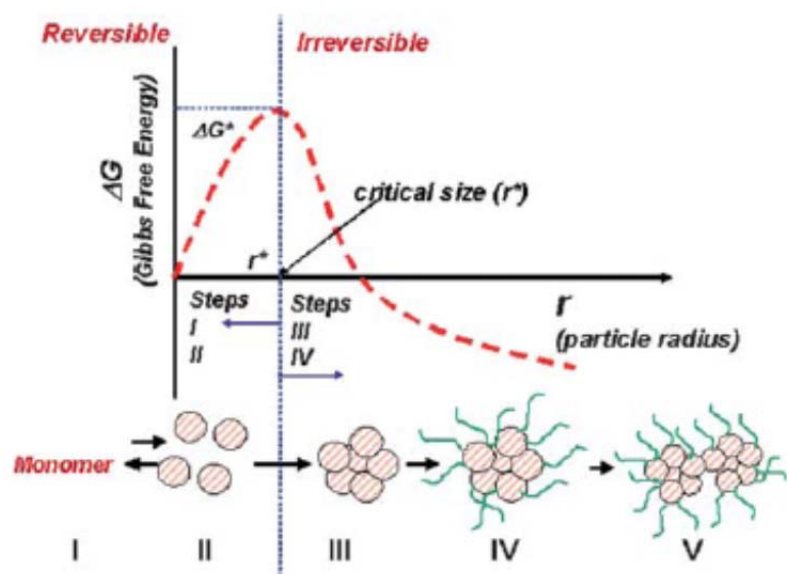


Figure 1.7- Schematic diagram of the nucleation and growth process showing the dependence of the Gibbs free energy (ΔG) on the crystal radius. Below a critical radius (r^*), reversible events leading to clusters formation take place; for $r > r^*$ the process becomes irreversible (source ⁵⁴).

To a first approximation, the shape of the crystal is controlled by energetic arguments (this is a thermodynamic condition). Geometric arrangements that minimize the surface energy will frame the cluster growth as proposed by Wulff, being this an important argument for predicting the final shape of a nanocrystal ^{54,58,59}. However molecules, ions or clusters can interfere in the process by undergoing preferential on the growing particle surface or by promoting adsorption/desorption of a stabilizer, thus originating an anisotropic crystal. In fact, the size and shape of nanocrystals have been controlled using a suitable combination of stabilizers and/or solvents. As illustrated in the last step (step V) interaction of the growing nanocrystals (step IV) may take place hence producing larger structures. This nanocrystal based self-assembly process is governed by particle–particle and particle–solvent interactions. Thus agglomerated (disordered assembly) nanocrystals or mesocrystals (mesoscopically structured crystals) may be formed. Needless to say, the above described process is an ideal one. One of the major obstacles to achieve a good control of the colloidal synthesis of nanocrystals is to separate the nucleation events from the growth process, and thus the synthetic routes that succeed to produce nanocrystals with controlled

size, size distribution and shape are directly correlated with the ability of controlling the nucleation and growth processes^{5,25,34,59,60}. Therefore particulate systems that present non uniform particle size and shape are often considered to reflect the overlap of both processes which may further affect particle morphology if significant particle size disparities are observed. This will be a fertile field for Ostwald ripening (OR). Ostwald ripening (OR) theory has been generally used to explain some crystal growth processes where larger particles grow at the expense of smaller ones^{54,61}. This mechanism contributes to the decrease of the system Gibbs free energy since as the smaller particles undergo solubilisation, their large surface energy contribution vanishes hence decreasing the overall system energy.

However in recent years, several studies have pointed out the inability of OR theory to describe adequately particle growth kinetics in several systems^{54,61,62}. The main reasons for this lack of agreement between theory and experimental data have been referred as; (a) the non-equilibrium condition between the solubilisation and precipitation processes contrarily to OR assumptions (b) the very low solubility of some inorganic compounds, even at the nanoscale and (c) the formation of nanostructures with complex shapes and the presence of defects, e.g., dislocations and planar defects. In the late 20th century, Penn and Banfield identified an important crystal growth mechanism of nanoparticles referred as “oriented attachment (OA)” or “oriented aggregation”⁶²⁻⁶⁴. This mechanism is based on the spontaneous self-organization of adjacent nanocrystals, resulting in particle growth by surface addition of a solid particle so that a common crystallographic orientation is shared following particles joining at a planar interface. Nanocrystal growth via the OA mechanism generally leads to the formation of anisotropic nanocrystals and particles with irregular shapes by consuming primary nanocrystals as “building blocks”, and the growth rate is size-dependent^{54,61,62}. OA has been identified as the predominant growth mechanism during the synthesis or hydrothermal/solvothermal treatment of several materials^{54,61-64}. One of the characteristics of the OA mechanism not found in the OR mechanism is the presence of a solid–solid interface between the nanocrystals, indicating that the growth process begins only after contact is established between particles, as schematically illustrated in Figure 1.8. The oriented attachment

mechanism has not been currently referred for describing the formation of hydroxyapatite nanoparticles⁶⁵.

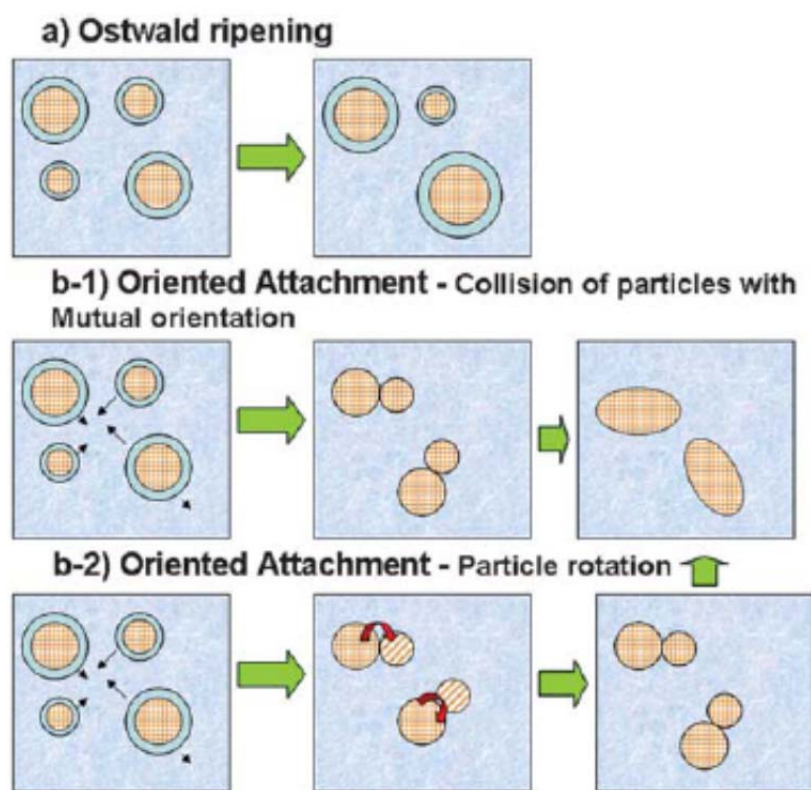


Figure 1.8- Scheme of nanocrystal growth controlled by: (a) Ostwald ripening mechanism; (b-1 and b-2) oriented attachment mechanism⁵⁴.

The synthesis of a nanocrystal is not a simple task, because it requires control over the chemical composition, size, size distribution and shape of the crystallographic phase, as well as the chemical state of the nanocrystal surface^{54,55,57}. Detailed investigations of nanocrystals growth process for understanding the experimental parameters determining crystal size and shape development are fundamental to build a tailoring ability of new nanostructured functional materials or to develop chemical protocols of high yield for producing nanocrystals with high reproducibility^{54,66,67}.

1.2.5. Citric acid and biological Hydroxyapatite particles

The control of particle size and shape in chemical synthesis methods at the nanometer level is commonly achieved by using organic molecules, usually

surfactants. Depending on the nature of the surfactant this could be a drawback as the surfactant can bind to other active agents especially biological molecules that can be used as drug.

Alternative approaches may rely on simpler organic molecules with physiological functions acting as solvent or reactant and/or as ligand for the control of the crystal size and shape may be suggested. By properly choosing organic additives that might have specific molecular complementarity with their inorganic counterparts, the growth of inorganic crystals can be rationally directed to yield products with desirable morphologies and/or hierarchical structures. Small chelating ligands such as citric acid known for their metabolic functions have already been used as “shape modifiers” to adjust and control the size and morphology of precipitated products. These organic molecules have been referred to modify the hydroxyapatite crystal growth by either promoting or inhibiting the crystal growth along specific crystallographic facets^{68,69}.

According to literature, Hap crystal dimensions, particularly the crystal thickness, are critical to the mechanical properties of bone, since a thickness of ~3 nm can prevent the propagation of cracks⁷⁰. Also, recent research showed that desirable osteoconductivity could be achieved with synthetic Hap resembling bone minerals in composition, size, and morphology⁷⁰. Many studies on bone biomineralization have been focused on the identification of proteins promoting or inhibiting the apatite crystal formation, such as a series of Glx-proteins⁷⁰. It has been hypothesized that proteins, such as osteocalcin provide recognition mechanisms of Hap surface and thus control the growth of biological crystals Hap⁷⁰. However, a recent and closer examination of the interface between collagen and bone apatite crystals by advanced solid-state NMR techniques (figure 1.9)⁷⁰ has revealed that citrate is the dominant organic ion at that interface, tightly bound to apatite and covering the surface with a density of one citrate molecule per 4 nm² (ca. 1/6 of the available area). About 80 wt % of the total body citrate is accumulated in bone. Carboxylate groups are key entities for regulating the formation of apatite, since they enable the molecular control of the size and stability of hydroxyapatite (Hap) nanocrystals in bone and *in vitro*⁷⁰. According to

Y.Y. Hu et al. citrate must remain in bone as an interfacial component that affects properties of the bone nanocomposite more profoundly than do simple substitutions of carbonate for phosphate or of sodium for calcium in apatite crystal lattice⁷¹. They propose that citrate bound to the nanocrystal surface stabilizes the apatite nanocrystals by preventing their further growth^{70,71}. Additionally, it is described in literature that citrate in bone provides more carboxylate groups than all the proteins other than collagen taken together. *In vitro* studies have shown that citrate in bone at higher concentrations results in smaller Hap nanocrystals⁷⁰.

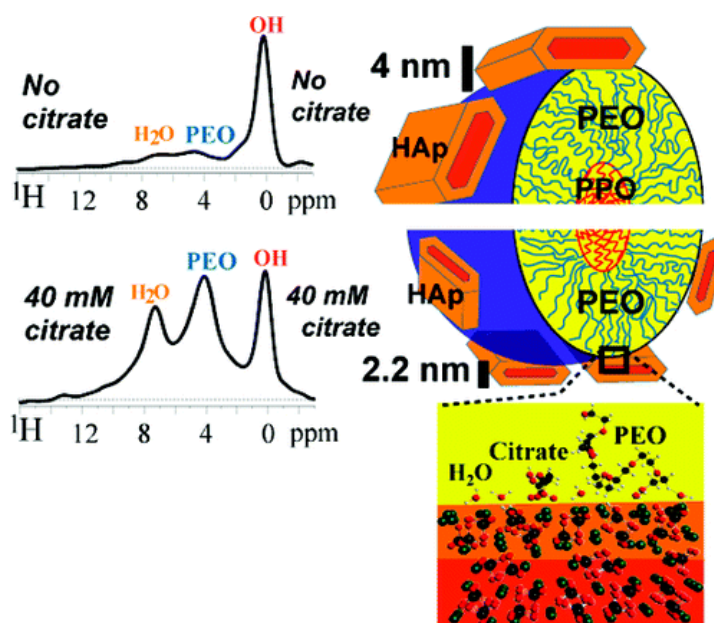


Figure 1.9- Schematic representation of the influence of citrate in bone formation (adapted from⁷⁰).

Moreover, citrate stabilizes Hap⁷⁰ and synthetic materials pre-treated with citrate give better biocompatibility in tissue repair⁷⁰. Despite these studies, the effect of citrate on Hap is still not well understood. Citrate molecules have three carboxyl groups with pKa values of 3.1, 4.8, and 6.4. At pH =7.5-8 they are completely ionized and can bind strongly to Ca^{2+} on Hap surface. Studies on citrate in natural bone⁷⁰ or on citrate *in vitro* interaction with Hap⁷⁰ have revealed that citrate is found on the surface of apatite crystals without being incorporated within the crystal lattice, due to the relatively larger size of citrate ion (figure 1.10) as compared with Hap lattice ions such as phosphate or OH^- . This indicates that once a citrate molecule occupies a certain surface area of a growing Hap particle, a

further crystal growth on the top of that area will be inhibited unless the citrate species departs or undergoes surface diffusion. In addition, surface-bound citrate molecules generate a negatively charged surface area,⁷⁰ which repels negatively charged phosphate ions, thus hindering further crystal growth. Via electrostatic repulsion, the negatively charged apatite surface also makes difficult the aggregation of the primary crystallites into bigger particles⁷⁰.

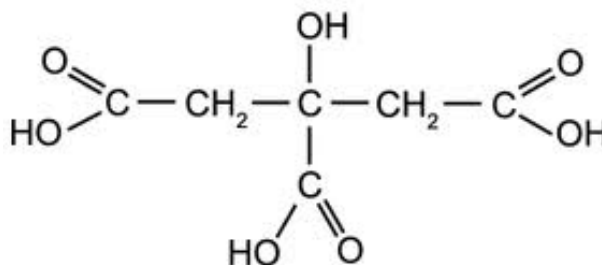


Figure 1.10- Schematic representation of citric acid molecule (adapt from ⁷²).

Citrate binding to biological apatite can help to understand the mechanism of apatite morphology control *in vivo* and to explain why the crystal morphology of apatite in bone is plate-like, whereas it is rod-like in human tooth enamel. The main reason is because the amount of citrate in both biological environments is quite different. In bone, it is relatively large at 5 wt% of the organic components⁷³.

According to X. Baoquan and H.Nancollas⁷³ both terminal carboxylate groups of citrate can interact with calcium ions of Hap at a distance of 0.3 nm, and all citrate carbons are found at approximately 0.4 nm from the top phosphate layer; the long axes of the citrate molecules are nearly parallel to the apatite surface, and the citrate methylene groups face outward. This unique high binding structure reduces the hydrophilic character of the surface, making it more compatible with the nonpolar proline and alanine residues of the collagen matrix. In this way, it decreases the interfacial energy between the thickness of nanocrystal and collagen layer and provides good interfacial compatibility. It also can help direct apatite nanocrystal growth, with the c-axis oriented along the long axis of a collagen fibril⁷³. This may be a reason for the formation of layer-by-layer composite structures frequently found in biological systems such as bones and teeth⁷³. However other alternative models have been proposed for citrate

interaction with Hap surface as is the case of W. Jiang et al.⁷⁴ who suggested that citrate ion coordinates only one surface calcium ion through a terminal carboxylic group. This coordination mode would facilitate the self-assembly of citrate molecules by intermolecular hydrogen bonding⁷⁴. Thus citrate interaction with Hap surface is still an issue under discussion.

1.2.6. Influence of citric acid on Hap synthesis

Focusing specifically on the role of citrate ion (Cit) as additive during the formation of hydroxyapatite nanoparticles, some phenomena related to the presence of Cit in the precipitating medium are interesting^{34,75}. When starting from an aqueous solution of Hap precursors added with citric acid, the strong chelation ability of citrate ion towards Ca^{2+} reduces the effective concentration of free Ca^{2+} in solution, thereby lowering Hap nucleation rate. It is possible that citrate-chelated calcium ions, such as $(\text{CaCit})^-$ and $\text{Ca}(\text{HCit})$, directly take part in the nucleation process^{34,75}. Once Hap particles are precipitated and regardless particle growth mechanism, the as-produced Hap particles are coated with citrate ions^{34,75}. These citrate ions have been considered important players at the Hap surface: their adsorption on early precipitated Hap particles (primary Hap particles) contributes to their surface energy reduction hence hindering the contact between Hap particles and the surrounding aqueous solution that otherwise would undergo an aggregation process. Furthermore particle coverage with Cit might help preventing crystal growth, particularly of citrate-covered facets, favoring the formation of needle-like Hap particles.

Citrate role is also affected by temperature^{34,35,75,76}. A temperature dependent adsorption mechanism of Cit on Hap surface was considered to account for the variation of Cit stabilization ability towards Hap particles. At a low-temperature the strong interaction between carboxylate ($-\text{COO}^-$) and Ca^{2+} may explain the linking ability of Ca sites belonging to two different Hap primary particles which may easily aggregate forming larger precipitates^{34,75}. As temperature increases according to C. Li et al.⁷⁵ the interactions between citrate and calcium ions are weakened, thus favouring the interruption of some inter-particle citrate–calcium links and hence the

increase of Hap particles negative surface charge. Consequently repulsive interparticle interactions arise, which in turn enable primary particles of large aggregates to get separated from one another ⁷⁵.

1.2.7. *In vitro* and *in vivo* performance of Hydroxyapatite nanostructures

In comparison with the conventional CaP porous ceramics, the nanomaterials that are composed of nanoscale grains and have high specific surface area surely possess micro/nanoscale porosities and more favourable surface topography ³⁶. These structural advantages are anticipated to display higher bioactivity and unexpected biological properties ³⁶. Unfortunately, little attention has been paid to the study of the biological effects to the CaP nanoparticles ³⁶ and only recently start to emerge some biological work with hydroxyapatite nanoparticles.

It is well known that the formation of a normal tissue goes through a series of cell biological actions, including proliferation, differentiation, and ultimately, spatial organization. Cell differentiation will be regulated by a cascade activated gene expression guided by the biological environment and tissue inducible factors to initiate and regulate substantially cell actions thereof ³⁶. When implanted into the body, biomaterials such as Hap, affect the biological environment and actions of cells, thus being able to participate in cell gene expression regulation and ultimately to induce cell differentiation into specific lineages. Hydroxyapatite nanostructures, normally presenting more sophisticated morphologies and structures than Hap microstructures, are expected to have higher bioactivity, hence with higher ability to affect the biological actions of cells ³⁶. Previous studies have indicated that a layer of bone-like nano apatite crystals formed on the surface of CaP particles with specific composition and structure can adsorb many osteogenic proteins, especially small molecular proteins which are selectively adsorbed (e.g. growth factors) ³⁶. However, when the surface topography of the biomaterials is nanostructured, the characteristics of surface protein adsorption are largely changed ³⁶.

Natural bone tissue can auto repair and heal, but synthetic biomaterials cannot. The key issue is that synthetic biomaterials for bone replacement do not display

osteoinductivity³⁶. This properties gap has driven humans to mimic the structures and properties of natural bone aiming to develop a new generation of biomaterials that might regulate the specific gene expression to differentiate along specific lineages, and ultimately regenerate the living tissues with the help of the body itself³⁶. To achieve this goal, the main strategies have incorporated growth factors or cultured living cells into materials scaffolds³⁶. However, due to the high cost of growth factors and a time-consuming process of cell culture, the clinical use of these biomaterials has been limited³⁶. Another important factor, affecting the osteoinductivity of the CaP particles is the phase composition. It is known that new bone tissue formation is preferentially induced by biphasic calcium phosphate (BCP) ceramics rather than by Hap ceramics. In the BCP, the high solubility of β -TCP phase (~40%) allows Ca^{2+} and PO_4^{3-} ions to be released. It is generally accepted that these ions can participate in the growth of a bone-like apatite layer at the ceramic surface under the regulation of endogenous biological molecules, which play crucial roles on affecting the biological behaviours of cells and provide the Ca^{2+} ions for new bone formation. It is also accepted that the released Ca^{2+} transmits a signal to a receptor on cell membranes thus affecting cell differentiation³⁶. Based on biological tests, a biological response of cell-nanoceramics interface can be proposed with respect to the osteoinductivity of the nanoceramics (fig 1.11)³⁶.

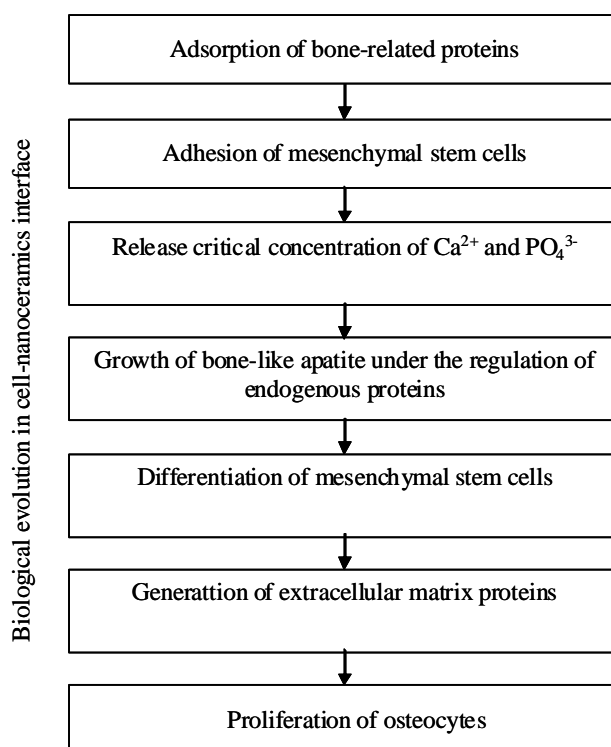


Figure 1.11- A proposed biological evolution of cell-nanoceramics interface according to *in vivo* and *in vitro* experimental results ³⁶.

Because of their nanoscale dimensions and hence large specific surface area, nanomaterials exhibit remarkable properties that favour biomedical applications ³⁶. Therefore it is necessary to investigate the potential threats of the CaP nanoparticles before clinic use. Ten years ago, Aoki et al. reported that the medium lethal dose of hydroxyapatite-sol (mean length: 50 nm, diameter: 10 nm) by injection into rats and dogs vein was determined as 160 mg/kg of animal. The main reason for hydroxyapatite-sol injection induced death was due to blockage of the capillaries. Injecting one-sixth of the medium lethal dose (i.e., 26 mg/kg) into veins, the blood components and pH, O₂ and CO₂ partial gas pressure, serum ions and enzymes undergo a change, but return to a normal state after one day. Repeated experiments by similar methods during 2 years showed that Hap nanoparticles would not cause chronic damage or permanent side effects to the living body by injecting less than one-sixth of medium lethal dose into blood ⁷⁷. It can be thus concluded that bellow a specific concentration Hap nanoparticles are safe.

According to literature, Xi's group has used neutron-activated Hap nanoparticles (length: 60–150 nm, diameter: 20–50 nm) to examine the *in vivo* distribution of the Hap nanoparticles via intravenous administration in mouse models ³⁶. They observed that after 1 h, lung, liver, and spleen present the highest concentration of the Hap nanoparticles, which is six-times higher than in other organs. After 72 h, however, the amount of these nanoparticles has decreased significantly in those three organs, suggesting that the Hap nanoparticles can be metabolized or excreted ³⁶. The study also showed that the concentration of the Hap nanoparticles in bone decreases gradually with time in other organs except in bone. The decrease can be well understood because a significant amount of nanoparticles has been metabolized or excreted. Contrarily in bone, the amount of the Hap nanoparticles increases slightly at first and then decreases. This nanoparticle increase in bone is due to the fact that bone is a store of calcium ³⁶. The Hap nanoparticles interact in mouse body will be collected into bone ³⁶. The metabolism of the Hap nanoparticles is further demonstrated by mouse's faeces whose calcium concentration always increases with time. This can be obviously attributed to the macrophages in spleen, lung and liver, which can capture the Hap nanoparticles. The nanoparticles in macrophages can be metabolized by common bile duct and finally excluded from body via faeces. Furthermore, experiments show that only a very low concentration of calcium is detected in the urine, suggesting the nanoparticles are not excluded via kidney ³⁶. Xi's group experiments have shown that the health of rats was not generally affected under the 9 mg/kg body weight dose of Hap nanoparticles, demonstrating that such dose is safe because it will be ultimately metabolized by liver.

Hap nanoparticles have been also cultured with cells, being found that Hap nanoparticles 20 nm sized have a great potential for stimulating mesenchymal stem cells bone regeneration (MSCs) and for inhibiting the growth of osteosarcoma cells *in vivo*. The behaviour induced by Hap nanoparticles with 40 and 80 nm in size is intermediate between that of commercial Hap and 20 nm Hap particles. This suggests the potential therapeutic utility of the 20 nm Hap for bone replacement and reconstruction, especially after partial ablation of bone tumors ⁷⁸. However, there is conflicting evidence that the 20 nm Hap are internalised,

appearing to influence cell proliferation which is significantly higher than for the control cells ⁷⁸. Shi et al. reported that both cell proliferation and cell apoptosis are related to the size of the Hap particles. Nanoparticles with 20 nm were the most effective at promoting osteosarcoma cell growth and inhibiting cell apoptosis ⁷⁹. These reports suggest that the proper dose of the Hap nanoparticles has low cytotoxicity to normal cells.

Interestingly, Hap nanoparticles are simultaneously reported as expressing low cytotoxicity to normal cells and as having considerable antitumor activity ^{36,80}. In 1993, Aoki accidentally found that the Hap nanoparticles can inhibit the proliferation of Ca-9 cells ³⁶. Later, Zhi-Su Liu found that Hap nanoparticles not only inhibit proliferation but also induce apoptosis of human hepatoma cell line BEL-7402 *in vitro* ⁸¹. Quiang Fu has demonstrated that synthesized spherical nanocrystalline Hap particles can function as an effective biomaterial for bone tumor rectomy repair, while having little adverse effect ⁸⁰. Chen's studies demonstrated that Hap nanoparticles inhibit the proliferation of SGC-7901 cells by inducing apoptosis and can regulate the expression of Bcl 2 gene and the expression of *Bax*, and furthermore activate caspase-3 and caspase-9 (cysteine proteases) to induce the apoptosis of tumor cells ⁸². This study allowed to conclude that Hap nanoparticles have the capability to induce the apoptosis of tumor cells.

B. Li have demonstrated that a proper concentration of Hap nanoparticles can significantly induce the apoptosis of malignant melanoma A375 cells, but do not affect to a significant extent the viability of fibroblasts ⁸³. In summary, the biological risks, cytotoxicity, and anticancer activity of Hap nanoparticles are size and dose-dependent. Hap nanoparticles are suggested to present low cytotoxicity and to be safe in animals for doses below 26 mg/kg, and are probably safe for clinic use.

1.2.8. Biomedical applications of hydroxyapatite nanoparticles

1.2.8.1. Bone repair

The rapid development of nanotechnology has prompted commercial solutions based on Hap nanoparticles for medical applications.

NanOss™ bone void filler from Angstrom Medica, Inc. is considered to be the first nanotechnological medical material which received the US Food and Drug Administration (FDA) approval in 2005. It is obtained by calcium orthophosphate nanoparticles precipitation from aqueous solutions, being the resulting powder then compressed and heated to form a dense, transparent and nanocrystalline material ⁵. NanOss™ mimics the microstructure, composition and performance of human bone, and is mechanically strong and osteoconductive, being thus used in sports medicine, trauma, spine and general orthopaedics markets.

Ostim® (Osartis GmbH & Co. KG, Obernburg, Germany) is a ready-to-use injectable bone matrix in paste form that received CE (Conformite Europeenne) approval in 2002. It is an aqueous suspension of synthetic nanocrystalline Hap (average crystal dimensions: $100 \times 20 \times 3 \text{ nm}^3$ and specific surface area of $106 \text{ m}^2 \text{ g}^{-1}$), prepared by a wet chemical reaction ⁸⁴. Ostim® does not harden off when mixed with blood and thus is highly suitable for increasing the volume of autologous or homologous material. Simultaneously, its viscosity enables its application to form-fit in close contact with bone. Ostim® can be used in metaphyseal fractures and cysts, acetabulum reconstruction and periprosthetic fractures during hip prosthesis exchange operations, osteotomies, filling cages in spinal column surgery, etc. ^{15,84,85}. It can be incorporated into bones, and new bone formation is visible after only 3 months ^{9,85}.

1.2.8.2. Dental applications

Dental caries is a worldwide oral disease. At the initial stage of caries lesions, bacteria cause damage to the enamel, which is the exterior coating of teeth possessing remarkable hardness and resistance. Filling with synthetic materials is a conventional treatment for repairing damaged enamel. However, secondary

caries frequently arise at the interfaces between the tooth and foreign materials^{9,86}.

Hap is often considered as a model compound for dental enamel due to their chemical similarity^{9,86}. Therefore, the remineralisation of enamel minerals by using synthetic apatite or other calcium orthophosphates has frequently been suggested in dental research^{9,86,87}. Unfortunately these chemical analogues of enamel are not widely applied in clinical practice. The native structure of enamel is too complex to be remodelled, and the synthesized apatite crystallites often have different dimensions, morphologies and orientations as compared to the natural ones, which result in poor adhesion and mechanical strength during dental restoration⁹. Recent advances in biomineralization also indicate that the features of smaller Hap nanoparticles may more closely approximate the features of biological apatite than do those of the larger Hap particles that are usually used^{9,87}. It has been demonstrated that Hap nanoparticles can be self-assembled to form enamel-like structures in the laboratory. Therefore, it is suggested that the localized repair of the enamel surface can be improved by Hap nanoparticles, analogous to the basic building blocks of enamel rods. Furthermore, it is found that nanosized Hap can adsorb onto the enamel surface strongly and can even be integrated into the natural enamel structure^{88,89}. This strategy may have potential applications in dentistry as it offers an easy but effective method to reconstruct tooth enamel that is suffering from mineral loss⁸⁹. Generally it can be also suggested that analogues of nanobuilding blocks of biominerals should be highlighted in biomineralization, despite the absence of the complicated morphology and structures of the natural materials.

1.2.8.3. Other applications

Several other applications of nanostructured hydroxyapatite can be also outlined. To prevent inflammation, to prevent dissolution in the case of low pH and potentiate the enhancement of bioactivity as well as to improve the conjugation ability with special functional groups, surface modification of hydroxyapatite nanoparticles with polymeric matrices has been performed⁹⁰⁻⁹⁴. Additionally, Hap

nanoparticles can be stably loaded with radioisotopes to be used in patients with rheumatoid arthritis and chronic knee synovitis ⁹⁵. Hydroxyapatite nanoparticles have also served as non-viral carriers for drug delivery, gene therapy and protein carrier because of their established biocompatibility, ease of handling and adsorption affinity ^{96,97}. Nanosized apatite particles after loading with genes or drugs by adsorption, acquire protective environment against degradation while providing a convenient pathway for cell membrane penetration and the controlled release of the gene/drugs ⁹⁸⁻¹⁰². The literature results have shown that nanodimensional Hap possesses a higher penetration rate into cell membranes and their transfection efficiency can be 25-fold higher than that of micrometric particles. Furthermore, nanosized Hap hold larger load amounts of drugs because of its larger specific surface areas as compared to coarser particles ^{99,103}. The transfer of nucleic acids (DNA or RNA) into living cells (transfection) is a major technique in current biochemistry and molecular biology ¹⁰⁴. As nucleic acids alone are unable to penetrate the cell wall, efficient carriers are required. Calcium orthophosphate nanoparticles as hydroxyapatite represent a unique class of the non-viral vector that can serve as efficient and alternative DNA carriers for targeted delivery of genes ^{100,101,104} and cells ¹⁰⁵. As mentioned before Hap nanoparticles generally possess versatile properties suitable for cellular delivery, including wide availability, high functionality, good biocompatibility, potential capability for targeted delivery (e.g. selectively destroying cancer cells) and controlled release of carried drugs ¹⁰⁵. Vaccination to protect against human infectious diseases may be enhanced by using adjuvants that can selectively stimulate immunoregulatory responses, and nanoparticles of calcium orthophosphates were found to be suitable for such purposes ¹⁰⁶.

Figure 1.12 shows a schematical overview of possible modifications on Hap nanoparticles allowing to design a smart biomedical nanodevice. As considered above the surface of the hydroxyapatite nanoparticles is biocompatible (top right) and to increase the attachment to specific cells (top left), specific molecules or antibodies can be adsorbed on the surface to develop an active-specific targeted system. Additionally, in order to be used as biomedical diagnostic using imaging systems, metallic particles as gold or silver can be conjugated on nanoparticle

surface (lower left). Finally it is also possible to associate therapeutic agents to the hydroxyapatite nanoparticle surface via electrostatic interactions or via covalent bonds. The stimuli-responsive release can be operated by a change in the pH or by enzymatic action.

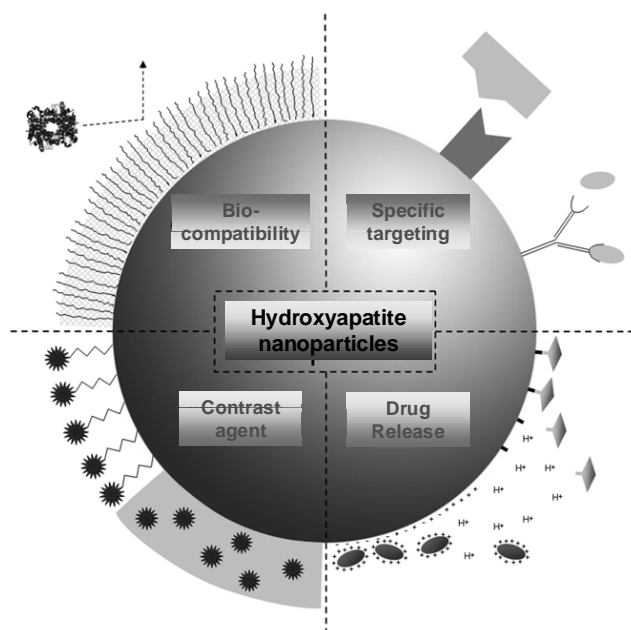


Figure 1.12- Schematic representation of a smart biomedical nanodevice.

Nanotechnology has been an extremely hot topic over the last decade. Two major areas of nanoparticle applications are material science and biomedicine. However, applications of nanoparticles in the biomedical field have not yet fulfilled the expectations. There is still a long way to go before nanotechnology can truly revolutionize patient care.

1.3. Noble metal nanoparticles and surface Plasmon resonance

Among the different classes of organic and inorganic nanoparticles, noble metal nanoparticles have fascinated scientists since historic times because of their unique size and shape-dependent optical properties¹⁰⁷⁻¹⁰⁹. Nowadays, the potential of noble metal nanoparticles is recognized to derive from the addressability of their interesting optical properties via spectroscopic and photonic

techniques. While Faraday recognized that the red colour is due to metallic gold in colloidal form, Mie was the first to explain this phenomenon theoretically in 1908 by solving Maxwell's equation for the absorption and scattering of electromagnetic radiation by spherical particles ^{109,110}.

Mie theory predicts the optical properties of homogeneous spherical particles. For very small particles of radius R (where $2R$ (diameter d) $\ll \lambda$, being λ the wavelength of light), the extinction cross-section can be expressed as:

$$C_{ext} = 24 \frac{\pi^2 R^3 \epsilon_m^{3/2}}{\lambda} \frac{\epsilon_i}{(\epsilon_r + 2\epsilon_m)^2 + \epsilon_i^2} \quad (1.1)$$

Where ϵ_r and ϵ_i represent the real and imaginary parts of the material dielectric function and ϵ_m is the dielectric constant of the surrounding/embedding medium. Equation 1.1 predicts an extinction maximum at wavelength λ where $\epsilon_r = -2\epsilon_m$. For a spherical nanoparticle much smaller than the wavelength of light ($d \ll \lambda$), an electromagnetic field at a certain frequency (ν) induces a resonant, coherent oscillation of the metal free electrons across the nanoparticle (figure 1.13).

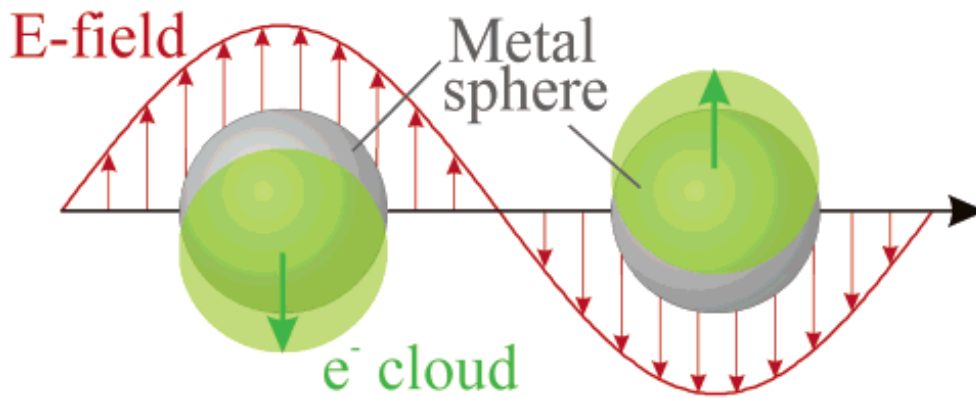


Figure 1.13.- Scheme of the interaction of a metal nanoparticle with light showing the displacement of the conduction electron charge cloud relative to the nuclei (adapted from ¹¹¹).

This electron oscillation around the particle surface causes a charge separation with respect to the ionic lattice, forming a dipole oscillation along the direction of the electric field of the light. The amplitude of the oscillation reaches a maximum at a specific frequency that is known as the surface Plasmon resonance (SPR) ¹¹². The surface Plasmon oscillation of the metal electrons results in a strong enhancement of absorption and scattering of electromagnetic radiation in resonance with the SPR frequency of the noble metal Au nanoparticles, giving them intense colours and interesting optical properties, that can be measured using a UV-Vis absorption spectrometer.

When this condition is fulfilled, the light field induces a resonant coherent dipolar oscillation of free electrons across the nanoparticles. For nanoparticles of Au the resonance condition is satisfied at visible wavelengths. This is the origin of their intense colours ^{109,110,112,113}. The SPR band is much stronger for Plasmon nanoparticles (noble metal, especially Au) than for other metals ¹¹². As the particle size, shape, structure, composition and dielectric constant of the surrounding medium of the Au nanoparticle changes, the optical properties also change only slightly as observed for the different samples of gold nanospheres in fig. 1.14. However, when an anisotropy is added to the nanoparticle, such as growth of nanorods, the optical properties of the nanoparticles change dramatically ^{114,115}.

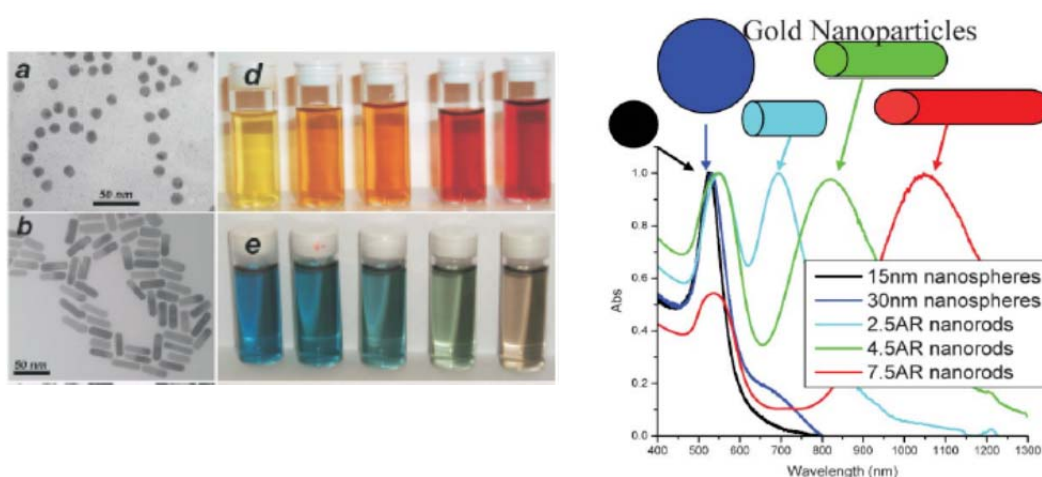


Figure 1.14- Tunable optical properties of gold nanoparticles by changing the particle aspect ratio. Gold nanoparticles of different aspect ratio (AR) exhibit different dimensions

as seen by TEM (a, b), different SPR wavelength (c) and in different colour (d, e) adapted from ^{114,115}.

According to equation developed by Mie, the real part of the dielectric constant of the metal determines the SPR position and the imaginary part determines the bandwidth. For spherical AuNPs of 5 nm diameter, the SPR is located at 520 nm in the visible region and the particles are orange-red, but they turn blue-purple upon aggregation to larger AuNPs ^{109,116}. As referred before the SPR band is affected by the particle size, if the size of the Au particles increases the SPR wavelength shifts for high wavelength and also increases the intensity. Also from the Mie theory, it follows that the frequency of the Plasmon band varies from spherical to non-spherical nanoparticles of various shapes. For instance with Au nanorods (AuNRs), two Plasmon bands are observed (fig. 1.15), one corresponding to oscillations along the length of the AuNRs (longitudinal Plasmon band) and the other along the width of the AuNRs (transversal Plasmon band). The position of these two bands varies with the AuNR aspect ratio (fig. 1.14) being the longitudinal plasmon absorption shifted for higher wavelength as the aspect ratio of the particles increases.

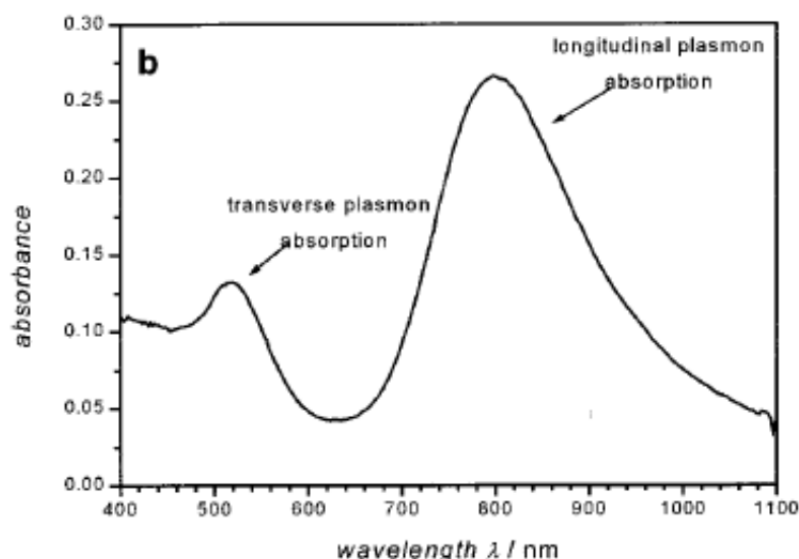


Figure 1.15- Shows the UV-vis absorption spectrum of colloidal gold nanorods solution. The absorption band at 520 nm is the transverse mode of the surface Plasmon

absorption, while the longitudinal mode absorbs around 800 nm for the nanorods, adapted from ¹¹⁰.

Since the aspect ratio influences the position of the Plasmon band absorption, the synthesis of AuNRs can be adjusted with a suitable ratio making them to correspond to commercial lasers (e.g. 360 nm, 787 nm and 1064 nm). Moreover, the shift of the Plasmon band to the near-IR region for AuNRs allows obtaining a penetration into living tissues that is much deeper than that of visible light. In addition the multi-component Plasmon absorption provides richer information than the single visible band of spherical AuNPs ¹¹⁶. Another way to shift Plasmon resonance is produce nanoparticles with a core-shell or hollow core. The decrease in shell/wall thickness of a core-shell or hollow core nanoparticle shifts the SPR ¹¹⁷. This fact allows the choice of gold nanoparticles (different size and/or morphology) depending on biomedical applications. Another interesting property of Au nanoparticles SPR referred previously is its sensitivity to the local refractive index/dielectric constant of the environment surrounding the nanoparticles surface ¹⁰⁹. The nanosphere Plasmon resonance shifts to higher wavelengths with increasing refractive index of the medium ¹⁰⁹. This phenomenon has been explored in the sensing of biomolecular analyses by monitoring a change in the SPR wavelength with the occurrence of an adsorption/binding event at the surface of Au nanoparticles by the biomolecules ¹⁰⁹. The possible biological applications of the AuNPs will be discussed later.

1.3.1. Synthesis of gold nanoparticles methods

AuNPs are available in the range of 1 to more than 120 nm, and their Plasmon band visible absorption can be observed above 3 nm ¹¹⁶. Many different techniques have been developed to generate gold nanoparticles (AuNPs). Nanoparticles can be prepared by physical and chemical methods. The physical methods, which frequently involve vapour deposition, depend on the principle of subdividing bulk precursors into nanoparticles (top down approach, figure 1.16). The chemical approaches involve reducing metal ions to metal atoms in the presence of stabilizers, followed by the controlled aggregation of atoms (bottom up approach, figure 1.16). The latter method of preparation (chemical method) is

more effective for small and uniform particles than the previous (physical method)

118.

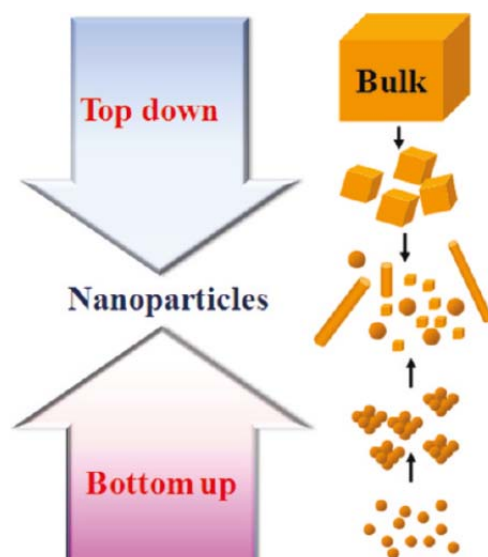


Figure 1.16- Schematic illustration of metal nanoparticles preparation methods ¹¹⁸.

Among the conventional chemical synthesis methods of spherical AuNPs by reduction of gold(III) derivatives, the most popular one which was introduced by Turkevich in 1951 uses the citrate reduction of commercial $\text{HAu}^{\text{III}}\text{Cl}_4$ to Au^0 in water ¹¹⁹. In this method the citrate is both the reducing agent and the stabilizer ¹²⁰. In this process, an aqueous solution of tetrachloroauric acid is brought up to boiling and a small volume of trisodium citrate is then added to it ^{114,115,119,120}. In ~10s, bluish colour appears, indicating formation of gold nuclei ^{119,120}. The formation of Au nanoparticles is revealed by a deep wine red colour observed after few minutes ^{114,115,119}. The completion of reaction may take several minutes depending upon the amount of citrate taken ¹²⁰. The Turkevich method is a procedure still used nowadays but replacing the citrate ligand by appropriate ligands of biological interest ¹¹⁶. Following Turkevich method, Frens et al. synthesized gold nanospheres using citrate as a particle size controlling agent. The resulting nanoparticle sizes are strongly governed by the stoichiometric ratio between gold and the reducing agent, and higher ratios lead to the formation of particles with larger diameters (~ 10-100 nm). Furthermore, citrate performs as a particle size stabilizer via electrostatic repulsion ^{115,117}. However, for particles

larger than 30 nm, deviation from a spherical shape is observed as well as a larger polydispersity. The major limitations of this method are the low yield and the restriction of using water as solvent ¹⁰⁸. The dual role of citrate as reducing reagent and as protection group has been well identified in the growth of gold and other noble metal nanocrystals ¹²¹. However, sodium citrate is known as weak base, which may change the solution pH to a certain extent if its concentration varies. It is known that the reactivity of gold complexes, reflected by their reduction potential, changes markedly by varying pH (figure 1.17) ^{121,122}. In addition, the molecular forces between citrate protection groups and gold surfaces and ξ -potential of gold nanocrystals were reported to be also strongly dependent on pH ¹²¹.

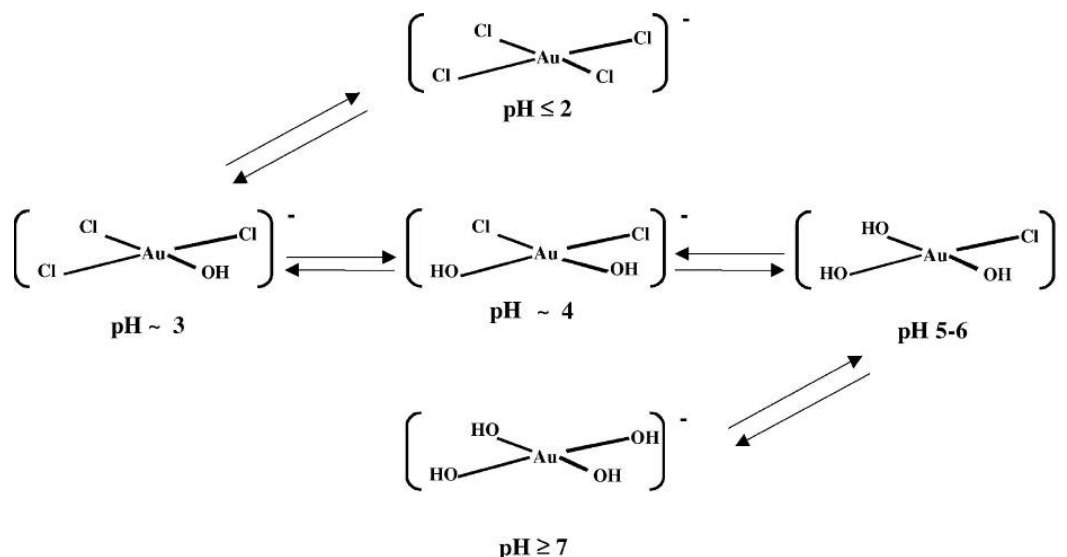
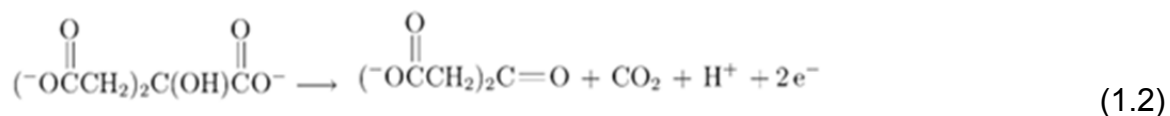


Figure 1.17- Schematic representation of equilibrium between gold species according to pH (adapted from ¹²²).

Although most of the reactions occurring in this method and the intermediates formed in the process are known, some of the steps are still not fully understood. In the following paragraph, the reactions that usually occur will be discussed.

According to S. Kumar et al. ¹²⁰ gold precipitation by Turkevich method can be systematized in three steps: the initial step comprises the oxidation of citrate to acetone dicarboxylic acid after which a second step consisting of auric salt (AuCl_3) reduction to aurous salt (AuCl) takes place. The third step involves the

disproportionation of aurous ions (Au^+) to gold atoms (Au^0). The equations corresponding to these three steps are respectively:



The last step (eq. 1.4) is facilitated by the acetone dicarboxylic specie that helps the formation of aurous species and dicarboxy acetone complexes which provide the combination of several aurous chloride molecules as required by equation (1.4). This is thus a multi-step process where serial and parallel oxidation/reduction reactions take place.

An schematic representation of the complex as well as of the dicarboxy acetone specie are presented in figure 1.18 which shows that three Au^+ can be tethered by a minimum of two dicarboxy acetone molecules ¹²⁰.

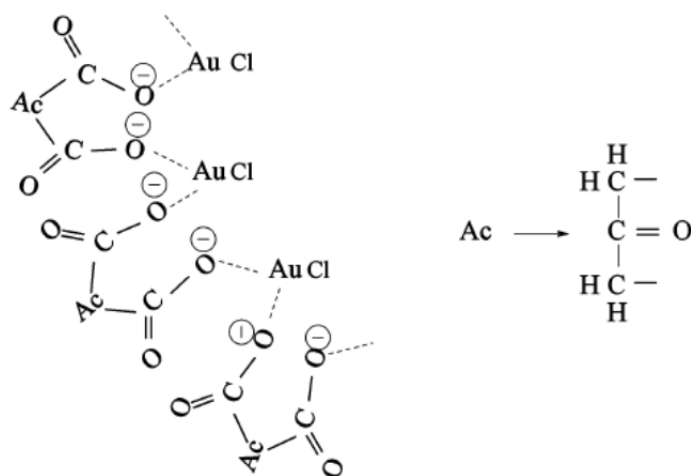


Figure 1.18- Schematic representation of dicarboxy acetone aurous complex species (adapted from ¹²⁰).

The complex disproportionates, and gold atoms are formed. These atoms adsorb Au^+ and, by complexation with dicarboxy acetone, form large aggregates¹²⁰. Further disproportionation leads to formation of still larger aggregates of gold atoms. When the size of the aggregate reaches a critical value, a nucleus of gold atoms is formed. The gold atoms produced by disproportionation are adsorbed by the particles, resulting in its growth^{119,120}. However, the stoichiometric ratio of citrate to gold required for complete conversion of auric chloride should be even larger than 1.5^{119,120}.

Another method that has become extremely popular for Au nanoparticle synthesis (ranging in diameter between 1.5 and 5.2 nm) is the two-phase reduction method reported in 1993 by Giersig and Mulvaney¹⁰⁸ and improved in 1994 by Brust-Schiffrin and co-workers^{114,123}. Basically, HAuCl_4 is dissolved in water and subsequently transported into toluene by means of tetraoctylammonium bromide (TOAB), which acts as a phase transfer agent. The toluene solution is then mixed and thoroughly stirred together with an aqueous solution of sodium borohydride (NaBH_4 a strong reductant), in the presence of thioalkanes or aminoalkanes, which readily bind to the Au nanoparticles formed. The colour of gold nanoparticles can change from orange to deep brown within few seconds changing the ratio of the Au salt and capping agent (thiol/amine)^{108,123}. Several enhancements of the preparative procedure have been reported^{114,123}. Murray and co-workers improved the method by offering a remarkable and well-designed alternative to the two-phase reduction method. They explored the place exchange of a controlled proportion of thiol ligands by various functional thiols and the subsequent reactions of these functional AuNPs¹²³. Other gold morphologies like polyhedral nanocrystals were obtained by a conventional polyol process. The polyol process was originally developed by Fievet and co-workers^{114,124}. In this process, liquid polyol or diol acts as both a solvent for precursors and as a mild reducing reagent and it has proven to be a convenient, versatile, and low-cost route for the synthesis of gold. Several other examples exist of the reduction of gold salts by organic solvents, like sulphur-containing ligands such as: xanthates and disulfides, di- and trithiols and resorcinarene tetrathiols¹²³. As mentioned above, deviations from spherical geometry strongly affect the optical properties of AuNPs. For this

reason, methods for the synthesis of nanoparticles with different shapes like: rods, wires, disks, prisms, cubes, tubes, triangles, shell, cage, polyhedral nanocrystals and hollow spheres, in solution are continuously being studied and reported^{107,112,115,118,123,124}. One of the most reported by a wide variety of strategies is gold nanorod. It is typically synthesized using a template method, based on the electrochemical deposition of gold within the pores of nanoporous polycarbonate or alumina template membranes^{108,125}. The diameter of the gold nanorods is determined by the pore diameter of the template membrane, while the length of the nanorod can be controlled through the amount of gold deposited within the pores of the membrane¹⁰⁸. The disadvantage of this synthesis method is the production of gold particles only on a small scale. However it represents a landmark in terms of shape control. Subsequently, Murphy and coworkers identified reduction conditions that enable the entire synthesis of Au nanorods to be carried out directly in solution¹²⁵, with excellent aspect ratio control. The method uses preformed Au seeds on which additional metal is grown in solution by means of a mild reducing agent (ascorbic acid), in the presence of CTAB to promote nanorod formation. The control of Au nanorods with different aspect ratios is done by addition of different volumes of the seed solution¹¹⁶. Besides the methods mentioned above, several other approaches have also been investigated for the synthesis of gold nanorods, including bio-reduction growth on mica surface and photochemical synthesis¹⁰⁸.

Malikova et al. synthesized Au nanoprisms in aqueous solution by reduction of neutralized HAuCl_4 with salicylic acid¹²⁶. Although the yield of nanoprisms was not outstanding, the formation of a thin film shows that strong optical coupling occurs when the nanoprisms are close enough to each other. The mechanisms involved in the synthesis of spherical metal nanoparticles are well understood in general, but those leading to preferential growth in one particular direction are still a subject of debate. Evidence for an aggregative mechanism in some cases has been demonstrated, but it is clear that such a mechanism does not always apply.

Figure 1.19 illustrates the precipitation of AuNPs by the chemical reduction method in solution.

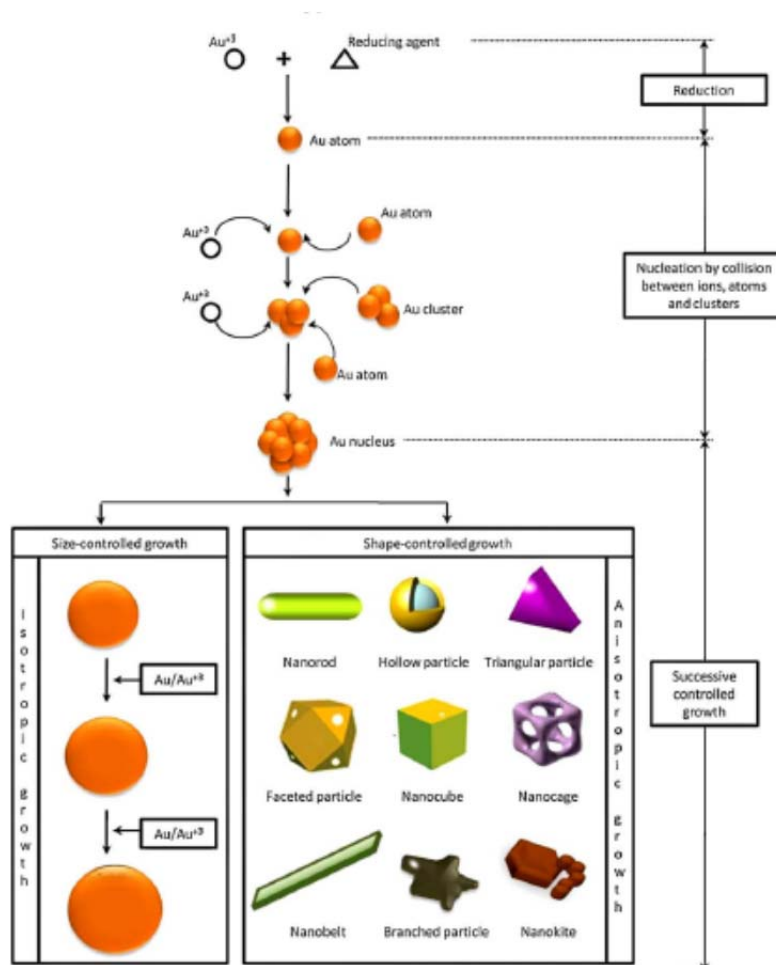


Figure 1.19 - Formation mechanism of AuNPs with various particle sizes and shapes by chemical reduction method ¹²⁴.

In summary, the affinity of the surface of AuNPs having various sizes and shapes for thiols, disulfides, dithiocarbamates and amines allows facile bioconjugation with a variety of biomolecules ¹¹⁶. Due to the fact that CTAB has been proven as a cytotoxic surfactant, other substances have been searched. For instance non-toxic liquid crystals have been used especially if the $NaBH_4$ reducer that leaves boride contamination is to be avoided. Thus, liquid-chlorin photosensitizers based on purpurin-18 from green algae *Spirulina maxima* and choline hydroxide were recently used to synthesize AuNPs in the absence of surfactant and other reducing agent ¹¹⁶.

1.3.2. Applications of gold nanoparticles

1.3.2.1. Labelling and imaging

Exogenous agents have been used to visualize the subcellular compartments. These cell images are achieved through the generation of colorimetric contrasts between different cells/subcellular organelles. Usual extraneous imaging agents include lanthanide chelates and organic fluorophores¹²⁷. However the fluorophores are prone to photobleaching, low quantum yields and broad emission window¹⁰⁸. Lanthanide chelates, on the other hand, are prone to nonselective localization in extravascular space. The shortcomings of the conventional imaging agent have limited their applications as biomedical diagnostic tools and have stimulated interest in typical nanomaterials, such as paramagnetic nanoparticles¹⁰⁸, Q-dots, and AuNPs as alternative contrasting agent^{108,109,127}. These new materials with nanometric size are optimal diagnostic tools since they eliminate most of the vulnerabilities of the conventional imaging agents. However, the intrinsic cytotoxicity and the potential human toxicity of most nanomaterials have limited their benefit in many *in vitro* and *in vivo* applications¹⁰⁹. AuNPs are unique exceptions because they are not susceptible to photobleaching or photoblinking and they are more tolerable, photostable^{112,128}, and biocompatible with cellular environment¹⁰⁹. However the cytotoxicity of AuNPs is dose dependent and believed to be in the range of 1-100 AuNPs per cell¹¹⁶. The facile bioconjugation and biomodification of AuNPs has been another factor motivating its use¹⁰⁹. However, the role of ligands in AuNPs cytotoxicity can be eventually more or less dependent on the cell type. According to some studies, AuNPs conjugated with biotin, cysteine, citrate and glucose do not appear to be toxic in human leukemia (K562) cells at concentrations up to 250 μ M in contrast to HAuCl₄ solutions which were found to be 90% toxic¹¹⁶. Further, AuNPs have been used as a radioactive label *in vivo* since the 1950s¹⁰⁹. Nevertheless the cytotoxic effects of AuNPs *in vivo* are not completely identified and many cytotoxicity studies report negative results. Additionally, it is confirmed that AuNPs are redox active and therefore reduce the production of reactive oxygen and nitrite species¹¹⁶.

As previously mentioned, the colour of the gold particles is controlled by the size¹¹⁹, shape^{107,112,115,118,123,124}, or surface modification of these particles, due to the SPR effect. When excited, the SPR of gold nanoparticles can scatter or absorb light in the visible (spherical particles) or near to the infrared (NIR) (particles with different size or shape of spherical). This property is extremely important for *in vivo* testing since it allows the use of various imaging techniques such as: i) photoacoustic using heat-induced liquid expansion, ii) reflectance confocal microscopy, iii) multiphoton Plasmon resonance microscopy (when illuminated by laser light in resonance with their Plasmon frequency, these AuNPs generate an enhanced multiphoton signal measured in a laser scanning microscope), iv) fluorescence microscopy that allows detection at the single particle level, v) photothermal coherence tomography that is an optical analogue to ultrasound with relative good penetration depth and resolution^{116,128}. Other noninvasive diagnostic tools such as MRI and X-ray computer tomography (X-ray CT) have utilized AuNPs as contrasting agent due to the ease of surface modification and higher X-ray absorption coefficient, respectively¹¹⁶.

Furthermore AuNPs exhibit special optical and electronic properties such as enhanced Raman scattering (SERS). These properties have been used in sensing and/or monitoring numerous molecular events including protein-protein interaction, protein aggregation and protein folding¹²⁷. For example, the SPR signals of AuNPs have been used not only to selectively detect DNAs but also to differentiate between perfect and mismatched DNA.

It is known that the SPR absorption and scattering cross-sections of Au nanoparticles are significantly superior to the absorbing and fluorescing dyes conventionally used in biological and biomedical imaging¹⁰⁹. Mie theory estimates that the optical cross-section of the Au nanospheres is typically four or five orders of magnitude more intense compared to the emission from the most efficient fluorophores^{109,128}.

1.3.2.2. Clinical diagnostics and therapy

Several varieties of engineering nanoparticles such as: metal nanoparticles, nanotubes nanowires, dendrimer, liposomes, polymeric micelles, ceramic nanoparticles, protein-based nanosystems, have been widely used for drug delivery, imaging, biomedical diagnostics and therapeutic applications ¹²⁷. Due to their small size (1 nm to 100 nm), some of these nanoparticles can have some degree of intracellular penetration. Furthermore the charge and its lipophilicity also play critical roles in their uptake by the cells ^{117,127}. Many are also known to be biocompatible, undetected by the immune system and biodegradable ¹²⁷. Additionally, many could possess unique optical and electrical properties; key examples include quantum dots and gold nanoparticles making it possible to track their intracellular trafficking and localization ¹²⁷. The current use of AuNPs in medicine will be next summarized. Cryotherapy, the use of gold in medicine, has been practiced since antiquity. Ancient cultures such as those in Egypt, India, and China used gold to treat diseases such as smallpox, skin ulcers, syphilis and measles ¹²⁷. Presently the gold is used in medical devices including pacemakers and gold plated stents, for the management of heart disease; middle ear gold implant and gold alloys in dental restoration ¹²⁷. Recently, several organogold complexes have shown a considerable potential as antitumor, antimicrobial, antimalarial, anti-HIV activities. They are also used in treatment of Cancer, Alzheimer, bronchial asthma, AIDS, Hepatitis B, Tuberculosis, and Diabetes ^{116,127,129}.

According to the World Health Organization, cancer accounted for 7.9 million deaths in 2007 making it one of the leading causes of death in the world. Deaths from cancer around the globe are expected to climb upwards with an estimated 12 million deaths by cancer in 2030 ¹³⁰. The frontiers of cancer research are therefore consistently challenged in order to advance the most effective means of cancer diagnosis, monitoring and treatment. Finding alternatives to cancer treatment would inevitably benefit mankind and will save countless lives ¹³⁰. Conventional strategies for cancer intervention include surgery, chemotherapy that suffers from dramatic side effects and radiation therapy that is also invasive to healthy tissues

along the radiation path. On the other hand, laser hyperthermia (photothermal therapy) that uses optical heating for tumour ablation is a mild solution that avoids all these drawbacks. Malignant cells require larger amounts of nutrients in order to sustain their accelerated growth and division. To reach this demand, solid tumours stimulate the production of new vasculatures through which increasing amounts of blood can be supplied (tumor angiogenesis). In contrast to normal vessels, the tumor neovasculature is characterized by a highly disordered endothelium with large gaps that permit the preferential penetration of nanosized conjugates ¹¹⁷ (fig 1.20). Several organic and inorganic photoabsorbers such as indocyanine green and iron oxide have been used for photothermal therapy ¹¹⁶. However to be effective it requires a lot of energy and large amounts of particles ¹¹⁶. The advantages of AuNPs come from their high absorption cross sections requiring only minimal irradiation energy besides being considered as non-toxic ¹¹⁶. Irradiation exploiting SPR of AuNPs is followed by fast conversion of light into heat ¹¹⁶.

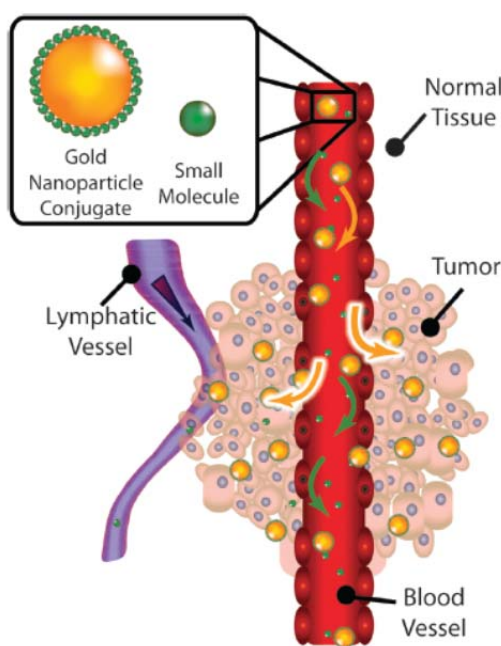


Figure 1.20- Schematic illustration of how large and small gold particles penetrate through blood vessels at tumor sites due to their disordered endothelial cells (adapted from ¹¹⁷).

Relatively small AuNPs (between 10-30 nm) are delivered more easily to cancer cells using various methods, like physiological transportation, conjugation with

antibodies among others, than larger AuNPs¹¹⁶. After delivery, these AuNPs are self-assembled into larger clusters of closely located AuNPs directly among tumor cells, resulting in laser-induced bubble formation that are more effective for cell killing and SPR shifts from the visible region to the 700-1000 nm NIR region¹¹⁶. The AuNPs can be advantageous in treating tumours in areas poorly accessible by surgery or with ill-defined margins¹¹⁷. For clinical therapy applications involving tumors located deep within bodily tissue, there is a need to use laser light in the near-infrared (NIR) region of the biological water window (650-900 nm)¹²⁸. Human tissues and physiological fluids (e.g. oxy/deoxyhemoglobin and water) have the highest transmissivity in this spectral region and the absorption is minimal in the near-infrared region (fig 1.21). The spherical AuNPs offer very limited tunability of their SPR frequency. As referred above with increasing nanosphere size, the SPR red-shifts to a very limited extent as a result of electromagnetic retardation effects in larger nanoparticles^{116,128}. Au nanospheres over a broad-size range have resonances in the 520 to 580 nm region¹²⁸. For that reason they are not ideal for NIR applications¹²⁸. However, changing the shape of AuNPs the SPR band may be tuned for longer wavelengths.

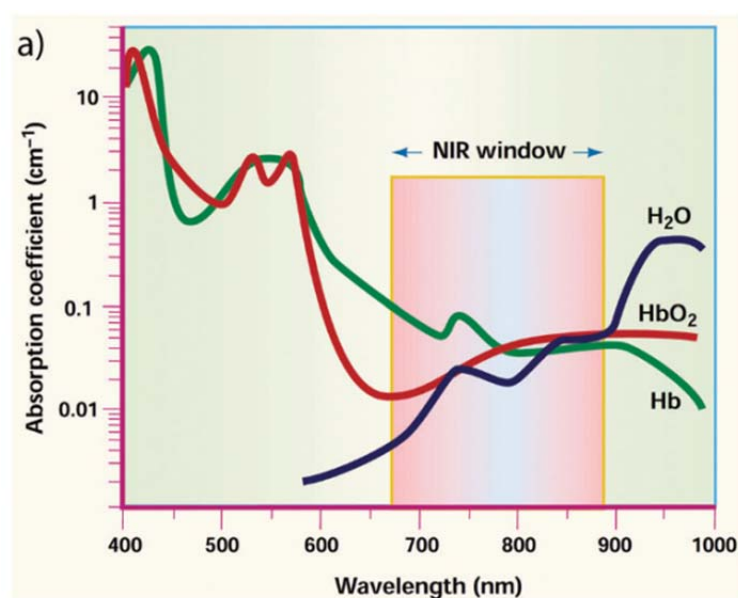


Figure 1.21 – Wavelength range of the near-infrared (NIR) tissue transmission window (adapted from¹¹⁷).

It is known that the localization of the tumour is extremely important and determines the laser potency applicability. According to literature Microwatt NIR lasers (FDA class 1) have an efficient penetration as much as 4 cm through skull/brain and deep muscle tissue and 10 cm through breast tissue. Higher power lasers (FDA class 3) have exhibited 7 cm penetration depths through muscle and neonatal skull/brain tissue ¹¹⁷. However, there are tumours that are not so deep like skin cancer and for these types of tumours spherical particles can be a good choice.

Another widely use of organogold compounds is in the treatment of rheumatoid arthritis ^{127,129}. Organogold compounds relieve arthritis symptoms such as joint pain, stiffness, swelling, bone damage, and also reduce the chance of joint deformity and disability ¹²⁷.

Drug attachment to and release from AuNPs is another challenging area. While the ease of surface modification makes AuNP attractive for drug delivery, the strength of drug attachment and timing of the release needs to be suitably controlled to produce the highest therapeutic efficacy ¹³⁰. Foremost, the method of release at the tumor site is dependent on how the drug is attached to the AuNPs, whether covalently or through non-covalent binding ¹³⁰. Generally, drugs in the active form are loaded non-covalently while the covalent-conjugation of the drug to AuNPs is in the pro-drug form, thereby requiring a second reaction to release the drug from the attachment as well as to activate it ¹³⁰. Although there have been quite a number of strategies proposed for the triggering of drug release at the tumour site, they can generally be narrowed down to three methods: light or photothermal release, glutathione-mediated and non-covalent encapsulation of the active drug with subsequent off-loading by diffusion through the membrane ¹³⁰. The other methods correspond to modification or combinations of these ones. However, given the vast array of AuNPs of different shapes and sizes, it is still unclear which type(s) of AuNPs would be the most suitable for drug delivery applications.

Drug delivery with nanotechnological products takes advantage of pathophysiological conditions and anatomical changes within unhealthy tissues, compared with normal tissues, to achieve site-specific and targeted delivery ¹²⁷. Nanosystems are often accumulated at higher concentrations than normal drugs, thereby enhancing bioavailability at the targeted site. The enhanced drug targeting to the unhealthy tissues usually leads to reduced systemic toxicity. Moreover, incorporation of drug molecules in nanosized systems could improve drug solubility.

Drug delivery (both drug and DNA) appears as one of the most promising future applications of AuNPs because they are biocompatible, easily bio-conjugable and very promising for imaging, diagnostics and cancer therapy applications as well as in a number of other human diseases. Literature describes a large variety of methods to functionalize AuNPs with a large panoply of substances, though few data on the functionalization of inorganic nanoparticles, like hydroxyapatite, with AuNPs are found in the literature. This reflects the easiness of conjugating different molecules to the surface of AuNPs.

Nanoparticles have been explored for non-invasive imaging, drug delivery, bacterial diagnostics, nerve repair and other therapeutic and diagnostic applications ^{99,131}. However, advances in nanoparticle engineering accompanied by a better fundamental understanding of their properties are needed.

1.4. Folic acid conjugation

Folic acid (FA), also known as pteroyl-L-glutamic acid or vitamin B₉, one of many “B” vitamins ¹³², is a water soluble vitamin required for normal tissue growth and development that plays an important role in the metabolism of amino acids and biosynthesis of DNA and RNA which is essential for humans ¹³³. All “B” vitamins help the body to convert food (carbohydrates) into fuel (glucose), being thus used to produce energy. Folic acid is the most oxidized, stable and synthetic analogue of the large family of folates. The generic term “folate” refers to the class of

compounds having a chemical structure and nutritional activity similar to that of folic acid ¹³⁴.

Folic acid is present, as folate, in several vegetables and citrus fruits, being very sensitive to light and oxygen. This is one of the reasons why there is a risk of deficiency in the population. Even if it is proven that when a supplementation of mixed fruits and vegetables is administered, the serum concentration of folate is increased, the majority of the population does not attain the recommended daily intake (RDI) of 400 µg through their diet ^{133,135}. This is the reason why folic acid is present in the majority of the nutritional vitamin supplements sold across the world. European Union allows the enrichment of bread and cereals with folic acid and in the United States, such an enrichment is even compulsory for cereals ¹³⁶. Since folate deficiency has been associated with the incidence of neural tube defects during the embryo development, higher intake (600 µg/day) is recommended for women before and during pregnancy. A low folate intake has also been associated with a number of health disorders, namely, Alzheimer's and coronary heart diseases. Osteoporosis, increased risk of breast and colorectal cancer, poor cognitive performance, hearing loss, and many others have been attributed to the folate deficiency. Therefore, an exogenous supply of folic acid appears inevitable to prevent nutritional deficiency especially in view of the inability of mammalian cells to synthesize this vital biomolecule ^{133,136}. Folic acid may also have potential applications in cancer prevention due to its retention capability of free-radical and antioxidant activity ¹³⁷.

Among the possible low molecular weight (MW) targeting agents, folic acid (MW 441 Dalton) could be exploited to actively target cancer cells. In addition, the folate receptor is efficiently cell internalized after binding with its ligand (folic acid) ¹³⁸. Thus, folic acid presents advantages as a targeting agent. First, it is stable, inexpensive, and not immunogenic compared with proteins. Second, folic acid has a very high affinity for its cell surface receptor (dissociation constant ($K_d \sim 1$ nM)) and it moves into the cell cytoplasm, which is an advantage for more efficient intracellular delivery of anticancer agents than using a cell membrane marker that is not cell internalized ¹³⁸⁻¹⁴⁰.

The use of FA as an adequate targeting is already well accepted owing to its smaller size, lack of immunogenicity, ready availability and low cost. Folic acid consists of a pterin ring (PT) system, a *p*-aminobenzoic acid (PABA) portion, and the amino acid glutamic acid (Glu) ¹⁴¹ as illustrated in figure 1.22. Folic acid has three dissociable groups on the molecule, the α and γ -carboxyl groups of the glutamyl moiety with dissociation constants (pK_a values) of 3.46 and 4.98 respectively, and the N-1 nitrogen in the pteridine moiety with pK_a 2.38 as reported by Zoltán Szakács et al ¹⁴².

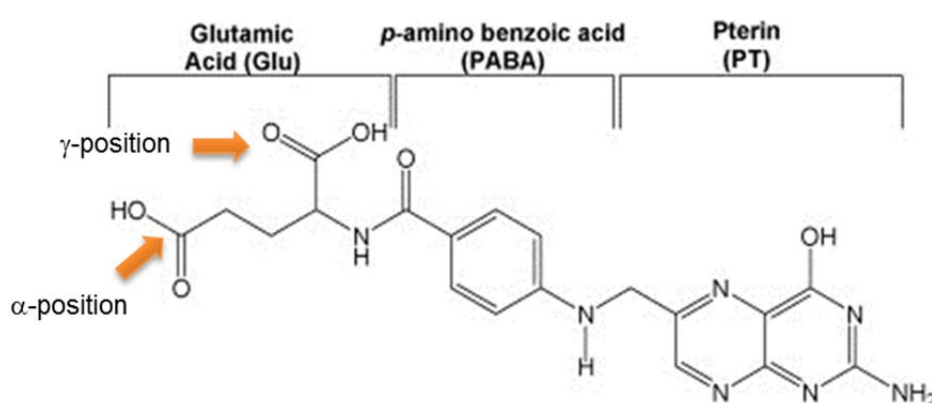


Figure 1.22- Chemical structure of folic acid (adapted from ¹⁴¹).

Folates are very sensitive to light, oxidants and pH. All these influences can drastically affect the stability of the compound. As mentioned the stability of reduced folates is pH-dependent, Veerle de Brouwer et al. have shown that at 37°C most folates are stable at pH values between 4 and 8 ¹⁴³. The chemical reactivity of some important folate compounds makes the vitamin one of the most vulnerable to losses during food processing. Considerable losses have been reported; oxidative degradation enhanced by oxygen, light and heat is responsible for a major part of these losses ¹³⁴.

Targeting the therapeutic load at the tumour site is essential to augment the efficacy per dose. It is currently recognized that only parts of intravenously administered drugs reach the *in vivo* site. This finding emphasizes the need of developing a tumour-specific targeting of therapeutic loads ¹⁴⁴. Nanoscience can play a significant role here by delivering multiple drugs on single nanoparticles in

an organ-specific manner. Moreover, the nanoscale size of these bioconjugates helps to prevent uptake by mononuclear phagocytic cells and allows for their penetration through the smallest capillary pores within the human vasculature. Therefore, if the particles bearing anticancer drugs can be delivered in a targeted fashion, it is expected that a better efficacy to inhibit tumour growth with reduced systemic toxicity will result ¹⁴⁴.

Folic acid receptors (FRs) exhibit limited expression on healthy cells but are often present in large numbers on cancer cells ¹⁴⁴. FRs are overexpressed on epithelial cancers of the ovary, uterus, mammary gland, colon, lung, prostate, nose, throat, and brain ^{138-140,144-146}. FRs are also overexpressed on hematopoietic malignancies of myeloid origin, including chronic and acute myelogenous leukemias. A strong correlation has been observed between FR expression and the grade and histological stage of a tumour ¹⁴⁴. Two tumour markers most commonly used as targets for directed therapy are the folic acid (FA) receptor and the EGFR-2 (erbB2/HER2) ²⁶. In general, highly undifferentiated metastatic cancers express considerably more FRs than their localized, low-grade counterparts. FR has also been found at significant levels in some normal epithelia involved in the retention and uptake of folate, primarily the choroid plexus, placenta, lung, intestine, and kidney ¹⁴⁴. However, these FRs are mostly inaccessible to blood folate conjugates, because they are localized to the apical surfaces of polarized epithelia. Therefore, toxicity to healthy tissues expressing FRs has not been observed ¹⁴⁴. Thus, FRs represents an important target for tumour-specific delivery of anticancer drugs. Therefore, controlling the attachment of the ligand, folic acid (FA), to nanoparticles constitutes an important step for FR mediated targeted delivery of nanoparticles or anticancer drugs ¹⁴⁴.

Today different strategies have been exploited for attaching FA on nanoparticles surfaces for the active targeting of cancer cells overexpressing folate receptors. Despite the large variety of formulations available, this bibliographic review will focus on the more recent published works, which includes natural and synthetic polymers, metal and ceramic nanoparticles.

In a very recent study, Dipsikha Bhattacharya et al. reported a study on the development and *in vitro* examination of bio-functionalized, magneto-fluorescent multifunctional nanoparticles (iron-oxide folate nanoconjugates) suitable for cancer-specific targeting, detection and imaging. They observed that nanoparticles show excellent aqueous dispersion stability over a range of physiological conditions. The cell-uptake behaviour of nanoparticles shows that cancer cells (HeLa) over-expressing the human folate receptor internalized a higher level of these nanoparticle-folate conjugates than normal cells (L929 cells) ¹⁴⁷. Sun et al. also used iron oxide nanoparticles conjugated with folic acid and poly(ethylene glycol) in cellular tests. They confirm that iron oxide nanoparticles conjugated with FA can be used to specifically target tumor cells that overexpress the FA receptor ¹⁴⁰. Gold nanoparticles are another class of metal nanoparticles that were found to target tumours when functionalized with FA. Retnakumari et al. have shown the success on the synthesis of a folic-acid-conjugated fluorescent gold nanocluster capable of specifically targeting molecular receptors on cancer cell membranes ¹⁴⁸. Additionally they have shown that gold nanoparticles conjugated with glutathione and folic acid, which are easily assembled onto gold surface, through the reaction between amino groups of FA and carboxyl group of glutathione, allow the selective detection of human HeLa cells ¹⁴⁹. Their work underscores the relevance of these nanoparticles for optical-imaging-based cancer detection. Zhang et al. discuss the chemical synthesis of a magnetic drug carrier system functionalized with PEG and subsequently coupled to the ligand folic acid. They observed that the magnetic drug carrier present a characteristic drug release ¹⁵⁰. Platinum nanoparticles were also used for developing new drug candidates. The work reported by Teow et al. using different capping agents (folic acid capped platinum nanoparticles and poly(N-vinyl-2-pyrrolidone-capped nanoparticles) show that the inherent toxicity of the platinum nanoparticles conferred an additional advantage to this nanocarrier by eliminating the need for attaching anticancer drugs to kill cancer cells ¹⁵¹. Polymer chemistry allows for many variations, whereby polymeric nanoparticles can be easily manipulated without the loss of their desired physical, chemical and biological properties. In one way, this principle can be used to greatly improve the function of the nanoparticles in cancer therapy

through the attachment of tumor-specific targeting moieties (e.g. folic acid), directed at cell surface markers unique to the cancer cell. Shen et al. prepared albumin nanospheres conjugated with folic acid. For that purpose they used 1-ethyl-3-(3-dimethylaminopropyl) carbodiimide as a catalyst. They confirmed that the presence of folic acid on albumin nanospheres provides an actively targetable drug delivery system to improve drug targeting to cancerous cells ¹³⁹. Another study reported by Yang et al. showed that chitosan nanoparticles were successfully conjugated with folic acid and loaded with 5-aminolaevulinic acid. Additionally, they verified that particles were taken up by HT29 and Caco-2 cell lines via receptor-mediated endocytosis. Their work emphasized the relevance of those particles for fluorescent endoscopic detection of colorectal cancer ¹⁵².

As mentioned, engineered nanoparticles have the potential to revolutionize the diagnosis (using e.g. gold nanoparticles) and treatment of many diseases for example, by allowing the targeted delivery of a drug (Folic Acid) to particular subsets of cells. However, so far, such nanoparticles have not proved to be capable of surmounting all of the biological barriers required to achieve this goal. Nevertheless, the developments on nanoparticle engineering supported, by the understanding of the effects of nanoparticle characteristics such as size, shape and surface properties on their biological performance are creating new opportunities for theragnostic nanoparticles. The recent progresses are thus expected to foster the rational design of such nanoparticles.

1.5. References

- 1 Cuimiao, Zhang; Jun, Yang; Zewei, Quan; Piaoping, Yang; Chunxia, Li; Zhiyao, Hou and Jun, Lin. "Hydroxyapatite Nano-and Microcrystals with Multiform Morphologies: Controllable Synthesis and Luminescence Properties". *Crystal Growth & Design* **9**, 2725–2733, (2009).
- 2 Yi, ping and Kam, W. Leong. "Quantum dot-based theranostics". *Nanoscale* **2**, 60-68, (2010).
- 3 Uskokovic, Vuk and Uskokovic, Dragan P. "Nanosized hydroxyapatite and other calcium phosphates: Chemistry of formation and application as drug and gene delivery agents". *Journal of Biomedical Materials Research B: Applied Biomaterials* **96B**, 151-191, (2011).

- 4 Sergey, V. Dorozhkin. "Nanodimensional and Nanocrystalline Apatites and Other Calcium Orthophosphates in Biomedical Engineering, Biology and Medicine". *Materials* **2**, 1975-2045, (2009).
- 5 Sergey, V. Dorozhkin. "Nanosized and nanocrystalline calcium orthophosphates". *Acta Biomaterialia* **6**, 715-734, (2010).
- 6 Hong-Bin, Yao; Hai-Yu, Fang; Xiao-Han, Wang and Shu-Hong, Yu. "Hierarchical assembly of micro-/nano-building blocks: bio-inspired rigid structural functional materials". *Chem.Soc.Rev.* 1-22, (2011).
- 7 Tal, Dvir; Brian, P. timko; Daniel, S. Kohane and robert, langer. "Nanotechnological strategies for engineering complex tissues". *Nature Nanotechnology* **6**, 13-22, (2011).
- 8 Vallet-Regi, Maria; Maria, Jos and Gonzalez-Calbet. "Calcium phosphate as substitution of bone tissue". *Progress in solid state chemistry* **32**, 1-32, (2004).
- 9 Yurong, Cai andand Ruikang, Tang. "Calcium phosphate nanoparticles in biomineralization and biomaterials". *J.Mater.Chem* **18**, 3775-3787, (2008).
- 10 Pilar Rivera, Gil; Dominik, Huhn; Loretta, L. del Mercato; Daniel, Sasse and Wolfgang, J. Parak. "Nanopharmacy: Inorganic nanoscale devices as vectors and active compounds". *Pharmacological Research* **62**, 115-125, (2010).
- 11 Seiichi, Tada; Ezharul, H. Chowdhury; Chong-Su, Cho and Toshihiro, Akaike. "pH-sensitive carbonate apatite as an intracellular protein transporter". *Biomaterials* **31**, 1453-1459, (2010).
- 12 Guifu, Zuo; Yizao, Wan; Xianguang, Meng; Qing, Zhao; Kaijing, Ren; Shiru, Jia and Jiehua, Wang. "Synthesis and characterization of a lamellar hydroxyapatite/DNA nanohybrid". *Materials Chemistry and Physics* **126**, 470-475, (2011).
- 13 Liam, C. Palmer; Christina, J. Newcomb; Stuart, R. Kaltz; Erik, D. Spoerke and Samuel, I. Stupp. "Biomimetic Systems for Hydroxyapatite Mineralization Inspired By Bone and Enamel". *Chem Rev.* **108**, 4754-4783, (2008).
- 14 Lijun, Wang andGeorge, H. Nancollas. "Calcium Orthophosphates: Crystallization and Dissolution". *Chem Rev.* **108**, 4628-4669, (2008).
- 15 Elliott, J. C.; Wilson, R. M. and Dowker, S. E. P. "Apatite structures". *JCPDS-International Centre for Diffraction Data* **45**, 172-181, (2002).
- 16 M.I.Kay; R.A.Young and A.S.Posner. "Crystal structure of Hydroxyapatite". *Nature* **204**, 1050-1052, (1964).
- 17 Marta Corno andAlbert Rimola, Vera Bolis and Piero Ugliengo. "Hydroxyapatite as a key biomaterial: quantum-mechanical simulation of its surfaces in interaction with biomolecules". *Phys. Chem. Chem. Phys.* **12**, 6309-6329, (2010).
- 18 N.H.Leeuw. "Computer simulations of structures and properties of the biomaterial hydroxyapatite". *J.Mater.Chem* **20**, 5376-5389, (2010).

- 19 Oliver, Hochrein; Rudiger, Kniep and Dirk, Zahn. "Atomistic simulation study of the order/disorder (monoclinic to hexagonal) phase transition of hydroxyapatite". *Chem.Mater.* **17**, 1978-1981, (2005).
- 20 Filgueiras, M. R. T.; D.Mkhonto and Leeuw, N. H.de. "Computer simulations of the adsorption of citric acid at hydroxyapatite surfaces". *Journal of Crystal Growth* **294**, 60-68, (2006).
- 21 Rai, Pradip Beena; T.K.Rao; Shailaja, Krishnamurthy; R.Vetrivel; J.Mielczarski and J.M.Cases. "Molecular modeling of interactions of Alkyl Hydroxamates with calcium minerals". *Journal of Colloid and Interface Science* **256**, 106-113, (2002).
- 22 L.D.Silverman; M.Saadia; J.S.Ishal; N.Tishbi; E.Leiderman; I.Kuyunov; B.Recca; C.Reitblat and R.Viswanathan. "Hydroxyapatite growth inhibition by Osteopontin Hexapeptide Sequences". *Langmuir* **26**, 9899-9904, (2010).
- 23 Huq, N. Laila and Keith J. Cross, Eric Reynolds. "Molecular Modelling of a multiphosphorylated sequence Motif bound to Hydroxyapatite surfaces". *Journal of Molecular Modeling* **6**, 35-47, (2000).
- 24 Rachinger, W.A. and P.P. Phakey, J. Palamara, H.J. Orams. "Planar faults in dental Hydroxyapatite". *Calcified Tissue International* **34**, 209-210, (1982).
- 25 Samar, J. Kalita; Abhilasha, Bhardwaj and Himesh, A. Bhatt. "Nanocrystalline calcium phosphate ceramics in biomedical engineering". *Materials Science and Engineering C* **27**, 441-449, (2007).
- 26 Luo, P. and Nieh, T. G. "Synthesis of ultrafine hydroxyapatite particles by a spray dry method". *Materials Science and Engineering: C* **3**, 75-78, (1995).
- 27 Chen, Fei; Wang, Zhou-Cheng and Lin, Chang-Jian. "Preparation and characterization of nano-sized hydroxyapatite particles and hydroxyapatite/chitosan nano-composite for use in biomedical materials". *Materials Letters* **57**, 858-861, (2002).
- 28 S.Sarig and F.Kahana. "Rapid Formation of nanocrystalline apatite". *Journal of Crystal Growth* **237-239**, 55-59, (2002).
- 29 Xu, J. L.; Khor, K. A.; Dong, Z. L.; Gu, Y. W.; Kumar, R. and Cheang, P. "Preparation and characterization of nano-sized hydroxyapatite powders produced in a radio frequency (rf) thermal plasma". *Materials Science and Engineering: A* **374**, 101-108, (2004).
- 30 Kuriakose, T. Anee; Kalkura, S. Narayana; Palanichamy, M.; Arivuoli, D.; Dierks, Karsten; Bocelli, G. and Betzel, C. "Synthesis of stoichiometric nano crystalline hydroxyapatite by ethanol-based sol-gel technique at low temperature". *Journal of Crystal Growth* **263**, 517-523, (2004).
- 31 Pang, Y. X. and Bao, X. "Influence of temperature, ripening time and calcination on the morphology and crystallinity of hydroxyapatite nanoparticles". *Journal of the European Ceramic Society* **23**, 1697-1704, (2003).

- 32 Bose, Susmita and Saha, Susanta Kumar. "Synthesis of Hydroxyapatite Nanopowders via Sucrose-Templated Sol-Gel Method". *Journal of the American Ceramic Society* **86**, 1055, (2003).
- 33 Shih, Wei-Jen; Chen, Yung-Feng; Wang, Moo-Chin and Hon, Min-Hsiung. "Crystal growth and morphology of the nano-sized hydroxyapatite powders synthesized from $\text{CaHPO}_4 \cdot 2\text{H}_2\text{O}$ and CaCO_3 by hydrolysis method". *Journal of Crystal Growth* **270**, 211-218, (2004).
- 34 M.A.Martins; C.Santos; M.M.Almeida and M.E.V.Costa. "Hydroxyapatite micro- and nanoparticles: nucleation and growth mechanisms in the presence of citrate species". *Journal of Colloid and Interface Science* **318**, 210-216, (2008).
- 35 Wang, Peipei; Li, Caihong; Gong, Haiyan; Jiang, Xuerong; Wang, Hongqiang and Li, Kaixing. "Effects of synthesis conditions on the morphology of hydroxyapatite nanoparticles produced by wet chemical process". *Powder Technology* **203**, 315-321, (2010).
- 36 Youliang, Hong; Hongsong, Fan; Bo, Li; Bo, Guo; Ming, Liu and Xingdong, Zhang. "Fabrication, biological effects, and medical applications of calcium phosphate nanoceramics". *Materials Science and Engineering R* **70**, 225-242, (2010).
- 37 Zhang, Ying; Liu, Yong; Ji, Xiaobo; Banks, Craig E. and Zhang, Wei. "Flower-like hydroxyapatite modified carbon paste electrodes applicable for highly sensitive detection of heavy metal ions". *Journal of Materials Chemistry* **21**, 7552-7554, (2011).
- 38 Chen, Feng; Zhu, Ying-Jie; Wang, Ke-Wei and Zhao, Kuai-Le. "Surfactant-free solvothermal synthesis of hydroxyapatite nanowire/nanotube ordered arrays with biomimetic structures". *CrystEngComm* **13**, 1858-1863, (2011).
- 39 Hagmeyer, Daniel; Ganesan, Kathirvel; Ruesing, Johannes; Schunk, Daniel; Mayer, Christian; Dey, Archan; Sommerdijk, Nico A. J. M. and Epple, Matthias. "Self-assembly of calcium phosphate nanoparticles into hollow spheres induced by dissolved amino acids". *Journal of Materials Chemistry* **21**, 9219-9223, (2011).
- 40 Liu, Dean-Mo; Yang, Quanzu; Troczynski, Tom and Tseng, Wenjea J. "Structural evolution of sol-gel-derived hydroxyapatite". *Biomaterials* **23**, 1679-1687, (2002).
- 41 Bigi, A.; Boanini, E. and Rubini, K. "Hydroxyapatite gels and nanocrystals prepared through a sol-gel process". *Journal of Solid State Chemistry* **177**, 3092-3098, (2004).
- 42 Zhai, Y.; Cui, F. Z. and Wang, Y. "Formation of nano-hydroxyapatite on recombinant human-like collagen fibrils". *Current Applied Physics* **5**, 429-432, (2005).
- 43 Guo, Guangsheng; Sun, Yuxiu; Wang, Zhihua and Guo, Hongyou. "Preparation of hydroxyapatite nanoparticles by reverse microemulsion". *Ceramics International* **31**, 869-872, (2005).
- 44 Sun, Yuxiu; Guo, Guangsheng; Wang, Zhihua and Guo, Hongyou. "Synthesis of single-crystal HAP nanorods". *Ceramics International* **32**, 951-954, (2006).

- 45 Liu, H. S.; Chin, T. S.; Lai, L. S.; Chiu, S. Y.; Chung, K. H.; Chang, C. S. and Lui, M. T. "Hydroxyapatite synthesized by a simplified hydrothermal method". *Ceramics International* **23**, 19-25, (1997).
- 46 Riman, Richard E.; Suchanek, Wojciech L.; Byrappa, Kullaiah; Chen, Chun-Wei; Shuk, Pavel and Oakes, Charles S. "Solution synthesis of hydroxyapatite designer particulates". *Solid State Ionics* **151**, 393-402, (2002).
- 47 Yeong, K. C. B.; Wang, J. and Ng, S. C. "Mechanochemical synthesis of nanocrystalline hydroxyapatite from CaO and CaHPO₄". *Biomaterials* **22**, 2705-2712, (2001).
- 48 Zhang, Yuanjian; Zhou, Liheng; Li, Di; Xue, Naicun; Xu, Xiudong and Li, Jinghong. "Oriented nano-structured hydroxyapatite from the template". *Chemical Physics Letters* **376**, 493-497, (2003).
- 49 He, Qianjun; Huang, Zhiliang; Liu, Yu; Chen, Wei and Xu, Tao. "Template-directed one-step synthesis of flowerlike porous carbonated hydroxyapatite spheres". *Materials Letters* **61**, 141-143, (2007).
- 50 Liu, Jingbing; Li, Kunwei; Wang, Hao; Zhu, Mankang and Yan, Hui. "Rapid formation of hydroxyapatite nanostructures by microwave irradiation". *Chemical Physics Letters* **396**, 429-432, (2004).
- 51 Wang, YingJun; Lai, Chen; Wei, Kun and Tang, ShaoQiu. "Influence of temperature, ripening time, and cosurfactant on solvothermal synthesis of calcium phosphate nanobelts". *Materials Letters* **59**, 1098-1104, (2005).
- 52 Lin, Kaili; Chang, Jiang; Cheng, Rongming and Ruan, Meiling. "Hydrothermal microemulsion synthesis of stoichiometric single crystal hydroxyapatite nanorods with mono-dispersion and narrow-size distribution". *Materials Letters* **61**, 1683-1687, (2007).
- 53 Han, Jae-Kil; Song, Ho-Yeon; Saito, Fumio and Lee, Byong-Taek. "Synthesis of high purity nano-sized hydroxyapatite powder by microwave-hydrothermal method". *Materials Chemistry and Physics* **99**, 235-239, (2006).
- 54 Cleocir Jose, Dalmaschio; Caue, Ribeiro and Edson Roberto, Leite. "Impact of the colloidal state on the oriented attachment growth mechanism". *Nanoscale* **2**, 2336-2345, (2010).
- 55 Fenoglio, Ivana; Fubini, Bice; Ghibaudi, Elena and Turci, Francesco. "Multiple aspects of the interaction of biomacromolecules with inorganic surfaces". *Advanced Drug Delivery Reviews* **63**, 1186-1209, (2011).
- 56 K.A.Hing; S.M.Best; K.E.Tanner and W.Bonfield. "Quantification of bone ingrowth within bone-derived porous hydroxyapatite implants of varying density". *Journal of Materials Science: Materials in Medicine* **10**, 663-670, (1999).
- 57 Changlian, Chen; Zhiliang, Huang; Wenjuan, Yuan; Jianqiu, Li; Xiaokun, Cheng and Ru-an, Chi. "Pressure effecting on morphology of hydroxyapatite crystals in homogeneous system". *CrystEngComm* **13**, 1632-1637, (2011).

- 58 R.L.Dobrushin; R.Kotecky and S.B.Shlosma. in *Wulff Construction: A Global SHape from Local Interaction - Translations of Mathematical Monographs No. 104* Vol. Typeset by AMS-TEX 1-180 (American Mathematical Society 1992).
- 59 Qiu, S. Roger andChristine, A. Orme. "Dynamics of Biomineral Formation at the Near-Molecular Level ". *Chem.Rev.* **108**, 4784-4822, (2008).
- 60 Jennpy.Glusker. "Citrate Conformation and Chelation: Enzymatic Implications ". *Ace.Chem.Res.* **13**, 345-352, (1980).
- 61 Jing, Zhang; Feng, Huang and Zhang, Lin. "Progress of nanocrystalline growth kinetics based on oriented attachment". *Nanoscale* **2**, 18-34, (2010).
- 62 Penn, R. Lee. "Kinetics of Oriented Aggregation". *J.Phys.Chem.B* **108**, 12707-12712, (2004).
- 63 Penn, R. Lee; Alan, T. Stone and David, R. Veblen. "Defects and Disorder: Probing the Surface Chemistry of Heterogenite (CoOOH) by Dissolution Using Hydroquinone and Iminodiacetic Acid". *J.Phys.Chem.B* **105**, 4690-4697, (2001).
- 64 Penn, R. Lee andJillian, f Banfield. "Morphology development and crystal growth in nanocrystalline aggregates under hydrothermal conditions: insights from titania". *Geochimica et Cosmochimica Acta* **63**, 1549-1557, (1999).
- 65 Guo, Xiaohui; Wang, Wanv; Wu, Guolong; Zhang, Ji; Mao, Chaochao; Deng, Yonghui and Xia, Haiqing. "Controlled synthesis of hydroxyapatite crystals templated by novel surfactants and their enhanced bioactivity". *New Journal of Chemistry* **35**, 663-671, (2011).
- 66 Weihua, Di; Marc-Georg, Willinger; Rute, A. S. Ferreira; Xinguang, Ren and Shaozhe, Lu. "Citric Acid-Assisted Hydrothermal Synthesis of Luminescent TbPO₄:Eu Nanocrystals: Controlled Morphology and Tunable Emission". *J.Phys.Chem.C* **112**, 18815-18820, (2008).
- 67 M.Martins. "Chemical preparation and properties of calcium phosphate based materials for biomedical applications". *Tese de Mestrado da Universidade de Aveiro*, (2004).
- 68 http://www.waters.com/waters/nav.htm?cid=10049055&locale=en_PT.
- 69 Qiu, S. R. andA. Wierzbicki, C. A. Orme, A. M. Cody, J. R. Hoyer, G. H. Nancollas, S. Zepeda, J. J. De Yoreo. "Molecular modulation of calcium oxalate crystallization by osteopontin and citrate". *PNAS* **101**, 1811-1815, (2004).
- 70 Hu, Y. Y.; X.P.Liu; X.Ma, A. Rawal; T.Prozorov; M.Akinc; S.K.Mallapragada and Rohr, K. Schmidt. "Biomimetic Self-Assembling CopolymerHydroxyapatite Nanocomposites with the Nanocrystal Size Controlled by Citrate". *Chem.Mater.* **23**, 2481-2490, (2011).
- 71 Hu, Y.-Y.; Rawal, A. and Schmidt-Rohr, K. "Strongly bound citrate stabilizes the apatite nanocrystals in bone". *Proceedings of the National Academy of Sciences* **107**, 22425-22429, (2010).

- 72 Achelhi, Karima; Masse, Sylvie; Laurent, Guillaume; Saoiabi, Ahmed; Laghzizil, Abdelaziz and Coradin, Thibaud. "Role of carboxylate chelating agents on the chemical, structural and textural properties of hydroxyapatite". *Dalton Transactions* **39**, 10644-10651, (2010).
- 73 Baoquan, Xie and H. Nancollas. "How to control the size and morphology of apatite nanocrystals in bone". *PNAS* **107**, 22369-22370, (2011).
- 74 Wenge, Jiang; Haihua, Pan; Yurong, Cai; Hinhui, Tao; Peng, Liu; Xurong, Xu and Ruikang, Tang. "Atomic force microscopy reveals hydroxyapatite-citrate interfacial structure at the atomic level". *Langmuir* **24**, 12446-12451, (2008).
- 75 Li, Cuicui; Zhao, Liping; Han, Jingjia; Wang, Ruifang; Xiong, Chengdong and Xie, Xingyi. "Synthesis of citrate-stabilized hydrocolloids of hydroxyapatite through a novel two-stage method: A possible aggregates-breakdown mechanism of colloid formation". *Journal of Colloid and Interface Science* **360**, 341-349, (2011).
- 76 Rodríguez-Clemente, R.; López-Macipe, A.; Gómez-Morales, J.; Torrent-Burgués, J. and Castaño, V. M. "Hydroxyapatite precipitation: A case of nucleation-aggregation-agglomeration-growth mechanism". *Journal of the European Ceramic Society* **18**, 1351-1356, (1998).
- 77 Hideo, Aoki; H. Aoki; T. Kutsuno; Wei, Li and Motoo, Niwa. "An in vivo study on the reaction of hydroxyapatite-sol injected into blood". *Journal of Materials Science: Materials in Medicine* **11**, 67-72, (2000).
- 78 Yurong, Cai; Yukan, Liu; Weiqi, Yan; Qinghong, Hu; Jinhui, Tao; Ming, Zhang; Zhongli, Shi and Ruikang, Tang. "Role of hydroxyapatite nanoparticle size in bone cell proliferation". *Journal of Materials Chemistry* **17**, 3780-3787, (2007).
- 79 Zhongli, Shi; Xin, Huang; Yurong, Cai; Ruikang, Tang and Disheng, Yang. "Size effect of Hydroxyapatite nanoparticles on proliferation and apoptosis of osteoblast-like cells". *Acta Biomaterialia* **5**, 338-345, (2009).
- 80 Fu, Q. iang; Nai, Zhou; Wenhai, Huang; Deping, Wang; Liying, Zhang and Haifeng, Li. "Preparation and characterization of a novel bioactive bone cement: Glass based nanoscale hydroxyapatite bone cement". *Journal of materials science: Materials in medicine* **15**, 1333-1338, (2004).
- 81 Zhi-Su, Liu; Sheng-Li, Tang and Zhong-Li, Ai. "Effects of hydroxyapatite nanoparticles on proliferation and apoptosis of human hepatoma BEL-7402 cells". *World Journal of Gastroenterology* **9**, 1968-1971, (2003).
- 82 Xiaojuan, Chen; Changsheng, Deng; Shengli, Tang and Ming, Zhang. "Mitochondria-Dependent Apoptosis Induced by Nanoscale Hydroxyapatite in Human Gastric Cancer SGC-7901 Cells". *Biol. Pharm. Bull.* **30**, 128-132, (2007).
- 83 Bo, Li; Bo, Guo; Hongsong, Fan and Xingdong, Zhang. "Preparation of nano-hydroxyapatite particles with different morphology and their response to highly malignant melanoma cells in vitro". *Applied Surface Science* **255**, 357-360, (2008).
- 84 Matthias, W. Laschke; Kristina, Witt; Tim, Pohlemann and Michael, D. Menger. "Injectable Nanocrystalline Hydroxyapatite Paste for Bone Substitution: In Vivo

- Analysis of Biocompatibility and Vascularization". *Journal of Biomedical Materials Research Part B: Applied Biomaterials*, 494-505, (2007).
- 85 Olaf, Kilian; R.Fuhrmann; V.Alt; T.Noll; S.Coskun; E.Dingeldein; R.Schnettler and R.P.Franke. "Plasma transglutaminase factor XIII induces microvessel ingrowth into biodegradable hydroxyapatite implants in rats". *Biomaterials* **26**, 1819-1827, (2005).
- 86 Legeros, R.Z. "Calcium Phosphate Materials in Restorative dentistry: a review". *Advances in Dental Research* **2**, 164-180, (1988).
- 87 Galler, Kerstin M.; D'Souza, Rena N. and Hartgerink, Jeffrey D. "Biomaterials and their potential applications for dental tissue engineering". *Journal of Materials Chemistry* **20**, 8730-8746, (2010).
- 88 Yamagishi, Kazue; Onuma, Kazuo; Suzuki, Takashi; Okada, Fumio; Tagami, Junji; Otsuki, Masayuki and Senawangse, Pisol. "Materials chemistry: A synthetic enamel for rapid tooth repair". *Nature* **433**, 819-819, (2005).
- 89 Arcís, Raul W.; López-Macipe, Anabel; Toledano, Manuel; Osorio, Estrella; Rodríguez-Clemente, Rafael; Murtra, Jaime; Fanovich, Maria A. and Pascual, Concepción Domingo. "Mechanical properties of visible light-cured resins reinforced with hydroxyapatite for dental restoration". *Dental Materials* **18**, 49-57, (2002).
- 90 Buckley, Joanna J.; Lee, Adam F.; Olivi, Luca and Wilson, Karen. "Hydroxyapatite supported antibacterial Ag₃PO₄ nanoparticles". *Journal of Materials Chemistry* **20**, 8056-8063, (2010).
- 91 Puvvada, Nagaprasad; Panigrahi, Pravas Kumar and Pathak, Amita. "Room temperature synthesis of highly hemocompatible hydroxyapatite, study of their physical properties and spectroscopic correlation of particle size". *Nanoscale* **2**, 2631-2638, (2010).
- 92 Wan, Chaoying and Chen, Biqiong. "Synthesis and characterization of biomimetic hydroxyapatite/sepiolite nanocomposites". *Nanoscale* **3**, 693-700, (2011).
- 93 Du, Mingchun; Song, Weixing; Cui, Yue; Yang, Yang and Li, Junbai. "Fabrication and biological application of nano-hydroxyapatite (nHA)/alginate (ALG) hydrogel as scaffolds". *Journal of Materials Chemistry* **21**, 2228-2236, (2011).
- 94 Chung, Eun Ji; Sugimoto, Matthew J. and Ameer, Guillermo A. "The role of hydroxyapatite in citric acid-based nanocomposites: Surface characteristics, degradation, and osteogenicity in vitro". *Acta Biomaterialia* **7**, 4057-4063, (2011).
- 95 Santos, Marla; Furtado, Rita; Konai, Monique; Castiglioni, Mario; Marchetti, Renata; Silva, Constancia and Natour, Jamil. "Effectiveness of radiation synovectomy with Yttrium-90 and Samarium-153 particulate hydroxyapatite in rheumatoid arthritis patients with knee synovitis: a controlled, randomized, double-blinded trial". *Clinical Rheumatology* **30**, 77-85, (2011).

- 96 Epple, M. and K. Ganesan, R. Heumann, J. Klesing, A. Kovtun, S. Neumannb and V. Sokolova. "Application of calcium phosphate nanoparticles in biomedicine". *J. Mater. Chem.* **20**, 18-23, (2010).
- 97 Tomada, Keishiro and Hidehiko Ariizumi, Takatomo Nakaji, Kimiko Makino. "Hydroxyapatite particles as drug carriers for proteins". *Colloids and Surfaces B: Biointerfaces* **76**, 226-235, (2010).
- 98 Klesing, J.; Chernousova, S.; Kovtun, A.; Neumann, S.; Ruiz, L.; Gonzalez-Calbet, J. M.; Vallet-Regi, M.; Heumann, R. and Epple, M. "An injectable paste of calcium phosphate nanorods, functionalized with nucleic acids, for cell transfection and gene silencing". *Journal of Materials Chemistry* **20**, 6144-6148, (2010).
- 99 C.Santos; C.F.Rovath; Franke, R. P.; M.M.Almeida and M.E.V.Costa. "Spray-dried hydroxyapatite-5-Fluorouracil granules as a chemotherapeutic delivery system". *Ceramics International* **35**, 509-513, (2009).
- 100 Akahane, Manabu; Ohgushi, Hajime; Kuriyama, Shigeki; Akahane, Takemi and Takakura, Yoshinori. "Hydroxyapatite ceramics as a carrier of gene-transduced bone marrow cells". *Journal of Orthopaedic Science* **7**, 677-682, (2002).
- 101 Shen, Hong; Tan, Jian and Saltzman, W. Mark. "Surface-mediated gene transfer from nanocomposites of controlled texture". *Nature Materials* **3**, 569-574, (2004).
- 102 Roy, Indrajit and, Susmita Mitra, Amarnath Maitra, Subho Mozumdar. "Calcium phosphate nanoparticles as novel non-viral vectors for targeted gene delivery". *International Journal of Pharmaceutics* **250**, 25-33, (2003).
- 103 Scharnweber, Tim; Santos, Catarina; Franke, Ralf-Peter; Almeida, Maria and Costa, Maria Elisabete. "Influence of Spray-dried Hydroxyapatite-5-Fluorouracil Granules on Cell Lines Derived from Tissues of Mesenchymal Origin". *Molecules* **13**, 2729-2739, (2008).
- 104 Welzel, T. and I. Radtke, W. Meyer-Zaika, R. Heumann, M. Epple. "Transfection of cells with custom-made calcium phosphate nanoparticles coated with DNA". *J. Mater. Chem* **14**, 2213-2217, (2004).
- 105 Xu, Zhi Ping and Qing Hua Zeng, Gao Qing Lu, Ai Bing Yu. "Inorganic nanoparticles as carriers for efficient cellular delivery". *Chemical Engineering Science* **61**, 1027 – 1040, (2006).
- 106 He, Qing; Mitchell, Alaina R.; Johnson, Stacy L.; Wagner-Bartak, Claus; Morcol, Tulin and Bell, Steve J.D. "Calcium Phosphate Nanoparticle Adjuvant". *Clinical and Diagnostic Laboratory Immunology* **7**, 899-903, (2000).
- 107 Nguyen, Dung The; Kim, Dong-Joo and Kim, Kyo-Seon. "Controlled synthesis and biomolecular probe application of gold nanoparticles". *Micron* **42**, 207-227, (2010).
- 108 Weibo, Cai; Ting, Gao; Hao, Hong and Jiangtao, Sun. "Applications of gold nanoparticles in cancer nanotechnology". *Nanotechnology, Science and Applications* **1**, 17-32, (2008).

- 109 Prashant, k Jain; Ivan, H. El-Sayed and Mostafa, A. El-Sayed. "Au nanoparticles target cancer". *Nanotoday* **2**, 18-29, (2007).
- 110 Stephan, Link andMostafa, A. El-Sayed. "Spectral Properties and Relaxation Dynamics of Surface Plasmon Electronic Oscillations in Gold and Silver Nanodots and Nanorods". *J.Phys.Chem.B* **103**, 8410-8426, (1999).
- 111 Kelly, K. Lance; Eduardo, Coronado; Lin Lin, Zhao and George, C. Schatz. "The Optical Properties of Metal Nanoparticles: The Influence of Size, SHape, and Dielectric Environment". *J.Phys.Chem B* **107**, 668-677, (2003).
- 112 Xiaohua, Huang andMostafa, A. El-Sayed. "Gold nanoparticles: Optical properties and implementations in cancer diagnosis and photothermal therap". *Journal of Advanced Research* **1**, 13-28, (2010).
- 113 Jean-Joseph, Max andCamille, CHapados. "Infrared Spectroscopy of Aqueous Carboxylic Acids: Comparison between Different Acids and Their Salts". *J.Phys.Chem A* **108**, 3324-3337, (2004).
- 114 Liz-Marzan, Luis M. "Nanometals: formation and color". *Materialstoday*, 26-31, (2004).
- 115 Susie, Eustis andMostafa, A. El-Sayed. "Why gold nanoparticles are more precious than pretty gold: Noble metal surface plasmon resonance and its enhancement of the radiative and nonradiative properties of nanocrystals of different shapes". *Chem.Soc.Rev* **35**, 209-217, (2006).
- 116 Elodie, Boisselier andDidier, Astruc. "Gold nanoparticles in nanomedicine: preparations, imaging, diagnostics, therapies and toxicity". *Chemical Society Reviews* **38**, 1759-1782, (2011).
- 117 Erik, C. Dreaden; Megan, A. Mackey; Xiaohua, Huang; Bin, Kang and Mostafa, A. El-Sayed. "Beating cancer in multiple ways using nanogold". *Chem Soc Rev* **40**, 3391-3404, (2011).
- 118 Hao Ming, Chen andRu-Shi, Liu. "Architecture of Metallic Nanostructures: Synthesis Strategy and Specific Applications". *J.Phys.Chem C* **115**, 3513-3527, (2011).
- 119 John, Turkevich; Peter Cooper, Stevenson and James, Hillier. "A study of the nucleation and growth processes in the synthesis of colloidal gold". *Discuss.Faraday Soc.* **11**, 55-75, (1951).
- 120 Sanjeev, Kumar; K.S.Gandhi and R.Kumar. "Modeling of formation of gold nanoparticles by citrate reduction". *Ind.Eng.Chem.Res.* **46**, 3128-3136, (2007).
- 121 Xiaohui, Ji; Xiangning, Song; Jun, Li; Yubai, Bai; Wensheng, Yang and Xiaogang, Peng. "Size control of gold Nanocrystals in citrate Reduction: the third role of citrate". *J.Am.Ceram.Soc.* **129**, 13939-13948, (2007).
- 122 S.Ivanova; C.Petit and V.Pitchon. "A new preparation method for the formation of gold nanoparticles on an oxide support". *Applied Catalysis A: General* **267**, 191-201, (2004).

- 123 Marie-Christine, Daniel and Didier, Astruc. "Gold Nanoparticles: Assembly, Supramolecular Chemistry, Quantum-Size-Related Properties, and Applications toward Biology, Catalysis, and Nanotechnology". *Chem.Rev.* **104**, 293-346, (2004).
- 124 Jun, Xu; Siyeu, Li; Jian, Weng; Xiaofeng, Wang; Zhimin, Zhou; Kun, Yang; Min, Liu; Xin, Chen; Qiang, Cui; Minyuan, Cao and Qiqing, Zhang. "Hydrothermal Syntheses of gold Nanocrystals: From Icosahedral to its Truncated Form". *Adv.Funct.Mater* **18**, 277-284, (2008).
- 125 Yu-Ying, Yu; Ser-Sing, Chang; Chien-Liang, Lee and Wang, C. R.Chris. "Gold Nanorods: Electrochemical Synthesis and Optical Properties". *J.Phys.Chem B* **101**, 6661-6664, (2011).
- 126 Jill E. Millstone and Sarah J. Hurst, Gabriella S. Metraux, Joshua I. Cutler, Chad A. Mirkin. "Colloidal Gold and Silver Triangular Nanoprisms". *Small* **5**, 646-664, (2009).
- 127 Po, C. Chen; Sandra, C. Mwakwari and Adegboyega, K. Oyelere. "Gold nanoparticles: From nanomedicine to nanosensing". *Nanotechnology, Science and Applications*, 45-66, (2008).
- 128 Prashant, k Jain; Xiaohua, Huang; Ivan, H. El-Sayed and Mostafa, A. El-Sayed. "Review of some interesting surface plasmon resonance-enhanced properties of noble metal nanoparticles and their applications to biosystems". *Plasmonics* **2**, 107-118, (2007).
- 129 C. Frank Shaw, III. "Gold-Based Therapeutic Agents". *Chem.Rev.* **99**, 2589-2600, (1999).
- 130 Zhao-Zhin Joanna, Lim; Jia-En Jasmine, Li; Cheng-Teng, Ng; Lin-Yeu Lanry, Yung and Boon-Huat, Bay. "Gold nanoparticles in cancer therapy". *Acta Pharmacologica Sinica*, 1-8, (2011).
- 131 Huppertz, Berthold. "Nanoparticles: Barrier thickness matters". *Nat Nano* **6**, 758-759, (2011).
- 132 Lawrence, Eleanor. "Why folic acid is so good for you". *Nature News*, (1999).
- 133 Iyer, Ramya and Tomar, S. K. "Folate: A Functional Food Constituent". *Journal of Food Science* **74**, R114-R122, (2009).
- 134 Forssen, Karin M.; Jagerstad, Margaretha I.; Wigertz, Karin and Wittho, Cornelia M. "Folates and Dairy Products: A Critical Update". *Journal of the American College of Nutrition* **19**, 100S-110S, (2000).
- 135 Lucock, Mark. "Folic Acid: Nutritional Biochemistry, Molecular Biology, and Role in Disease Processes". *Molecular Genetics and Metabolism* **71**, 121-138, (2000).
- 136 E.Deconinck; S.Crevits; P.Baten; P.Courselle and Beer, J. De. "A validated ultra high pressure liquid chromatographic method for qualification and quantification of folic acid in pharmaceutical preparations". *Journal of Pharmaceutical and Biomedical Analysis* **54**, 995-1000, (2011).

- 137 Li, Guifeng; Magana, Donny and Dyer, R. Brian. "Photoinduced Electron Transfer in Folic Acid Investigated by Ultrafast Infrared Spectroscopy". *The Journal of Physical Chemistry B* **116**, 3467-3475, (2012).
- 138 Barbara, Stella; Silvia, Arpicco; Maria Teresa, Peracchia; Didier, Desmaele; Johan, Hoebeke; Michel, Renoir; Jean, D'Angelo; Luigi, Cattel and Patrick, Couvreur. "Design of Folic Acid-Conjugated Nanoparticles for Drug Targeting ". *Journal of Pharmaceutical Sciences* **89**, 1452-1464, (2000).
- 139 Zheyu, Shen; Yan, Li; Kazuhiro, Kohama; Brian, Oneill and Jingxiu, Bi. "Improved drug targeting of cancer cells by utilizing actively targetable folic acid-conjugated albumin nanospheres". *Pharmacological Research* **63**, 51-58, (2011).
- 140 Conroy, Sun; Raymond, Sze and Miqin, Zhang. "Folic acid-PEG conjugated superparamagnetic nanoparticles for targeted cellular uptake and detection by MRI". *Journal of Biomedical Materials Research Part A*, 550-557, (2006).
- 141 Martin, Christopher B.; Walker, David and Soniat, Michael. "Density functional theory study of possible mechanisms of folic acid photodecomposition". *Journal of Photochemistry and Photobiology A: Chemistry* **208**, 1-6, (2009).
- 142 Szakács, Zoltán and Noszál, Béla. "Determination of dissociation constants of folic acid, methotrexate, and other photolabile pteridines by pressure-assisted capillary electrophoresis". *Electrophoresis* **27**, 3399-3409, (2006).
- 143 De Brouwer, Veerle; Zhang, Guo-Fang; Storozhenko, Sergei; Van Der Straeten, Dominique and Lambert, Willy E. "pH stability of individual folates during critical sample preparation steps in prevision of the analysis of plant folates". *Phytochemical Analysis* **18**, 496-508, (2007).
- 144 Resham, Bhattacharya; Chitta Ranjan, Patra; Alexis, Earl; Shanfeng, Wang; Aaron, Katarya; Lichun, Lu; Beng; Jayachandran, N. Kizhakkedathu; Michael, J. Yaszemski; Philip, R. Greipp; Debabrata, Mukhopadhyay and Priyabrata, Mukherjee. "Attaching folic acid on gold nanoparticles using noncovalent interaction via different polyethylene glycol backbones and targeting of cancer cells". *Nanomedicine: Nanotechnology, Biology, and Medicine* **3**, 224-238, (2007).
- 145 Lilian, E. van Vlerken and Mansoor, M. Amiji. "Multi-functional polymeric nanoparticles for tumour-targeted drug delivery". *Expert Opin. Drug Deliv.* **3**, 205-216, (2006).
- 146 Sreeja, Narayanan; Binulal, N. S.; Ullas, Mony; Koyakutty, Manzoor; Shantikumar, Nair and Deepthy Menon. "Folate targeted polymeric 'green' nanotherapy for cancer". *Nanotechnology* **21**, 1-13, (2010).
- 147 Bhattacharya, Dipsikha; Das, Manasmita; Mishra, Debashis; Banerjee, Indranil; Sahu, Sumanta K.; Maiti, Tapas K. and Pramanik, Panchanan. "Folate receptor targeted, carboxymethyl chitosan functionalized iron oxide nanoparticles: a novel ultradispersed nanoconjugates for bimodal imaging". *Nanoscale* **3**, 1653-1662, (2011).

- 148 Retnakumari, Archana andal., Et. "Molecular-receptor-specific, non-toxic, near-infrared-emitting Au cluster-protein nanoconjugates for targeted cancer imaging". *Nanotechnology* **21**, 055103, (2010).
- 149 Zhaowu, Zhang; Jing, Jia; Youqun, Lai; Yanyan, Ma; Jian, Weng and Liping, Sun. "Conjugating folic acid to gold nanoparticles through glutathione for targeting and detecting cancer cells". *Bioorganic & Medicinal Chemistry* **18**, 5528-5534, (2010).
- 150 Zhang, J.; Rana, S.; Srivastava, R.S. and Misra, R.D.K. "On the chemical synthesis and drug delivery response of folate receptor-actived, polyethylene glycol-functionalized magnetite nanoparticles". *Acta Biomaterialia* **4**, 40-48, (2008).
- 151 Yiwei, Teow and Suresh, Valiyaveetil. "Active targeting of cancer cells using folic acid-conjugated platinum nanoparticles". *Nanoscale*, 1-7, (2010).
- 152 Yang, Shu-Jyuan; Lin, Feng-Huei; Tsai, Kun-Che; Wei, Ming-Feng; Tsai, Han-Min; Wong, Jau-Min and Shieh, Ming-Jium. "Folic Acid-Conjugated Chitosan Nanoparticles Enhanced Protoporphyrin IX Accumulation in Colorectal Cancer Cells". *Bioconjugate Chemistry* **21**, 679-689, (2010).

Chapter 2

Materials processing and experimental techniques

2.1. Introduction

As mentioned in chapter 1, for tailoring Hap particles with predefined shapes and sizes an appropriate method of synthesis is required. In this research, as already referred a hydrothermal synthesis (HS) and a wet chemical method (WCS) assisted by citrate ion (Cit) were selected to produce Hap-NPs.

Experimental details of the synthesis conditions and the variations of the parameters such as the molar ratio Cit:Ca of the starting solution and synthesis time will be described aiming to understand their influence on Hap particle size and shape evolutions and on the control of particles physicochemical characteristics. Additionally a complete description of the experimental characterization techniques of the synthesized Hap particles is also addressed.

As *in vitro* studies require sterilized materials, the sterilization impact on the particles properties was evaluated as well. The experimental procedure used in the autoclaving sterilization is detailed.

In an attempt to characterize the toxicity and to assess the biological performance of the synthesized materials their cellular response was also analyzed. The experimental methods used for biodistribution and toxicological studies of Hap-NPs with different particles concentrations and culture times are described.

The possibility of functionalizing Hap-NPs surface with gold nanoparticles (AuNPs) and then with folic acid (FA) for multifunction purposes (diagnosis and therapy, for instance) was also exploited in the present work. The techniques employed to characterize the produced particles as well as the experimental procedure used on the assessment of the biological response of Hap-NPs functionalized with AuNPs and FA are also detailed in this chapter.

2.2. Hydroxyapatite particles synthesis

2.2.1. Hydrothermal Method (HS)

Chemicals: All reagents were of analytical grade and used as received. Citric acid monohydrate ($C_6H_8O_7 \cdot H_2O$, 99.5%), calcium nitrate-4-hydrate ($Ca(NO_3)_2 \cdot 4H_2O$, 99%), ammonia solution (NH_4OH , 25%) were purchased from Riedel-deHaën. Ammonium hydrogenophosphate ($(NH_4)_2HPO_4$, 99%) was purchased from Merck. Water used in the experiment was obtained with a water-purification appliance.

Preparation of Hap particles: in a typical procedure, an aqueous citric acid solution (0.6 M) was prepared. Under constant stirring, ammonia solution was added for adjusting the pH to a value close to 8.1. After that the appropriate amounts of $Ca(NO_3)_2 \cdot 4H_2O$ 0.2 M and $(NH_4)_2HPO_4$ 0.2 M solutions were added. The prepared solution was transferred into a 50 ml Teflon-lined stainless steel autoclave (see figure 2.1a), and was 50% capacity of the total volume of the autoclave (figure 2.1b) were filled (50 ml). The autoclave was sealed and heated at 180 °C for 24 h and then cooled to room temperature with water (figure 2.1c). The precipitate Hap particles were obtained by filtration, through a 0,22 µm Millipore and then washed with distilled water several times. After that, the products were dried in a desiccator. To study the growth of the as-prepared products, the concentration of citric acid (cit) was systematically varied (0.7; 0.8; 1.4 M) while the calcium nitrate (Ca) concentration was maintained constant. The used Cit:Ca ratio (R) were 3:1; 3.5:1; 4:1; 7:1 respectively.

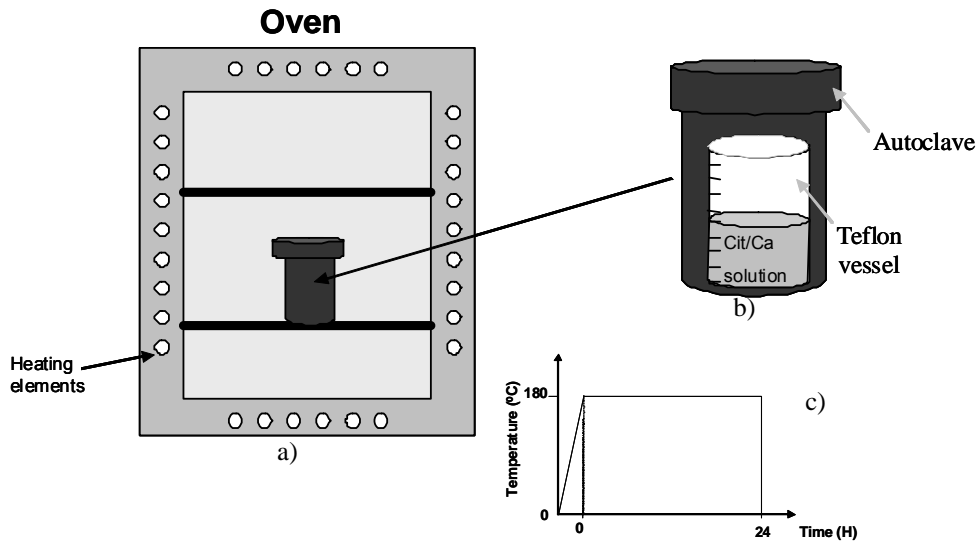


Figure 2.1- a) Schematic diagram of the oven setup used to precipitate hydroxyapatite particles. b) Detail of the calcium/citrate solution inside of the Teflon vessel and was 50% capacity of the total volume of the autoclave were filled; c) thermal cycle used for precipitating Hap particles.

2.2.2. Wet Chemical Method (WCS)

The technique followed to prepare hydroxyapatite nanoparticles was the method reported by M.A. Martins et al. ¹. The necessary supersaturated solutions were prepared by mixing citric acid (Riedel-deHaën, 99.5% purity), calcium nitrate (Riedel-deHaën, 99% purity) (0.2 M) and ammonium hydrogen phosphate (Merck, 99% purity) (0.2 M) as follows: an aqueous citric acid solution (0.6 M) was added with small amounts of ammonia (Riedel-deHaën) (25 vol. %) for pH adjustment to 8.1 and then mixed with appropriate amounts of calcium nitrate and of ammonium hydrogen phosphate solutions. The mixture of all the reagents was performed under continuous stirring, at room temperature. The resulting homogeneous (calcium/citrate/phosphate) solution was put in a glass vessel and maintained at 37°C in a thermostatic water bath for 24 hours (figure 2.2). After that time the precipitated particles were collected by filtering the suspensions through a glass filter Millipore 0.22 μm and washed repeatedly with deionised water. The obtained powders were dried in a desiccator.



Figure 2.2- Image of the thermostatic water bath used in WCS precipitation.

2.2.3. Sterilization procedure

The so prepared Hap particles (HS and WCS) were sterilized in a steel autoclave at 121°C during 20 minutes, according to the standard procedure used in dentistry². After being submitted to sterilization, the particles obtained by HS and WCS methods were here labelled as HS_{ster} and WCS_{ster}, respectively.

2.3. Surface nano-functionalization of Hap nanoparticles

2.3.1. Gold nanoparticles

For precipitating gold particles, 86.5 μL of an acidic solution of hydrogen tetrachloroaurate III (HAuCl_4 30 wt % solution in dilute hydrochloric acid (Aldrich, 99.99%)) were added to 500 mL of deionized water being obtained a gold solution 0.25×10^{-3} M and with pH ~ 3 . 25 mL of the so prepared gold diluted solution were subsequently heated at $\sim 100^\circ\text{C}$ ³ for 3 minutes. Then 50 mg of the previously synthesized Hap-NPs particles (HS) were added to the boiling gold diluted solution. The resulting suspension was kept without stirring for different reaction times: 5, 10 or 20 minutes. After that the particles were collected and filtered using a glass Millipore filter vessel with a 0.22 μm pore size. The particles were then identified as HS-AuNPs 5, HS-AuNPs 10 and HS-AuNPs 20.

2.3.2. Folic acid molecule

The Hap-NPs prepared by HS method and Hap-NPs functionalized with gold nanoparticles HS-AuNPs were selected for the attachment of folic acid (FA) onto the nanoparticles surface. Folic acid (FA) (0.050 g) was added to 100 ml phosphate buffer solution (PBS) with a pH of 7.6. After that 0.1 g of the HS and HS-AuNPs were suspended, in separated vessels, in PBS buffer with FA for 48H, in the dark, at room temperature. Finishing this process, the nanoparticles were then repeatedly washed in a glass filter Millipore water followed by filtration (0.22 μm millipore).

2.3.3. Interaction of MG63 osteoblast-like cells with Hap-NPs

MG63 osteoblast-like cells are malignant bone tumor cells with abnormal cellular functions ⁴. However, the osteosarcoma-derived cells are commonly used for osteoblastic models ⁴.

MG63 osteoblast-like cells, originally isolated from a human osteosarcoma, were used in this thesis to assay the cellular effects of the different Hap-NPs. The selection of this cells line is due to the fact that MG63 cells have been well characterized, and widely used in biomaterials testing ^{5,6}. In this work the MG63 osteoblast-like cells (ATCC number CRL-1427) were cultured in α -Minimal Essential Medium containing 10% fetal bovine serum, 50 $\mu\text{g/ml}$ ascorbic acid, 50 $\mu\text{g/ml}$ gentamicin and 2.5 $\mu\text{g/ml}$ fungizone, at 37°C in a humidified atmosphere of 5% CO₂ in air. For subculture, adherent cells were enzymatically released (0.05% trypsin, 0.25% EDTA) and the cell suspension was cultured (10^4 cell/cm²) in standard polystyrene tissue culture plates. After 24 hours, the medium was removed and fresh medium containing WCS_{ster} and HS_{ster} Hap-NPs, 50 $\mu\text{g/ml}$ – 5 mg/ml, was added to the adherent cells. Cultures were maintained for further 3 and 6 days, without any medium change. Cultures performed in the absence of Hap-NPs were used as control. For functionalized Hap nanoparticles the same procedure as used for WCS and HS was followed. After 24 hours, the medium was removed and fresh complete culture medium, containing sterilized HS, HS-AuNPs, HS-FA or HS-AuNPs-FA nanoparticles - 1, 10, 100 and 500 $\mu\text{g/ml}$ - was

added to the adherent cells. These cultures were maintained for further 1, 3 and 7 days without any medium change.

2.4. Hap-NPs characterization techniques

2.4.1. Physical characterization

2.4.1.1. X-Ray diffraction analysis

The crystalline phases of the hydroxyapatite precipitated particles before and after the sterilization step (HS, HS_{ster}, WCS and WCS_{ster}), as well as the Hap-NPs functionalized with Au nanoparticles (HS-AuNPs), were first identified by powder X-ray diffraction (XRD) analysis. The measurements were performed using an X-ray diffractometer, model Rigaku PMG-VH with a Cu-K α incident radiation (1.5405 Å). The diffraction patterns were recorded at room temperature over the 2 θ range of 10–70 at 3°/min in continuous mode. A characteristic pattern for each compound in a powdery form is produced by plotting the angular positions and intensities of the resultant diffracted peaks. The unit-cell parameters of Hap and other probable calcium phosphates were refined using Celref software (JCPDS, cards No. 9-432 for Hydroxyapatite and N° 071-4614 for gold).

Furthermore, in order to establish a semi-quantitative relationship between the peak width and the crystallite size D (diameter of the coherently scattering domains) of the prepared WCS (WCS_{ster}) and HS (HS_{ster}) particles the Scherrer equation ⁷ was applied. Considering this the crystallite sizes of HS, HS_{ster}, WCS and WCS_{ster} particles were estimated from the X-ray diffractograms using the Scherrer formula ¹

$$D = k\lambda/\beta_{1/2} \cos \theta \quad (2.1)$$

where D is the crystallite size (Å) estimated using the reflection (002), k is a shape factor equal to 0.9, λ is the X-ray wavelength (1.5405 Å), θ is the diffraction Bragg angle related to the reflection (002), and $\beta_{1/2}$, expressed in radians, is defined as

$$\beta_{1/2} = (B - b^2)^{1/2}, \quad (2.2)$$

B being the diffraction peak width at half height and b the experimental width of the instrument ^{8,9}.

2.4.1.2. Differential thermal analysis and thermogravimetry

The thermal behaviour of the prepared samples was studied by thermogravimetric and differential thermal analysis (TG-DTA) from room temperature up to 900°C using a 10°C/min heating rate under nitrogen flow (Setaram Labsys 1600).

2.4.1.3. Specific Surface Area Analysis, Brunauer-Emmett-Teller (BET)

Specific surface area (SSA) analysis materials is often assessed via a gas adsorption method, where a nonreactive gas (nitrogen) is adsorbed on the particles surface at or near the boiling point (77 K) of the adsorptive liquid at a single or at multiple pressures. The amount of gas molecules required to form a monolayer of adsorbed gas on the particles surface is determined. This is done via mathematic modelling the adsorption isotherms (amount adsorbed vs adsorptive pressure), with the most established theory developed by Brunauer, Emmett and Teller (BET) in 1938 ¹⁰. Indeed, the BET method is now accepted as a standard procedure for the determination of the surface area of a wide range of fine powders and porous materials. Porous materials are classified according to the size of pores and the geometries: pores less than 2 nm are called micropores, pores between 2 and 50 nm are called mesopores, and pores greater than 50 nm are macropores ¹¹. The evaluation of the pore geometries (figure 2.3) is generally associated with the isotherm (adsorption and desorption) shape type, well known as hysteresis loops (HL). The current IUPAC classification of adsorption isotherms establishes four types of hysteresis loops designated as H1, H2, H3, and H4. These types are illustrated in figure 2.4.

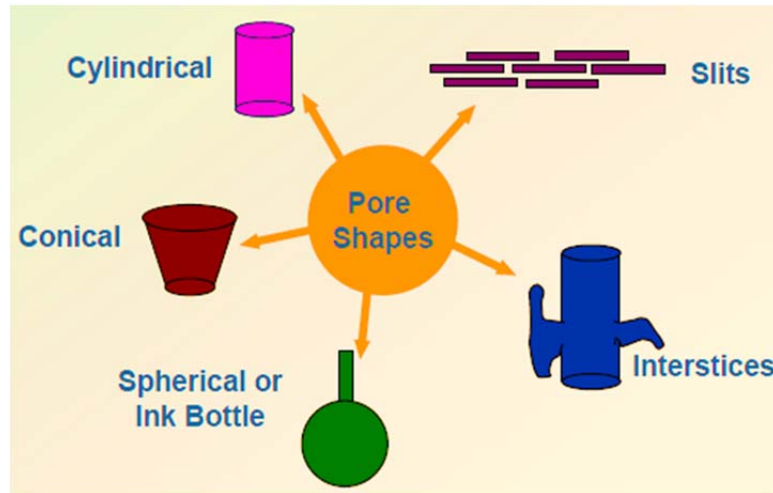


Figure 2.3- Schematic representation of the pore geometry, present in a porous material (adapted from ¹¹).

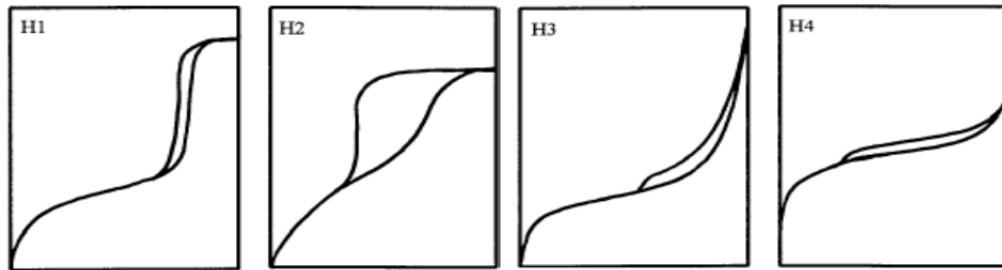


Figure 2.4- Schematic representation of IUPAC classification of sorption hysteresis loops (adapted from ^{11,12}).

Two extreme types are shown as H1 (formerly Type A) and H4 in figure 2.3 and figure 2.4. In the former the two branches are almost vertical and nearly parallel over an appreciable range of gas uptake, whereas in the latter they remain nearly horizontal and parallel over a wide range of p/p^0 . In certain respects Types H2 and H3 (formerly termed Types E and B, respectively) may be regarded as intermediate between these two extremes. A feature common to many hysteresis loops is that the steep region of the desorption branch leading to the lower closure point occurs (for a given adsorbate at a given temperature) at a relative pressure which is almost independent of the nature of the porous adsorbent but depends mainly on the nature of the adsorbate (e.g. for nitrogen at its boiling point at p/p^0 0.42). Type H1 is often associated with porous materials known, from other

evidence, to consist of agglomerates or compacts of approximately uniform spheres in fairly regular array, and hence to have narrow distributions of pore size. Many porous adsorbents tend to give Type H2 loops, but in such systems the distribution of pore size and shape is not well-defined. Indeed, the H2 loop is especially difficult to interpret: in the past it was attributed to a difference in mechanism between condensation and evaporation processes occurring in pores with narrow necks and wide bodies (often referred to as 'ink bottle' pores). The Type H3 loop, which does not exhibit any limiting adsorption at high p/p^0 , is observed with aggregates of plate-like particles giving rise to slit-shaped pores. Similarly, the Type H4 loop is often associated with narrow slit-like pores, but in this case the Type I isotherm character is indicative of microporosity¹³.

The specific surface area (SSA) and the hysteresis loops of the prepared Hap samples were determined by N₂ gas adsorption, using the multipoint Braunauer-Emmett-Teller isotherm (BET) Micromeritics-Gemini 2370 V5 equipment. The samples were outgassing for 24 hours.

2.4.2. Morphological characterization

2.4.2.1. Scanning electron microscopy

Classical microscopes are limited in resolution to the dimension of wavelength of visible light (400-750 nm). The scanning electron microscope (SEM) is one type of electron microscope capable of producing high-resolution images of a sample surface^{14,15}. With scanning electron microscopes, much smaller objects can be observed because high energy electrons are used for imaging^{14,15}. When an electron beam interacts with a solid, various types of elastic and inelastic processes occur, including electron scattering and excitation. Secondary electrons are emitted from the samples with an energy less than 50 eV. The secondary electron current reaching the detector is recorded and the microscope image consists of a plot of this current against probe position on the surface. The contrasts in a micrograph arise from variations in the surface topography, additionally contain information about the sample surface, composition^{14,15}.

The microstructure and size of the obtained Hap particles with micrometric size were observed by scanning electron microscopy (SEM) using a Hitachi SU-70 (Schottky emission) and a JEOL JSM-7001F (field emission). Samples were held onto aluminium stubs using adhesive carbon tabs and imaged in high vacuum mode with an applied 25 kV (Hitachi SU-70) and 15 kV (JEOL JSM-701F) accelerating voltage respectively and a working distance of 15 mm for energy dispersive X-ray analysis (EDX). EDX analysis was performed using an Oxford INCA instruments EDX spectrometer in order to determine elemental compositions (which can be obtained with accuracy for elements of atomic number from carbon upwards).

2.4.2.2. Transmission electron microscopy

Today the ability to understand and control particles at dimensions of few nanometers is just possible due to a powerful tool, the transmission electron microscope (TEM), that allows the observation and the characterization to nanoscale of virtually all types of materials ^{16,17}. Instead of using optical light for imaging, transmission electron microscope employs electrons with energies in the range of 50 to 1000 KeV ¹⁷. This technique is aimed at investigation of the properties of crystal with a spatial resolution that provides the observation into the unit cell of the crystal ¹⁸. In the transmission electron microscope, in addition to the high spatial resolution, the strong interaction of the electrons with matter allows the interaction volume to be extremely small ¹⁸. The interaction of the electron beam with the specimen provides different types of information such as, microstructural, crystallographic and chemical, that can be used to characterize the material.

The microstructure and morphological features of all prepared Hap particles were characterised *via* transmission electron microscopy (TEM) using bright-field imaging and selected area electron diffraction (SAED) using a Hitachi H-9000-NA operated at an accelerating voltage of 200 kV. For measurements, samples were dispersed in ethanol, and applied dropwise onto a holey carbon film supported on a 300 Mesh copper grid.

In separate experiments the particles co-culture with cells were selected. For these sample preparations, adherent cells were enzymatically released (0.05% trypsin, 0.25% EDTA) and the cell suspensions were centrifuged at 2000 rotations/min for 10 min. The resulting pellet was fixed with 2.5% glutaraldehyde, post fixed with 2% osmium tetroxide, dehydrated in ethanol (p.a.) and later embedded in Epon, using routine methods. Ultra-thin (100 nm) sections mounted in copper grids (300 Mesh) were contrasted with uranyl acetate and lead citrate for TEM analysis. The TEM observation was performed using a Zeiss EM 10A operated at an accelerating voltage 60kV.

2.4.2.3. Confocal Laser Scanning Microscope

The conventional optical microscope was a milestone for biological medical sciences which allowed many important innovations. However, the desire of scientists to look in more and more details into biological materials stumbled against several limitations of the instrument. The optical microscope, for instance, does not allow observing details of living tissues. The development of the confocal laser scanning microscope (CLSM) enabled to overcome this limitation. Many fields in life sciences have taken advantage of the exceptional quality of images provided by confocal microscopy. For instance, in biology and pharmacology, the high resolution and improved contrast have been exploited for histological observation of the tissues at cellular level. Contrary to conventional light microscopy, CLSM enables direct examination of tissues at high resolution (0.2 μm) without requiring fixation and sectioning¹⁹⁻²¹.

The confocal principle is now reasonably well known. A light source (typically a laser) is focused to a diffraction-limited spot (Airy disk) at the specimen by the objective lens. Reflected light or emitted fluorescence is focused by the same lens to a spot at the detector. At this point a pinhole is placed, so that only the in-focus spot will pass to the detector — light from out-of-focus planes does not form a spot and so will be blocked by the pinhole. By scanning successive planes, a three-dimensional image of the sample can be created²⁰.

The morphological features of the MG63 cells cultured with WCS_{ster}, HS_{ster}, HS and HS-AuNPs nanoparticles were examined by a confocal laser scanning microscope (CLSM). For microscope observation the cultures exposed to WCS_{ster} and HS_{ster} nanoparticles, 50 and 500 µg/ml, and to HS and HS-AuNPs, 1, 10, 100 and 500 µg/ml, were fixed in 4% formaldehyde (methanol free), permeabilized with 0.1% Triton (5 min, RT) and incubated in 10 mg/ml bovine serum albumin (BSA, 1 h, RT) with 100 µg/ml RNase. Following, F-actin filaments were stained with Alexa-Fluor-conjugated phalloidin® (1:100, 1 h, RT) and nuclei were counterstained with 10 µg/ml propidium iodide (10 min, RT). Labelled cultures were mounted in Vectashield® and examined with a confocal laser scanning microscope (CLSM) Leica SP2 AOBS (Leica Microsystems).

2.4.3. Chemical characterization

2.4.3.1. Fourier transforms infrared spectroscopy

Infrared spectroscopy is a technique based on the vibration of the atoms of a molecule. An infrared spectrum is commonly obtained when radiation with appropriated wavelength is focused on a sample and the fraction of the incident radiation absorbed at a particular energy is determined. The resulting spectrum represents the molecular absorption and transmission, creating a molecular fingerprint of the sample. Because each different material is a unique combination of atoms, no two compounds produce the exact same infrared spectrum ²². However, for a molecule to show infrared absorption it must possess a specific feature, i.e. an electric dipole moment of the molecule must change during the vibration ²². Infrared spectroscopy (FTIR Spectroscopy) is a type of absorption spectroscopy that uses the infrared part of the electromagnetic spectrum (wavelength (λ) 760 nm up to 500 µm). It may be observed that the wavelength λ is inversely proportional to the frequency ν (number of cycles per second) and is governed by the relationship $\nu = c/\lambda$, where c is the speed of light (figure 2.5). Also the energy is directly proportional to the frequency:

$$E = h\nu \quad (2.3)$$

where h is the Planck's constant^{22,23}.

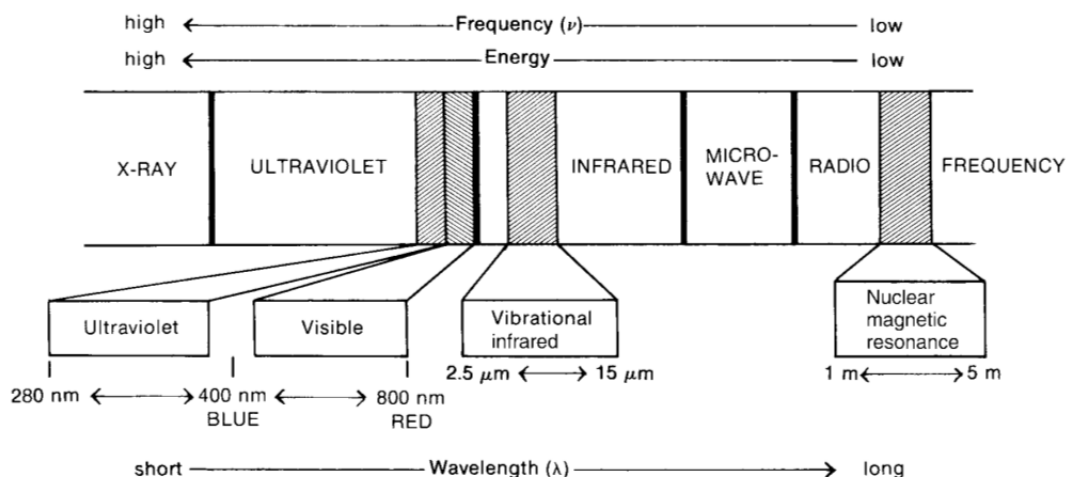


Figure 2.5- A portion of the electromagnetic spectrum showing the relationship of the vibrational infrared to other types of radiation²³.

Molecules vibrate when they absorb infrared radiation. The simplest types, or modes, of vibrational motion in a molecule are the stretching and bending modes (figure 2.6). However, other, more complex types of stretching and bending are also active. In general, asymmetric stretching vibrations occur at higher frequencies than symmetric stretching vibrations; also, stretching vibrations occur at higher frequencies than bending vibrations. The terms scissoring, rocking, wagging, and twisting are commonly used in the literature to describe the origins of infrared bands (figure 2.6). Additionally, a ligand (ion or molecule) could be coordinated to another ion or molecules. This coordination usually causes: (i) the appearance of new bands and splitting of the degenerate modes due to lowering of the symmetry, (ii) frequency shifts of the bands, and (iii) intensification of the spectra²⁴. The main types of coordinating modes are described in literature²⁴.

In this work special attention is given to the interaction between a carboxylate ligand and a cation, since this form of coordination will be important in several results discussion. The carboxylate group can act as an uncoordinated anion ("ionic" structure) or form a monodentate ligand, a bidentate chelate, a bidentate bridging structure, or pseudo bridging (Figure 2.7)²⁴. The type of coordination can

be determined from differences in absorption frequencies in infrared spectra as can be seen in table 2.1.

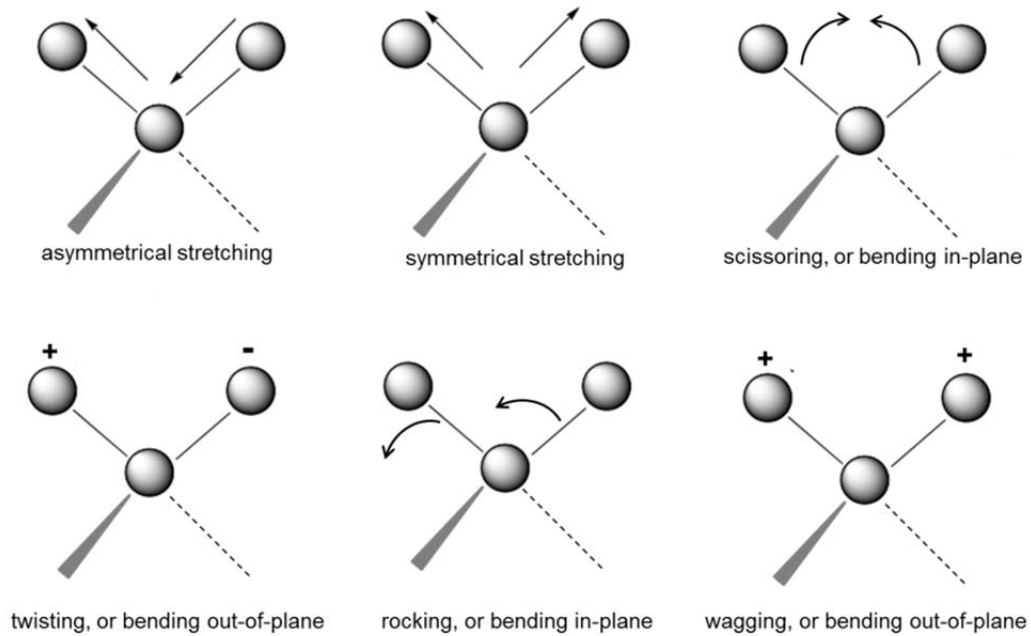


Figure 2.6.- Typical molecular vibrations of the molecules (adapted from ²³).

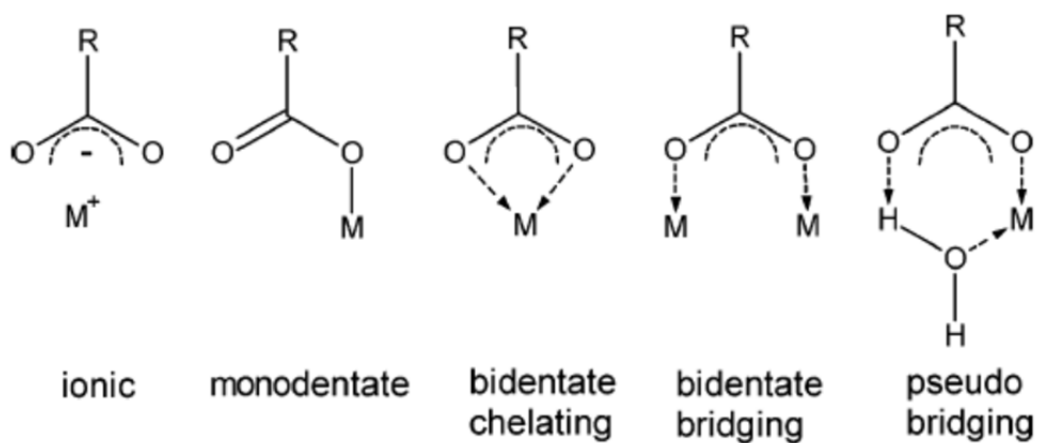


Figure 2.7- Main types of interaction between a carboxylate ligand and a cation (adapted from ²⁴).

Table 2.1- Literature-reported carboxylate stretching bands for the main coordination types between a carboxylate ligand and a cation (adapted from ²⁴).

Type of interaction	Wavenumber shifts (cm ⁻¹)		
	$\nu_{as} \text{ COO}^-$	$\nu_s \text{ COO}^-$	$\Delta = \nu_{as} \text{ COO}^- - \nu_s \text{ COO}^-$
ionic	~1560	~1409	~151
monodentate	~1602	~1342	~260
bidentate	~1542	~1440	~102
bidentate bridging	~1556	~1393	~163
pseudobridging	~1588	~1391	~197

Fourier transform infrared spectroscopy (FTIR) was used to identify the infrared absorption peaks of the prepared particles. The spectral scan was carried out in the frequency range spanning from 4000 to 400 cm⁻¹ using a Mattson galaxy 3020 spectrophotometer. The test samples were prepared by mixing ~2 mg of Hap powder with ~300 mg of spectroscopic-grade KBr (Merck) and pressing the mixture as a disk.

2.4.3.2. Zeta potential

Zeta potential is a physical property which is exhibited by any particle in suspension. It depends on properties of the surface particles and on the suspending medium. Zeta potential is not measurable directly but it can be calculated using theoretical models and an experimentally determined electrophoretic mobility or dynamic electrophoretic mobility. In practice, zeta potential of the particles is measured by applying an electric field across the dispersion. Charged particles within the dispersion will migrate towards the electrode of opposite charge with a velocity proportional to the magnitude of their zeta potential.

From a theoretical point of view, zeta potential is the electric potential in the interfacial double layer (DL) at the location of the slipping plane versus a point in the bulk fluid away from the interface (figure 2.8). In other words, zeta potential is the potential difference between the dispersion medium and the stationary layer of fluid attached to the dispersed particle.

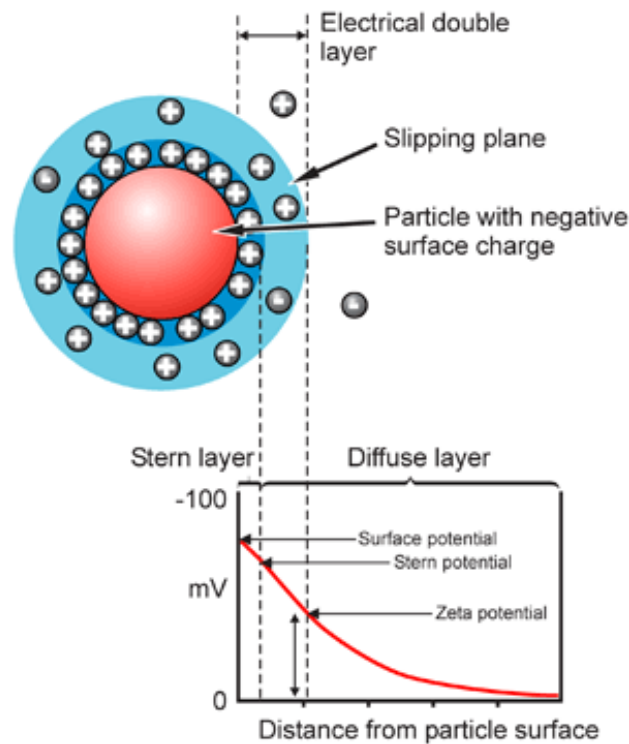


Figure 2.8 - Schematic representation of the structure of the electric double layer ²⁵.

Evaluation of zeta potential is one of the most critical tests to validate the stability of the particles via a study of their electrophoretic behaviour. The relationship between suspension stability and zeta-potential arises from the mutual repulsion that occurs between equally charged particles. For this reason, particles with a high surface charge tend not to agglomerate, since surface charges are the same in all particles and the tendency is for the repulsion. Typically accepted zeta-potential values are summarized below in Table 2.2 ²⁶.

Table 2.2- Zeta potential and associate stability

Zeta Potential (absolute values)	Stability
0	Little or not stability
15	Some stability but settling lightly
30	Moderate stability
45	Good stability, settling possible
60	Very good stability, little settling likely

The measurement of the electrophoretic mobility of the synthesized particles in aqueous suspensions was performed at 25° C, using a Malvern equipment Zetasizer Nano ZS (with a zetasizer nano series 6.00 software). This equipment makes use of non-invasive back scatter (NIBS) technology to perform particle size analysis in the range of 0.6 nm to 6 mm. In addition, it performs zeta potential analysis by the combination of laser Doppler velocimetry and phase analysis light scattering (PALS) in a Malvern's patented M3-PALS technique. A small amount of the particles was suspended in a 2×10^{-3} M KCl solution in order to ensure a constant electrical double-layer thickness and then allowed to equilibrate for two hours before measurement. The measurements were done in triplicate for each pH value. HCl and NaOH solutions were used to decrease or to increase the suspension pH, respectively.

2.4.3.3. Ultra Violet-Visible spectrophotometer (UV-Vis)

As observed in figure 2.5 the ultraviolet (UV) and visible radiation comprise only a small part of the electromagnetic spectrum. As referred before, when radiation interacts with matter, a number of processes can occur but in general, when measuring UV-Visible spectra only absorbance is concerned ²⁷. In some molecules and atoms, photons of UV and visible light have enough energy to cause transition between the different electronic energy levels. The wavelength of light absorbed has energy required to move an electron from a lower to a higher energy level. These transitions should result in a very narrow absorbance band at wavelength characteristic of the difference in energy levels of the absorption

species. In molecules, many transitions with different energies can occur, for that reason the bands are broadened (figure 2.9)²⁷.

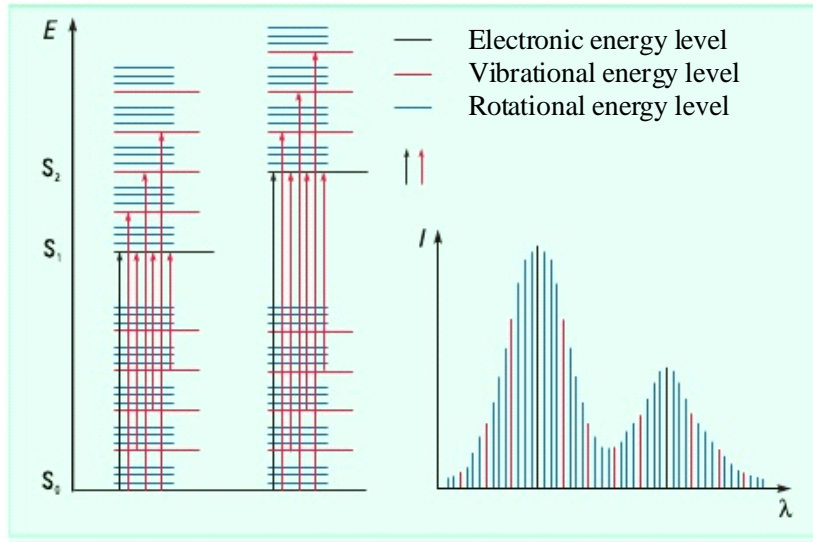


Figure 2.9- Electronic transition and UV-visible spectra in molecules (adapted from ²⁷).

An optical spectrometer records the wavelengths at which absorption occurs, together with the degree of absorption at each wavelength. The resulting spectrum is presented as a graph of absorbance (A) versus wavelength. Beer-Lambert's Law is given as:

$$A = \epsilon \cdot b \cdot c \quad (2.4)$$

where ϵ is the absorption coefficient ($\text{dm}^3 \text{mol}^{-1} \text{cm}^{-1}$) of the absorbing medium, c is the concentration (mol dm^{-3}) of the sample and b is the path length (cm) through the sample. According to Beer-Lambert's law, absorption is directly proportional to concentration and the path length. The unknown concentrations of the sample can be measured by plotting the absorption (A) versus known concentration (c) of the standard samples. This results in a linear plot, following the Beer-Lambert's law.

In this work was important to test the Hap particles coupled with gold by UV-Vis technique, however it is not possible to use Beer-Lambert's law to test solid materials by this technique. For a solid material the absorption spectrum in the

ultraviolet and visible is determined by a transmission experiments, by replacing the cell of liquids for a thin wafer of the solid ²⁸. Due to the fact that measuring the absorption of the power was determined indirectly, not by measuring the absorption as such, the measurement of the reflection from the absorbing solid is used ²⁸. For large particles one can treat the components of reflection, refraction, and diffraction separately using the classical work of Mie ²⁸, but this is not possible for small particles where the three effects are indivisibly mixed together ²⁸. For these cases there are several theories, but the most general and also most widely accepted is the Kubelka-Munk theory ²⁸.

The Kubelka-Munk theory is based upon the premise that the reflection is diffuse. It also assumes that the incident radiation is diffuse, i.e. that the intensity is the same in all directions ^{28,29}. The rearrangement of several equations gives an expression that is known as the Kubelka-Munk equation ^{28,29}:

$$\frac{Ac}{S} = \frac{K}{S} = \frac{(1-R)^2}{2R} \quad (2.5)$$

Where, R is the reflectance, k and S are the absorption and scattering coefficients respectively. c is the concentration of the absorbing species and A the absorbance.

The advantages of measuring powder directly in the UV-Vis equipment is to obtain simultaneously information about the adsorbent (in this study HS) and adsorbate (gold nanoparticles) ²⁸. The samples used for UV-Vis analysis were the particles HS, HS-AuNPs 5; HS-AuNPs 10 and HS-AuNPs 20 min. The reflectance values of the particles were measured from 200 to 700 nm in a double beam, Shimadzu MPC-3100 PC series spectrophotometer. The white standard was BaSO₄ whose reflectance was taken to be 100%. Both samples and standards (as dry powder) were bulk-filled into aluminium frames and then gently pressed to minimize preferential orientations. These powders were covered with a glass. The reflectance measurements were converted to absorption according to Kubelka-Munk equation, using the software installed in the equipment.

2.4.3.4. Liquid Chromatography

Modern liquid column chromatography, now called high-performance liquid chromatography (HPLC) is one of fastest growing techniques in analytical chemistry. It enables to perform rapid, efficient separations of complex mixtures of organic, inorganic, pharmaceutical and biochemical compounds ³⁰.

The theoretical, chemical and physical aspects of HPLC are quite complex. However, the technique is easy to understand from a practical standpoint (figure 2.10). HPLC utilizes a liquid mobile phase to separate the components of a mixture. The stationary phase can be a liquid or a solid phase. These components are first dissolved in a solvent, and then forced to flow through a chromatographic column under a high pressure. In the column, the mixture separates into its components. The amount of resolution is important, and is dependent upon the extent of interaction between the solute components and the stationary phase. The stationary phase is defined as the immobile packing material in the column. The interaction of the solute with mobile and stationary phases can be manipulated through different choices of both solvents and stationary phases. As a result, HPLC acquires a high degree of versatility not found in other chromatographic systems and it has the ability to easily separate a wide variety of chemical mixtures. There are many detection principles used to detect the compound eluting from a HPLC column. The most common are: spectroscopic detection, refractive index detection and fluorescence detection. Additionally there are various types of HPLC, their main characteristics are summarized in the table 2.3.

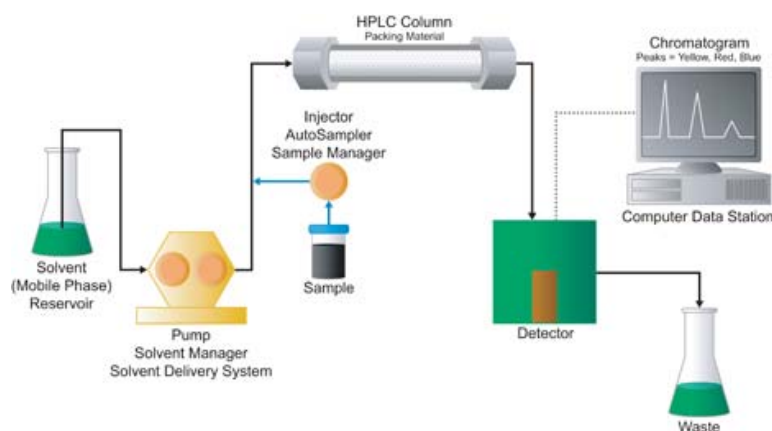


Figure 2.10- Schematic diagram of an HPLC unit (re-printed from ³¹).

Table 2.3- Various types and applications of HPLC.

Type	Sample polarity	Molecular weight range	Stationary phase	Mobile phase
Adsorption	non-polar to somewhat polar	$10^0 - 10^4$	silica or alumina	non-polar to polar
Partition (reversed-phase)	non-polar to somewhat polar	$10^0 - 10^4$	non-polar liquid adsorbed or chemically bonded to the packing material	relatively polar
Partition (normal-phase)	somewhat polar to highly polar	$10^0 - 10^4$	highly polar liquid adsorbed or chemically bonded to the packing material	relatively non-polar
Ion Exchange	highly polar to ionic	$10^0 - 10^4$	ion-exchange resins made of insoluble, high-molecular weight solids functionalized typically with sulfonic acid (cationic exchange) or amine (anionic exchange) groups	aqueous buffers with added organic solvents to moderate solvent strength
Size Exclusion	non-polar to ionic	$10^3 - 10^6$	small, porous, silica or polymeric particles	polar to non-polar

In this thesis the high-performance liquid chromatography (HPLC) measurements were obtained with the collaboration of Instituto Superior Tecnico de Lisboa. This technique was used for accessing the presence of citrate groups on the surface of the precipitated Hap particles. For that purpose a column YMC-Pack ODS-AQ, gel lot 9110 250x4.6mm ID, 5 mm, 12 nm AQ12S05-2546WT, PART# 0425026662 (W) was used. The eluents used were: C: 20 mM KH_2PO_4 at pH 5.29 and D: 20 mM H_3PO_4 , pH 2.60. The calibration of the column was made in the following way:

0,5 min 0%C e 100%D at 2200 psi, in the oven at temperature of 30°C

0,5 min 100%D for 75%D linear

0,5 min 25%C and 75%D step

0,5 min 75%D for 100%D linear

4,5 min 0%C and 100%D step

The flow used was 1.0 mL/min, during 15 min, and the detection by UV spectrophotometer was at 254 nm. All the tested samples were dissolved in phosphoric acid 1M and injected 50 μ L in the equipment.

2.4.4. Biological characterization

The biological characterization was obtained with the collaboration of Faculdade de Medicina Dentaria da Universidade do Porto. For that reason the description of the used techniques is as detailed as the previous ones, since the assays were monitored but not prepared in full by the author.

2.4.4.1. Cell Viability/proliferation

Many methods have been developed to measure cell proliferation including those based on direct counting of viable cells, measurement of metabolic activity and cellular DNA content. The traditional cell counting methods such as trypan blue dye exclusion assay using a hemacytometer are simple and inexpensive but very time consuming and sometimes inaccurate³². Measurement of mitochondrial metabolic rate using MTS a tetrazolium compound (3-(4,5-dimethylthiazol-2-yl)-5-(3-carboxymethoxyphenyl)-2-(4-sulfophenyl)-2H-tetra-zolium) to indirectly reflect viable cell numbers has been widely applied^{32,33}. MTS in vitro cytotoxicity assay is a method for assessing cell viability³⁴. The concept of this assay is based on the conversion of a tetrazolium salt into a yellow-colored, aqueous soluble formazan product by mitochondrial activity of viable cells at 37°C. The amount of formazan produced by dehydrogenase enzymes is proportional to the number of living cells in culture³⁴. Usually the color modification of formazan in experiments is analyzed using a spectrophotometer in absorbance mode. In this study the absorbance was measured at 492 nm (visible region fig. 2.5) using an ELISA reader (Synergy HT, Biotek®). The referred spectrophotometer works with the same principles as UV-visible spectrophotometer (described previously) obeying the Beer-Lambert's law. Cell cultures were exposed to Hap-NPs, 50 – 5000 μ g/ml and Hap-AuNps, 1-500 μ g/ml. Control cultures and those exposed to nanoHap were incubated with MTS, a tetrazolium compound [3-(4,5-dimethylthiazol-2-yl)-5-(3-carboxymethoxyphenyl)-2-(4-sulfophenyl)-2H-tetrazolium] (20 μ l /well, in 96-well plates), during the last 4 h

of the culture periods tested (3 and 6 days) at 37 °C. Six replicates were set up at each condition.

2.4.4.2. Immunofluorescent staining of F-actin cytoskeleton filaments and nuclei

To evaluate the physical cellular processes that include: cell adhesion, migration and division, a confocal laser scanning microscope (CLSM) was used. The main functionalities of the CLMS were described previously in microscope section in this chapter. Each of these mentioned processes (adhesion, migration and division) requires precise regulation of cell shape and mechanical force generation which is regulated by the dynamic mechanical behaviors of actin cytoskeleton ³⁵. The morphology of the actin cytoskeleton changes rapidly in response to a wide variety of internal and external stimuli. The actin cytoskeleton is a dynamic network that is regulated by a variety of extracellular signals. Growth factors or extracellular matrix (ECM) proteins transmit signals with actin modulating intracellular trafficking, cell morphology and cell migration ³⁶. Dynamic structural modifications of the actin cytoskeleton require polymerization, depolymerization, stabilization, branching, and severing of actin filaments. Rapid extension and retraction of filopodia and lamellipodia through F-actin assembly and disassembly is the driving force that permits cells to explore and navigate in response to extracellular signals. This is evident in cell spreading and migration ³⁶. As mentioned the morphological evaluation of F-action cytoskeleton filaments and nuclei was done using CLMS and the samples preparation was previously described in detail.

2.4.4.3. Apoptosis

The process of programmed cell death, or apoptosis, is generally characterized by distinct morphological characteristics and energy-dependent biochemical mechanisms ³⁷. Apoptosis is considered a vital component of various processes including normal cell turnover, proper development and functioning of the immune system, hormone-dependent atrophy, embryonic development and chemical-induced cell death. Inappropriate apoptosis is a factor in many human conditions including neurodegenerative diseases, ischemic damage, autoimmune disorders and many types of cancer ³⁷.

The apoptosis of the tested cells in presence of WCS_{ster} and HS_{ster} was evaluated by flow cytometry. Flow cytometry is a powerful technique for the analysis of multiple parameters of individual cells within heterogeneous populations. Flow cytometers are used in a range of applications from immunophenotyping, to ploidy analysis, to cell counting and GFP expression analysis. The flow cytometer performs this analysis by passing thousands of cells per second through a laser beam and capturing the light that emerges from each cell as it passes through. The data gathered can be analyzed statistically by flow cytometry software to report cellular characteristics such as size, complexity, phenotype, and health.

In this thesis, it is presented in a summary way how a flow cytometer works, how scattered light and fluorescence are detected by a flow cytometer, and how the resulting data can be analyzed. The figure 2.11 shows the primary systems of the flow cytometer schematically, which are: the fluidic system, which presents samples to the measuring point and takes away the waste; the lasers, which are the light source for scatter and fluorescence; the optics, which gather and direct the light; the detectors, which receive the light; and, the electronics and the peripheral computer system, which convert the signals from the detectors into digital data and perform the necessary analyses³⁸.

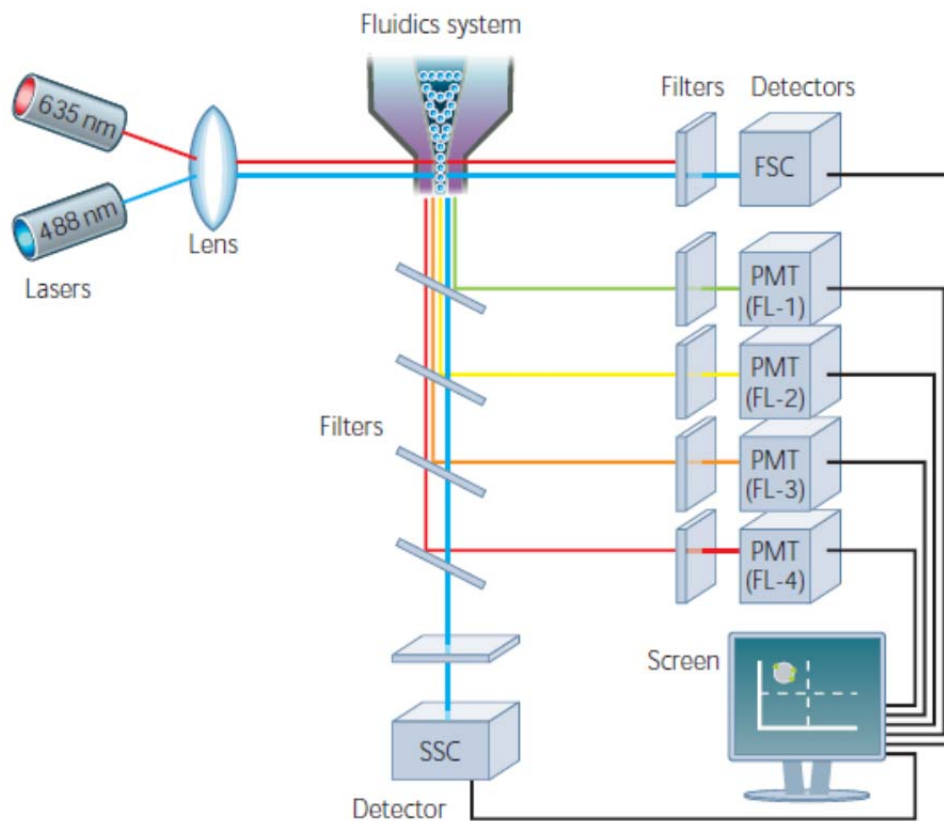


Figure 2.11- Schematic overview of a typical flow cytometer setup (adapted from ³⁸).

As a cell passes through the laser, it will refract or scatter light at all angles. Forward scatter, or low-angle light scatter, is the amount of light that's scattered in the forward direction as laser light strikes the cell. The magnitude of forward scatter is roughly proportional to the size of the cell. Light is quantified by a detector that converts intensity into voltage. In most cytometers, a blocking bar (called an obscuration bar) is placed in front of the forward scatter detector. The obscuration bar prevents any of the intense laser light from reaching the detector. As a cell crosses the laser, light is scattered around the obscuration bar and is collected by the detector ³⁸.

Cells have traditionally been gated according to physical characteristics. For instance, subcellular debris and clumps can be distinguished from single cells by size, estimated by forward scatter. Also, dead cells have lower forward scatter and higher side scatter than living cells. The different physical properties of cells allow them to be distinguished from each other and from cellular contaminant ³⁸.

Adherent 24 hour MG63 cells were exposed to WCS_{ster} or HS_{ster} Hap nanoparticles, 50 $\mu\text{g/ml}$, for three days, and evaluated by flow cytometry for the presence of apoptosis. Cells were enzymatically released (0.05% trypsin, 0.25% EDTA) and approximately 10^6 cells were processed with the TACS Annexin V-FITC Apoptosis Detection kit, following the manufacturer's instructions. Annexin V, an anticoagulant protein, binds negatively charged phospholipids (phosphatidylserine) on the outer leaflet of the cytoplasmic membrane, following phospholipid asymmetry disruption in early apoptotic event. The combination of annexin V-FITC and propidium iodide allows the differentiation between early apoptotic cells (annexin V-FITC positive), late apoptotic and/or necrotic cells (annexin V-FITC and propidium iodide positive) and viable cells (unstained).

2.4.4.4. Gene expression by Reverse-Transcription Polymerase Chain Reaction (RT-PCR)

In the present thesis different aspects of cell-cell and cell-Hap NPs interaction were evaluated at the gene level. Several steps in the gene expression process may be modulated, including the transcription, RNA splicing, translation, and post-translational modification of a protein. Gene regulation gives the cell control over structure and function, and is the basis for cellular differentiation, morphogenesis and the versatility and adaptability of any organism. Generation of RNA from DNA is known as transcription. In other word transcription is the process of creating a complementary RNA copy of a sequence of DNA.

Adherent 24-hour MG63 cells were exposed to WCS_{ster} , HS_{ster} , HS-AuNPs, HS-AuNPs-FA, 50 $\mu\text{g/ml}$, for three days, and evaluated by Reverse-Transcription Polymerase Chain Reaction (RT-PCR) for the expression of the housekeeping gene GAPDH (glyceraldehyde 3 phosphate dehydrogenase) and the osteoblastic genes collagen 1 (Col 1), alkaline phosphatase (ALP), Runx-2 and Bone Morphogenetic Protein-2 (BMP-2). Total RNA was extracted using RNeasy® Mini Kit (QIAGEN) according to manufacturer's instructions. The concentration and purity of total RNA in each sample were determined by UV spectrophotometry at 260 nm and by calculating the $A_{260\text{nm}}/A_{280\text{nm}}$ ratio, respectively. The mechanism

and the principle functionality of UV spectrophotometry were already described in this chapter (section of Ultra Violet-Visible spectrophotometer). Half microgram of total cellular RNA from each sample was reverse transcribed and amplified (25 cycles) with the Titan One Tube RT-PCR System (Roche), with an annealing temperature of 55°C. The primers used are listed on Table 2.4. The RT-PCR products were separated on a 1% (w/V) agarose gel and visualized by Ethidium Bromide staining. Ethidium Bromide is a DNA intercalator, inserting itself into the spaces between the base pairs of the double helix^{39,40}. Ethidium Bromide possesses UV absorbance maxima at 300 and 360 nm. Additionally, it can absorb energy from nucleotides excited by absorbance of 260 nm radiation. Ethidium re-emits this energy as yellow/orange light centered at 590 nm^{39,40}.

The images of the gel were captured with a camera and analyzed with Image J 1.41 software. To obtain a semi-quantitative assessment of gene expression, data were expressed as normalized ratios by comparing the integrated density values for all genes tested with those for GAPDH.

Table 2.4 – Primers used on RT-PCR analysis of MG63 cell cultures.

Gene	5' Primer	3' Primer
GAPDH	5'-CAGGACCAGGTTACCAACAAGT-3'	5'-GTGGCAGTGATGGCATGGACTGT-3'
COL1	5'-TCCGGCTCCTGCTCCTCTTA-3'	5'-ACCAGCAGGACCAGCATCTC-3'
ALP	5'-ACGTGGCTAAGAATGTCATC-3'	5'-CTGGTAGGCGATGTCCTTA-3'
BMP-2	5'-GCAATGGCCTTATCTGTGAC-3'	5'-GCAATGGCCTTATCTGTGAC-3'
RUNX-2	5'-CCCCACGACAACCGCACCAT-3'	5'-CACTCCGGCCCAAAATC-3'

2.5. References

- 1 M.A.Martins; C.Santos; M.M.Almeida and M.E.V.Costa. "Hydroxyapatite micro- and nanoparticles: nucleation and growth mechanisms in the presence of citrate species". *Journal of Colloid and Interface Science* **318**, 210-216, (2008).
- 2 S.V.Dorozhkin; M.Schmitt; J.M.Bouler and G.Daculsi. "Chemical transformation of some biologically relevant calcium phosphates in aqueous media during a steam sterilization". *Journal of Materials Science: Materials in Medicine* **11**, 779-786, (2000).

- 3 John, Turkevich; Peter Cooper, Stevenson and James, Hillier. "A study of the nucleation and growth processes in the synthesis of colloidal gold". *Discuss.Faraday Soc.* **11**, 55-75, (1951).
- 4 Pautke, Christoph; Schieker, Matthias; Tischer, Thomas; Kolk, Andreas; Neth, Peter; Mutschler, Wolf and Milz, Stefan. "Characterization of Osteosarcoma Cell Lines MG-63, Saos-2 and U-2 OS in Comparison to Human Osteoblasts ". *Anticancer Research* **24**, 3743-3748, (2004).
- 5 S. Hattar; A. Berdal; A. Asselin; S. Loty; Greenspan, D.C. and Sautier, J-M. "Behaviour of Moderately Differentiated Osteoblast-like cells in Contact with Bioactive Glasses". *European Cells and Materials* **4**, 61-69, (2002).
- 6 Montanaro, L.; Arciola, C. R.; Campoccia, D. and Cervellati, M. "In vitro effects on MG63 osteoblast-like cells following contact with two roughness-differing fluorohydroxyapatite-coated titanium alloys". *Biomaterials* **23**, 3651-3659, (2002).
- 7 Fabian, Peters; Karsten, Schwarz and Matthias, Eppe. "The structure of bone studied with synchrotron X-ray diffraction, X-ray absorption spectroscopy and thermal analysis". *Thermochimica Acta* **361**, 131-138, (2000).
- 8 Robert, E. Dinnebier and S.J.L. Billinge. *Powder diffraction: theory and practice*. Vol. Royal Society of Chemistry (2008).
- 9 Robert, E. Dinnebier and Simon, J. L. Billinge. *Principles of Powder Diffraction*. (2011).
- 10 Sing, Kenneth. "The use of nitrogen adsorption for the characterisation of porous materials". *Colloids and Surfaces A: Physicochemical and Engineering Aspects* **187-188**, 3-9, (2001).
- 11 Kaneko, Katsumi. "Determination of pore size and pore size distribution. Adsorbents and catalysts ". *Journal of Membrane Science* **96**, 59-89, (1994).
- 12 F.Rojas; I.Kornhauser; C.Felipe; J.M.Esparza; S.Cordero; A.Dominguez and J. L. Riccardo. "Capillary condensation in heterogeneous mesoporous networks consisting of variable connectivity and pore-size correlation". *Phys.Chem.Chem.Phys* **4**, 2346-2355, (2002).
- 13 Sing, K. S. W. "IUPAC Commission on Colloid and Surface Chemistry Including Catalysis. Reporting Physisorption Data for Gas/Solid Systems with Special Reference to the Determination of Surface Area and Porosity". *Pure Appl. Chem.* **57**, 603-619, (1985).
- 14 Ernest, Meyer; Hans Josef, Hug and Roland, Bennewitz. *Scanning Probe microscopy*. (2004).
- 15 Weili, Zhou and Zhong Lin, Wang. *Scanning microscopy for nanotechnology: techniques and applications*. (2006).
- 16 David Bernard, Williams and Carter, C. Barry. *Transmission electron microscopy: a textbook for materials science Parte 3*. Vol. Second Edition (2009).

- 17 Rolf, Erni. *Aberration-Corrected Imaging in Transmission Electron Microscopy: An introduction*. (Imperial College Press, 2010).
- 18 Andreas, Rosenauer. *Transmission electron microscopy of semiconductor nanostructures: an analysis of composition and strain state*. (2003).
- 19 Wright, Shirley J.; Centonze, Victoria E.; Stricker, Stephen A.; DeVries, Peter J.; Paddock, Stephen W. and Schatten, Gerald. in *Methods in Cell Biology* Vol. Volume 38 (ed Matsumoto Brian) 1-45 (Academic Press, 1993).
- 20 Guy, Cox. "Biological confocal microscopy". *Materials Today* **5**, 34-41, (2002).
- 21 Dürrenberger, Markus B.; Handschin, Stephan; Conde-Petit, Béatrice and Escher, Felix. "Visualization of Food Structure by Confocal Laser Scanning Microscopy (CLSM)". *LWT - Food Science and Technology* **34**, 11-17, (2001).
- 22 Barbara, H. Stuart. *Infrared spectroscopy: fundamentals and applications*. (2004).
- 23 Donald, L. Pavia; Gary, M. Lampman; George, S. Kriz and James, R. Vyvyan. *Introduction to spectroscopy*. Vol. fourth edition (2009).
- 24 Adriyan, S. Milev; Kannangara, G. S.Kamali and Michael, A. Wilson. "Template-Directed Synthesis of hydroxyapatite from a Lamellar Phosphonate". *Langmuir* **20**, 1888-1894, (2004).
- 25 *Zeta potential*, 2011).
- 26 A.Ghadimi; R.Saidur and H.S.C.Metselaar. "A review of nanofluid stability properties and characterization in stationary conditions". *International Journal of Heat and Mass Transfer* **54**, 4051-4068, (2011).
- 27 Tony, Owen. *Fundamentals of modern UV-visible spectroscopy*. (Agilent Technologies, 2000).
- 28 J.P.Bonnelle; Bernard, Delmon and E.G.Derouane. *Surface properties and catalysis by non-metals*. (D.Reidel Publishing Company, 1983).
- 29 V.Barron and J.Torrent. "Use the Kubelka-Munk theory to study the influence of iron oxides on soil colour". *Journal of soil science* **37**, 499-510, (1986).
- 30 Whan, Ruth E. *Materials characterization*. Vol. 10 (ASM Handbook, 1986).
- 31 http://www.waters.com/waters/nav.htm?cid=10049055&locale=en_PT.
- 32 Wang, Piwen; Henning, Susanne M. and Heber, David. "Limitations of MTT and MTS-Based Assays for Measurement of Antiproliferative Activity of Green Tea Polyphenols". *Plos One* **5**, e10202, (2010).
- 33 Tan, Jian and Saltzman, W. Mark. "Biomaterials with hierarchically defined micro- and nanoscale structure". *Biomaterials* **25**, 3593-3601, (2004).

- 34 Malich, Gregor; Markovic, Boban and Winder, Chris. "The sensitivity and specificity of the MTS tetrazolium assay for detecting the in vitro cytotoxicity of 20 chemicals using human cell lines". *Toxicology* **124**, 179-192, (1997).
- 35 Stricker, Jonathan; Falzone, Tobias and Gardel, Margaret L. "Mechanics of the F-actin cytoskeleton". *Journal of Biomechanics* **43**, 9-14, (2010).
- 36 Pamela J. Woodring; E. David Litwack; Dennis D.M. O'Leary; Ginger R. Lucero; Jean Y.J. Wang and Hunter, Tony. "Modulation of the F-actin cytoskeleton by c-Abl tyrosine kinase in cell spreading and neurite extension". *The Journal of Cell Biology* **156**, 879-892, (2002).
- 37 Elmore, Susan. "Apoptosis: A Review of Programmed Cell Death". *Toxicol Pathol.* **35**, 495-516, (2007).
- 38 Rahman, Misha. in *Introduction to Flow Cytometry* Vol. 4 (ed Serotec Ltd) (Serotec Ltd. Endeavour House, Langford Business Park, Langford Lane, Kidlington, Oxford OX5 1GF, UK, 2006).
- 39 Nafisi, Shohreh; Saboury, Ali Akbar; Keramat, Nahid; Neault, Jean-Francois and Tajmir-Riahi, Heidar-Ali. "Stability and structural features of DNA intercalation with ethidium bromide, acridine orange and methylene blue". *Journal of Molecular Structure* **827**, 35-43, (2007).
- 40 Zhang, Guowen; Hu, Xing and Fu, Peng. "Spectroscopic studies on the interaction between carbaryl and calf thymus DNA with the use of ethidium bromide as a fluorescence probe". *Journal of Photochemistry and Photobiology B: Biology* **108**, 53-61, (2012).

Chapter 3

*Citrate assisted synthesis of
hydroxyapatite nano and micro crystals
with different morphologies*

3.1. Introduction

As referred in Chapter 1 hydroxyapatite has been extensively involved in bone related therapies due to its excellent biocompatibility and bone bonding ability and also due to its structural (nanometric sized crystallites) and compositional similarity to the mineral phase of human bones. It can also be used in other biomedical applications such as: non-viral carriers for drug delivery, gene therapy and protein carrier due to its ease of handling and notorious adsorption ability ^{1,2}.

Nanotechnology offers opportunities to interface with biology in new ways and with unprecedented precision. In some of the above mentioned applications like drug delivery systems, nanoparticles with specific size, shape and other physico-chemical properties are required, since they may modulate cellular pathways ^{3,4}. Recent studies have shown that depending on many factors, including particle morphology issues, sedimentation effects of large and dense particles, and the composition of the protein corona on the particle, a favorable or adverse cell response will be induced ^{5,6}. Although being extensively studied this subject is not yet fully understood. The development of successful nano engineered particles and the clarification of its impact on cellular response remains a challenge.

For controlling the particle morphology, an appropriate method of synthesis is required. Therefore, new synthesis methods enabling to produce particles with predetermined morphology are thus currently needed. During the past few decades, considerable research efforts have converged to the development of synthesis processes able to produce hydroxyapatite nanoparticles with different sizes and shapes. Several methods have been proposed including wet chemical precipitation, sol-gel, hydrothermal synthesis, multiple emulsion, biomimetic deposition and electrodeposition technique ⁵⁻⁷, among others. Many experimental variables can be manipulated to control the characteristics of the Hap nanoparticles. The effect of some of these variables such as: additives (organic or inorganic chemical species), temperature, pressure, etc, can change dramatically the shape and size of the obtained particles.

A conventional hydrothermal synthesis method was the technique chosen in this research for obtaining at low cost hydroxyapatite nanoparticles with high degree of crystallinity and thus easily characterizable. Additionally this method is also particularly suitable for the growth of large crystals while maintaining good control over their composition. To maintain a good control of precipitated particles morphology an additive is used frequently as a tailoring agent, which main function is to *draw* the shape and size of the particle. The additive used in this study is citric acid. The selection of citric acid is justified by citrate ion chelant properties which account for its current use in food and drinks industry ⁸. An important physiological function of citric acid is also found in Krebs cycle, in which it plays a key role contributing to energy production in mitochondria ⁹. Another biological role of citrate is found at the interface of bone apatite and collagen where it stabilizes the apatite platelet morphology ¹⁰. It is known that about 80% wt.% of the total citrate present in the body is accumulated in bone ¹⁰. Bio inspired by nature, citrate assisted growth of Hap particles is envisaged as a promising synthesis technique in terms of the ability of particle morphology control.

In the present work, the production of Hap particles by hydrothermal synthesis (HS) at high temperature (180°C) with different morphologies is studied. The effects of citrate concentration on the Hap nucleation and growth at high temperature will be here analysed.

The chapter is organized as follows: The effects of different amounts of citrate ion (Cit) on the final morphology of Hap particles obtained after a synthesis time of 24H are firstly discussed and then the morphology evolution with the synthesis time is analysed for two of the citrate concentrations corresponding to the lower and upper limits of the covered Cit concentrations, attempting to correlate the particle morphology development with the interplay among citrate (or citrate derived species) and other relevant precipitating variables.

3.2. Synthesis of Hap particles

3.2.1. Effects of (Citrate:Calcium) ratio on Hap particle morphology

Hap particles were precipitated under different citrate calcium (Cit:Ca) ratios as described in table 3.1. Table 3.1 summarizes the characteristics of the Hap particles selected for the present work. For convenience the Hap particles samples are labelled according to the used Cit:Ca ratios. The XRD (X-ray diffraction) patterns of the obtained particles under different Cit:Ca ratio, at 180°C for 24 hours are shown in figure 3.1. It is observed that hydroxyapatite is the precipitated crystalline phase in all the precipitating media regardless (Cit:Ca) since all of the diffraction peaks can be assigned to hexagonal hydroxyapatite (space group *P63/m*) according to JCPDS N° 09-0432. No secondary crystalline phases could be identified in any of the various precipitating conditions.

Table 3.1- Characteristics of Hap particles precipitated from solutions with different (Cit:Ca) ratios.

Cit:Ca ratio	Sample code	Crystallite size (nm) (002)	Specific Surface Area (m ² /g)	Pore size (nm)	SHape
3:1	HS 3:1	38	55	12,5	Rod like
3,5:1	HS 3,5:1	35	48	20,2	Hedgehogs like
4:1	HS 4:1	33	43	16,1	Hedgehogs like
7:1	HS 7:1	34	17	16,7	Bundle like

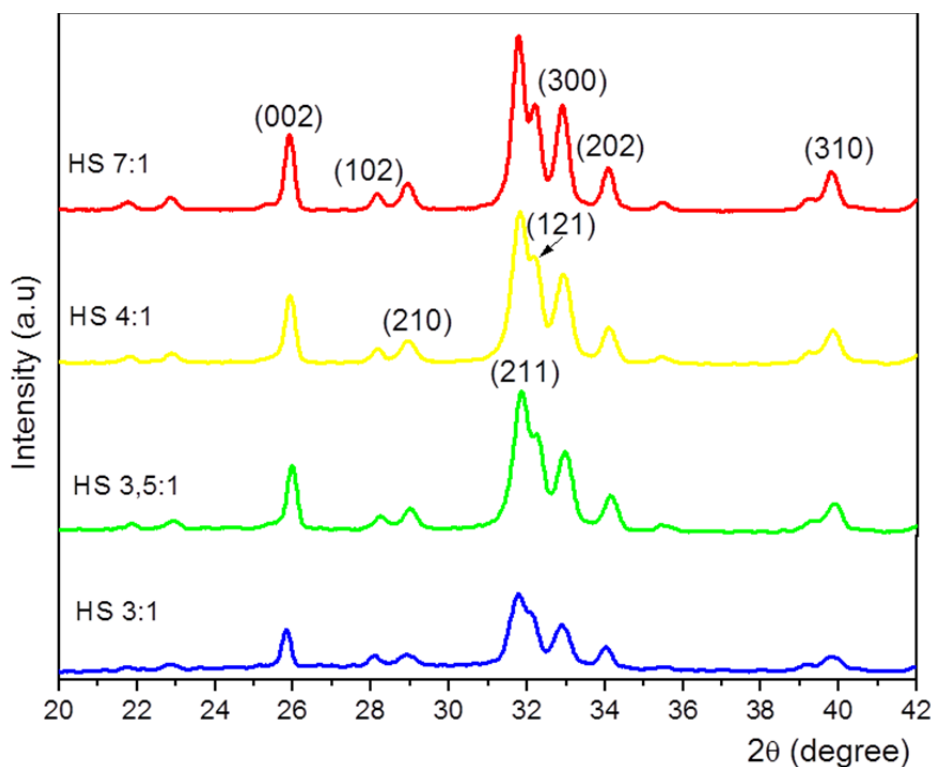


Figure 3.1- XRD patterns of Hap particles synthesized by HS method under different (Cit:Ca) ratios, after 24 hours.

The crystallite size estimated according to Scherrer equation was seen to be of the same order of magnitude for the different Hap particles (table 3.1). Wu et al. have precipitated fluoroapatite particles in presence of citric acid and EDTA ¹¹ and did observe a variation on $(h00)/(00l)$ peak ratio which was indicative of a preferential growth along c axis. The present XRD results do not evidence significant variation of $(h00)/(00l)$ peak ratio as (Cit:Ca) increases. This reflects possibly the fact that a combination of citric acid and EDTA as that used by Wu et al. might be more effective for complexing Ca ions than citrate ion and thus affect more severely the coherence length of the crystallite along the $[100]$ axis ¹¹.

Figure 3.2 shows the microstructures of Hap particles synthesized at 180°C after 24 hours from solutions containing different (Cit:Ca) ratios. First, it can be seen that Hap particles synthesized under different (Cit:Ca) ratios have different morphologies. Additionally it is also shown that when an increase in the initial

molar ratio of citric acid to calcium (Cit:Ca) takes place, a strong modification of Hap morphology also occurs, i.e. the rod like shaped particles obtained with a HS 3:1 (fig 3.2a) change to hedgehogs (3,5:1- 4:1) (fig 3.2 b and c) and to bundle like shaped particles (HS 7:1) (fig 3.2 d). Moreover the size of the resulting particles increases from the nanometric size of HS 3:1 up to a micrometric size observed for the others ratios. It is worth mentioning that a Cit:Ca ratio of 2:1 was also attempted giving place to an instantaneous precipitation. This fact indicated that a certain amount of Ca^{2+} ions remained uncomplexed after citric acid addition and thus were free to react promptly with PO_4^{3-} ions hence giving place to the ready precipitation of hydroxyapatite particles with non-uniform morphology. However when an additional small amount of citrate ions was added to the system, i.e. (Cit:Ca) was increased to (3:1), nucleation was inhibited at room temperature as the solution remained clear and transparent for several hours. As the temperature was increased then nucleation took place and precipitation occurred.

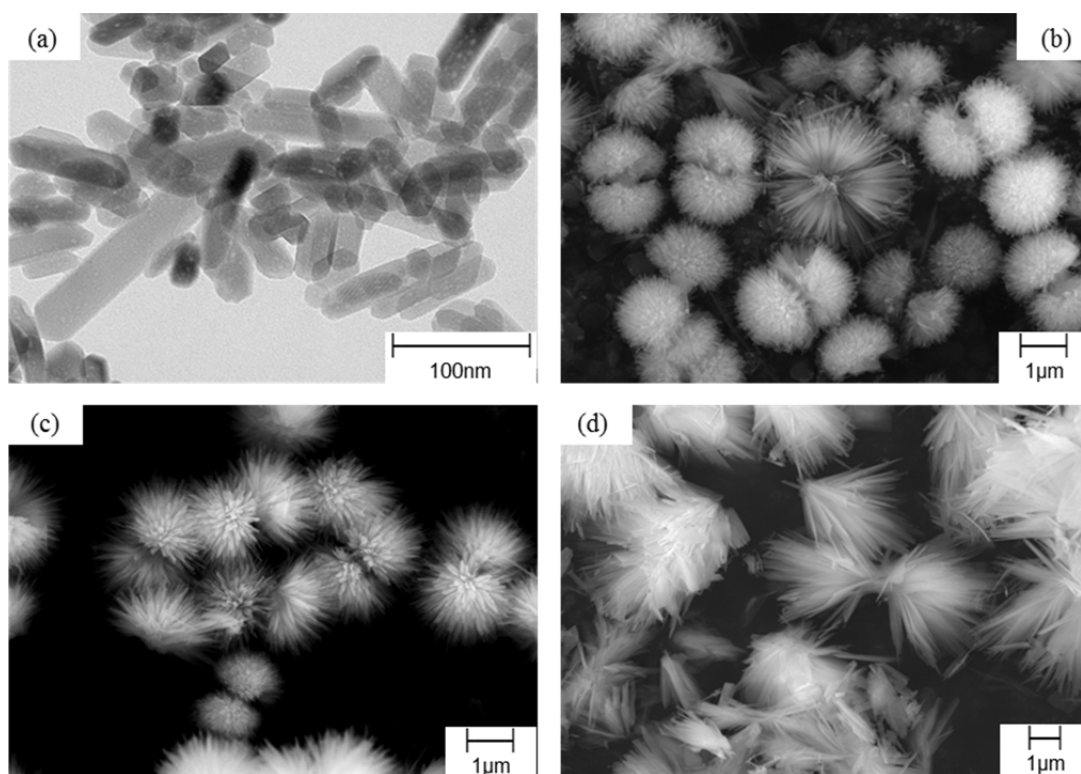


Figure 3.2- TEM and SEM micrographs of Hap particles synthesized from solutions with different (Cit:Ca) ratios: (a) 3:1; (b) 3.5:1; (c) 4:1 and (d) 7:1.

To obtain a more detailed information about particle morphology and preferential growth, transmission electron micrographs were acquired (figure 3.3). Figure 3.3 (a) shows the TEM micrographs of the Hap nanoparticles obtained with a Cit:Ca ratio of 3:1, being visible that the size of the nanorods is approximately 20 nm in width while the length varies between 20 and 100 nm. The thickness is about 15 nm. The clearly visible lattice fringes are indicative of the high crystallinity of the Hap nanoparticles (fig 3.3 (b))¹². It is evidenced that particles have hexagonal crystal structure and grow preferentially along c-axis. The prismatic facets seem differently developed as larger facets alternate with less developed ones. The obtained results indicate that the citrate or citrate-related species assist the precipitation of Hap particle as additives binding to specific crystallographic facets of hydroxyapatite crystal hence limiting the growth perpendicular to such facets. These results are in line with the conclusions of M. A. Martins et al. who pointed out that citrate binds preferentially to lateral prismatic facets and thus favours the rod like morphology of Hap particles precipitated under specific conditions of citrate concentration and pH⁷. Others authors reported similar results but using others synthesis methods¹³⁻¹⁶.

As already referred, further addition of citrate ions causes significant modifications to the particle morphology. This effect is sharply felt when Cit:Ca ratio changes from 3:1 to 3.5:1 leading to hedgehogs formation. As observed in fig 3.3 ((c) and (d)) TEM micrographs show two well defined populations of particles: one that is nanometric sized and a second one composed of longer sized particles. Hedgehogs particles are composed by multiple fiber-like particles irradiating from a central junction (fig 3.2 (b)). The length of such fibers is around 800 nm and their width is about 20 nm (figure 3.3 (c)). The central region reveals a large number of small Hap nanoparticles, hence suggesting that the central junction may result from Hap nanoparticle assemblage in a early stage of particle growth.

Additional increase of the Cit:Ca ratio beyond 3.5:1 has now a less pronounced impact on the final shape of the Hap particles as observed in figure 3.2 (c) and (d). Nevertheless it is visible by SEM and TEM (fig 3.2 and 3.3) that nano fibers in hedgehogs particles become longer. The length varies between 1,2 and 1,5 μm

and the width is now around 35 nm (figure 3.3). A closer look on these particles (figure 3.3 (f)) reveals that small Hap particles are now less abundant. When the maximum concentration of citric acid is added to the synthesis medium, i.e. the Cit:Ca ratio increases to 7.1, the morphology of the Hap structures changes from a fiber-structured particle to a sheet-like structured particle. Apparently fiber-like Hap particles underwent an oriented aggregation process which enabled fibre lateral attachment hence resulting in bundled sheet-like units (figure 3.3 (g) and (h)). Under Cit:Ca = 7:1 the fiber-like particles seem to have grown preferentially in length as compared to other Cit:Ca ratios: a length of 2-3 μm and a width of 42 nm could be observed in the images of figure 3.3 ((g) and (h)).

It is known that citric acid possesses three carboxylic and one hydroxyl group, which can provide chelating ability and bind selectively to specific crystallographic facets¹⁷. In the beginning of the precipitation process, citrate ion reacts with Ca^{2+} ions to form calcium complexes hence decreasing the concentration of free Ca^{2+} ions in the bulk solution. When the solution temperature increases complexes stability is changed allowing Ca^{2+} ions to get free and combined with PO_4^{3-} leading to the precipitation of hydroxyapatite. Under hydrothermal conditions and depending on the used Cit:Ca ratio, citrate ion helps tailoring different particle morphologies which seem mainly related either to selective growth of primary particle along certain crystallographic directions or to particular assemblage mode of primary particles thereby resulting in differently nanostructured Hap particles.

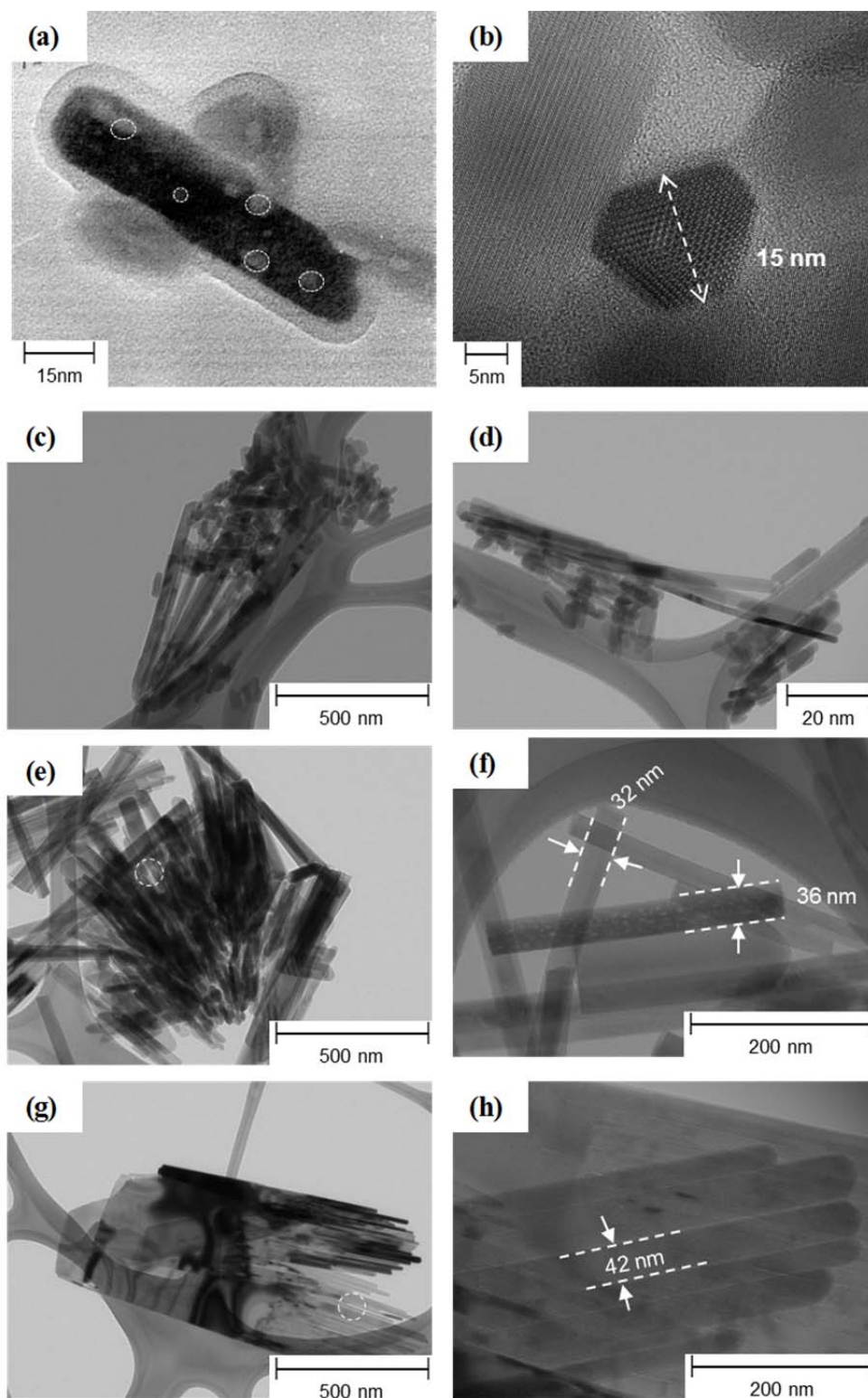


Figure 3.3- TEM images of Hap particles precipitated at 180°C after 24 H from solutions with different (Cit:Ca) molar ratios: 3:1 (a, b); 3,5:1 (c, d); 4:1 (e, f) and 7:1 (g, h). Images f) and h) are amplified views of particular sample regions identified by dotted circles on the images e) and g), respectively. As Cit:Ca ratio increases from 3:1 to 7:1, particle

morphology changes from prism (with approximate thickness and width of 15 nm and 20 nm, respectively, and 20 to 100 nm in length) ((a) and (b) to bundled fiber-like particles exhibiting fiber later attachment indicative of oriented aggregation process ((g) and (h)).

The strong influence of (Cit:Ca) ratio on the morphology of the particles is also expressed through the specific surface area (SSA) of the different particles as can be seen in table 3.1. The specific surface area is 55 m²/g for nanometric Hap particles (HS 3:1) and 17 m²/g for nanostructured Hap particles (HS 7:1). The significant reduction in SSA reflects the size increase of the particles. N₂ adsorption/desorption isotherms for different types of particles are presented in figures 3.4. According to IUPAC classification the synthesized Hap particles present a type IV isotherm which exhibits the characteristic hysteresis loop (HL) of a mesoporous material. For all the obtained Hap particles (figure 3.4) the obtained HLs reflect a H1 isotherm indicative of tubular pores¹⁸. Although the morphologies of the obtained particles are rather different, the type of pores evidenced by HLs is similar. The porosity of the precipitated Hap particles is also evidenced by TEM results. As observed in figure 3.3 (a) the HRTEM image of a HS 3:1 particle allows some pores to be detected (indicated by dotted circles and/or arrows). The average pore size (BJH analysis of adsorption curve) evolves from 12.5 nm for HS 3:1 to 16,7 nm for HS 7:1, respectively, whereas the total N₂ adsorbed amount suffers a drastic reduction with the increase of the (Cit:Ca) molar ratio (figure 3.4). Such pore size increase during precipitation may result from the merging of smaller pores accompanying the particle structure evolution as reported for other inorganic materials, like silica¹⁹. Although particles synthesized with Cit:Ca 7:1 present a bigger pore size when compared with Cit:Ca 3:1 the volume adsorbed by Cit:Ca 7:1 is significantly lower. This result shows that HS 3:1 particles are not only smaller than HS 7:1 particles but also have a larger amount of pores. These are thus two cooperative attributes explaining the larger surface area of HS 3:1 particles which are thus expected to have enhanced adsorptive capability. Literature reports on Hap pore morphology are relatively scarce. J. Chen et al. synthesized rod Hap particles with slit-shaped pores, but the experimental conditions used by the authors were different from those used in this study²⁰. Dodecylamine, CaCl₂ and H₃PO₄ were mentioned as reagents as well as a high

pH value (10), a shorter precipitation time (12 hours) and a lower synthesis temperature of 100°C²⁰ as precipitating conditions which are rather different as compared to the ones adopted in this work.

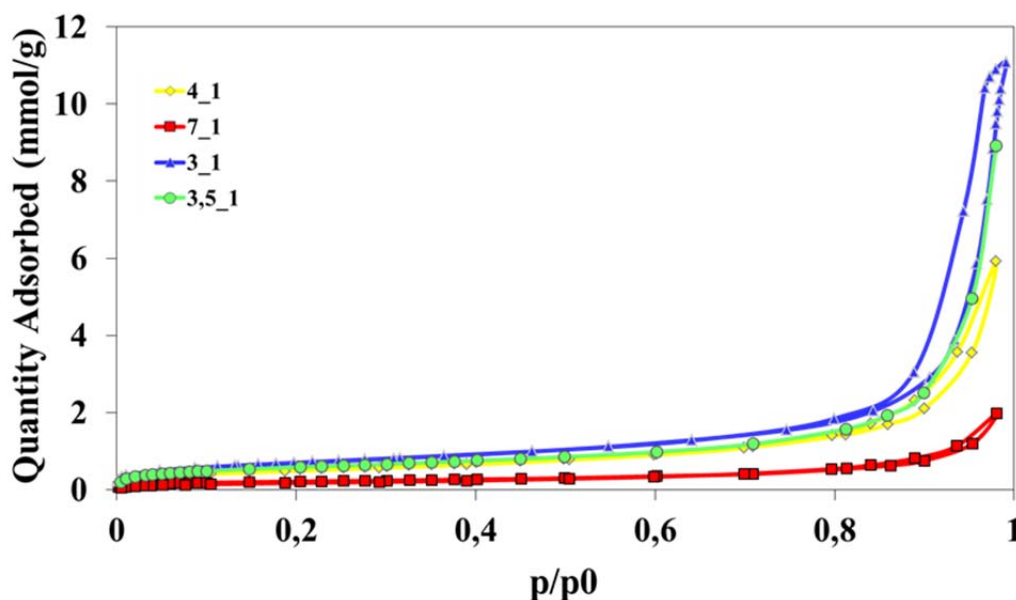


Figure 3.4- Nitrogen adsorption and desorption isotherms of Hap particles synthesized from solutions with different Cit:Ca ratios.

It is known that citrate ion binds strongly to the surface of calcium phosphate particles²¹ but the particular features respecting the binding mode of citrate species on Hap particle surface is still poorly defined and thus remains a challenging issue. The binding mode of citrate cannot be dissociated from the configuration of citrate as adsorbate which in turn may help to understand the different morphologies of the synthesized particles while giving us clues about the possible growth mechanisms. Recent literature has proposed different models for interfacial structures of adsorbed citrate on Hap surface. Y.-Y. Hu et al suggested that citrate adsorbs on (100) face, coordinating strongly to three surface calcium ions via its three carboxylic groups²¹. This adsorption model is based on the correct matching of carboxylate groups inter-spacings in citrate molecule with those of calcium ions along the apatite c-axis. A different coordination mode was suggested by W. Jiang et al²² according to which citrate ion coordinates only one surface calcium ion through a terminal carboxylic group. This coordination mode

would benefit the self-assembly of citrate molecules by intermolecular hydrogen bonding²².

The presence of adsorbed citrate species on the prepared Hap particles with different Cit:Ca ratio can be examined through FTIR analysis. Figure 3.5 shows the FTIR spectra of Hap particles synthesized from solutions with 3:1; 3.5:1; 4:1 and 7:1 Cit:Ca ratios. All the graphs show the characteristic bands of PO_4^{3-} groups at 1096, 1047, 962, 601, 563 and 472 cm^{-1} ²³. The broadening bands attributed to absorbed water are observed at about 3440 and 1637 cm^{-1} . For all samples the hydroxyl bonds (OH) absorption bands at 3572 cm^{-1} and 633 cm^{-1} corresponding to stretching and vibration modes respectively are also observed²³. Moreover the broad band detected at 3200 cm^{-1} in the spectra of the samples corresponding to Cit:Ca ratios of 3:1 and 3.5:1 can be ascribed to ammonium ion. Despite the common features, some marked differences are clearly detected in the 1200-1900 cm^{-1} region.

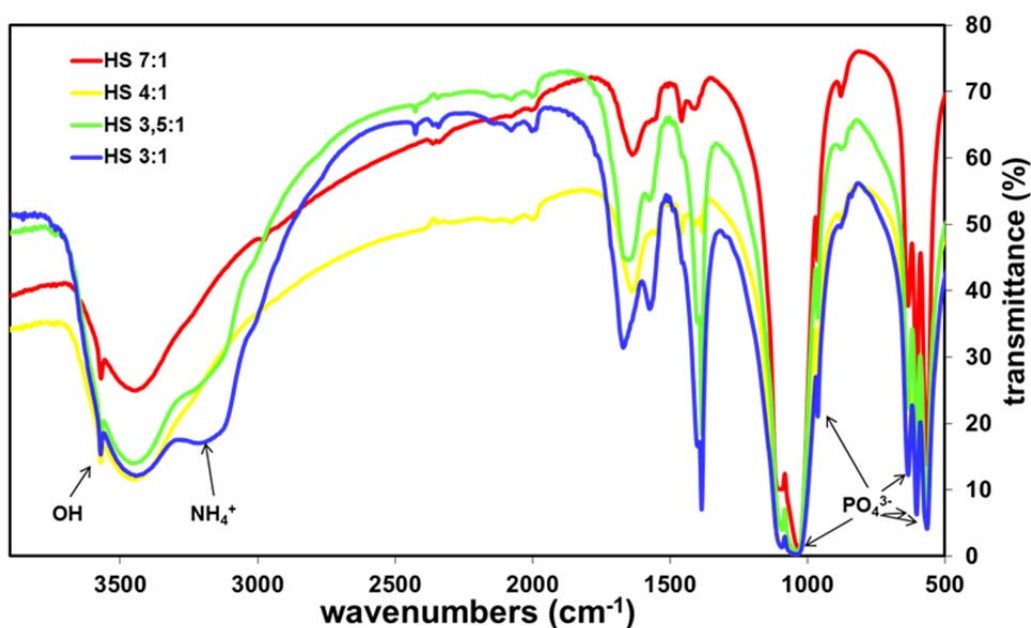


Figure 3.5- FTIR spectra of Hap particles synthesized from solutions with different Cit:Ca ratios at 180°C during 24 hours.

For an easier analysis, a magnification of the FTIR spectra in the range of 1300-1800 cm^{-1} is presented in Figure 3.6. As observed the intensity of the 1384 cm^{-1}

band attributed to $-\text{CH}_2-$ scissoring mode of citrate or citrate-derived compounds²⁴ decreases as Cit:Ca molar ratio increases²⁴. Another visible difference regards the 1670 cm^{-1} band, recognized as $\text{C}=\text{O}$ band in monodentate configuration, whose intensity decreases as the Cit:Ca ratio increases besides shifting to low wavenumbers. Other bands were also identified in the same spectral region which were attributed to the antisymmetric (1650 and 1567 cm^{-1}) and to the symmetric (1458 and 1402 cm^{-1}) stretching modes of carboxylate groups coordinated to Hap surface Ca^{2+} cations²⁵⁻²⁸ either in a monodentate or in a bidentate manner²⁹⁻³¹, respectively (see the illustration of the different coordination modes in figure 3.7). It is visible that the antisymmetric vibrations in both (monodentate and bidentate) configurations are less expressed as Cit:Ca ratio increases. Therefore the present results indicate that the position and intensity of carboxylate related bands get changed as citrate concentration increases in the starting solution, i.e. suggesting that less carboxylate groups remain adsorbed but in a different coordination mode to Hap surface.

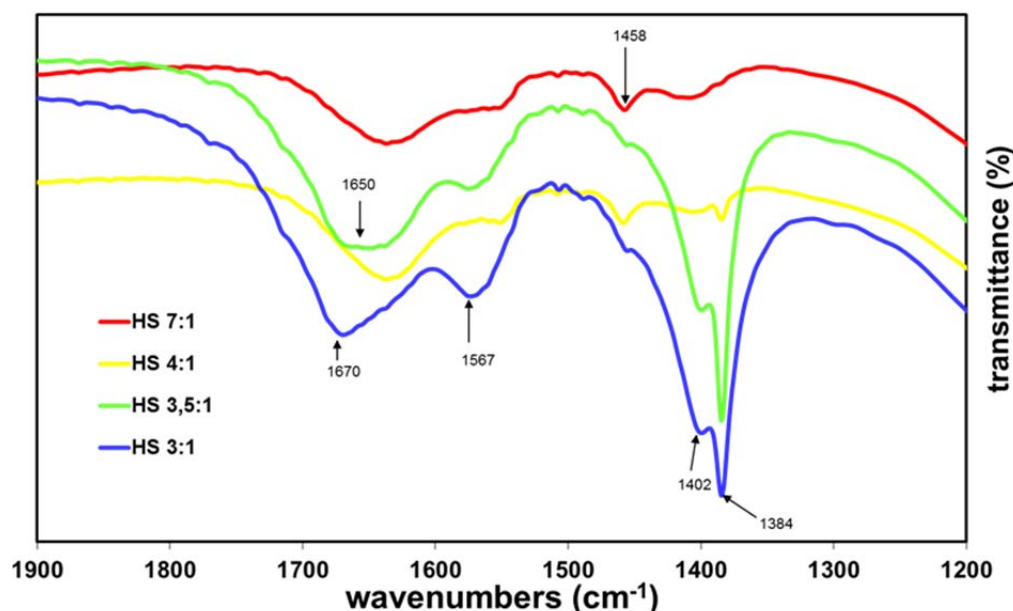


Figure 3.6- FTIR results corresponding to Hap particles synthesized from solutions with different Cit:Ca ratios at 180°C during 24 hours: magnification of the $1900\text{-}1200\text{ cm}^{-1}$ spectral region.

The presence of the original citrate ions (Cit) as adsorbed species on Hap particle surface is highly questionable: instead smaller carboxylated ions resulting from citric acid decomposition under the high temperature and pressure used for Hap thermal synthesis will probably exist. It was already reported that citric acid may degrade at $T > 145^{\circ}\text{C}$ ^{9,32,33} leading to reaction products that include different dehydroxylated or decarboxylated acids and anhydrides depending on the used heating ramp temperature and pressure ⁹. It is thus hypothesized that citrate ion derived species containing carboxylate groups exist as adsorbed entities on Hap particle surface. This hypothesis is furthermore supported by the absence of the 1270 and 1305 cm^{-1} bands on Hap particles spectra normally assigned to citrate skeletal vibrations and free OH group, respectively ³⁴.

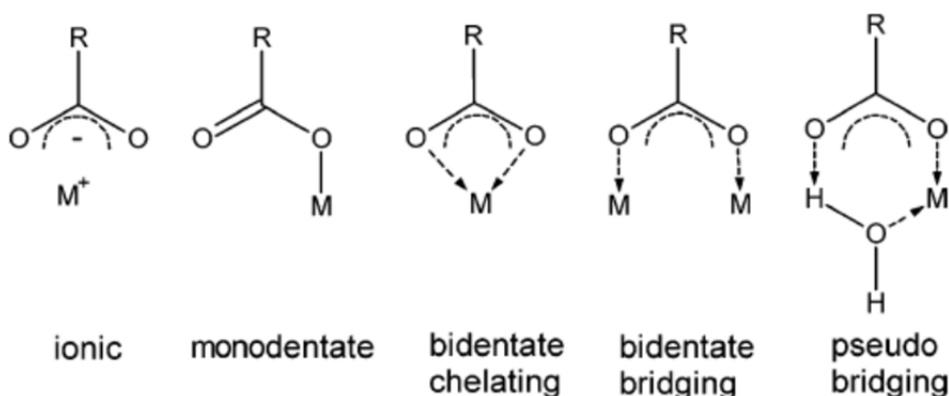


Figure 3.7- Different coordination modes of carboxylate ligands to a surface metal cation (adapted from ³¹).

High-performance liquid chromatography (HPLC) measurements were used for accessing the existence of citrate groups on the surface of the precipitated Hap particles. Figure 3.8 shows the chromatogram of a citric acid solution having different citric acid concentrations and using acetic acid as internal standard. The first peak observed at 5,6 min corresponds to the internal standard, whereas the peak at 7,0 min corresponds to citric acid. Figure 3.9 shows the HPLC chromatogram corresponding to Hap particles obtained from solutions with different Cit:Ca ratio. The Hap particles were firstly solubilized in phosphoric acid. As observed a new peak is detected at 4,7 min which cannot be attributed to the acetic acid neither to citric acid. Instead this new peak should presumably

correspond to a chemical species having a smaller number of atoms as compared to acetic acid, since the peak retention time is shorter than that of acetic acid. Formic acid molecular weight is lower than of acetic acid and may be thus a hypothesis to be considered.

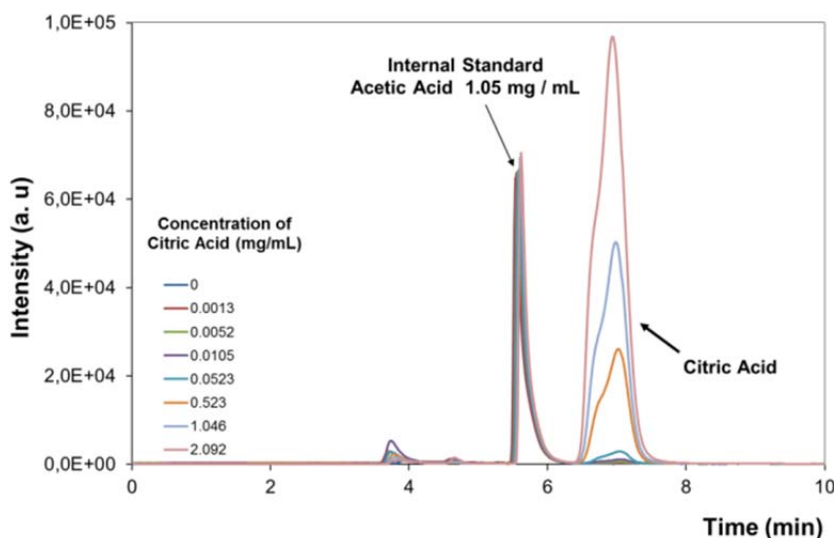


Figure 3.8- HPLC chromatogram corresponding to citric acid solution having different citric acid concentrations when using acetic acid as internal standard.

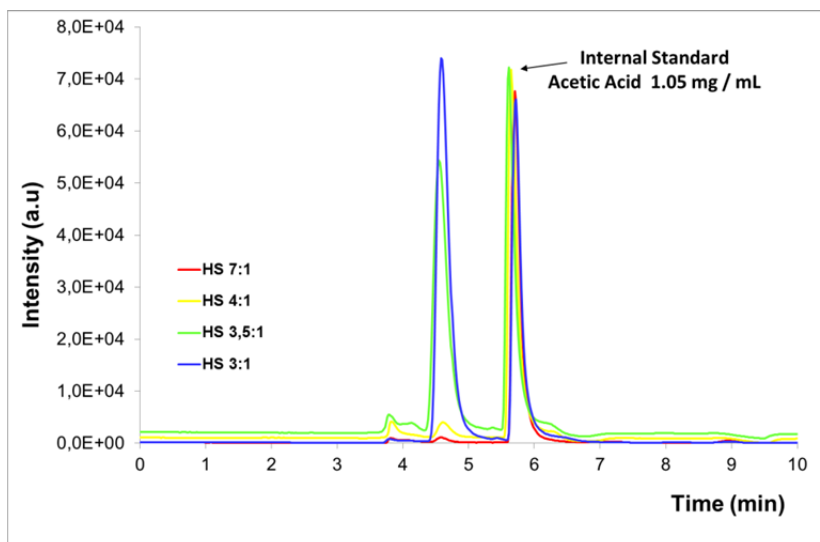


Figure 3.9- HPLC chromatogram of the Hap particles prepared under different Cit:Ca molar ratios after being dissolved in a phosphoric acid solution. The peak at 4,7 min which cannot be attributed to the acetic acid neither to citric acid.

Furthermore it is observed that the new peak intensity decreases as the Cit:Ca ratio increases in the precipitating medium of Hap particles, thus indicating that the amount of the chemical species under analysis decreases as Cit:Ca increases. It is worthy to remind that this trend correlates well with the evolution of FTIR results at the region $1300\text{--}1800\text{ cm}^{-1}$ where carboxylate related bands intensity decreases as the Cit:Ca ratio increases (figure 3.6). It is thus thought that the chemical species detected by HPLC might be related to the carboxylic group detected in FTIR spectra.

Thermogravimetric analyses of the synthesized particles give further evidence of adsorbed organics. Figure 3.10 compares the thermal behaviour of Hap samples prepared under different molar ratios of Cit:Ca. It is observed that the total weight loss decreases substantially as the Cit:Ca ratio increases namely for Cit:Ca ratios above 3.5:1. Additionally, three distinct weight losses could be identified in the thermogravimetric curves corresponding to the two lower Cit:Ca ratios, i.e. Cit:Ca = 3:1 and 3.5:1. The first loss (Δw_1) takes place beneath $\sim 120^\circ\text{C}$ and is followed by a well-defined endothermic peak which can be assigned to the loss of weakly adsorbed water. A second steep weight loss (Δw_2) is detected in the temperature range between $\sim 140^\circ\text{C}$ and $\sim 250^\circ\text{C}$, also accompanied by an endothermic effect. This second loss accounts for 2.5% of the total weight loss, approximately. Following literature data ³⁵ this loss may be ascribed to the release of NH_3 resulting from ammonium ion whose presence was clearly denounced by the FTIR results of the samples HS 3:1 and HS 3.5:1 as previously pointed out. The third loss (Δw_3) is the strongest one as it accounts for at least 3.5% of the total weight loss in both cases. The temperature range corresponding to (Δw_3) is comprised by a broad exothermic band. The interpretation of both features is the oxidative burning out of the existing organic residues (citrate derived ones). It is also worth to mention a last and smaller weight loss observed at 800°C that can be attributed to the phase transition from Hap to $\beta\text{-TCP}$ ³⁵. Comparing now the thermal behaviours of these two samples with those of (4:1) and (7:1) samples one main evidence comes up: (i) the organic content of these two last samples is $\leq 2\%$, i.e. almost half of the content of the former samples (HS 3:1 and HS 3.5:1). Thermal analyses data thus corroborate FTIR and HPLC results as far as particle organics

content is concerned. As just demonstrated this amount decreases as Cit:Ca ratio increases.

As a conclusion the variation of Hap particle morphology induced by different Cit:Ca ratios is accompanied by variations on the absorption bands of adsorbed carboxylate groups, i.e., band type and intensity. These adsorbed species apparently help to tailor the particle morphology. As observed Hap particles grow further along *c* direction as (Cit:Ca) increases but undergo lateral attachment under the highest Cit:Ca ratio (7:1). Accordingly the formed carboxylic species and/or their attachment mode to Hap surface seems conditioned by the solution citrate initial content.

More detailed studies aimed at elucidating the mechanism underlying the formation of these peculiar structures will be presented in the next section.

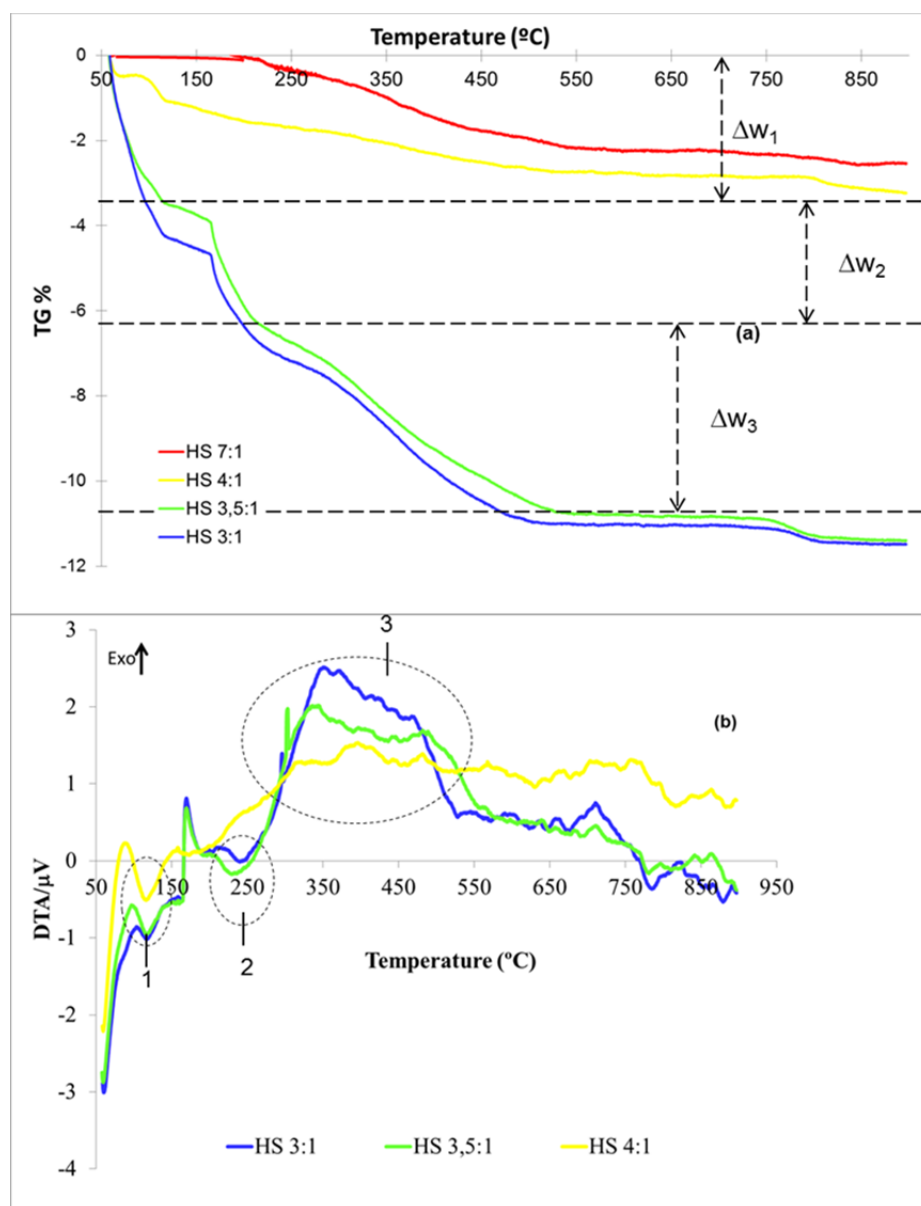


Figure 3.10.- (a) Thermogravimetric and (b) Differential thermal analyses plots of Hap nanoparticles precipitated from solutions containing different (Cit:Ca) ratios: 3:1, 3.5:1 and 4:1. The dotted circles 1, 2 and 3 identify the endo and exothermic effects that accompany the weight losses Δw_1 , Δw_2 and Δw_3 , respectively.

3.3. Morphology evolution with growth time

The results respecting Hap particles obtained after different precipitation times, i.e. 15, 30, 45 and 60 min, are here presented and discussed for the particular (Cit:Ca) ratios of (3:1) and (7:1). The samples under analysis are identified in the table 3.2.

Table 3.2- Identification of the samples precipitated under different (Cit:Ca) ratios and during different times.

Precipitation time (min)	(Cit:Ca) molar ratio	
	3:1	7:1
15	HS 3:1/15	-----
30	HS 3:1/30	-----
45	HS 3:1/45	HS 7:1/45
60	HS 3:1/60	HS 7:1/60

The morphologies of the particles precipitated after the different times are illustrated in figure 3.11. The samples HS 3:1 obtained after 15 min and 30 min (figure 3.11(a), and (b)) show the formation of needle like nanoparticles. When the precipitation time was increased to 45 and 60 min, the TEM images reveal particles (HS 3:1/45 and HS 3:1/60) tending to a rod like morphology (figure 3.11 (c) and (d)). The width and the length of the particles are in the ranges of 5-10 nm and 50-75 nm, respectively. No bundle like Hap nanostructure was observed under this Cit:Ca ratio of (3:1). Furthermore it is worthy emphasizing that nucleation and growth processes already took place after 15 min.

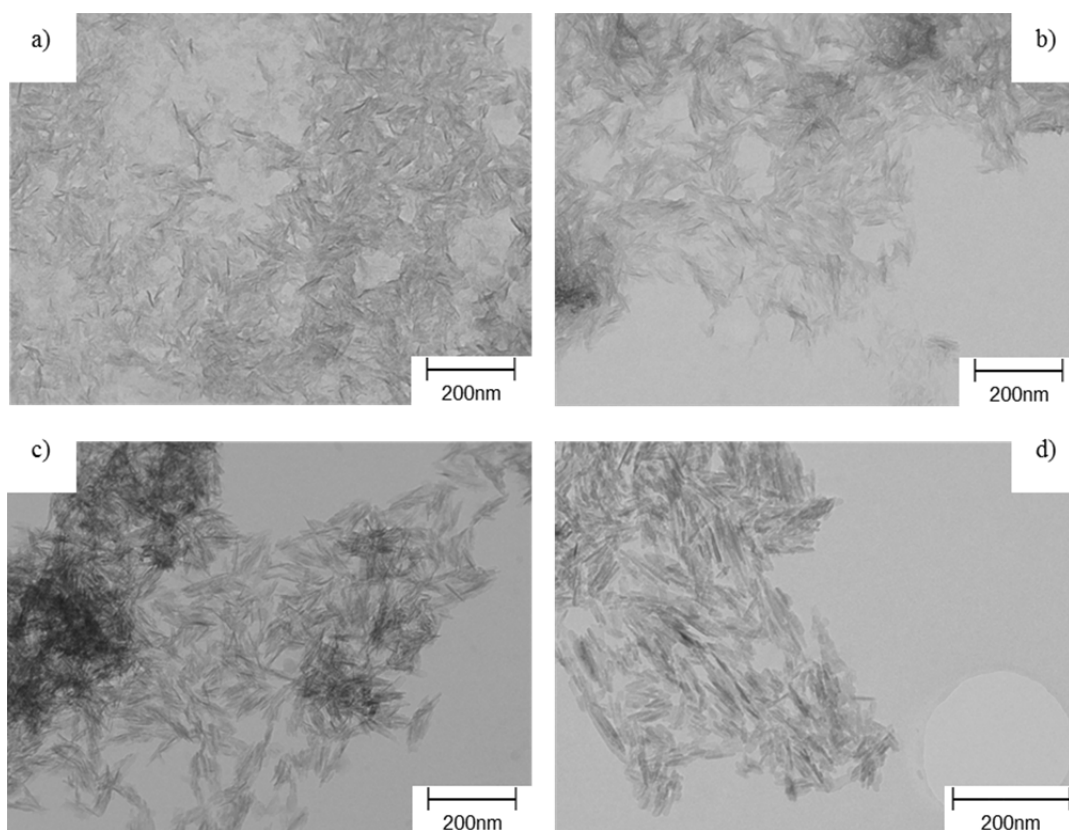


Figure 3.11- TEM images of Hap nanoparticles precipitated from solutions containing (Cit:Ca)= (3:1) after different times: (a) 5 min, (b) 30 min, (c) 45 min and (d) 60 min.

The specific surface areas of the particles obtained for HS 3:1 after 15, 45 and 60 minutes of precipitation are 11, 80 and 96 m²/g, respectively. As observed the specific surface area increases with the synthesis time, and this effect could be related with the presence and/or type of pores present in Hap particles. Figure 3.12 shows the N₂ adsorption–desorption isotherms of Hap nanoparticles precipitated from solutions containing (Cit:Ca)= (3:1) after different times: (a) HS 3:1/15, (b) HS 3:1/45 and (c) HS 3:1/60. It is visible that the different samples present different hysteresis loops (HLs). The sample with low time of precipitation (15 minutes) presents a H1 type type according to IUPAC classification, which indicates that pores network effects are not dominating the N₂ sorption behaviour of Hap particles ³⁶. With the increase of the precipitation time a strong HL modification is observed: after 45 minutes a H2 type hysteresis loop is observed whilst after 60 minutes a H3 type is obtained. The main difference between these

two hysteresis loops is related with the pore shape: ink-bottle shaped pores are present when H2 is observed and slit-shaped pores when the hysteresis loop is of H3 type ³⁶. These HL differences may be a consequence of the adsorbed species on the Hap surface and/or reflect the synthesis conditions (time/ temperature) since the temperature of the precipitating keeps increasing during approximately 45 min which is the time required to reach the final set-point temperature (180°C).

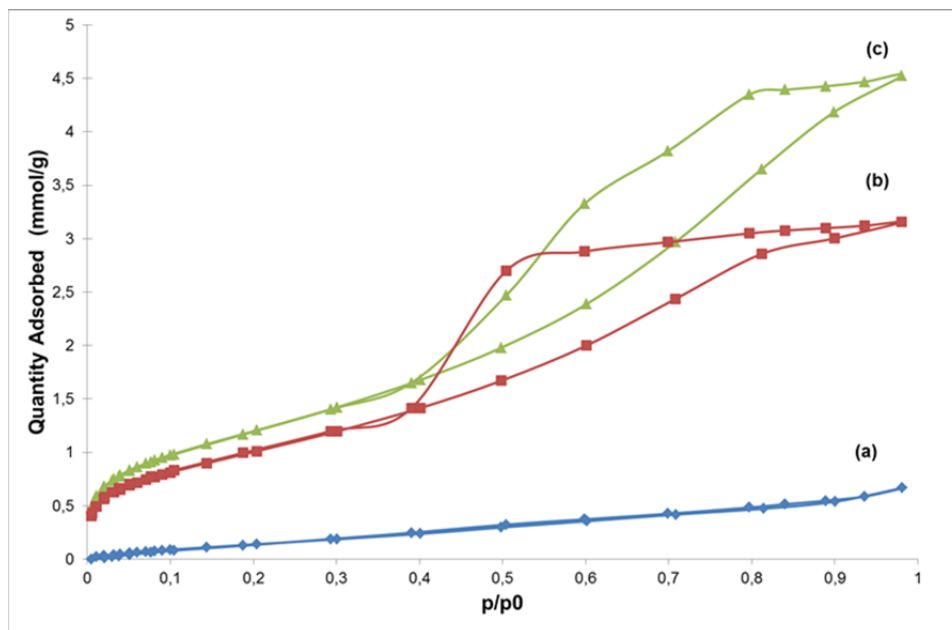


Figure 3.12- N_2 adsorption–desorption isotherms of Hap nanoparticles precipitated from solutions containing (Cit:Ca)= (3:1) after different times: (a) 15 min, (b) 45 min and (c) 60 min. It is visible that the different samples present different hysteresis loops (HLs).

The XRD patterns of the samples HS 3:1 obtained after different precipitation times are shown in figure 3.13. The sample precipitated after 15 min shows broad peaks characteristics of a poorly crystalline hydroxyapatite. However several other peaks well defined are also visible. It is believed that those peaks can be assigned to precursor compounds of hydroxyapatite. The XRD spectra of HS 3:1 after 45 and 60 min show that all the peaks matched well to those of Hap phase (JCPDS 9-432), and no other secondary phase peaks could be detected. These results indicate that the precursor compounds detected after 15 min gave place to Hap. Moreover it is possible to observe that Hap peaks become sharper with the increase of synthesis time (fig 3. 13).

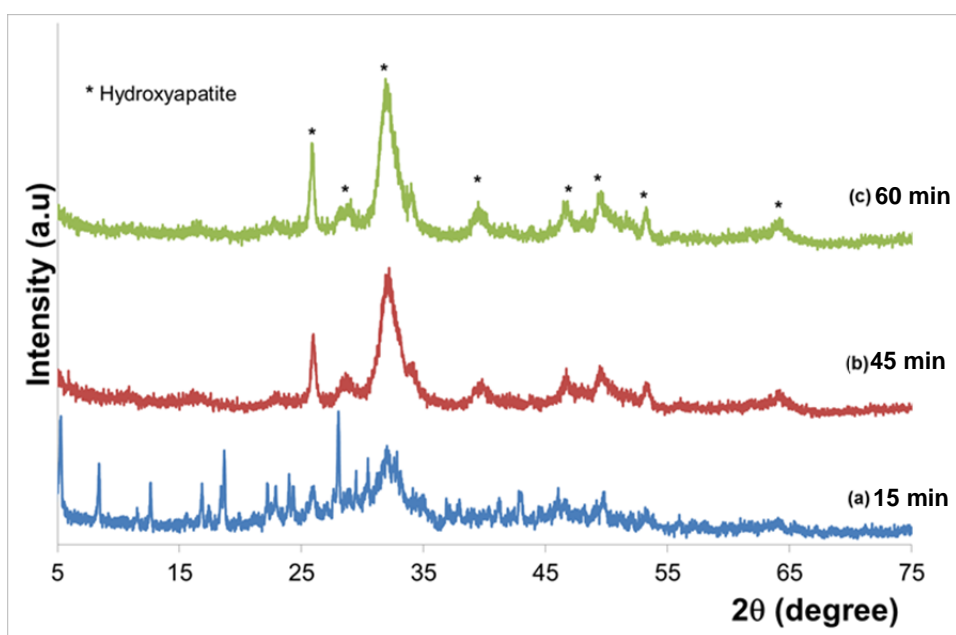


Figure 3.13- X-ray spectra of Hap nanoparticles precipitated from solutions containing (Cit:Ca)= (3:1) after different times: (a) 15 min, (b) 45 min and (c) 60 min. The sample (a) shows broad peaks characteristics of a poor crystalline hydroxyapatite.

FTIR spectra of the samples precipitated with different times are presented in figure 3.14 (a) and (b). The main vibrational bands assigned to the hydroxyapatite PO_4^{3-} groups (figure 3.14 (a)) are observed in all spectra, although the bands intensity and definition are less evident for HS 3:1/15. The intensity of these bands increases with the time of precipitation due to the increasing degree of crystallinity of the precipitated particles. Moreover in the range of $1200\text{--}1700\text{ cm}^{-1}$ bands assigned to citrate carboxylate (COO^-) groups are present in all studied samples as is the case of 1270 , 1305 , 1384 , 1402 , 1436 , 1458 , 1540 , 1567 and 1610 cm^{-1} bands. The band at 1270 cm^{-1} can be assigned to coupled stretches and bends of carboxylate groups³⁷ or skeletal vibrations of citrate species³⁴. The band observed at 1305 cm^{-1} can be attributed to citrate OH group able to rotate freely around its C-OH axis³⁸ and the band at 1436 cm^{-1} is given as $-\text{CH}_2-$ bending mode³⁷. Two bands are also visible at 1540 cm^{-1} and 1610 cm^{-1} which can be associated with antisymmetrical stretching vibration of carboxylate groups (COO^-)^{31,39}. The band at 1540 cm^{-1} could also represent a type A substitution where the CO_3^{2-} anions are partially occupying OH^- position^{5,40}. The bands detected at 1458 , 1402 and 1567 cm^{-1} , were already identified as symmetric or antisymmetric

stretching vibrations of carboxylate groups. Initially (after 15 min) a pseudobridging configuration (1610 and 1402 cm^{-1}) of carboxylate groups is observed; with the increase of the precipitation time a broad band is observed at 1590 cm^{-1} which may result from an overlap of two bands, i.e. a band at 1610 cm^{-1} and the band at 1567 cm^{-1} . This suggests that there are changes in the coordination geometry of the carboxylic ions to Hap surface. The comparison of the spectra of Cit:Ca synthesized after different times thus indicates that the intensity of the characteristic bands of citrate (detected at 1270 , 1305 , 1436 cm^{-1}) decreases with the increase of the synthesis time. These results suggest that original citrate groups may exist as adsorbed species at the surface of the precipitated particles if short synthesis times are meant. Moreover the carboxylate groups seem weakly bonded to the surface of the particles since they are able to undergo coordination rearrangements. Apparently the stability of the citrate species adsorbed on Hap surface is largely dictated by the precipitation time and has influence in the final morphology of the Hap particles.

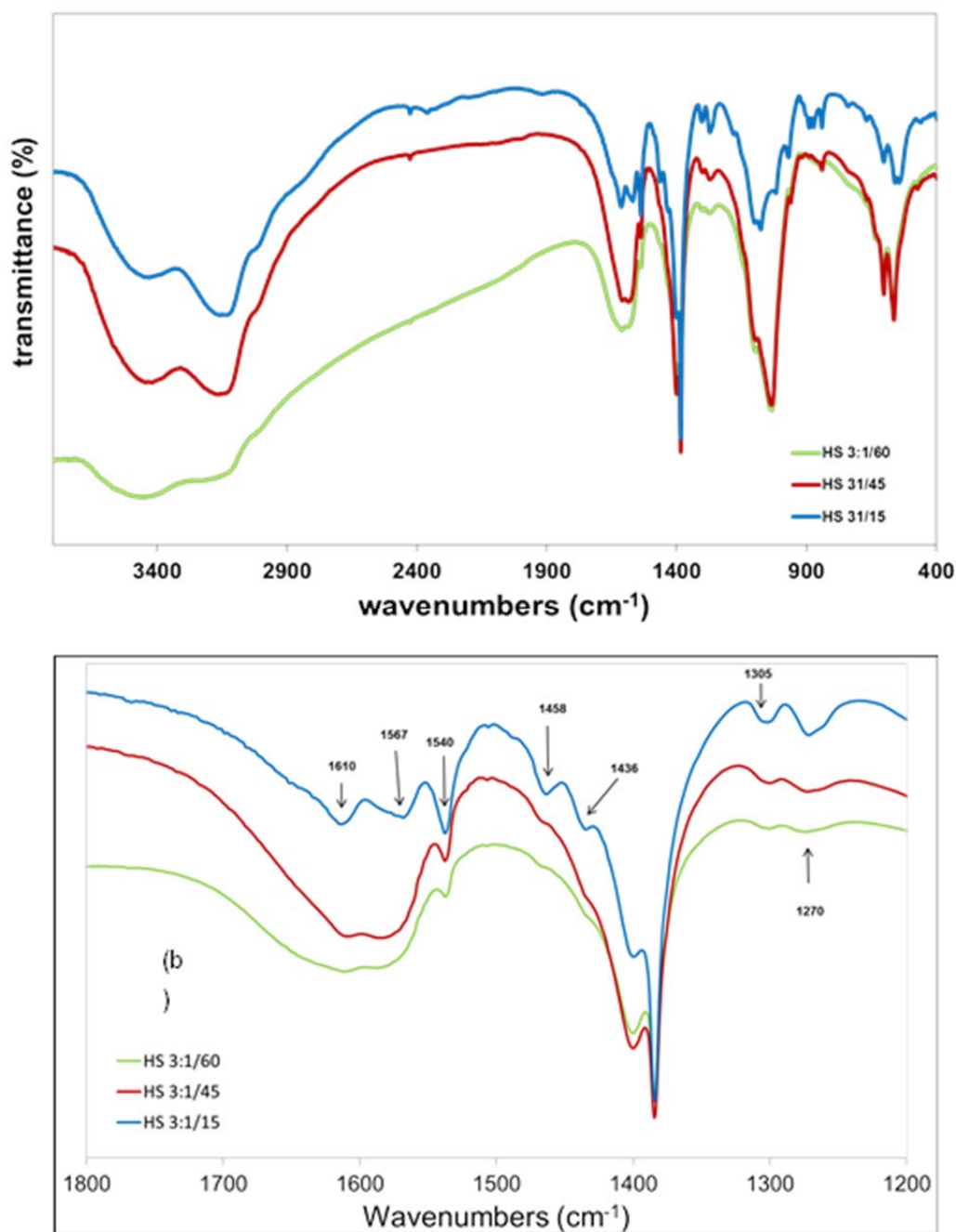


Figure 3.14- (a) FTIR spectra of Hap nanoparticles precipitated from solutions containing (Cit:Ca)= (3:1) after different times: 15 min, 45 min and 60 min ;(b) FTIR details of the 1200-1800 cm^{-1} spectral region.

Figure 3.15 compares the thermal behaviour of the obtained Hap particles after different precipitation times (samples HS 3:1/15; 3:1/45 and 3:1/60). The first weight loss occurs at temperatures up to $\sim 100^{\circ}\text{C}$ and is followed by an

endothermic effect. This weight loss can be assigned to the release of weakly adsorbed water on the precipitated particles. The second weight loss is detected between 180 and 280°C, being also followed by endothermic effects including a peak at 150°C and a shoulder at 230°C. A very steep weight loss is then identified being accompanied by an endothermic peak centred at 300°C. When temperature increases beyond 300°C a lower slope is recovered until 500°C. The 300°C-500°C region is covered by an exothermic band. As compared to this curve, the thermograms of HS 3:1/45 and 3:1/60 samples have only one endothermic feature adjacent to 200°C and an almost constant weight loss rate extending from 180°C until 500°C. These different thermal behaviours are in line with XRD results that showed the existence of precursor compounds in HS 3:1/15 whose decomposition is expected to produce additional endothermic features. It is also observed that the total weight losses are significantly higher in HS 3:1/15 (42%) as compared to its counterparts HS 3:1/45 and 3:1/60 (25 and 22%, respectively). These differences are assigned to the precursor compounds contributions. According to FTIR results some of these precursors may be citrate based compounds which could not be successfully identified yet.

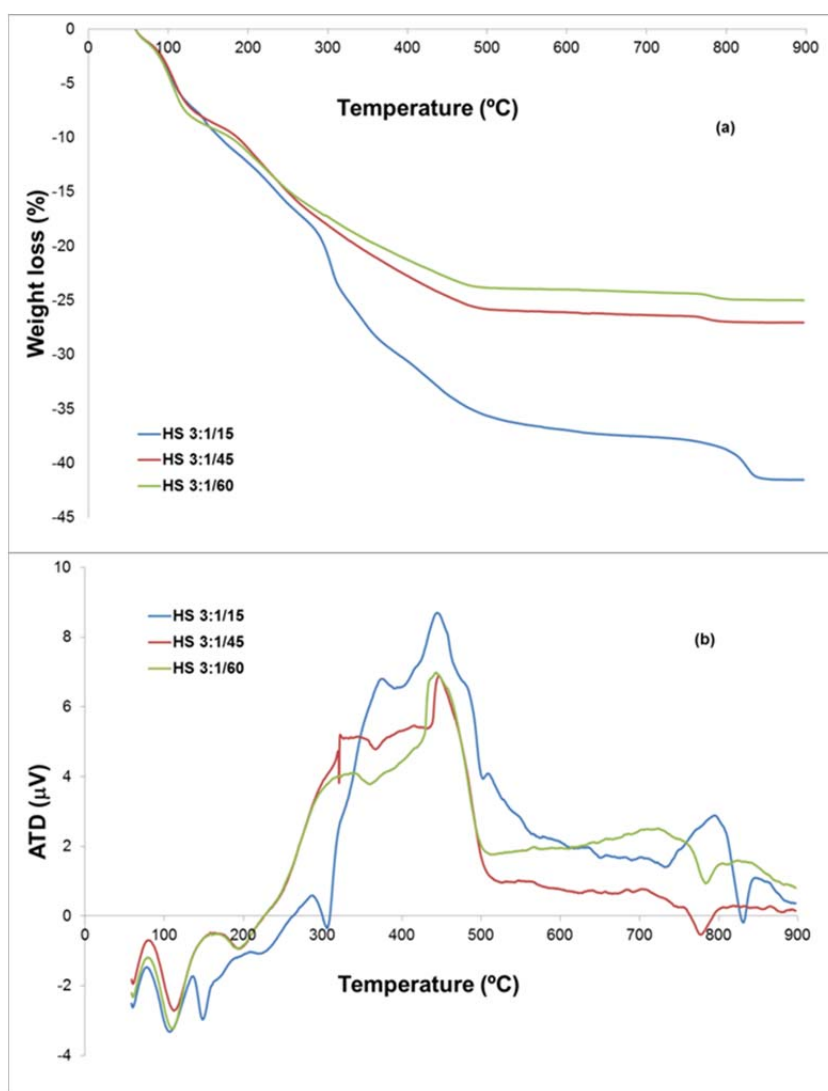


Figure 3.15- (a) Thermogravimetric plots and (b) Differential thermal analyses plots of Hap nanoparticles precipitated from solutions containing (Cit:Ca)= (3:1) after different times: 15 min, 45 min and 60 min.

The Hap particles precipitated from solutions containing (Cit:Ca) = 7:1 after 45 and 60 min were characterized as poorly crystallized hydroxyapatite as found for HS 3:1. The analysis of the XRD spectra (figure 3.16) shows a slight increase in crystallinity with the increase in time of precipitation.

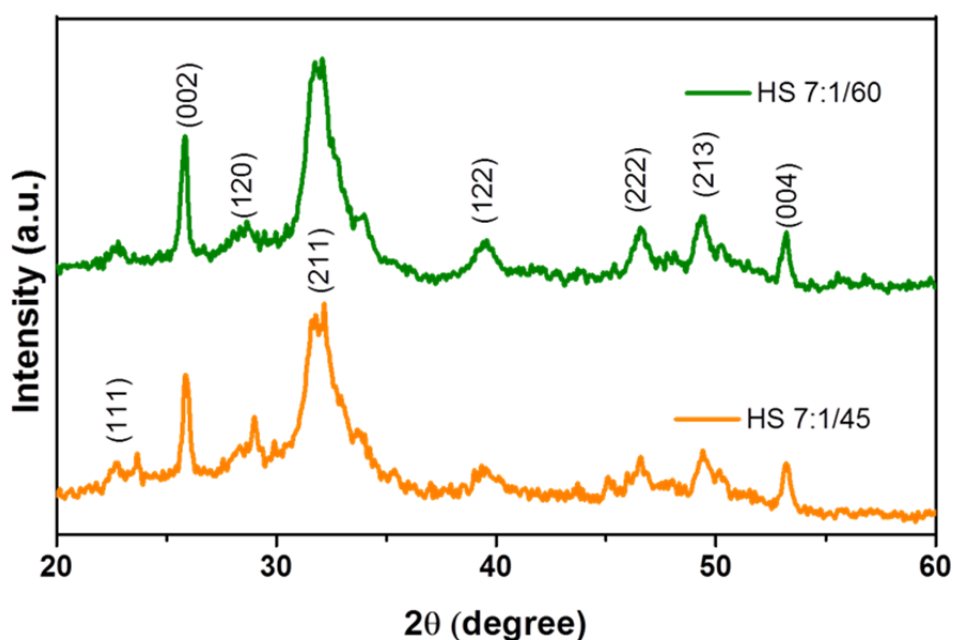


Figure 3.16- XRD patterns of Hap nanoparticles precipitated from solutions containing (Cit:Ca)= (7:1) after different times: 45 min (HS 7:1/45) and 60 min (HS 7:1/60).

The morphologies of the Hap particles precipitated from solutions containing (Cit:Ca)= (7:1) after different times (HS 7:1/45 and HS 7:1/60) are illustrated in figure 3.17. As observed, further increase of (Cit:Ca) ratio from (3:1) to (7:1) resulted in the formation of particles with a cotton like aspect as shown in the SEM and TEM images provided in Figure 3.17((a) and (b)). The average size of these Hap particles is around 600 nm and 800 nm respectively. However it should be pointed out that precipitation could not be observed before a period of time of 45 min. Moreover, comparing the morphological results obtained for two studied Cit:Ca ratios (3:1 and 7:1) it is observed that the nucleation and initial growth of Hap particles are different in these two conditions. The increase in the amount of citrate ion in the starting calcium solution delayed considerably the nucleation of Hap. Thus the calcium citrate complexes formed under the larger amounts of citrate remained stable for longer periods as compared to (Cit:Ca) = (3:1) conditions. This indicates the chemistry of citrate calcium complexes to be particularly sensitive to the ratio of Cit:Ca which in turn determines the stability of the resulting complexes.

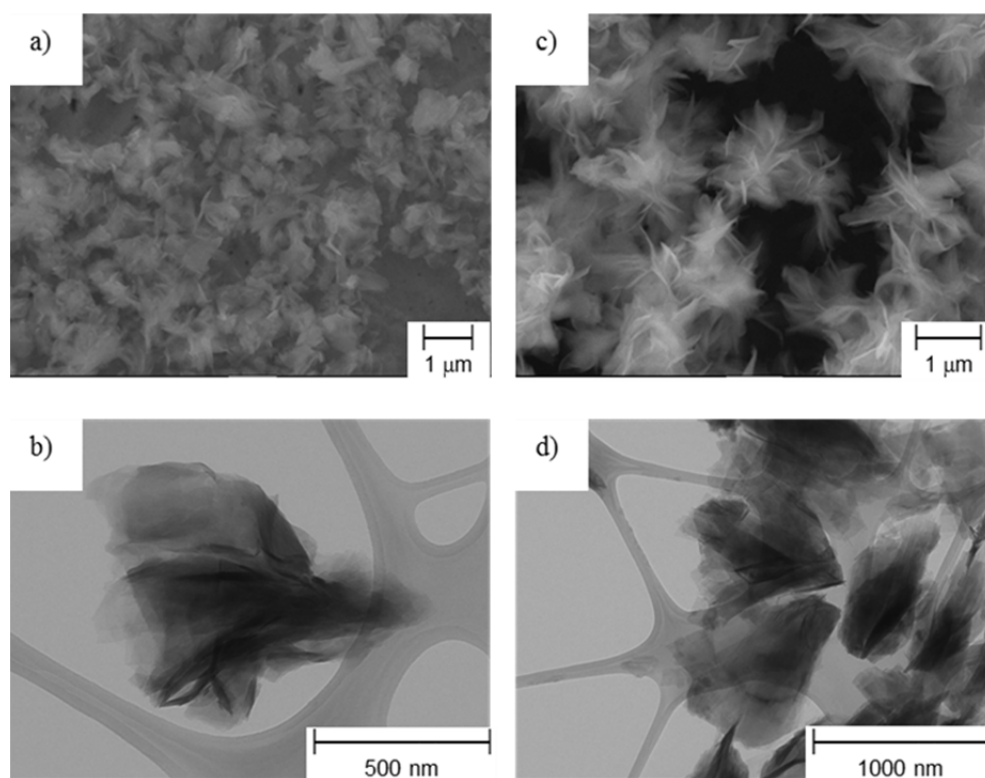


Figure 3.17- SEM and TEM images of Hap particles precipitated from solutions with a (Cit:Ca) ratio of (7:1) and after different times: (a, b) 45 min and (c, d) 60 min.

FTIR spectra of the samples precipitated with different times are present in figure 3.18 (a) and (b). As in HS 3:1 the main vibrational bands assigned to the hydroxyapatite PO_4^{3-} groups (figure 3.18 (a)) are observed in all spectra which confirms the formation of hydroxyapatite. The spectrum of HS 7:1/45 is different in the range of $1200\text{--}1700\text{ cm}^{-1}$ as compared to that of HS 7:1/60 and HS 7:1. It is clearly shown that the sample HS 7:1/45 present a larger number of vibration bands than the others samples. As observed, this FTIR spectrum is similar to that of HS 3:1/15 with well-defined absorption bands assigned to citric acid. Moreover comparing HS 7:1/45 to HS 7:1/60 it is seen that the bands detected at 1270 , 1305 , 1436 cm^{-1} are no longer present in HS 7:1/60. A similar trend with precipitation time was found in HS 3:1 results suggesting that adsorption of citrate species on Hap particles is dependent on the synthesis time, i.e., on the solution temperature. Despite this trend similarity, citrate bands could not be identified in

the samples obtained with HS 7:1 after 60 minutes whereas they are still present in samples with HS 3:1/60, although with a reduced intensity.

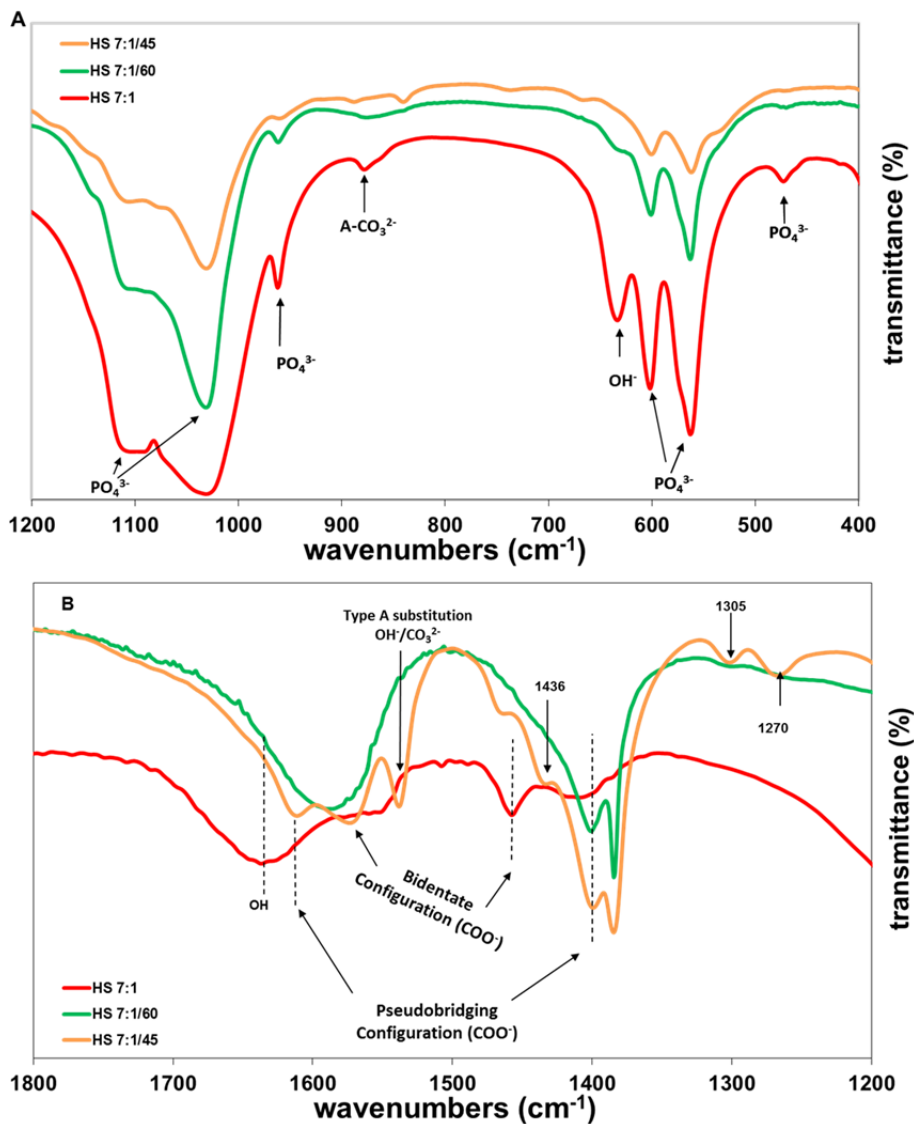


Figure 3.18- FTIR spectra of Hap particles obtained from solutions with a (Cit:Ca) ratio of (7:1), at 180°C and after different synthesis times (—) 45 min, (—) 60 min and (—) 24 hours. Figure 3.18 (A) covers the wavenumbers range of 400 to 1200 cm^{-1} and figure 3.18 (B) covers the range from 1200 to 1800 cm^{-1} .

As previously discussed a further increase of the synthesis time to 24 hours FTIR results indicate that citrate bands are no more present in FTIR spectra.

The TG curves of the HS 3:1 and HS 7:1 after 60 minutes of synthesis are compared in figure 3.19. As seen the total weight losses of HS 3:1/60 and HS 7:1/60 samples are ~25% and ~70% respectively. In this last case of huge weight loss, it can be precised that around 30% of the sample total weight is lost in 300°C-500°C temperature interval which is the region of organics burning out against 7.5% for HS 3:1/60. Attempting to correlate these findings with FTIR results it is found that, although carboxylate bands are better differentiated in HS 3:1/60 samples as compared to HS 7:1/60, the amount of citrate derived organics existing in HS 7:1/60 particles largely surpasses the equivalent organic content of HS 3:1/60. It may be thus concluded that, after a short precipitation time (such as 45 min) the amount of carboxylate species adsorbed on Hap surface roughly correlates with the amount of citrate initially introduced in the system. However as the synthesis time increases, carboxylate related species probably undergo thermal decomposition being part of the reaction products desorbed and released back to the solution thus depleting the organic content of particle surface. The reason why after 24 H organics depletion is fairly stronger in HS 7:1 as compared to 3:1 may rely on the different possibilities for citrate decomposition reaction path as reviewed by Cody, G.D et al.⁹. Accordingly, if gaseous reaction products are formed (like acetone) a larger pressure increase will take place in the case of HS 7:1 which may dramattically condition the reaction prosecution. This may explain why different products would be originated and consequently affect the type and final amount of adsorbed organics: citrate derived species specifically produced in HS 7:1 system would easily desorb from Hap surface and restore appropriate conditions for lateral particle attachment. Particle nucleation and growth mechanisms are thus strongly dependent on the amount of citrate ion introduced in the starting solution.

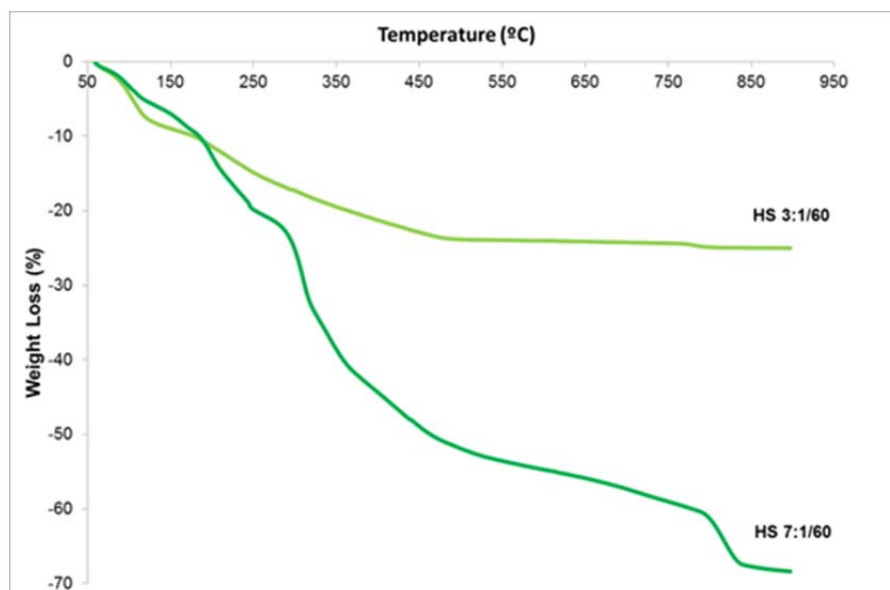


Figure 3.19- (a) Thermogravimetric analysis (TGA) plots of Hap nanoparticles precipitated from solutions containing (Cit:Ca) ratios of (3:1) and (7.1), after 60 min.

The main conclusions to be withdrawn from the present chapter are:

Hap particles were precipitated from calcium/citrate/phosphate solution at 180°C by a hydrothermal method. The morphology of the precipitated particles has evidenced a great dependence on the experimental conditions, principally on the citrate/calcium molar ratio. Nanometric or micrometric Hap particles with different morphologies could be obtained by varying the solution Cit:Ca ratio. This morphology dependence on citrate initial amount can be explained as a result of the amount and configuration of carboxylate groups adsorbed on particles surface. For the experimental conditions selected in this study, the amount of adsorbed citrate derived species on Hap surface after 24 hours of synthesis decreases as the Cit:Ca ratio increases, which conditions particle growth and agglomeration leading to the formation of microparticles. The present studies also demonstrate that during the early growth stages (<60 min) the particles carry a large organics content which becomes strongly reduced after a time of 24 h. It is thus concluded that initial citrate species undergo thermal decomposition as the synthesis time increases being followed by rearrangement and/or desorption processes with a strong impact on particle morphology which may vary from a nanometric to a micrometric size which is particularly evident for the higher Cit:Ca molar ratio.

3.4. References

- 1 Epple, M. and K. Ganesan, R. Heumann, J. Klesing, A. Kovtun, S. Neumannb and V. Sokolova. "Application of calcium phosphate nanoparticles in biomedicine". *J. Mater. Chem.* **20**, 18-23, (2010).
- 2 Tomada, Keishiro and Hidehiko Ariizumi, Takatomo Nakaji, Kimiko Makino. "Hydroxyapatite particles as drug carriers for proteins". *Colloids and Surfaces B: Biointerfaces* **76**, 226-235, (2010).
- 3 Ferrari, M. "Nanogeometry: beyond drug delivery". *Nature Nanotechnology* **3**, 131-132, (2008).
- 4 Jiang, Wen; Kim Betty, Y. S.; Rutka, James T. and Chan Warren, C. W. "Nanoparticle-mediated cellular response is size-dependent". *Nat Nano* **3**, 145-150, (2008).
- 5 Koutsopoulos, S. "Synthesis and characterization of hydroxyapatite crystals: A review study on the analytical methods". *Journal of Biomedical Materials Research* **62**, 600-612, (2002).
- 6 Bose, Susmita and Saha, Susanta Kumar. "Synthesis and Characterization of Hydroxyapatite Nanopowders by Emulsion Technique". *Chemistry of Materials* **15**, 4464-4469, (2003).
- 7 M.A.Martins; C.Santos; M.M.Almeida and M.E.V.Costa. "Hydroxyapatite micro- and nanoparticles: nucleation and growth mechanisms in the presence of citrate species". *Journal of Colloid and Interface Science* **318**, 210-216, (2008).
- 8 Soccol, Carlos R.; Vandenberghe, Luciana P. S.; Rodrigues, Cristine and Pandey, Ashok. "New Perspectives for Citric Acid Production and Application". *Food Technol. Biotechnol.* **44**, 141-149, (2006).
- 9 Cody, G. D.; Boctor, N. Z.; Hazen, R. M.; Brandes, J. A.; Morowitz, Harold J. and Yoder, H. S. "Geochemical roots of autotrophic carbon fixation: Hydrothermal experiments in the system citric acid, H_2O -(FeS)-(NiS)". *Geochimica et Cosmochimica Acta* **65**, 3557-3576, (2001).
- 10 Hu, Y. Y.; X.P.Liu; X.Ma, A. Rawal; T.Prozorov; M.Akinc; S.K.Mallapragada and Rohr, K. Schmidt. "Biomimetic Self-Assembling CopolymerHydroxyapatite Nanocomposites with the Nanocrystal Size Controlled by Citrate". *Chem.Mater.* **23**, 2481-2490, (2011).
- 11 Yu-Ju, Wu; Yao-Hung, Tseng and Jerry, C. C. Chan. "Morphology control of Fluorapatite crystalline by citrate ions". *Crystal Growth & Design* **10**, 4240-4242, (2010).
- 12 Wan, Chaoying and Chen, Biqiong. "Synthesis and characterization of biomimetic hydroxyapatite/sepiolite nanocomposites". *Nanoscale* **3**, 693-700, (2011).
- 13 Yamagishi, Kazue; Onuma, Kazuo; Suzuki, Takashi; Okada, Fumio; Tagami, Junji; Otsuki, Masayuki and Senawangse, Pisol. "Materials chemistry: A synthetic enamel for rapid tooth repair". *Nature* **433**, 819-819, (2005).

- 14 Arcís, Raul W.; López-Macipe, Anabel; Toledano, Manuel; Osorio, Estrella; Rodríguez-Clemente, Rafael; Murtra, Jaime; Fanovich, Maria A. and Pascual, Concepción Domingo. "Mechanical properties of visible light-cured resins reinforced with hydroxyapatite for dental restoration". *Dental Materials* **18**, 49-57, (2002).
- 15 Zhengrong, R. Tian; James, A. Voigt; Jun, Liu; Bonnie, Mckenzie; Matthew, J. Mcdermott; Mark, A. Rodriguez; Hiromi, Konishi and Huifang, Xu. "Complex and oriented ZnO nanostructures". *Nature Materials* **2**, 821-826, (2003).
- 16 Seungho, Cho; Ji-Wook, Jang; Seung-Ho, Jung; Bo Ram, Lee; Eugene, Oh and Kun-Hong, Lee. "Percursor effects of citric acid and citrates on ZnO crystal formation". *Langmuir* **25**, 3825-3831, (2009).
- 17 Yang, Mei; You, Hongpeng; Zheng, Yuhua; Liu, Kai; Jia, Guang; Song, Yanhua; Huang, Yeju; Zhang, Lihui and Zhang, Hongjie. "Hydrothermal Synthesis and Luminescent Properties of Novel Ordered Sphere CePO_4 Hierarchical Architectures". *Inorg. Chem.* **48**, 11559-11565, (2009).
- 18 S.J.Gregg and K.S.W.Sing. in *Adsorption, Surface Area and Porosity* (Academic Press, 1982).
- 19 Zhao, Dongyuan; Feng, Jianglin; Huo, Qisheng; Melosh, Nicholas; Fredrickson, Glenn H.; Chmelka, Bradley F. and Stucky, Galen D. "Triblock Copolymer Syntheses of Mesoporous Silica with Periodic 50 to 300 Angstrom Pores". *Science* **279**, 548-552, (1998).
- 20 Jing Di, Chen; Ying Jun, Wang; Kun, Wei; Shu Hua, Zhang and Xue Tao, Shi. "Self-organization of hydroxyapatite nanorods through oriented attachment". *Biomaterials* **28**, 2275-2280, (2007).
- 21 Y.-Y. Hu; X. P. Liu; X. Ma; A. Rawal; T. Prozorov; M. Akinc; Mallapragada, S. K. and Schmidt-Rohr, K. "Biomimetic Self-Assembling Copolymer Hydroxyapatite Nanocomposites with the Nanocrystal Size Controlled by Citrate". *Chem. Mater.* **23**, 2481-2490, (2011).
- 22 Wenge, Jiang; Haihua, Pan; Yurong, Cai; Hinhui, Tao; Peng, Liu; Xurong, Xu and Ruikang, Tang. "Atomic force microscopy reveals hydroxyapatite-citrate interfacial structure at the atomic level". *Langmuir* **24**, 12446-12451, (2008).
- 23 Wei-Jen, Shih; Yung-Feng, Chen; Moo-Chin, Wang and Min-Hsiung, Hon. "Crystal growth and morphology of the nano-sized hydroxyapatite powders synthesized from $\text{CaHPO}_4 \cdot 2\text{H}_2\text{O}$ and CaCO_3 by hydrolysis method". *Journal of Crystal Growth* **270**, 211-218, (2004).
- 24 M.S.Bootharaju and T.Pradeep. "Uptake of Toxic Metal Ions from Water by Naked and Monolayer Protected Silver Nanoparticles: An X-ray Photoelectron Spectroscopic Investigation". *J.Phys.Chem.C* **114**, 8328-8336, (2010).
- 25 Matthew, J. Olszta; Xingguo, Cheng; Sang Soo, Jee; Rajendra, Kumar; Yi-Yeoun, Kim; Michael, J. Kaufman; Elliot, P. Douglas and Laurie, B. Gower. "Bone structure and formation: A new perspective". *Materials Science and Engineering R: Reports* **58**, 77-116, (2007).

- 26 Sujin, Kim; Hyun-Seung, Ryu; Hyunho, Shin; Hyun Suk, Jung and Kug Sun, Hong. "In situ of hydroxyapatite nanocrystal formation from amorphous calcium phosphate in calcium-rich solutions". *Materials Chemistry and Physics* **91**, 500-506, (2005).
- 27 YingJun, Wang; Shuhua, Zhang; Kun, Wei; Naru, Zhao; Jingdi, Chen and Xudong, Wang. "Hydrothermal Synthesis of Hydroxyapatite nanopowders using cationic surfactant as templates". *Materials Letters* **60**, 1484-1487, (2006).
- 28 S.W.K.Kweh; K.A.Khor and P.Cheang. "The production and characterization of hydroxyapatite (HA) powders". *Journal of Materials Processing Technology* **89-90**, 373-377, (1999).
- 29 Masayuki, Nara and Masaru, Tanokura. "Infrared spectroscopic study of the metal-coordination structures of calcium-binding proteins". *Biochemical and Biophysical Research Communication* **369**, 225-239, (2008).
- 30 Mineyuki, Mizuguchi; Masayuki, Nara; Keiichi, Kawaro and Katsutoshi, Nitta. "FT-IR study of the Ca^{2+} -binding to bovine α -lactalbumin". *FEBS Letters* **414**, 153-156, (1997).
- 31 Adriyan, S. Milev; Kannangara, G. S.Kamali and Michael, A. Wilson. "Template-Directed Synthesis of hydroxyapatite from a Lamellar Phosphonate". *Langmuir* **20**, 1888-1894, (2004).
- 32 K.Van, Werde; D.Mondelaers; G.Vanhoyland; D.Nelis; M.K.Van, Bael; J.Mullens and L.C.Van, Poucke. "Thermal decomposition of the ammonium zinc acetate citrate precursor for aqueous chemical solution deposition of ZnO". *Journal of Materials Science* **37**, 81-88, (2002).
- 33 Suk-Woo, Ha; Roland, Reber; Karl-Ludwig, Eckert; Marc, Petitmermet; Jorg, Mayer and Erich, Wintermantel. "Chemical and Morphological Changes of Vacuum-Plasma-Sprayed Hydroxyapatite Coatings during Immersion in Simulated Physiological Solutions". *J.Am.Ceram.Soc* **81**, 81-88, (1998).
- 34 Kurt, Lackovic; Bruce, B. Johnson and Michael J.Angove and, John D. Wells. "Modeling the adsorption of citric acid onto Mulloorina illite and related clay minerals". *Journal of Colloid and Interface Science* **267**, 49-59, (2003).
- 35 Bow, Jong-Shing; Liou, Sz-Chian and Chen, San-Yuan. "Structural characterization of room-temperature synthesized nano-sized β -tricalcium phosphate". *Biomaterials* **25**, 3155-3161, (2004).
- 36 F.Rojas; I.Kornhauser; C.Felipe; J.M.Esparza; S.Cordero; A.Dominguez and and, J. L. Riccardo. "Capillary condensation in heterogeneous mesoporous networks consisting of variable connectivity and pore-size correlation". *Phys.Chem.Chem.Phys* **4**, 2346-2355, (2002).
- 37 Imali, A. Mudunkotuwa and Vicki, H. Grassian. "Citric acid adsorption on TiO_2 Nanoparticles in Aqueous suspensions at acidic and circumneutral pH: surface coverage, surface speciation, and its impact on nanoparticles-nanoparticle interactions". *J.Am.Chem.Soc* **132**, 14986-14994, (2010).

- 38 Simon, Floate; Mirghasem, Hosseini; Mohammad, R. Arshadi; David, Ritson; Karen, L. Young and Richard, J. Nichols. "An in-situ infrared spectroscopic study of the adsorption of citrate on Au(111) electrodes". *Journal of Electroanalytical Chemistry* **542**, 67-74, (2003).
- 39 Farhikhteh, Shayan; Maghsoudipour, Amir; Raissi, Babak and Mozaffari, Babak. "Synthesis of high specific surface area YSZ ($\text{ZrO}_2\text{-8Y}_2\text{O}_3$) nanocrystalline powder by modified polymerized complex method". *Journal of Sol-Gel Science and Technology* **49**, 60-65, (2009).
- 40 Neira, S.; Kolen'ko, Yury V; Lebedev, Oleg I; Tendeloo, Gustaaf Van; Gupta, Himadri S; Guitian, Francisco and Yoshimura, and Masahiro. "An Effective Morphology Control of Hydroxyapatite Crystals via Hydrothermal Synthesis". *Crystal Growth & Design* **9**, 466-474, (2009).

Chapter 4

*Viability and proliferation of MG-63
osteoblastic cells exposed to
hydroxyapatite nanoparticles with
different characteristics*

4.1. Introduction

Although conventional calcium phosphate materials have been well studied and shown to be biocompatible, the utility of smaller Hap particles as biomaterial materials is now receiving strong attention. It has been reported that nanosized Hap particles can be a better candidate in biomedical applications^{1,2} since they have less inflammatory response when compared with microsized particles. The recent research efforts on this field have been particularly focused on the need of controlling Hap particle morphology. Some reports have shown the possibility of synthesizing Hap nanoparticles with well-defined size and shape³⁻⁵. It was also demonstrated in the previous chapter that crystalline Hap particles with a well-defined prismatic shape but maintaining nanometric dimensions may be produced by a hydrothermal method under the presence of an organic additive, i.e. citric acid, provided the ratio of the organic specie to the calcium ion is maintained close to 3:1. However, the particle size and shape impact on the various biomedical application possibilities of Hap nanoparticles are still far from being completely covered. Furthermore questions concerning the mechanisms whereby cells detect and respond to Hap nanometric particles are still unresolved⁶. It is likely that these mechanisms involve modulation of the interfacial forces that guide the organization of cytoskeletal elements and membrane receptors cells. This, in turn, may modify intracellular signaling, binding sites of proteins and integrin signaling^{7,8}. This hypothesis suggests that it may be possible to optimize the functionality of cells on the basis of the size and other features of Hap nanoparticles.

This reasoning provides the main motivation for the present study in which Hap nanoparticles with different morphological attributes tailored under specific synthesis conditions will be then exposed to osteoblastic cells (MG63) aiming to access the effects of particle morphology and concentration on cell response.

Two Hap synthesis methods were selected for producing Hap nanoparticles with different characteristics: the hydrothermal method assisted by citric acid under a specific (Cit:Ca) ratio of 3:1 (one of the conditions discussed in the previous chapter, chapter 3) and a second wet chemical synthesis method

previously reported in the literature ⁵. The particles obtained by the first method and second method will be referred hereafter as HS and WCS, respectively. Reminding that the ultimate application of Hap nanoparticles will demand the produced particles to be sterilized before subsequent *in vivo* application, the sterilized particles corresponding to HS and WCS, i.e. HS_{ster} and WCS_{ster} respectively, will here be addressed as the true targets to be studied. Moreover, the as prepared particles (HS and WCS) will be contrasted to their sterilized counterparts (HS_{ster} and WCS_{ster}, respectively) for accessing the influence of autoclaving sterilization on the chemical and physical properties of the two synthesized Hap nanoparticles.

For the *in vitro* studies, HS_{ster} and WCS_{ster} will be examined for their effects on human osteoblastic cells aiming to elucidate the impact of the particle physicochemical profile and concentration on the *in vitro* cell culture behaviour.

The experimental results will be discussed in the present chapter by the following order: the different physicochemical characteristics of Hap nanoparticles obtained by two synthesis procedures will be firstly analyzed and then the modification of Hap nanoparticles characteristics induced by autoclaving sterilization will be addressed. Finally osteoblastic cells response to the distinct sterilized Hap nanoparticles will be evaluated.

4.2. Comparing the characteristics of hydroxyapatite nanoparticles synthesized by hydrothermal (HS) and Wet Chemical Method (WCS)

Figures 4.1 show the XRD patterns of HS and WCS particles. The peaks of the XRD patterns of all the examined specimens can be attributed to hexagonal hydroxyapatite (space group *P63/m*, $a = b = 9.4320 \text{ \AA}$, $c = 6.8810 \text{ \AA}$) according to the data referenced by JCPDS N° 09-0432. For both WCS and HS particles it is noticed an XRD baseline hump centred on the 2θ region of $20\text{-}35^\circ$ which is usually ascribed to amorphous calcium phosphate (ACP) ⁹. However it is worth mentioning the better defined XRD spectrum of HS nanoparticles with sharper peaks which indicate HS particles to have higher crystallinity than WCS which is

furthermore confirmed by the larger crystallite size estimated for HS as compared to WCS (see table 4.1).

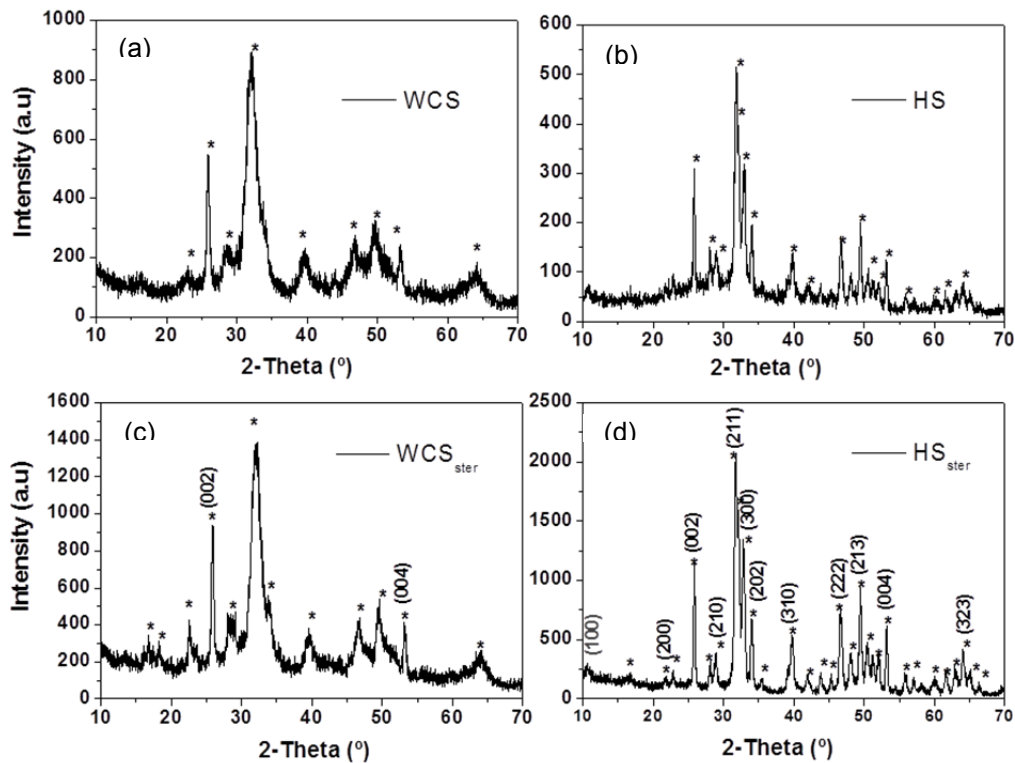


Figure 4.1- X-ray diffraction patterns (XRD) of (a) WCS particles (b) HS particles as prepared; (c) WCS_{ster} after being sterilized and (d) HS_{ster} after being sterilized.

The size and morphologies of the obtained nano-Hap particles were characterized by transmission electron microscope (TEM). Figure 4.2 shows the TEM images of the obtained WCS and HS particles. HS and WCS nanoparticles are both seen to be well dispersed particles as well (Figures 4.2(a) and 4.2(b)). It is observed that WCS present a needle like shape with a width of few nanometres and a length (l) around 100 nm (figure 4.2(a)). The particles obtained by hydrothermal method (HS) as already described in chapter 3, present a prismatic rod-like shape with hexagonal cross section, whose average length (l) and width (w) are $20 \text{ nm} < l < 100 \text{ nm}$ and $w \approx 20 \text{ nm}$, respectively (figure 4.2(b)) and, hence a smaller aspect ratio (l/w).

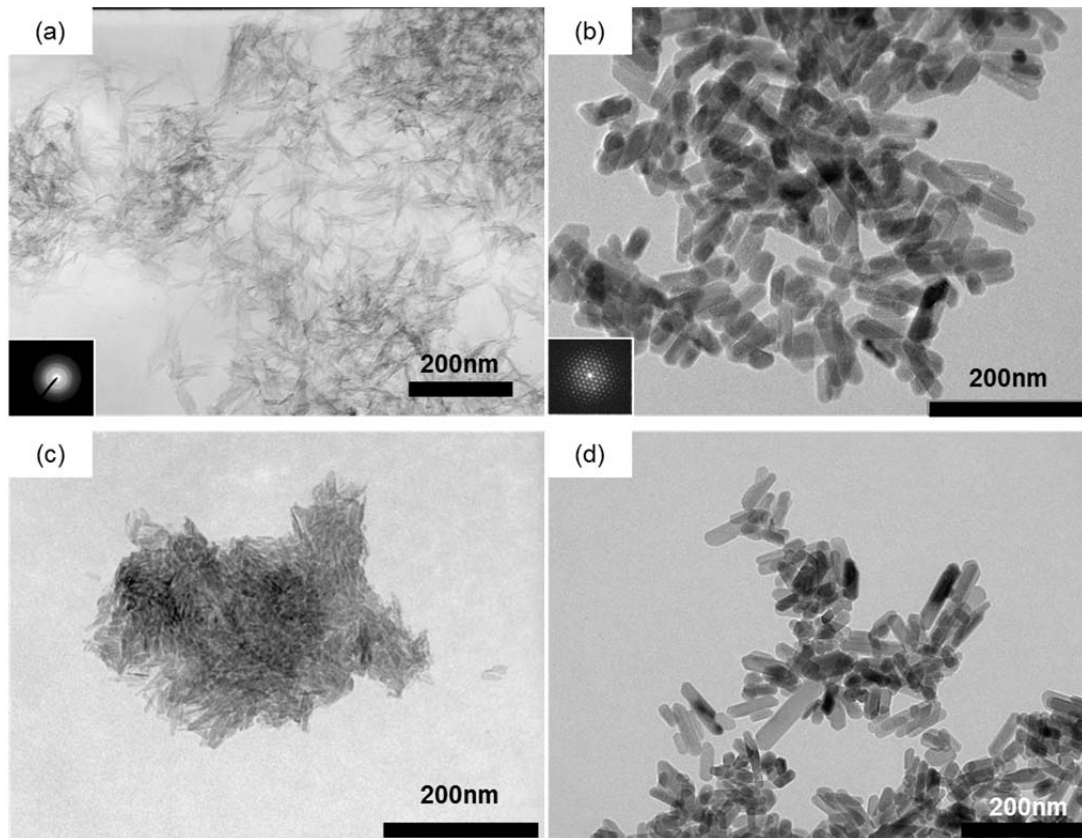


Figure 4.2- TEM images of nano-Hap synthesized by (a) Wet chemical method (WCS) method, (b) Hydrothermal (HS) method, (c) nano-Hap WCS after sterilization in autoclave (WCS_{ster}) and (d) nano-Hap HS after sterilization in autoclave (HS_{ster}).

The morphology and crystallinity dissimilarities between the synthesized WCS and HS nanoparticles reflect the temperature and pressure conditions that distinguish the two synthesis methods used for particle precipitation. Such differences are in line with frequent reports showing that Hap synthesis at high temperature ($T > 100^{\circ}\text{C}$) leads to crystalline and well defined prismatic particles while lower temperature synthesis generally favours thinner particles with less perceptible contours and lower crystallinity¹⁰⁻¹³.

Table 4.1 compares some physical and chemical characteristics of the hydroxyapatite particles obtained by Wet Chemical precipitation (WCS) and by Hydrothermal synthesis (HS). The EDX technique used to measure particle Ca/P ratio revealed the values of 1.62 and 1.70 for HS and WCS particles, respectively. These results evidence a negligible deviation from the stoichiometric value of 1.67¹⁴⁻¹⁶.

The specific surface area (SSA) of the prepared nano-Hap particles was determined by N₂ adsorption using the multipoint Brunauer-Emmett-Teller isotherm (BET) as reported in chapter 2.2. SSA values of 170 m²/g and 55 m²/g were found for WCS and HS, respectively. These results reflect the different particle sizes described above, being the larger SSA exhibited by the thinner WCS particles. In line with the observations from Naruporn Monmaturapoj et al. who sustained that the wet chemical method produces Hap particles with greater specific surface area than the hydrothermal method ¹⁷ the present work points out that under equivalent conditions of pH and Cit:Ca ratio larger nanometric Hap particles are obtained by the Hydrothermal method.

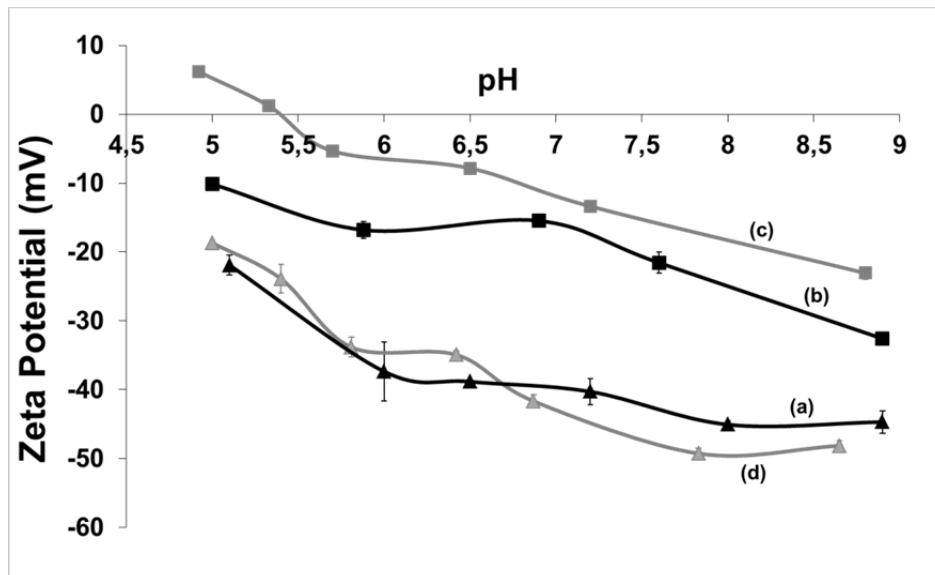
Table 4.1. Properties of hydroxyapatite particles obtained by wet chemical precipitation (WCS and WCS_{ster}) and by hydrothermal synthesis (HS and HS_{ster}): particles as prepared (WCS and HS, respectively) and after being sterilized (WCS_{ster} and HS_{ster}, respectively).

Sample Code	Ca/P ratio	SSA [m ² /g]	Morphology	Crystallite size (nm) [002]
WCS	1,70	171	needle like shape	17
HS	1,62	55	rod like shape	38
WCS _{ster}	1,71	22	rod like shape	21
HS _{ster}	1,69	55	rod like shape	37

Figure 4.3 shows the pH dependence of zeta potential (ξ) for the nanoparticles under analysis. The observed ξ values are constantly negative for both (WCS and HS) nano-Hap particles in the examined pH range as revealed by the curves (a) and (b) respectively. Hap particles of different morphologies obtained by hydrothermal synthesis were reported with different zeta potential at physiological pH namely: nanorod shape -11,4 mV ¹⁸, spherical -5,5mV ¹⁸, whiskers -17,8 mV ¹⁹. In the present study the values of zeta potential for Hap nanoparticles (HS) produced by hydrothermal method is -20 \pm 1 mV, slightly higher than reported, however is within the same range of values. WCS nanoparticles present more negative ξ values as compared to HS nanoparticles in the examined pH range. At physiological pH (~7.4) the zeta potential of WCS

is -40 ± 5 mV, whereas the zeta potential for HS is -20 ± 1 mV. The present results thus indicate that the particle synthesis temperature conditions the particle surface chemical groups which in turn affect considerably the particles zeta potential.

Figure 4.3- pH dependence of zeta potential (ξ) for the (a) WCS nanoparticles (b) HS



nanoparticles; for the (c) HS_{ster} sterilized and (d) WCS_{ster} sterilized. The observed (ξ) values are constantly negative for WCS and HS.

Fig 4.4 ((a) and (b)) compares the FTIR spectra of WCS and HS particles which both reveal the main vibration bands normally attributed to Hap which were already discussed in chapter 3. The features distinguishing WCS from HS particles include: (i) an intense shoulder at 3200 cm^{-1} less evident in HS spectra attributed to ammonium ions ^{5,20}; (ii) a small band at 877 cm^{-1} , only visible in HS spectra, indicating the presence of CO_3^{2-} in a B type substitution ^{21,22} and (iii) the peaks at 3570 cm^{-1} and 632 cm^{-1} , absent in WCS, assigned to the stretching (vs) and vibrational modes (ν_L) of the structural hydroxyl anions, respectively ²³. The $1250\text{--}1700\text{ cm}^{-1}$ spectral region where citrate related bands are expected to be found is detailed in the amplified view shown in figures 4.4 (c) and 4.4 (d). Common features are identified including the sharp peak at 1384 cm^{-1} which has been assigned to the $-\text{CH}_2-$ scissoring mode ²⁴ and the bands attributed to the antisymmetric (1650 and 1567 cm^{-1}) and to the symmetric (1465 and 1402 cm^{-1}) stretching modes of carboxylate groups coordinated to Hap surface Ca^{2+}

cations^{10,25-27} either in a monodentate or in a bidentate manner²⁸⁻³⁰. However some dissimilar bands that distinguish the two particles spectra are remarked: the 1614 and 1434 cm^{-1} bands absent in HS which may be attributed to the asymmetric (ν_a) and symmetric (ν_s) modes of a carboxylate group acting as uncoordinated anion ("ionic" structure)³⁰ and the band at 1540 cm^{-1} in WCS but not evident in HS. This last band may be ascribed to a ν_3 vibration of a CO_3^{2-} group substituting OH^- being found at 1465 cm^{-1} and 880 cm^{-1} the remaining characteristic bands of such substitution in WCS^{31,32}. However other contributions likely related to differently coordinated carboxylate groups are not ruled out for explaining the origin of this 1540 cm^{-1} band as it is questionable that thermally untreated Hap powders (as is the case of WCS particles) might exhibit a so developed CO_3 band. Other meaningful differences include the 1270 cm^{-1} band in WCS spectrum assigned to the skeletal vibrations of citrate species³³ together with a well-defined band at 1305 cm^{-1} attributed to citrate OH group able to rotate freely around its C-OH axis³⁴.

Due to the presence of citric acid in the starting precursor solutions of both types of particles, the presence of adsorbed carboxylate groups was expected on both WCS and HS particle surface. As just discussed, FTIR results revealed carboxylate species coordinated under different manners thus denoting the influence of their different synthesis temperatures. Citric acid degrades at $T > 145^\circ\text{C}$ ^{35,36} leading to reaction products that may include different dehydroxylated or decarboxylated acids and anhydrides depending on the used heating rate and temperature. This legitimates the assumption that original citrate ions might not exist as adsorbed species on HS particle surface but instead smaller carboxylated ions resulting from citrate ion decomposition under the high temperature (180°C) and pressure used for HS thermal synthesis. The absence in HS spectrum of the 1270 and 1305 cm^{-1} bands respectively assigned to citrate skeletal vibrations and free OH group³³ is in line with this reasoning. The presence of unreacted citrate species together with uncoordinated carboxylate ions also detected on WCS surfaces could perHaps account for the more negative zeta potential measured for these particles. As the surface charge of Hap particles may modulate the cellular pathways by modifying intracellular signalling and the binding sites of proteins and integrin

signalling, it is here concluded that particle synthesis details like temperature might condition particle electrical surface charge and hence the mechanisms operating at the particle/biological environment interface.

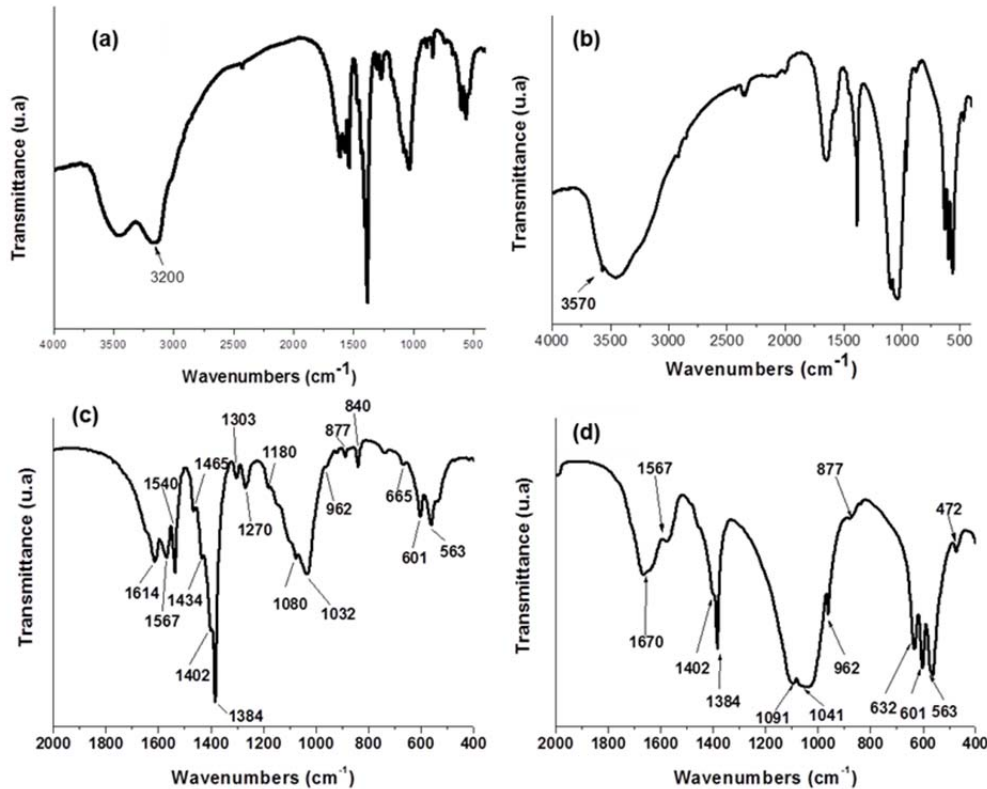


Figure 4.4 - FTIR spectra of (a) WCS particles (b) HS particles as prepared; amplified view of FTIR spectra in the range of 400-2000 cm^{-1} for (c) WCS and (d) HS.

4.3. Sterilization process of HS and WCS nanoparticles

The sterilization method used in the present study was autoclaving. Figures 4.1 (c) and (d) show the XRD patterns of HS and WCS particles, respectively, after being sterilized. It is observed that both sterilized Hap particles exhibit an increased intensity of XRD peaks though WCS_{ster} nanoparticles crystallinity still stays behind that of HS_{ster} nanoparticles. A flattening of the amorphous hump (2-Theta- 20-35°) with sterilization is also noticed in both types of particles. The Table 4.1 compares the crystallite size evolution of WCS and HS particles during sterilization. A slight increase in WCS_{ster} crystallite size is observed which denotes larger coherent crystalline domains⁹. Figure 4.2 ((d) and (e)) shows the TEM images of the particles after sterilization (HS_{ster} and WCS_{ster}). It

is observed that sterilization induces a significant modification of WCS features: besides looking significantly agglomerated (figure 4.2(d)) the particles undergo a thickening process as they become less transparent to the electronic beam after sterilization. Thus WCS morphologic evolution indicates that sterilization conditions promoted both a shape modification and a visible particle agglomeration as WCS_{ster} particles appeared clearly outlined as rod like units but merged into large aggregates. It is difficult to quantify WCS thickening amount since the thickness of the WCS particles prior to sterilization is of very difficult estimation. Regarding HS nanoparticles they do not suffer any significant morphology change as documented by figure 4.2 (e). The evolution of the specific surface area (SSA) of both type of particles is in line with the morphology changes previously referred: HS particles SSA is not appreciably affected by sterilization (Table 4.1) while a large SSA decrease occurs for WCS during sterilization, from 171,0 m²/g to 22,3 m²/g. As referred, the sterilization process exposed WCS particles to a temperature higher than that of synthesis, furthermore assisted by a saturated steam atmosphere. It is here suggested that such conditions allowed the smaller sized amorphous calcium phosphate (ACP) particles to undergo a partial dissolution subsequently followed by a re-precipitation process which contributed to the growth of the existing Hap coherent crystalline regions. Moreover, it is also postulated that these phenomena might have occurred preferably in the neighbourhood of larger particles where enhanced Oswald ripening driving forces would operate³⁷. The large aggregates observed after sterilization are thus envisaged as resulting from re-precipitation processes that allowed adjacent particles to get chemically bonded. These events would explain the large decrease of WCS specific surface area, from 171 to 22 m²/g, and the observed crystallite growth during sterilization as documented in table 4.1. In line with the previous reasoning the hump flattening in WCS_{ster} XRD is thought to reflect the ACP decrease due to the referred dissolution. The present results interpretation are consistent with previous literature reports showing that a combined high temperature and saturated steam regime promotes the local dissolution of the extremely unstable and hydrolysable ACP phase and its recrystallization as Hap phase^{38,39}. Regarding the steam sterilization behaviour of HS particles some crystallite size variations are also remarked but with a smaller extent as compared to those of

WCS (Table 4.1). Since particle size, shape and surface area are maintained practically unchanged during autoclaving it is concluded that dissolution and re-precipitation processes, if any, were negligible. Additionally the crystallite size results (Table 4.1) together with the amorphous calcium phosphate depletion inferred from the flattened HS_{ster} XRD baseline are interpreted as expressing the amorphous calcium phosphate (ACP) reorganization into Hap crystalline phase under the favourable high temperature and H_2O enriched atmosphere conditions underlying the sterilization process^{26,39,40}.

The pH dependence of zeta potential (ξ) of the sterilized nanoparticles is presented in figure 4.3 ((c) and (d)). The observed ξ values are negative in the examined pH range except for HS_{ster} which display positive ξ values for the lowest pH values ($pH < 5.4$). In addition it is shown that WCS_{ster} nanoparticles present more negative ξ values than HS_{ster} nanoparticles. Moreover WCS and WCS_{ster} particles are seen to display close ξ curves in the range $5 < pH < 7$ becoming then WCS_{ster} more negative as pH increases. As for HS nanoparticles it is remarked that their ξ curve is shifted towards more negative potential values as compared to HS_{ster} thereby indicating HS nanoparticle surface charge to become less negative upon sterilization.

The FTIR spectra of WCS_{ster} and HS_{ster} sterilized nanoparticles are depicted in figures 4.5. As mentioned the WCS or WCS_{ster} spectra (fig 4.5 (a) and (c)) are distinct from those of HS or HS_{ster} (fig 4.5 (b) and (d)) particles but no remarkable changes are detected between non-sterilized nanoparticles and their sterilized counterpart. When comparing sterilized and unsterilized particle spectra, no visible differences are detected between WCS and WCS_{ster} and only minor ones are observed between HS and HS_{ster} . These include the shoulder at 1402 cm^{-1} and the broad band centred at 1670 cm^{-1} which appears less intense in HS_{ster} . This may indicate a partial loss of adsorbed citrates carboxylate groups by HS particle.

The different morphology variations suffered by HS and WCS particles during sterilization were accompanied by different trends in surface charge variation: whereas WCS surface charge remained practically unchanged with sterilization in the lower pH range ($5 \leq pH \leq 7$), HS particles tended to a less negative surface

charge. The FTIR results have evidenced that the configurations of some carboxylate groups adsorbed on the surfaces of WCS or WCS_{ster} and HS or HS_{ster} particle are different. As previously referred, the intensity of some carboxylate related bands in HS FTIR spectra tended to decrease upon sterilization being thus concluded that a partial desorption of adsorbed carboxylated species on Ca²⁺ might explain the small increase of HS_{ster} zeta potential. WCS_{ster} appear to be less prone to surface charge modifications by sterilization. Considering that no visible variations were detected in WCS FTIR spectra after sterilization the adsorbed citrate ions seem to behave as a buffer chemical layer whose thermal stability plays a key role on its surface charge maintenance.

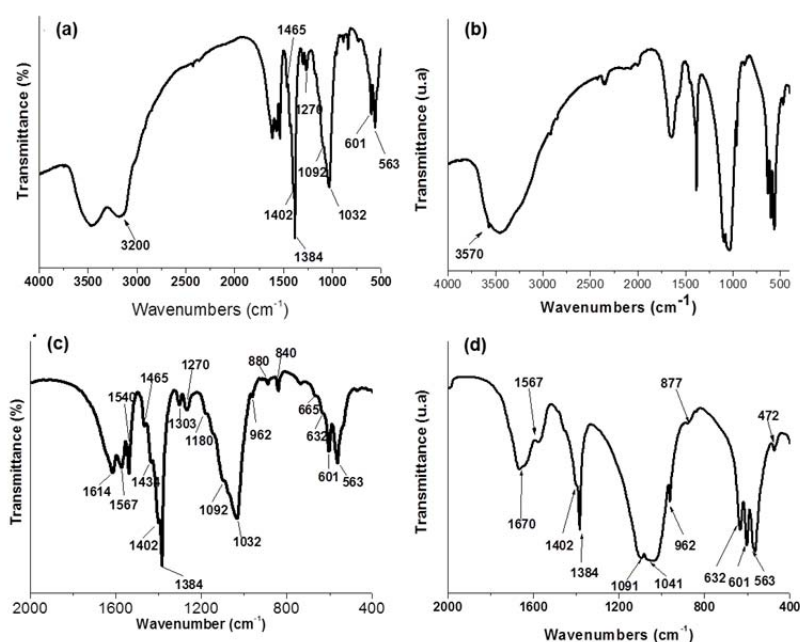


Figure 4.5- FTIR spectra of sterilized (a) WCS_{ster} particles, (b) HS_{ster} particles; amplified FTIR area of (c) WCS_{ster} particles and (d) HS_{ster} particles.

4.4. Interaction of Hap nanoparticles with osteoblastic cells after sterilization

4.4.1. Cell viability/proliferation

As mentioned before the particles to be used in cellular culture should be sterilized. For that reason only the WCS_{ster} and HS_{ster} nanoparticles will be

analysed in this section. Figure 4.6 shows the proliferation of MG-63 osteoblast-like cells in contact with various concentrations of WCS_{ster} and HS_{ster} nanoparticles during 3 and 6 days. Osteoblast-like cells without any contacts with nano-Hap were used as a control. As observed, both types of nano-Hap induced concentration-dependent deleterious effects in the cell viability/proliferation of MG63 osteoblast cells at concentration levels higher than 500 $\mu\text{g/ml}$. At 1000 and 5000 $\mu\text{g/ml}$, a large amount of particles were seen in the well plate, covering completely the cell layer. For these concentrations, WCS_{ster} particles caused an inhibition of cell proliferation slightly higher than HS_{ster} . From these results it is also observed that, as the percentage of the inhibition of cell growth was higher at day 6, than on day 3, the deleterious effects were time-dependent. With this information, cell response was further characterized in the cultures exposed to 50 and 500 $\mu\text{g/ml}$, to evaluate in more detail the effects in the cell behavior.

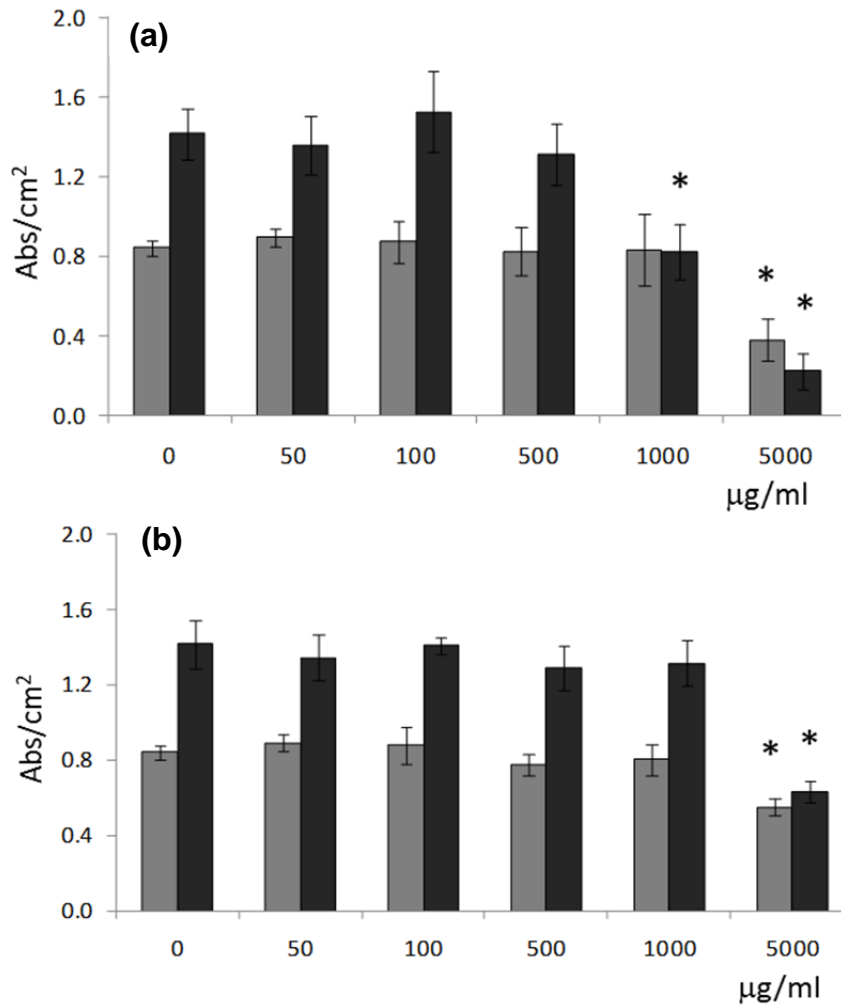


Figure 4.6- Cell viability/proliferation of MG63 cell cultures exposed to (a) WCS_{ster} and (b) HS_{ster} nanoparticles, after 3 and 6 days for a nanoparticles concentration range between (50-5000 µg/ml). *Significantly different from control. Both types of nano-Hap induced concentration-dependent deleterious effects in the cell viability/proliferation of MG63 osteoblast cells at concentration levels higher than 500 µg/ml.

4.4.2. F-actin cytoskeleton organization

The cultures studied were also analysed by confocal laser scanning microscopy (CLSM). Figure 4.7 shows the CLSM images of MG63 cells cultures exposed to a concentration of 500 µg/ml of WCS_{ster} and HS_{ster} nanoparticles during 3 and 6 days. The selection of that concentration is due to the fact that cell viability/proliferation is affected at a nano-Hap level greater than 500 µg/ml. Observation of the cultures, show that the control cells displayed an elongated morphology, cell to cell contact and the formation of a continuous cell layer by

day 6; in addition, the F-actin cytoskeleton of these cells stained mainly within the dense peripheral actin ring. At day 6 the presence of 500 $\mu\text{g/ml}$ nano-Hap appeared to induce some changes on the overall cell morphology, reflected by a lower intensity of the F-actin at the cell limits; besides, it is also noticed the presence of intercellular gaps and retraction of the cell layer from the culture substratum. Such effects are particularly clear in the cultures exposed to the WCS_{ster} particles. The observation of the cells exposed to 50 $\mu\text{g/ml}$ nano-Hap was also done but they displayed a similar appearance and therefore the results were not documented.

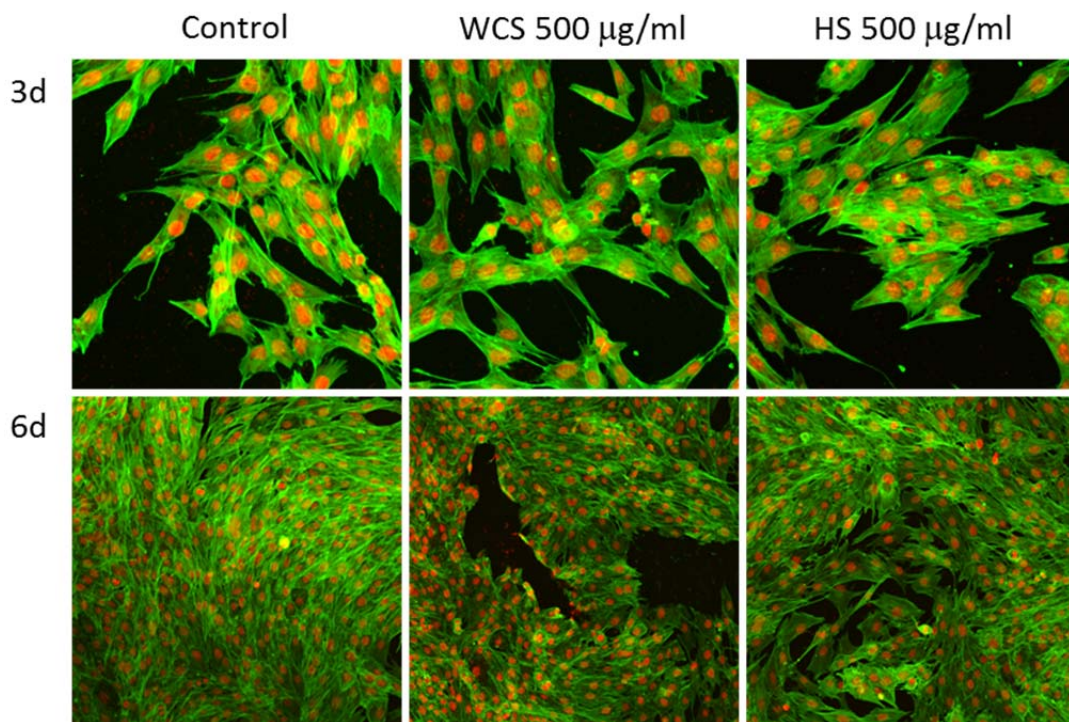


Figure 4.7- CLSM images of MG63 cell cultures exposed to the WCS_{ster} and HS_{ster} nanoparticles, for a nanoparticles concentration of 500 $\mu\text{g/ml}$, during 3 and 6 days. Observation of the cultures, show that the control cells displayed an elongated morphology, cell to cell contact and the formation of a continuous cell layer by day 6; in addition, the F-actin cytoskeleton of these cells stained mainly within the dense peripheral actin ring.

4.4.3. Apoptosis

The apoptosis is the programmed cell death by the fragmentation of DNA, cell shrinkage, followed by cell fragmentation and formation of membrane vesicles called apoptosis bodies^{41,42}. To quantify the cell apoptosis, the MG63 cells cultures were exposed to WCS_{ster} and HS_{ster} (50 µg/ml and 500 µg/ml) during 3 days and analysed by flow cytometry as illustrated by figure 4.8. Cultures exposed to 50 µg/ml nanoHap for 3 days presented a low percentage of apoptotic cells, similar to control. However, interaction with 500 µg/ml particles showed an increase in the number of cells in apoptosis, Figure 4.8.

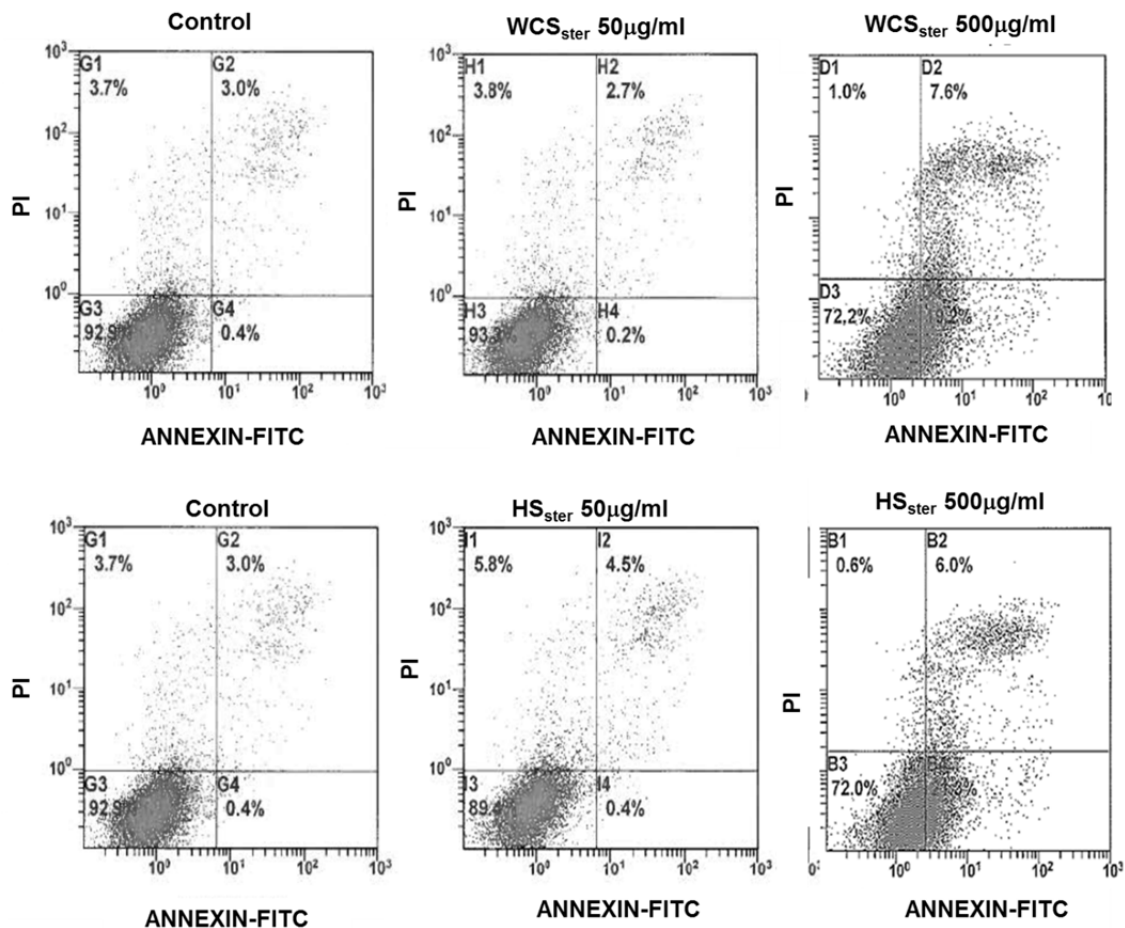


Figure 4.8- Rate of apoptosis of MG63 cell cultures exposed to WCS_{ster} and HS_{ster} nanoparticles during 3 days for the 50 and 500 µg/ml concentrations.

4.4.4. Gene expression of osteoblastic proteins

The RNA was analysed by RT-PCR for the expression of the housekeeping gene glyceraldehyd-3-phosphate dehydrogenase (GAPDH), collagen (Col I), alkaline phosphatase (ALP) and bone morphogenetic protein 2 (BMP-2), respectively using a densitometric analysis (figure 4.9). Under the same experimental conditions as the apoptosis tests, RT-PCR analysis showed WCS_{ster} and HS_{ster} particles, 50 and 500 µg/ml, did not affect the expression of collagen type I but caused significant effects in the expression of ALP and BMP-2, figure 4.9. HS_{ster} particles caused a dose-dependent increase in the expression of ALP and BMP-2. WCS_{ster} particles induced significantly the expression of ALP and BMP-2 at 50 µg/ml, but decreased values were observed in the presence of 500 µg/ml.

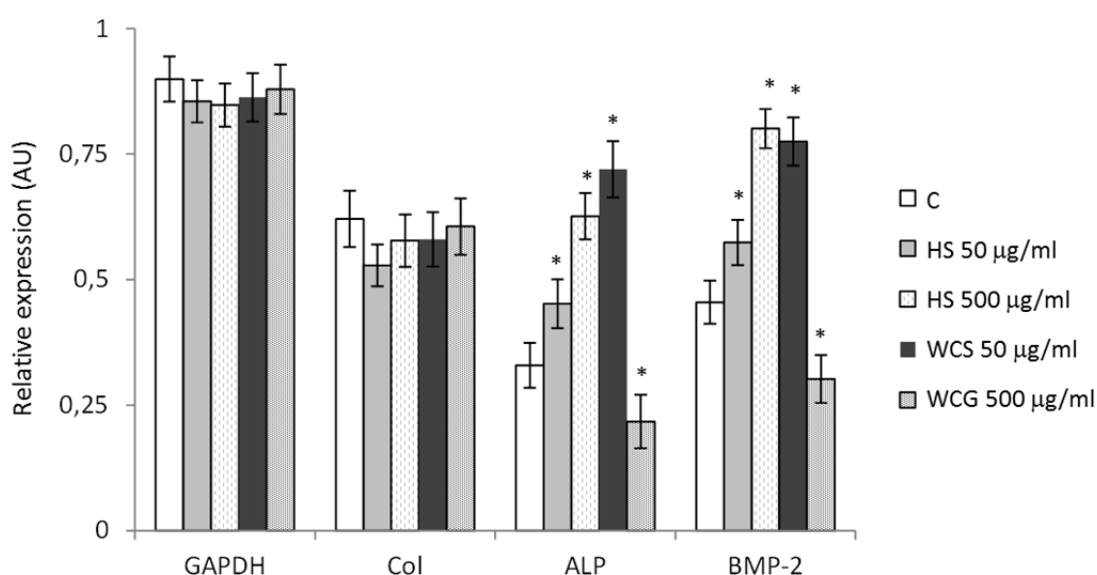


Figure 4.9- Gene expression of Collagen, ALP, BMP-2 of MG63 cell cultures exposed to WCS_{ster} and HS_{ster} nanoparticles, 50 µg/ml and 500 µg/ml, for 3 days. RT-PCR, the PCR products were subjected to a densitometric analysis and normalization to the corresponding GAPDH value. *Significantly different from control.

4.4.5. Nano-Hap cell uptake

MG63 cells cultured with 50 and 500 µg/ml of nanoparticles for 3h, 24h and 3 days were observed by TEM, Figures 4.10, 4.11 and 4.12. It can be seen that in the cell environments, isolated nanoparticles and aggregates of various sizes

were detected, interacting with the cell membrane. Furthermore it can also be observed that HS_{ster} particles maintained their shape within the aggregates, but a different behaviour was revealed by WCS_{ster} particles which appeared more loosely than that seen in the compact aggregates, before contacting with the cell culture medium (figure 4.10 and 4.11).

Control cells showed a fusiform shape with intact cytoplasmic and nuclear membranes. These cells presented a normal distribution of the intracellular organelles, i.e. nucleus with uniformly dispersed chromatin and clear nucleolus and the cytoplasm containing randomly distributed organelles and electrondense granules. As can be seen in figures 4.10 and 4.11, following nano-Hap interactions, cells readily internalized the nanoparticles. Uptake of the particles was apparently initiated by the emission of pseudopod-like projections towards nanoparticles with further fusion of their membranes, which entraps particles inside endosomes (figures 4.10 and 4.11). Several vesicles of different sizes and loaded with particles were observed scattered within the cytoplasm (figures 4.10 and 4.11); besides, isolated particles were not detected either in the cytosol, cell nucleus or in other organelles. As cells exposed during 3 days to 500 µg/ml of HS_{ster} and WCS_{ster} nano-Hap presented huge loaded vesicles, the uptake of the nanoparticles seemed to be time and concentration-dependent. Furthermore, it was also noticed several cells exhibiting characteristic signs of apoptosis, i.e. cell membrane shrinkage with blebs formation, cytoplasm budding with vacuolization, and chromatin condensation at the nuclear periphery (figures 4.10 and 4.11). Cellular debris were also present in HS_{ster} and WCS_{ster} cultures, mainly after 3 days of exposure, which probably result from the progressive degeneration of apoptotic bodies. At high magnification, Figure 4.12, it is observed a close interaction between the nanoparticles and the cell membrane and the vesicles loaded with clustered particles; after 3 days, a high percentage of particles, especially HS_{ster}, maintained their rod-like morphology. However, particle dissolution seemed to have occurred, particularly in WCS_{ster} particles. This might reflect the lower crystallinity of WCS_{ster} particles, compared to HS_{ster}, favouring their dissolution.

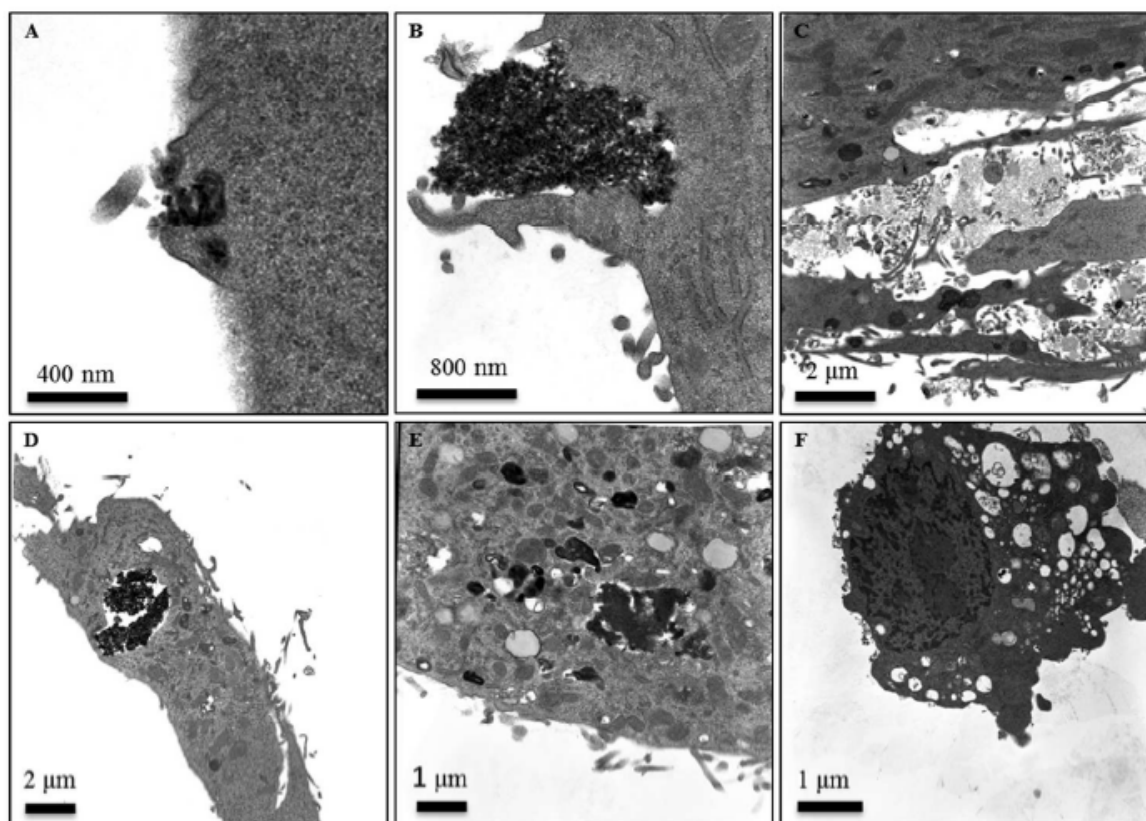


Figure 4.10- Representative TEM micrographs of MG63 cell cultures exposed to WCS_{ster} nanoparticles, 50 and 500 $\mu\text{g/ml}$, during different periods (3 hours, 24 hours and 3 days). The emission of pseudopods surrounding adjacent nanoparticles is observed in A (3 hours, 50 $\mu\text{g/ml}$) and B (3 hours, 500 $\mu\text{g/ml}$); D (24 hours, 500 $\mu\text{g/ml}$) and E (3 days, 500 $\mu\text{g/ml}$), depict clusters of nanoparticles entrapped in endosomes. Apart the entrapped nanoparticles within endosomes, it can be also observed in C (24 hours, 50 $\mu\text{g/ml}$) cellular debris in intercellular space. A cell with early signals of apoptosis, such as the rounded shape, the cytoplasmic vacuolization and signs of blebs formation is shown in F (3 hours, 50 $\mu\text{g/ml}$).

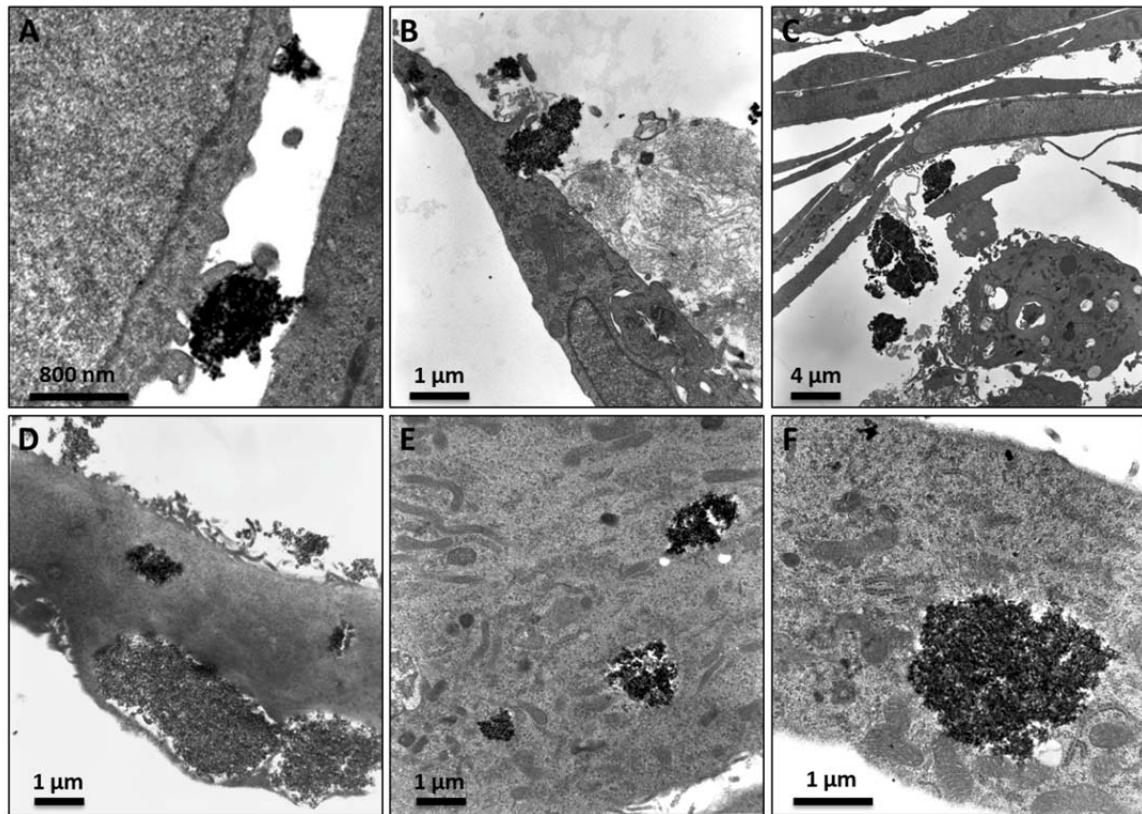


Figure 4.11- Representative TEM micrographs of MG63 cell cultures exposed to HS_{ster} nanoparticles, 50 and 500 µg/ml, during different periods (3 hours, 24 hours and 3 days). A (3 hours, 50 µg/ml) and B (3 days, 50 µg/ml) depict the emission of pseudopods surrounding nanoparticles and in D (24 hours, 500 µg/ml), E (3 days, 50 µg/ml), and F (3 days, 500 µg/ml) it can be observed clusters of nanoparticles entrapped in endosomes. An apoptotic cell with a rounded shape, condensed chromatin at nuclear periphery, cytoplasmic vacuolization and signs of blebs formation is shown in C (24 hours, 500 µg/ml).

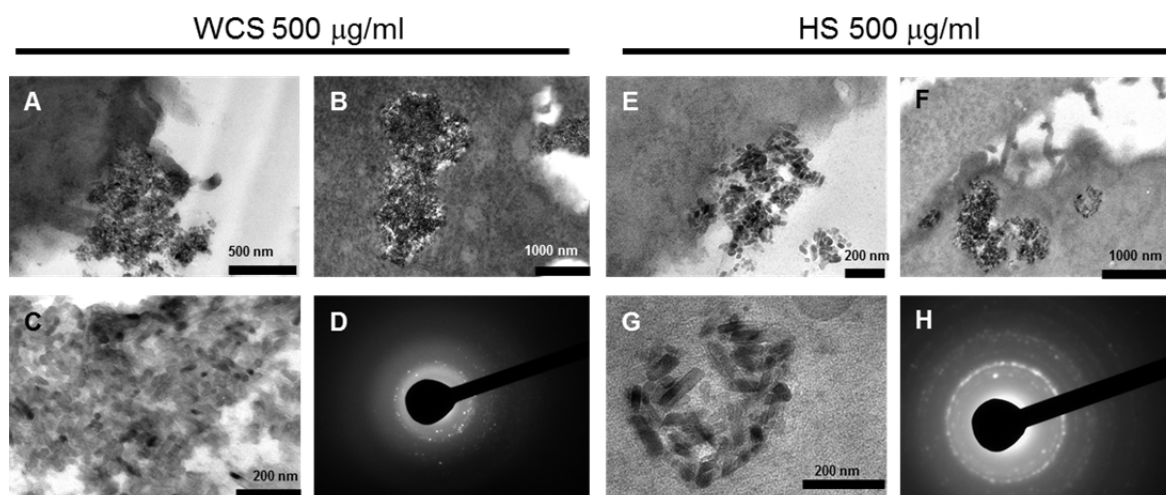


Figure 4.12- High magnification TEM images of MG63 cell cultures exposed to WCS_{ster} and HS_{ster} nanoparticles, 500 µg/ml, for 24 hours. A and E show the close interaction of the nanoparticles with the cell membrane, and B and F the intracellular vesicles loaded with the particles. C and G, a high magnification of B and F, respectively, display the nanoparticles within the intracellular vesicles, showing signs of particle dissolution. D and H display the electron diffraction patterns of the internalized nanoparticles.

As observed, sterilization induced significant effects in the physicochemical profile of WCS particles, being the most relevant changes observed in the morphology (size and shape), in the crystallinity and surface electrical charge. Culture medium was supplemented with foetal bovine serum which contains a variety of proteins and other bioactive molecules that quickly form an adhesion layer on the reactive surface of the nanoparticles, favouring the formation of agglomerates of attached particles, as also seen in previous studies involving several cell types⁴³⁻⁴⁵. The biological relevance of surface adsorbed proteins has been highlighted and the particle with its “protein-corona” is considered the effective unit of interest in the cell nanomaterial interaction. Regarding nano-Hap particles, surface adsorbed serum proteins was reported to alter the surface biochemistry and also physicochemical properties such as size, surface charge, aggregation behaviour and solubility⁴⁵. WCS and HS particles were both negatively charged at physiological pH, but WCS particles exhibited a much lower zeta potential value (figure 4.3), which is expected to influence the composition, and stability of this protein corona. However, as the zeta potential of the resulting particle-protein complex is not recognized, the relevance of the

different surface charge of WCS and HS particles on cell uptake and response is not known.

TEM images of cultures exposed to WCS_{ster} and HS_{ster} nano-Hap showed a close interaction of the particles with the cell membrane, followed by an internalization process by endocytosis pathways, with a time and dose-dependent uptake. The presence of intracellular Hap loaded vesicles induced alterations on the overall cell morphology, particularly in the presence of high levels, 500 µg/ml. Cells displaying signals of apoptosis were also seen; this appeared to result from the presence of big sized filled vesicles that damaged the cell structure, causing the cell degeneration. For both WCS_{ster} and HS_{ster} nano-Hap, cultures presented a high variability concerning particles uptake, i.e. the percentage of cells showing internalized particles and the number and size of the loaded vesicles. This is probably because, in the experimental protocol used, a suspension of particles was added to the adherent cells and, thus, the particle-cell interaction was associated with a great heterogeneity. Previously, nano-Hap internalization was observed in periodontal ligament cells ⁴³, liver cancer cells ⁴⁴, macrophages ⁴⁶ and mesenchymal stem cells ⁴⁷ interacting with isolated particles, or in rabbit osteoblastic cells and U2OS cells ⁶ and MG63 cells ⁴⁸ growing over nanoparticles films. In these studies, a great variability on the uptake of the nanoparticles was observed, which might be related with the cell type ⁶ and, in the same cell type, with the particles properties ⁴⁶. At high nano-Hap levels, 500 µg/ml, CLSM images also showed signals of deleterious effects in the cell layer, namely a lower definition of the F-actin peripheral ring, especially the cultures exposed to the WSC particles. F-actin plays a critical role in cell architecture and mobility, and the observed effects might suggest cellular responses to mechanical strain, probably arising from the presence of the nano-Hap loaded vesicles, as suggested before regarding endothelial cells ^{49,50}.

In spite of the deleterious effects of WCS_{ster} and HS_{ster} nano-Hap at high levels, it is worth to mention that the interaction with low levels, 50 µg/ml, results in a rapid internalization without affecting cell viability/proliferation, cell morphology and the percentage of apoptosis. Besides, a significant increase in the gene expression of the osteoblastic markers ALP and BMP-2 was observed in the

presence of HS_{ster} particles. This is in line with previous studies showing that Hap nanoparticles exhibit functional properties, namely modulating the expression of several genes in osteoblastic cells, including ALP expression⁵¹. It was also reported⁴⁷ an increased ALP activity in periodontal ligament cells interacting with nanoHap⁴³.

Dissolution of nano-Hap has been previously suggested to occur in osteoblasts⁵¹ and macrophages⁴⁶. The dissolution process may induce the saturation of the lysosome environment regarding calcium, phosphate and hydroxide ions and the elevation of the local pH^{52,53}, which might contribute to inhibit further Hap dissolution⁴⁶. Such behaviour might explain the relatively low dissolution of WCS_{ster} and HS_{ster} nano-Hap particles after 3 days. It has been suggested that diffusion of calcium and phosphate ions from the lysosome to the cytoplasm plays a relevant role in the modulation of cell behavior by nano-Hap. In the cytoplasm, calcium concentration is lower than 200 nM but higher concentrations (400 to 600 μ M) can be reached within the lysosome⁵², and even minor changes in cytoplasmic calcium has significant effects in cell behavior, as this ion has a major role as a second messenger modulating a variety of cellular functions⁵⁴.

In the present work, WCS_{ster} and HS_{ster} particles exhibited some differences on the induced cell response, namely in the cytotoxic potential and in the gene expression of osteoblastic markers. Main differences in the physicochemical profile of the sterilized particles are the more negative zeta potential and the lower crystallinity of WCS_{ster} nano-Hap, conditioning the interaction with proteins and cells and the particles dissolution rate. Particles also differed on the amount of adsorbed citrate ions, which may be of biological significance, as citrate is an important metal ion binder, with a high affinity for calcium, being involved in key physiological functions and intracellular metabolic events⁵⁵. However, no single property was identified to explain the differences seen in the response of MG63 cells, which is in line with previous studies^{6,43,46,48-52}, showing a great variability in the cell response to nano-Hap. These studies involved a variety of experimental conditions, i.e. characteristics of the Hap nanoparticles, the cell type, the exposure conditions and the characterization of the cell response. In

some of the works, particles were poorly characterized and, in others, the physicochemical profile of sterilized nanoparticles prepared at room temperature was not assessed. Nevertheless, results suggested that the elicited response depends on the combined interaction of various nanoparticles characteristics, i.e. crystallinity, size, surface charge and surface area, leading to a different profile of protein adsorption, particle aggregation, uptake, degradation/dissolution and rate of intracellular release of calcium ions, justifying a nanoparticle targeted research, oriented to the intended application.

In conclusion, the results reported in this study indicate that the WCS and HS nanoHap particles display different morphological attributes, i.e. size and shape. Besides, their different surface chemical condition is reflected in both zeta potential curves and FTIR spectra. Furthermore, the sterilization modified markedly the shape, size and aggregation state of WCS nanoparticles whose high surface area suffered a drastic reduction during autoclaving. Sterilized WCS and HS nanoHap particles were readily internalized by MG63 osteoblastic cells, by an endocytic pathway, and exhibited some differences in the elicited cell response. Low levels, not associated with deleterious effects in the cell viability/proliferation, F-actin cytoskeleton organization and apoptosis rate, were able to increase the expression of ALP and BMP-2. Only at high nanoparticles concentrations deleterious effects on cell behaviour were observed, probably due to the vesicular entrapment of the particles and their low degradability. As a consequence of their low toxicity and their potential for the modulation of the osteoblastic cell behaviour, WCS and HS nanoHap particles are likely to exhibit an interesting profile for bone tissue applications.

4.5. References

- 1 Tomada, Keishiro and Hidehiko Ariizumi, Takatomo Nakaji, Kimiko Makino. "Hydroxyapatite particles as drug carriers for proteins". *Colloids and Surfaces B: Biointerfaces* **76**, 226-235, (2010).
- 2 Epple, M. and K. Ganesan, R. Heumann, J. Klesing, A. Kovtun, S. Neumann and V. Sokolova. "Application of calcium phosphate nanoparticles in biomedicine". *J. Mater. Chem.* **20**, 18-23, (2010).

- 3 Sergey, V. Dorozhkin. "Nanosized and nanocrystalline calcium orthophosphates". *Acta Biomaterialia* **6**, 715-734, (2010).
- 4 Samar, J. Kalita; Abhilasha, Bhardwaj and Himesh, A. Bhatt. "Nanocrystalline calcium phosphate ceramics in biomedical engineering". *Materials Science and Engineering C* **27**, 441-449, (2007).
- 5 M.A.Martins; C.Santos; M.M.Almeida and M.E.V.Costa. "Hydroxyapatite micro- and nanoparticles: nucleation and growth mechanisms in the presence of citrate species". *Journal of Colloid and Interface Science* **318**, 210-216, (2008).
- 6 Yurong, Cai; Yukan, Liu; Weiqi, Yan; Qinghong, Hu; Jinhui, Tao; Ming, Zhang; Zhongli, Shic and Ruikang, Tang. "Role of hydroxyapatite nanoparticle size in bone cell proliferation". *Journal of Materials Chemistry* **17**, 3780-3787, (2007).
- 7 Kim, Jong Ah; Aberg, Christoffer; Salvati, Anna and Dawson, Kenneth A. "Role of cell cycle on the cellular uptake and dilution of nanoparticles in a cell population". *Nature Nano* **7**, 62-68, (2012).
- 8 Santos, C.; Gomes, P.S.; Duarte, J.A.; Franke, R.P.; Almeida, M. M.; Costa, M. E. V. and Fernandes, and M.H. "Osteoblastic cell response to different Hydroxyapatite nanoparticles and relevance of sterilization-induced effects on particle physicochemical profile". *Journal of the Royal Society Interface* **accepted**, (2012).
- 9 Suk-Woo, Ha; Roland, Reber; Karl-Ludwig, Eckert; Marc, Petitmermet; Jorg, Mayer and Erich, Wintermantel. "Chemical and Morphological Changes of Vacuum-Plasma-Sprayed Hydroxyapatite Coatings during Immersion in Simulated Physiological Solutions". *J.Am.Ceram.Soc* **81**, 81-88, (1998).
- 10 YingJun, Wang; Shuhua, Zhang; Kun, Wei; Naru, Zhao; Jingdi, Chen and Xudong, Wang. "Hydrothermal Synthesis of Hydroxyapatite nanopowders using cationic surfactant as templates". *Materials Letters* **60**, 1484-1487, (2006).
- 11 Aili, Wang; Dong, Liu; Hengbo, Yin; Huixiong, Wu; Yuji, Wada; Min, Ren; Tingshun, Jiang; Xiaonong, Cheng and Yiqing, Xu. "Size-controlled synthesis of hydroxyapatite nanorods by chemical precipitation in the presence of organic modifiers". *Materials Science and Engineering C* **27**, 865-869, (2007).
- 12 Feng, Wang; Mu-Sen, Li; Yu-Peng, Lu; yong Xin, Qi and Yu-Xian, Liu. "Synthesis and microstructure of hydroxyapatite nanofibers synthesized at 37°C". *Materials Chemistry and Physics* **95**, 145-149, (2006).
- 13 Lopez-Macipe;, Anabel; Gomez-Morales;, Jaime and Rodriguez-Clemente;, Rafael. "Nanosized Hydroxyapatite precipitation from Homogeneous Calcium/Citrate/Phosphate Solutions Using Microwave and Conventional Haeting". *Advanced Materials* **10**, 49-53, (1998).
- 14 Raynaud, S.; Champion, E.; Bernache-Assollant, D. and Thomas, P. "Calcium phosphate apatites with variable Ca/P atomic ratio I. Synthesis, characterisation and thermal stability of powders". *Biomaterials* **23**, 1065-1072, (2002).
- 15 Elliott, J. C.; Wilson, R. M. and Dowker, S. E. P. "Apatite structures". *JCPDS-International Centre for Diffraction Data* **45**, 172-181, (2002).

- 16 Bilton, Matthew; Milne, Steven J. and Brown, Andrew P. "Comparison of Hydrothermal and Sol-Gel Synthesis of Nano-Particulate Hydroxyapatite by Characterisation at the Bulk and Particle Level". *Journal of Inorganic Non-metallic Materials* **2**, 1-10, (2012).
- 17 Monmaturapoj, Naruporn andYatongchai, Chokchai. "Effect of Sintering on Microstructure and Properties of Hydroxyapatite Produced by Different Synthesizing Methods ". *Journal of Metals, Materials and Minerals* **20**, 53-61, (2010).
- 18 Sadat-Shojai, Mehdi; Atai, Mohammad; Nodehi, Azizollah and Khanlar, Leila Nasiri. "Hydroxyapatite nanorods as novel fillers for improving the properties of dental adhesives: Synthesis and application". *Dental Materials* **26**, 471-482, (2010).
- 19 Zhang, Hongquan andDarvell, Brian W. "Formation of Hydroxyapatite Whiskers by Hydrothermal Homogeneous Precipitation Using Acetamide". *Journal of the American Ceramic Society* **94**, 2007-2013, (2011).
- 20 Larrubia, M. Angeles; Gianguido, Ramis and Guido, Busca. "An FT-IR study of the adsorption of urea and ammonia over V₂O₅-MoO₃-TiO₂ SCR catalysts". *Applied Catalysis B: Environmental* **27**, 145-151, (2000).
- 21 Fleet, Michael E. "Infrared spectra of carbonate apatites: ν_2 - Region bands". *Biomaterials* **30**, 1473-1481, (2009).
- 22 Michael, E. Fleet andXiaoyang, Liu. "Location of type B carbonate ion in type A-B carbonate apatite synthesized at high pressure". *Journal of Solid State Chemistry* **177**, 3174-3182, (2004).
- 23 Neira, S.; Kolen'ko, Yury V; Lebedev, Oleg I; Tendeloo, Gustaaf Van; Gupta, Himadri S; Guitian, Francisco and Yoshimura, and Masahiro. "An Effective Morphology Control of Hydroxyapatite Crystals via Hydrothermal Synthesis". *Crystal Growth & Design* **9**, 466-474, (2009).
- 24 M.S.Bootharaju andT.Pradeep. "Uptake of Toxic Metal Ions from Water by Naked and Monolayer Protected Silver Nanoparticles: An X-ray Photoelectron Spectroscopic Investigation". *J.Phys.Chem.C* **114**, 8328-8336, (2010).
- 25 Matthew, J. Olszta; Xingguo, Cheng; Sang Soo, Jee; Rajendra, Kumar; Yi-Yeoun, Kim; Michael, J. Kaufman; Elliot, P. Douglas and Laurie, B. Gower. "Bone structure and formation: A new perspective". *Materials Science and Engineering R: Reports* **58**, 77-116, (2007).
- 26 Sujin, Kim; Hyun-Seung, Ryu; Hyunho, Shin; Hyun Suk, Jung and Kug Sun, Hong. "In situ of hydroxyapatite nanocrystal formation from amorphous calcium phosphate in calcium-rich solutions". *Materials Chemistry and Physics* **91**, 500-506, (2005).
- 27 S.W.K.Kweh; K.A.Khor and P.Cheang. "The production and characterization of hydroxyapatite (HA) powders". *Journal of Materials Processing Technology* **89-90**, 373-377, (1999).

-
- 28 Masayuki, Nara and Masaru, Tanokura. "Infrared spectroscopic study of the metal-coordination structures of calcium-binding proteins". *Biochemical and Biophysical Research Communication* **369**, 225-239, (2008).
- 29 Mineyuki, Mizuguchi; Masayuki, Nara; Keiichi, Kawaro and Katsutoshi, Nitta. "FT-IR study of the Ca^{2+} -binding to bovine α -lactalbumin". *FEBS Letters* **414**, 153-156, (1997).
- 30 Adriyan, S. Milev; Kannangara, G. S. Kamali and Michael, A. Wilson. "Template-Directed Synthesis of hydroxyapatite from a Lamellar Phosphonate". *Langmuir* **20**, 1888-1894, (2004).
- 31 Neuman, S. Resende; Marcio, Nele and Vera, M. M. Salim. "Effects of anion substitution on the acid properties of hydroxyapatite". *Thermochimica Acta* **451**, 16-21, (2006).
- 32 Donald, L. Pavia; Gary, M. Lampman; George, S. Kriz and James, R. Vyvyan. *Introduction to spectroscopy*. Vol. fourth edition (2009).
- 33 Kurt, Lackovic; Bruce, B. Johnson and Michael J. Angove and, John D. Wells. "Modeling the adsorption of citric acid onto Mulloorina illite and related clay minerals". *Journal of Colloid and Interface Science* **267**, 49-59, (2003).
- 34 Simon, Floate; Mirghasem, Hosseini; Mohammad, R. Arshadi; David, Ritson; Karen, L. Young and Richard, J. Nichols. "An in-situ infrared spectroscopic study of the adsorption of citrate on Au(111) electrodes". *Journal of Electroanalytical Chemistry* **542**, 67-74, (2003).
- 35 M. Rajendran and Rao, M. Subba. "Formation of BaTiO_3 from Citrate Precursor". *Journal of Solid State Chemistry* **112**, 239-247, (1994).
- 36 K. Van, Werde; D. Mondelaers; G. Vanhoyland; D. Nelis; M. K. Van, Bael; J. Mullens and L. C. Van, Poucke. "Thermal decomposition of the ammonium zinc acetate citrate precursor for aqueous chemical solution deposition of ZnO ". *Journal of Materials Science* **37**, 81-88, (2002).
- 37 Jiang, Shu-Dong; Yao, Qi-Zhi; Zhou, Gen-Tao and Fu, Sheng-Quan. "Fabrication of Hydroxyapatite Hierarchical Hollow Microspheres and Potential Application in Water Treatment". *The Journal of Physical Chemistry C* **116**, 4484-4492, (2012).
- 38 Lijun, Wang and George, H. Nancollas. "Calcium Orthophosphates: Crystallization and Dissolution". *Chem Rev.* **108**, 4628-4669, (2008).
- 39 Chung-Wei, Yang and Truan-Sheng, Lui. "Kinetics of hydrothermal crystallization under saturated steam pressure and the self-healing effect by nanocrystallite for hydroxyapatite coatings". *Acta Biomaterialia* **5**, 2728-2737, (2009).
- 40 Jiwen, Wang and Leon, L. Shaw. "Morphology-Enhanced Low-Temperature Sintering of Nanocrystalline Hydroxyapatite". *Advanced Materials* **19**, 2364-2369, (2007).

- 41 Meena, Ramovatar; Kesari, Kavindra; Rani, Madhu and Paulraj, R. "Effects of hydroxyapatite nanoparticles on proliferation and apoptosis of human breast cancer cells (MCF-7)". *Journal of Nanoparticle Research* **14**, 1-11, (2012).
- 42 Yuan, Yuan; Liu, Changsheng; Qian, Jiangchao; Wang, Jing and Zhang, Yuan. "Size-mediated cytotoxicity and apoptosis of hydroxyapatite nanoparticles in human hepatoma HepG2 cells". *Biomaterials* **31**, 730-740, (2010).
- 43 W.Sun; C.Chu; J.Wang and H.Zhao. "Comparison of periodontal ligament cells responses to dense nanophase hydroxyapatite". *J.Mater Sci: Mater Med* **18**, 677-683, (2007).
- 44 Bauer, I. W.; Li, S. P.; Han, Y. C.; L.Yuan and Jin, Z. M. "Internalization of hydroxyapatite nanoparticles in liver cancer cells". *J.Mater Sci: Mater Med* **19**, 1091-1095, (2008).
- 45 Hails, L. A.; Babister, J. C.; Inglis, S.; Davis, S. A.; Oreffo, R. O. C. and S.Mann. "Inhibition of hydroxyapatite nanoparticle-induced osteogenic activity in skeletal cells by adsorption of serum proteins". *Small* **6**, 1986-1991, (2010).
- 46 M.Motskin; D.M.Wright; K.Muller; N.Kyle; T.G.Gard; A.E.Porter and J.N.Skepper. "Hydroxyapatite nano and microparticles: Correlation of particle properties with cytotoxicity and biostability". *Biomaterials* **30**, 3307-3317, (2009).
- 47 Gonzalez-McQuire, R.; Green, D. W.; Partridge, K. A.; Oreffo, R. O. C.; S.Mann and Davis, S. A. "Coating of human mesenchymal cells in 3D culture with bioinorganic nanoparticles promotes osteoblastic differentiation and gene transfection". *Advanced Materials* **19**, 2236-2240, (2007).
- 48 Zhongli, Shi; Xin, Huang; Yurong, Cai; Ruikang, Tang and Disheng, Yang. "Size effect of Hydroxyapatite nanoparticles on proliferation and apoptosis of osteoblast-like cells". *Acta Biomaterialia* **5**, 338-345, (2009).
- 49 S.Pezzaatini; R.Solito; L.Morbidelli; S.Lamponi; E.Boanini; A.Bigi and M.Ziche. "The effect of hydroxiapatite nanocrystals on microvascular endothelial cell viability and functions". *J.Biomed.Mat.Res.* **76A**, 656-663, (2006).
- 50 S.Pezzaatini; R.Solito; L.Morbidelli; S.Lamponi; E.Boanini; A.Bigi and M.Ziche. "Nanostructured HA crystas up-regulate FGF-2 expression and activity in microvascular endothelium promoting angiogenesis". *Bone* **41**, 523-534, (2007).
- 51 Xu, J. L.; Khor, K. A.; Sui, J. J.; Zhang, J. H. and Chen, W. N. "Protein expression profiles in osteoblasts in response to differentially shaped hydroxyapatite nanoparticles". *Biomaterials* **30**, 5385-5391, (2009).
- 52 Christensen, K. A.; Myers, J. T. and Swanson, J. A. "pH-dependent regulation of lysosomal calcium in macrophages". *J.Cell Sci.* **115**, 599-607, (2002).
- 53 Bloebaum, R. D.; Lundeen, G. A.; Bachus, K. N.; Ison, I. and Hofmann, A. A. "Dissolution of particulate hydroxyapatite in a macrophage organelle model". *J.Biomed.Mat.Res.* **40**, 104-114, (1998).
- 54 Clapham, D. E. "Calcium signaling". *Cell* **131**, 1047-1058, (2007).

- 55 Srere, P A. "The molecular physiology of citrate". *Curr Top Cell Regul* **33**, 261-275, (1992).

Chapter 5

Functionalization of Hydroxyapatite nanostructures

5.1. Introduction

Nanotechnology is currently offering various stimulating possibilities in many scientific areas being 'nanomedicine' a new paradigm in the biomedical field ¹. Theragnostics is a strategy that integrates therapeutics with diagnostics to develop new personalized treatments with enhanced efficacy and safety which imply diagnostic imaging with high sensitivity and molecular specificity ². Depending on the molecular imaging modality and contrast agent used, theragnostics benefits include treatment planning, drug and dosage selection, and therapeutic response monitoring ². Various nanoparticles (NPs) with high target specificity and often combining multifunctions for more than one clinical purpose are being actively studied for theragnostics. Iron oxide, gold, and quantum dots exhibiting intrinsic imaging abilities ¹ are examples of such nanoparticles. Photothermal imaging and therapy are novel techniques closely related to theragnosis. Photothermal imaging consists of detecting and imaging thermal energy converted from light while photothermal therapy consists on cancer cells destruction by thermal energy converted from light. Metal nanostructures of noble metals like gold or silver are excellent thermal conductors and photothermal converters as they strongly absorb light at a particular wavelength and can convert light energy into thermal energy very quickly, being thus excellent theragnostic candidates ³.

Theragnostic nanoparticles have been produced from various building blocks ^{1,4-8}, but drawbacks including synthesis limitations, handing and loading difficulties, poor stability and potential toxicity ¹ still persist.

In the present study hydroxyapatite nanoparticles are proposed as templates for theragnostic particles due to their excellent biocompatibility ⁹ and enhanced adsorptive ability ¹⁰⁻¹². Addressing the combination of these exceptional properties with the unique characteristics of gold nanoparticles, new materials based on coupled Hap and gold nanoparticles (Hap-Au) are envisaged with interesting biomedical potential.

The present chapter exploits the possibility of Hap nanoparticles functionalization with gold aiming at novel applications in which coupled therapeutic and contrasting functionalities are demanded.

Hap nanoparticles precipitated from a solution containing citric acid by the hydrothermal method (HS) as previously described in chapter 2 (section 2) are here addressed as templates for gold precipitation. The experimental results comprising the characteristics of the nanometric gold precipitates will be here discussed.

While benefits of gold nanoparticles (AuNPs) have been widely publicized ¹³, the discussion of the potential effects of AuNPs coupled to hydroxyapatite nanoparticles on the proliferation, differentiation, and mineralization of human osteoblast-like cells *in vitro* has not been addressed so far. Thus, MG63 cells response to Hap nanoparticles with coupled AuNPs will be also examined and compared to the response to Hap-NPs.

A second objective of this chapter was to design a folic acid (FA)-conjugated nanoparticle for the specific recognition of the soluble form of the folate receptor expressed at the surface of cells. The adopted method relies on FA adsorption on nanoparticles surface ^{14,15} whose results will be also discussed. The results of *in vitro* studies covering the interaction of the prepared nano materials with MG63 cells will be examined as well.

5.2. Precipitation of nanosized gold dots on hydroxyapatite nanoparticles facets

The choice of nano hydroxyapatite particles obtained by the hydrothermal method (particles HS 3:1 which will be simply referred as HS) as templates for gold precipitation and folic acid functionalization relies on the following reasons: firstly, HS are obtained by a simple procedure, which allows Hap particles with a high level of reproducibility and stability to be produced. Additionally this method uses an organic additive, i.e. a citric acid, which the human body is able to recognize. Thus HS nanoparticles which were found not to show toxicity effects (chapter 4), have a nanometric size and possess on their surface organic

species (citric acid related groups) which are envisaged as chemical entities potentially able to act as reducing agents towards gold ions or to be linked with folic acid.

5.2.1. Crystal structure and microstructure

Figure 5.1 presents the optical pictures of the collected HS particles after being exposed during different periods of times to hydrogen tetrachloroaurate solution. It is observed that the original yellowish colour of HS (fig 5.1 (a)) becomes a purple-like colour after 5 min and deeper purple after a longer reaction time of 20 min (fig 5.1 (b) and (d)). These colour changes anticipate the presence of nanometric sized gold particles in the collected particles ¹⁶. Further evidences of gold precipitation are provided by the particle X-ray diffraction (XRD) patterns shown in figure 5.2 ((b) and (c)): the presence of metallic gold (Au) is revealed by the peak detected at $2\theta \sim 38^\circ$ which denotes the presence of metallic gold ^{17,18}. This is the more intense peak in Au XRD pattern according to the JCPDS N° 071-4614. Other smaller peaks may also be present but superimposed on hydroxyapatite peaks thus being indistinguishable from Hap XRD pattern.

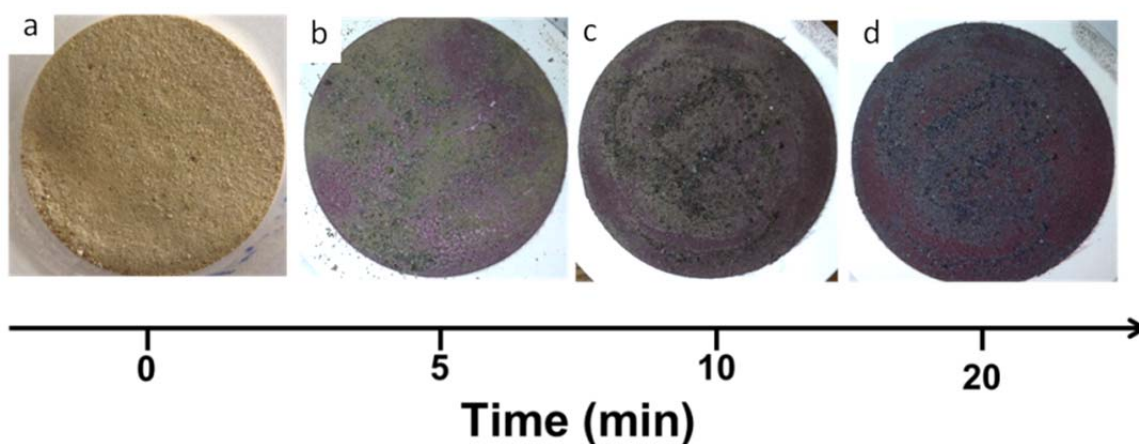


Figure 5.1- Optical pictures of HS particles (a) as synthesized at 180°C or after reacting with hydrogen tetrachloroaurate solution during (b) 5 min, (c) 10 min and (d) 20 min.

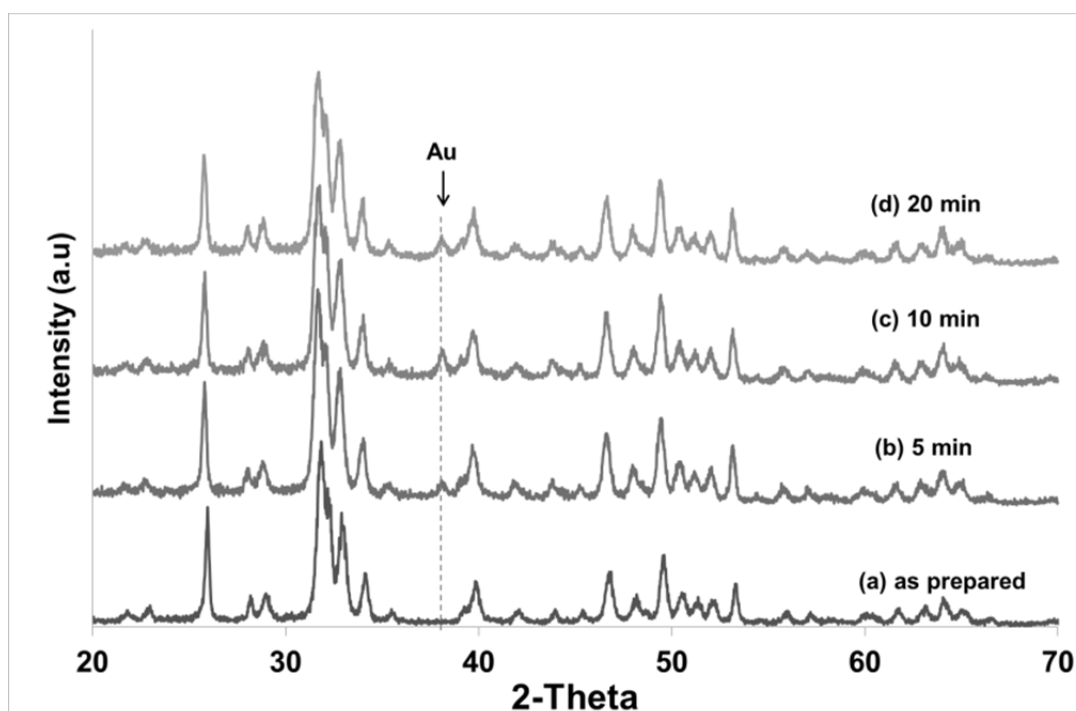


Figure 5.2- X-ray diffraction patterns of hydroxyapatite particles (HS) as prepared (a), and after reacting with HAuCl_4 solution during (b) 5 min, (c) 10 min and (d) 20 min. The presence of metallic gold (Au) is revealed by the peak detected at $2\theta \sim 38^\circ$.

Figure 5.3 shows the TEM images of the Hap particles collected after different precipitation times. It is clearly observed that the prismatic HS particles surfaces previously imaged in chapter 3, in figure 3.3 ((a) and (b)), are now uniformly spotted with nanosized dark dots, whose dimensions vary approximately from 1,5 to 2,5 nm as the reaction time increases from 5 min (fig. 5.3 (a), (b)) to 20 min (fig. 5.3 (c), (d)). These are metallic gold nanosized dots which were precipitated on Hap facets accounting for the previously described colour variations of HS. Thus the used strategy allowed to couple nanometric sized gold particles (AuNPs) to the facets of hydroxyapatite nanoparticles (HS) forming a nanostructured assemblage of gold metal and hydroxyapatite (HS-AuNPs). It was also found that HS-AuNPs after 20 min of reaction apparently have a lower density of larger AuNPs dots on their surface which indicates that AuNPs have grown during the reaction period. The growth of AuNPs may be explained by an Ostwald ripening mechanism which would favour the growth of larger Au particles at the expense of smaller ones ¹⁹⁻²¹. Although the dots become larger, they apparently preserve a spherical shape which is known to

be the lowest-energy shape and that observed for most of the metal nanoparticles usually obtained from metal salts reaction with reducing agents²². The colour evolution of HS-AuNPs described before is thus in line with the AuNPs size variations revealed by TEM analysis. The present precipitation technique proved to be highly reproducible, consistently yielding uniform spherical nanoparticles without the need of any additional surfactant for stabilization.

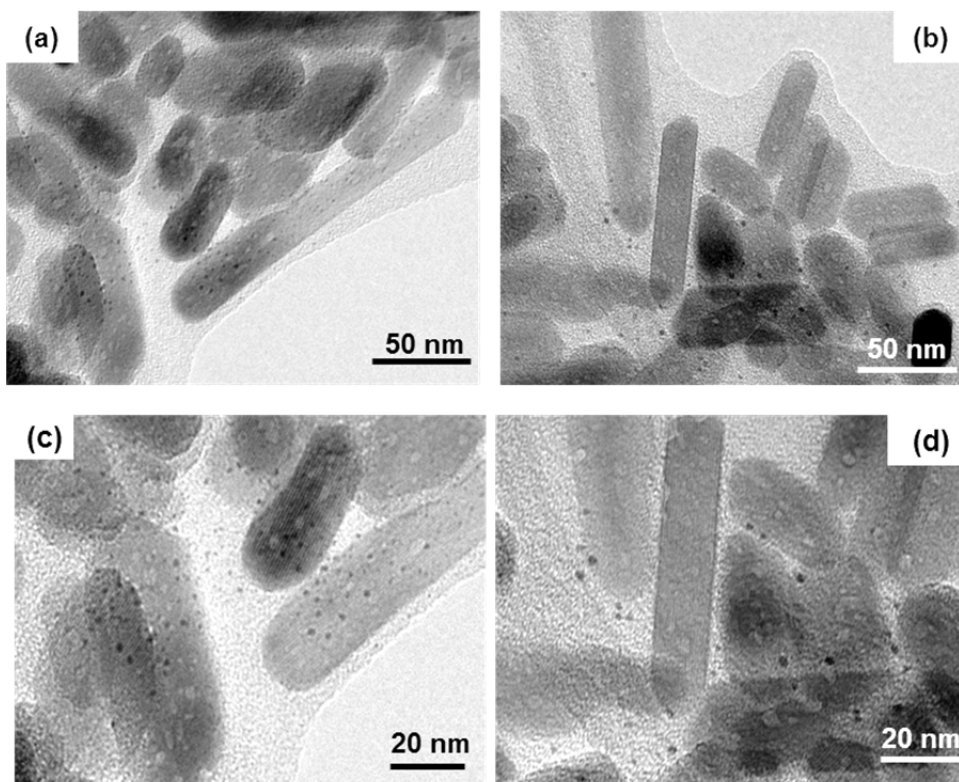


Figure 5.3- TEM images of HS particles coupled with Au nanoparticles after different reaction times with HAuCl_4 solution: 5 min ((a) and (c)) and 20 min ((b) and (d)).

Recent literature conveys a large amount of interest on Hap-Au synthesis and properties optimization. Yanjun Ding and co-workers produced a hybrid material by assembling gold nanoparticles previously synthesized onto nano-hydroxyapatite using a sonicated method¹⁰. T.P Sastry and co-workers developed physiologically clotted fibrin capped gold nanoparticles to be used as support for growing hydroxyapatite in order to improve osteoinductive properties²³. Santosh Aryal et al. firstly immobilized collagen on gold nanoparticles and then precipitated hydroxyapatite by a wet chemical method to be applied in bone tissue repair and regeneration²⁴. With a similar purpose Yogita Gupta et

al. synthesized primarily the polymer (Poly-(9-(4-vinylbenzyl)-purin-6-yl)-amino caproic acid (AP-1)), subsequently hydrolyzed octacalcium phosphate and finally synthesized gold nanoparticles on the prepared composite particles ²⁵. Sujatha K. Arumugam et al. synthesized gold nanoparticles on hydroxyapatite surface, i.e using commercial hydroxyapatite they adsorbed a gold salt (HAuCl_4) on the Hap surface, and then reduced the gold with hydrazine hydrate. These particles are intended to control platelet adhesion and to enhance blood compatibility ¹⁷. The authors found that Hap-Au nanoparticles can be combined in a single construct, allowing simultaneous targeting, diagnosis, and therapeutic functionality which can be chemically tailored for a particular patient or disease. As compared with these methods the prepared HS particles can act simultaneously as reducing agent of gold salt and present low toxicity and the potential for the modulation of the osteoblastic cell behaviour ¹².

Considering the nanometric size of the gold particles precipitated in the present work, particular optical properties were foreseen for HS-AuNPs ²⁶. Figure 5.4 shows the UV-Vis spectra of (a) HS as prepared and of (b, c and d) HS-AuNPs after 5, 10 and 20 min reaction times. HS particles as prepared do not show any absorption band in the range of 300-800 nm (fig 5.4 (a)). Similar results were already reported by other authors ^{17,25,27}. Conversely, a characteristic Surface Plasmon Resonance (SPR) band of gold nanoparticles (AuNPs) at 553 nm is clearly detected for the all studied samples (5, 10 and 20 min) confirming that AuNPs were precipitated. Furthermore the obtained SPR band at 553 nm suggests the formation of AuNPs with spherical shape by this synthesis method. As predicted by Gan theory, when the shape of AuNPs change from spheres to different morphologies like: rods, nanocages, etc, the SPR band is split into two bands: a strong band in the region (650-900 nm) corresponding to electron oscillations along the long axis, and a weak band in the visible region (520 nm) at a wavelength similar to that of gold nanospheres ^{16,28}. However, the SPR band exhibited around 553 nm is slightly shifted away from the well-known value of 520 nm referred for isotropic spherical particles (<20 nm) dispersed in water ^{29,30}. It can be argued that the slight shift in SPR band may be due to the fact that the refractive index of hydroxyapatite (1.63-1.64), i.e. the substrate, is higher than that of water (1.33) which is the solvent usually referred ²⁷. A similar effect was reported for other materials, namely silica nanoparticles ^{31,32}.

Normally this band accounts for the strong colour changes observed on the particles³³. As referred previously the spherical gold particles exhibit a SPR in visible region which is not optimal for *in vivo* applications because its attenuation by biological fluids and tissues is giant^{6,34}. However the presence of SPR effect on the synthesized HS-AuNPs could be interesting for the treatment of a skin-type cancer and/ or a near-surface cancer where the wavelength of the laser should be less intense and the effect of SPR is maximized. Another possible application could be to use HS-AuNPs as a targeted X-ray contrast agent for labelling microdamage in bone tissue^{35,36}. Repetitive loading of bone tissue can lead to the accumulation of microdamage, observed histologically as microcracks or diffuse damage, and to degradation of mechanical properties. Microdamage accumulation in bone has been implicated with clinical scenarios for increased risk of fracture, including stress fractures in active individuals and fragility fractures in the elderly. However, the role of microdamage in clinical bone fragility is not well understood due, in part, to limited capabilities for detecting microdamage non-destructively^{35,36}. The gold nanoparticles can be used as targeted X-ray contrast agent and the Hap particles will be useful in the calcification of this microdamage^{35,36}. Moreover Hap particles could be also functionalized through adsorption of biological molecules that exist *in vivo* and hence functionalized Hap particles can be attracted by bone mineral crystals exposed on the surface of microcracks and thus detect this microdamage^{43,44}. Finally, another possible application for these particles is as immunosensor, due to Hap high absorbing ability and other multifunctional advantages such as high surface area, good biocompatibility and solubility. Yanjun Ding et al. demonstrated this immunosensor application, preparing gold/hydroxyapatite hybrid nanomaterial for the detection of α -Fetoprotein (AFP), an important indicator in the clinical diagnosis of cancers¹⁰.

Examples of encapsulation or functionalization of gold nanoparticles are recurrent in the literature, but most of them are focused on nonspherical gold nanoparticles (including nanorods, nanocages, stars, cubes) because they possess multiple plasmonic absorptions, where attenuation by biological fluids and tissues is minimal^{6,37}. Studies involving spherical nanoparticles are still of interest for those biomedical applications targeted to bodily surface treatments as is the case of skin cancer.

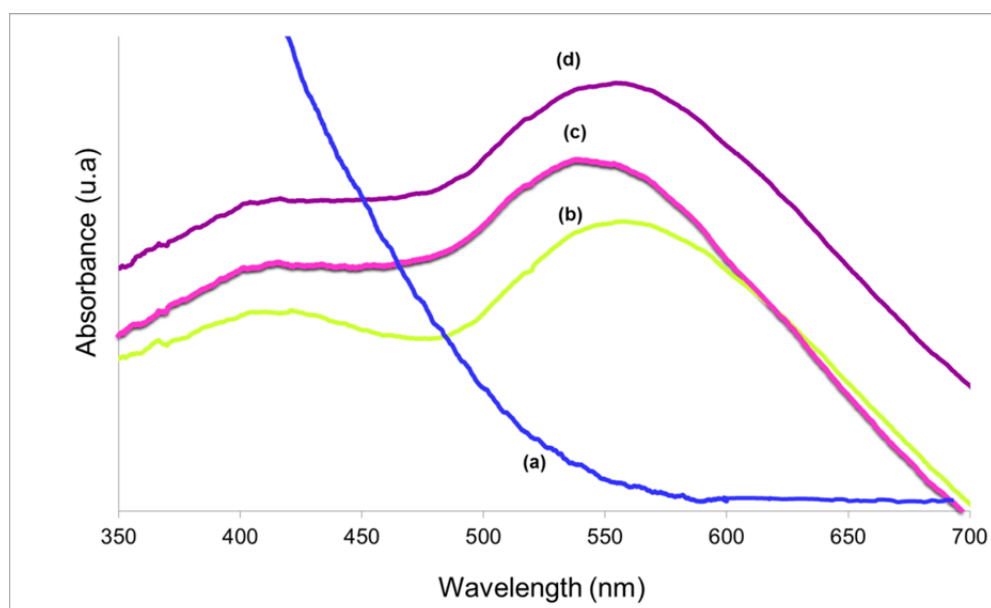


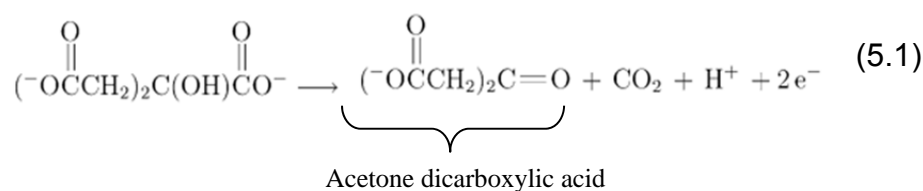
Figure 5.4-UV-Visible spectra of as prepared HS nanoparticles (a) and of HS-AuNPs after a reaction time of 5 min (b), 10 min (c) and 20 min (d).

5.3. Gold precipitation and surface-characteristics of HS-AuNPs

The process of AuNPs growth on HS surfaces was also followed by FTIR spectra analysis aiming to assess the evolution of adsorbed species. Figure 5.5-A compares the full spectrum of HS particles as prepared with those of HS-AuNPs collected after 5, 10 and 20 min, being the details of the FTIR region ($1350\text{--}1680\text{ cm}^{-1}$) magnified in the figure 5.5-B. It is important to remark that the general Hap FTIR features are detected in all samples (figure 5.5-A), although in those spectral region of HS particles coupled with Au some slight differences are remarked^{38,39}. This is the spectrum region where some groups derived from citrate decomposition are likely to be identified. Such groups as mentioned in chapter 3 result from citrate decomposition reactions under the used hydrothermal conditions⁴⁰. The more significant differences observed in the $1350\text{--}1680\text{ cm}^{-1}$ FTIR region, (figure 5.5 B) include the band at 1384 cm^{-1} assigned to $\text{--CH}_2\text{--}$ scissoring mode⁴¹ whose intensity undergoes a drastic decrease in HS-AuNPs as well as the band at 1567 cm^{-1} corresponding to the antisymmetric stretching mode of carboxylate groups in bidentate configuration. Additionally the band at 1670 cm^{-1} that can be attributed to C=O stretch in carbonyl containing species⁴² is unobserved in HS-AuNPs³⁹. FTIR results also

reveal some groups remaining regardless Au synthesis process. This is the case of the bands at 1402 cm^{-1} and 1458 cm^{-1} that may be attributed to the symmetric stretching mode of carboxylate groups in monodentate and bidentate configuration which indicate the species not involved in Au precipitation reactions. Conversely the bands affected by Au growth on the surface of the hydroxyapatite are interpreted either as denoting organic compounds playing active role in Au precipitation process or as indicating organics prone to easy desorption when exposed to the boiling HAuCl_4 solution.

According to S. Kumar et al.⁴³ gold precipitation by Turkevich method can be systematized in three steps: the initial step comprises the oxidation of citrate to acetone dicarboxylic acid after which a second step consisting of auric salt (AuCl_3) reduction to aurous salt (AuCl) takes place. The third step involves the disproportionation of aurous ions (Au^+) to gold atoms (Au^0). The equations corresponding to these three steps are respectively:



The last step (eq. 5.3) is facilitated by the acetone dicarboxylic specie that helps the formation of aurous species and dicarboxy acetone complexes which provide the combination of several aurous chloride molecules as required by equation (5.3). This is thus a multi-step process where series and parallel oxidation/reduction reactions take place. Based on the obtained results a mechanism of AuNPs synthesis using Hap (HS) particles as templates is here proposed. The following observations are worthy of mention:

- (i) in the absence of the HS nanoparticles no precipitation of gold occurs during the gold solution heating;
- (ii) Once HS particles are added to the heated ($\sim 100^\circ\text{C}$) gold solution, gold nanoparticles start to be deposited on HS particles surfaces. This is

detected by the modification of the particle colour that changes from light yellow to brown-purple after 2-3 min and to red-purple after 20 min (fig 5.1).

Based on these evidences the mechanism proposed is similar to that described by S. Kumar et al.⁴³. In the present work and as mentioned before, the thermal decomposition of citrate ions during hydrothermal synthesis of HS particles may originate diacids products (aconitic and/or itaconic acid, for instance). These acidic products could also be oxidized to dicarboxylic acids which in turn would play an organizing role equivalent to that of suggested by S. Kumar et al.⁴³ for the acetone dicarboxylic acid above described. Thus the assumption that citrate degradation derived compounds could have equivalent ability for reducing trivalent gold and consequently lead to the formation of gold nanoparticles is here confirmed. In this mechanism proposal citrate derived compounds play the role attributed to citrate in Turkevich method.

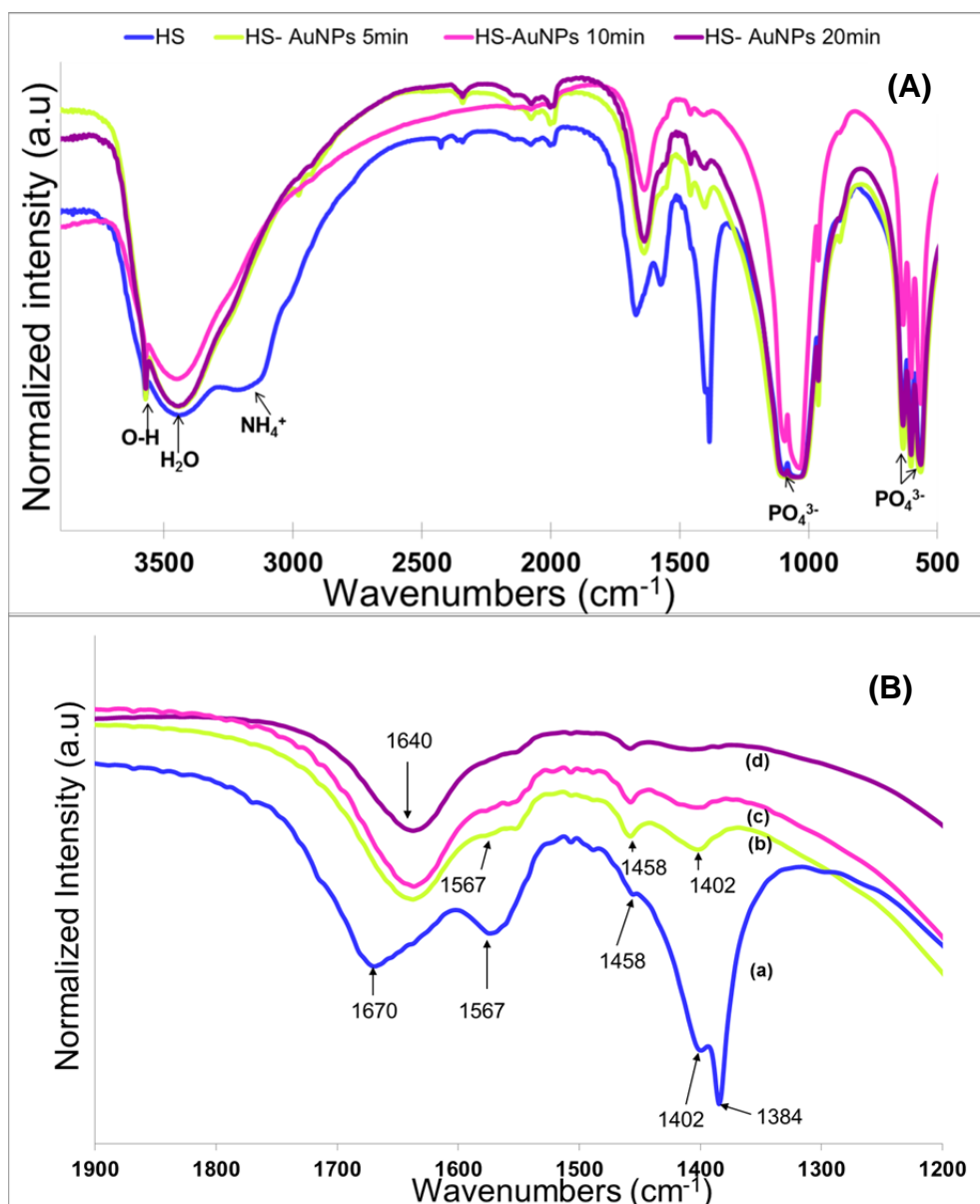


Figure 5.5- A) FTIR spectra of HS and HS-AuNPs nanoparticles; (B) Spectra magnification in the region of 1200-1900 cm^{-1} for HS (a) and for HS-AuNPs after different times of gold precipitation : 5 min (b), 10 min (c) and 20 min (d).

To evaluate the surface charge of the produced particles, zeta potential measurements were performed. The relation between the particles zeta potential (ξ) and the suspension pH is depicted in figure 5.6. HS nanoparticles have negative zeta potential in the examined pH range (fig. 5.6, curve (a)), due to the prevalence of negatively charged species in the Stern layer of the electrical double layer of Hap which are thought to include carboxylate groups,

PO_4^{3-} and OH^- surface ions⁴⁴⁻⁴⁷. Zeta potential values appear practically unchanged in the (5.7 -7) pH interval ((fig. 5.6, curve (a)), being this behaviour assigned to phosphate ions buffer capability according to the studies of Dušica R. Vučinić et al⁴⁶ on Hap zeta potential variation within the specific pH range of (6-9). As pH increases from 7 to 10 the amount of OH^- ions adsorbing on Hap surface also increases hence incrementing further the Hap negative zeta potential⁴⁶. Comparing HS and HS-AuNPs curves shown on figure 5.6 a main difference is remarked within the pH interval of (6.5-7.5) where HS-AuNPs are seen to bear a more negative ζ -potential than do HS particles. According to literature AuNPs present normally a negative zeta potential in the pH interval of 4 to 12^{48,49}. In the present case it is thought that citrate derived compounds containing carboxylic groups participated actively on Au^0 precipitation (as explained before) thus leaving behind newly unbound calcium ions which would be free for adsorbing OH^- ions. This could explain the apparently higher ability of HS-AuNPs particles to adsorb OH^- as compared to HS particles in this pH range. The strong negative zeta potential observed in all prepared particles denotes a high electrical surface charge which will protect the particles from aggregation and thus result in more stable dispersions of these nanoparticles which might be an advantage in biological tests applications.

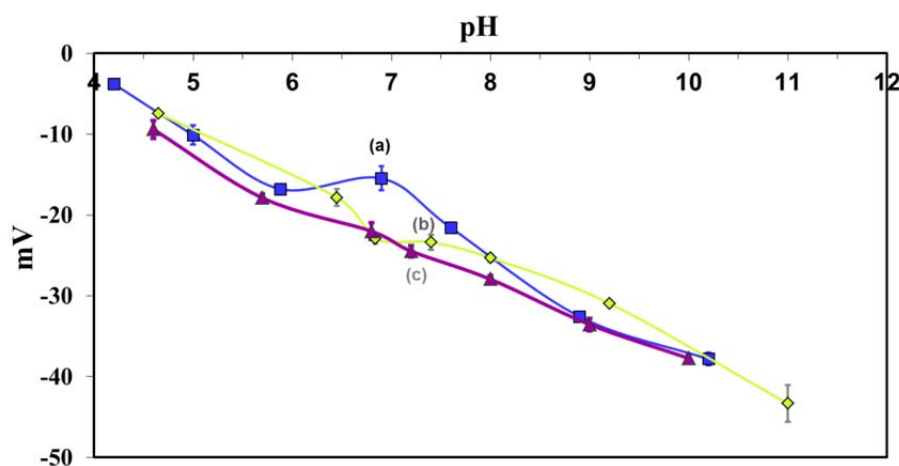


Figure 5.6- Zeta potential (ξ) as a function of pH for: (a) HS nanoparticles, (b) HS-AuNPs after 5 min of synthesis and (c) AuNPs after 20 min of synthesis. The strong negative zeta potential is observed in all prepared particles.

Some recent studies reported the synthesis of Au and Hydroxyapatite, although so far the method proposed in the present work for growing AuNPs on the surface of hydroxyapatite (Hap) is being reported for the first time. It combines the dual role of citrate ions as complexing agents of calcium ion during the synthesis of hydroxyapatite particles and as reducing agent for the nucleation and growth of gold on hydroxyapatite surface.

The facile strategy here reported to grow gold nanoparticles on the surface of the HS particles with a controlled nanometric size is a completely new approach in terms of AuNPs nucleation which was not used in any other kind of material so far. Additionally, the potential usefulness of the obtained materials for applications in the novel field of theragnosis is here enhanced.

5.4. Interaction of HS-AuNps with osteoblastic cells

The samples selected to be studied in the interaction of particles with cells were HS and HS-AuNPs synthesized during 5 minutes.

In this study, as in the last chapter, human osteosarcoma-derived MG63 osteoblastic-like cells were used. The selection of this human cell line has for long been applied for cytotoxicity and biocompatibility assays within the biological evaluation of materials, especially in those aiming for bone tissue repair/regeneration context. These cells, at a low density, show a characteristic oval to spindle-shaped morphology, with fine branching cytoplasmic cell processes, similar to those of human osteoblasts in culture⁵⁰. Furthermore, these cells express several characteristic markers of osteoblasts, being positive for alkaline phosphatase (ALP), osteocalcin (OC), osteonectin, osteopontin, osteoprotegerin (OPG), collagen type I (COL I), bone morphogenetic proteins, collagen type III, bone sialoprotein and decorin. They have also been shown to express Runx-2, the earliest known transcription regulator of osteoblast differentiation and consequently demonstrated the commitment of these cells toward the osteogenic pathway^{50,51}.

In this experimental work, MG63 human osteoblast-like cells were cultured at a density of 10^4 cells/cm² on the surface of standard tissue culture plates. After 24 hours, the medium was removed and fresh complete culture medium, containing the appropriate concentration of sterilized HS or HS-AuNPs nanoparticles was added, and cultures were maintained for further 1, 3 and 7

days. The results regarding cell viability/proliferation (MTS assay) in presence of different concentration (1-500 $\mu\text{g/ml}$) of studied particles are shown in figure 5.7.

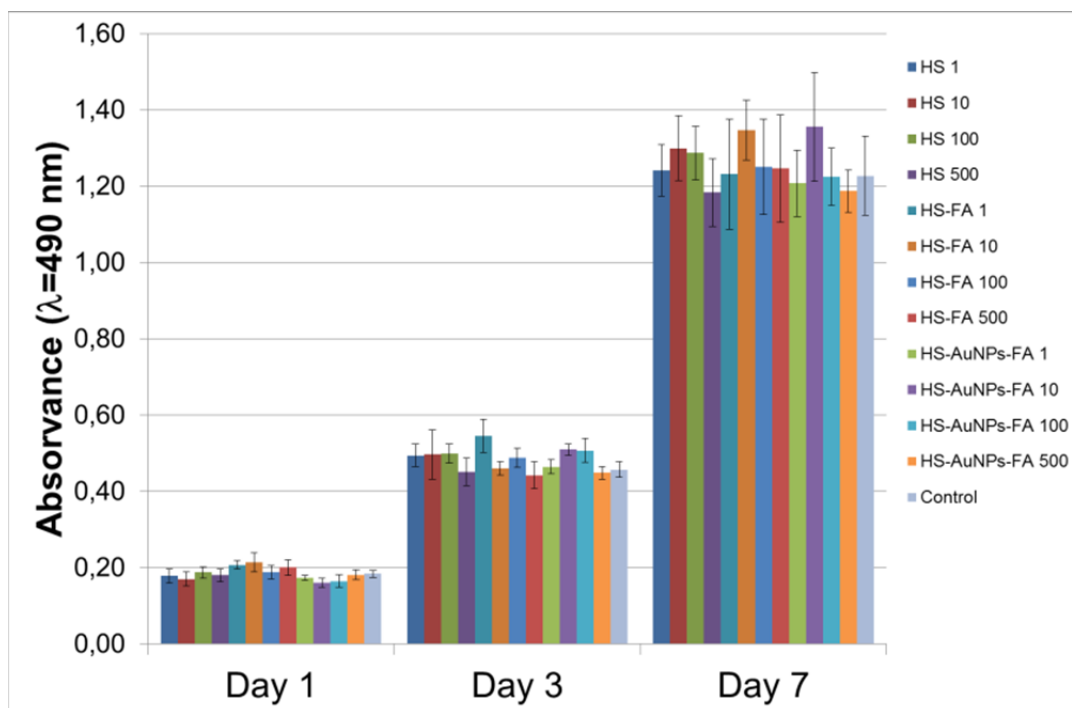


Figure 5.7- Cell viability/proliferation of MG63 cell cultures exposed to HS, HS-AuNPs and HS-AuNPs-FA nanoparticles, during 1, 3 and 7 days for a nanoparticles concentration range between (1-500 $\mu\text{g/ml}$). It can be seen that the cell viability remain high cells in presence of different particles.

MTS is metabolized to a purple formazan salt by mitochondrial enzymes in living cells and the absorbance read is proportional to the number of viable cells in the sample. Figure 5.7 shows the viability/proliferation of MG63 cell cultures after being exposed to HS and HS-AuNPs for different periods (1, 3 and 7 days). From the figure, it can be seen that the cells growing in the absence of nanoparticles (control) presented a high proliferation rate throughout the entire culture period (figure 5.7). Similarly, cultures established in the presence of HS or HS-AuNPs nanoparticles, at the assayed concentrations, revealed a similar behavior, which supports the non-cytotoxic behavior of the assayed particles, even to the relatively high dose of 500 $\mu\text{g/ml}$.

For more clearly determine cell viability in contact with the HS and HS-AuNPs, cell morphology studies were carried out. The cell morphology was addressed by confocal laser scanning microscope (CLSM) following staining for F-actin

cytoskeleton and nucleus counterstaining. Representative images of the established cultures for 1, 3 and 7 days are shown in figure 5.8, 5.9 and 5.10 respectively. Control cultures revealed, at day 1 (figure 5.8), that cells had spread out and presented an elongated morphology, establishing elementary cell-to-cell contacts; at day 3 (figure 5.9), areas of high cell density could already be visualized with confluent zones of intensive cell growth; at day 7 (figure 5.10), cells were organized in continuous cell multilayers. Cultures established with both nanoparticles (HS and HS-AuNPs), at the assayed concentration range (1-500 $\mu\text{m}/\text{ml}$), displayed a similar behavior to control regarding cell structural organization, staining intensity and morphological features, as addressed by CLSM (figure 5.8, 5.9 and 5.10).

These results reveal that the interaction between cells and the nanoparticles HS and HS-AuNPs is similar, which suggests that differences observed in particles are not sufficiently expressive to cause detectable effect on MG63 cells. However, those data converge to substantiate the cytocompatibility of the assessed particles, at the tested concentrations.

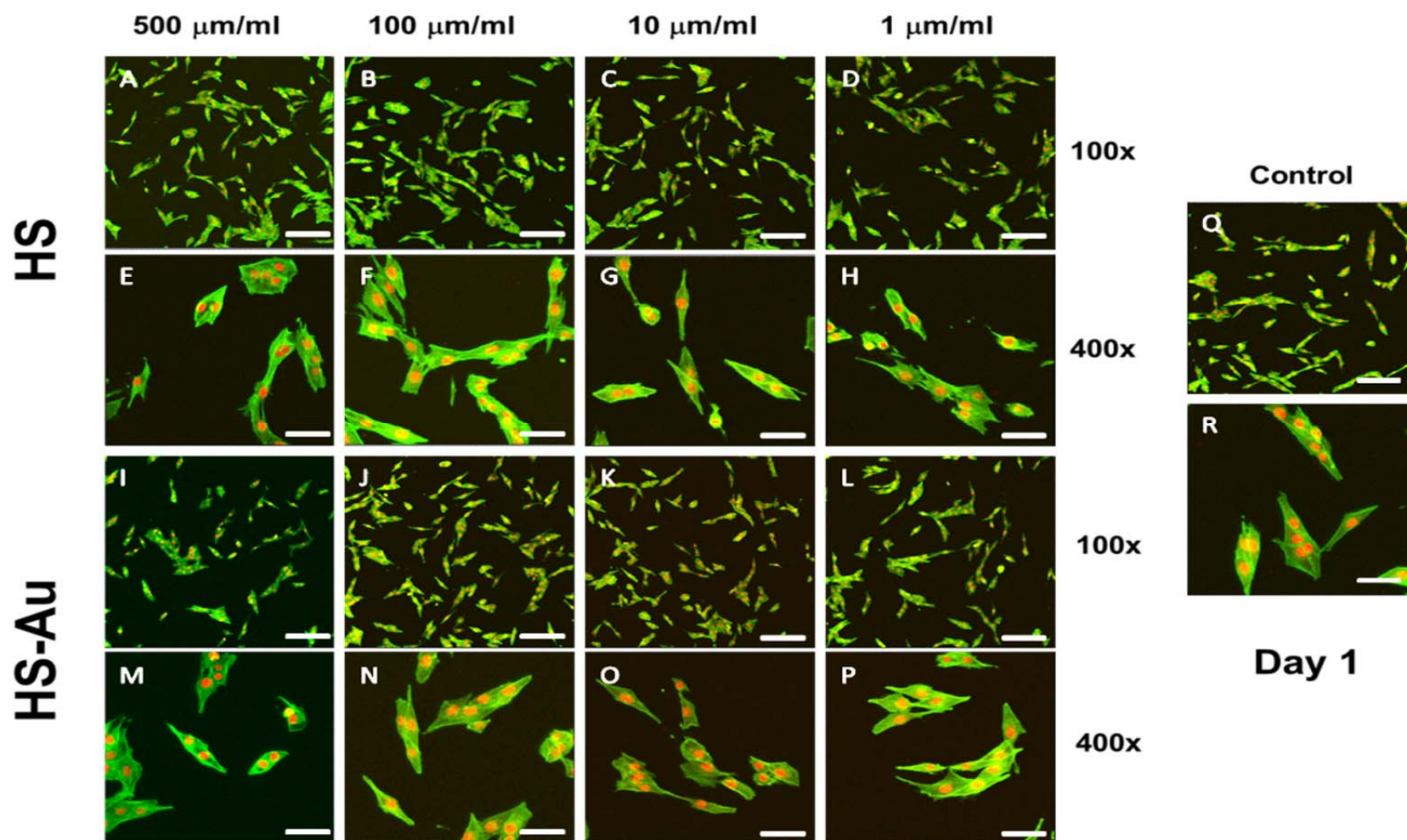


Figure 5.8- CLSM images of MG63 cell cultures exposed to the HS and HS-AuNPs, for a nanoparticles range concentration of 1-500 $\mu\text{g/ml}$, during 1 day.

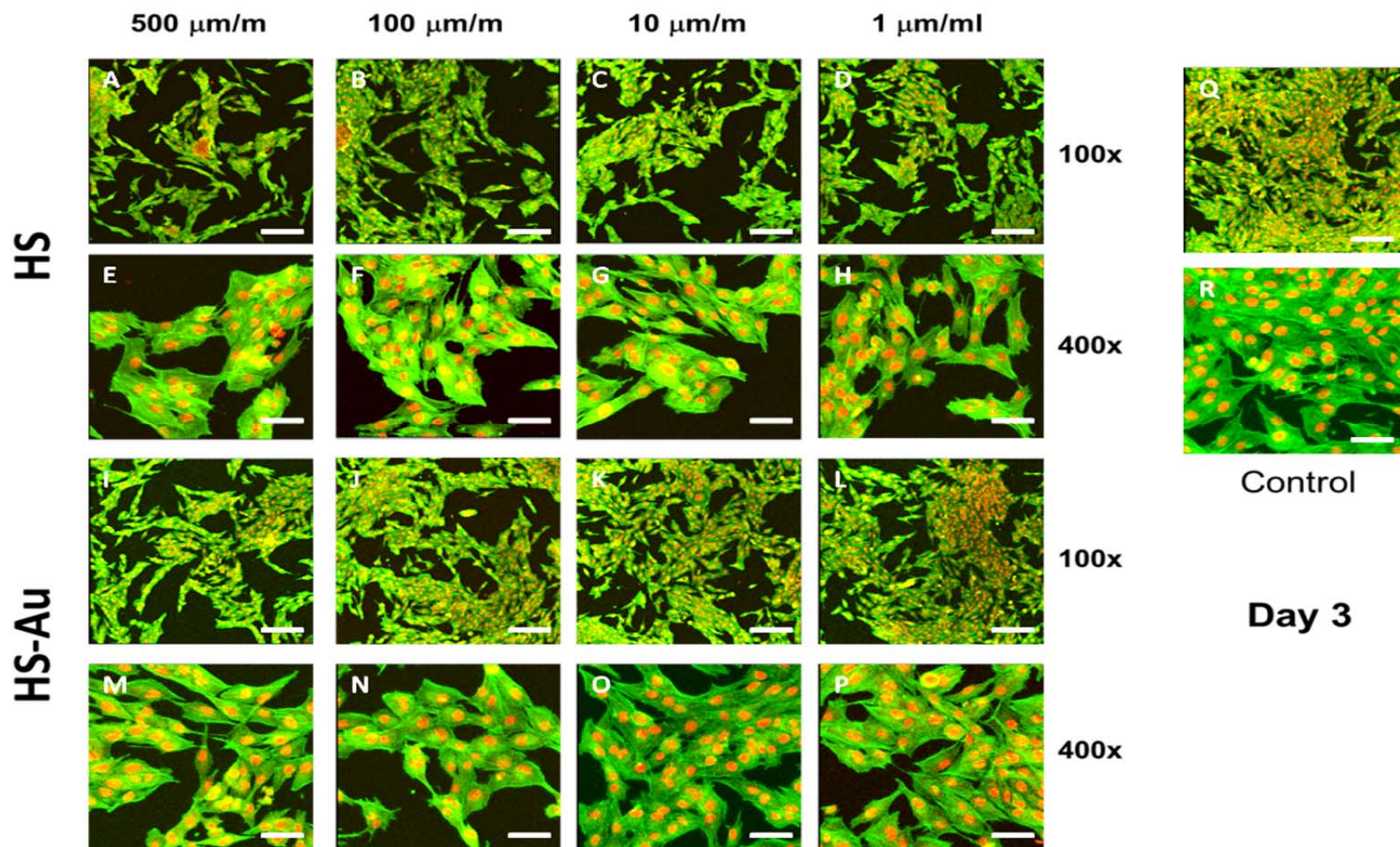


Figure 5.9- CLSM images of MG63 cell cultures exposed to the HS and HS-AuNPs, for a nanoparticles range concentration of 1-500 $\mu\text{g/ml}$, during 3 days.

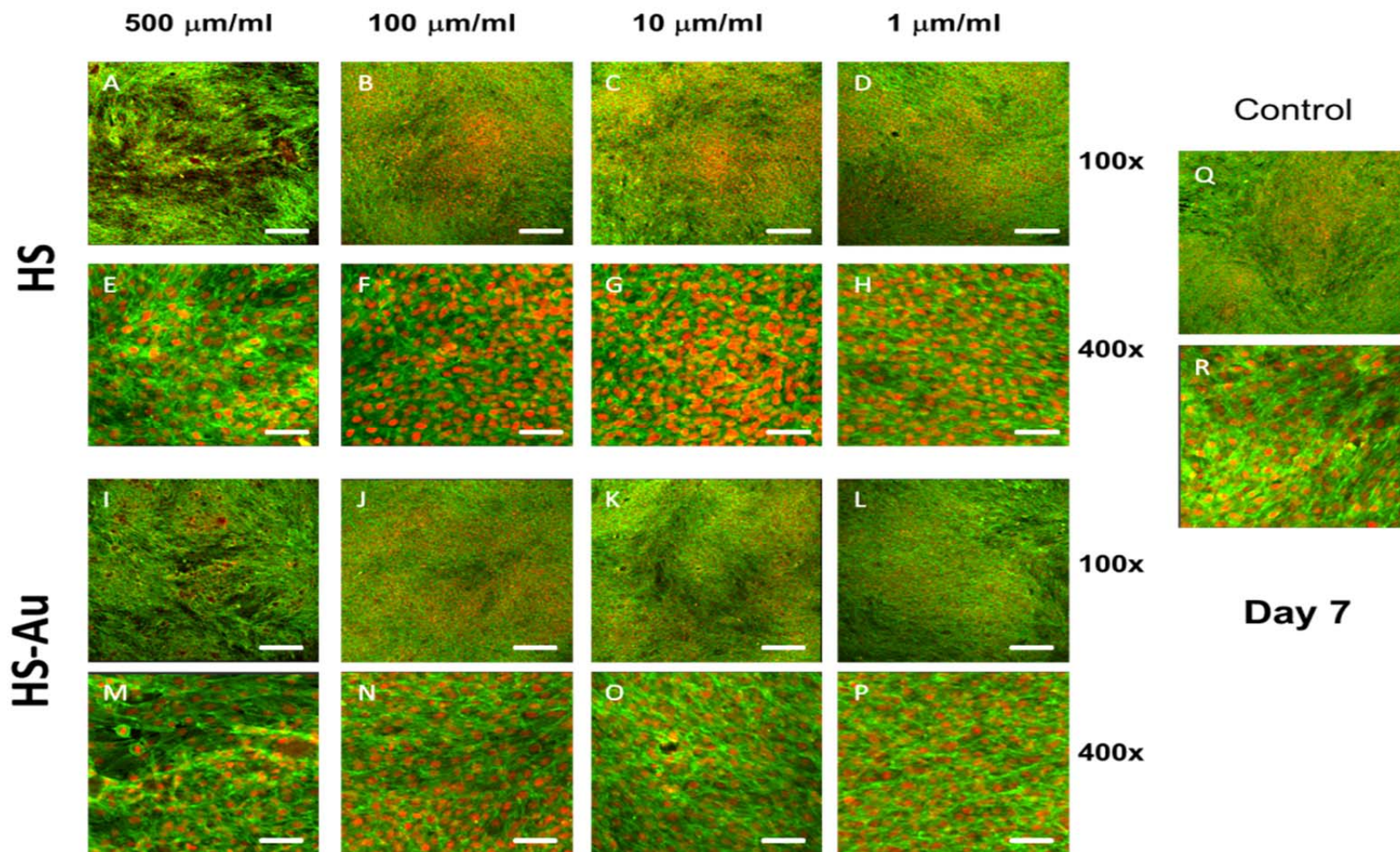


Figure 5.10- CLSM images of MG63 cell cultures exposed to the HS and HS-AuNPs, for a nanoparticles range concentration of 1-500 $\mu\text{g/ml}$, during 7 days.

Additionally gene expression by reverse-transcription polymerase chain reaction (RT-PCR) was performed to investigate the effect of HS and HS-AuNPs nanoparticle incorporation at various seeding densities on osteogenic signal expression. The effect of both HS and HS-AuNPs particles, at 100 $\mu\text{g/ml}$, was evaluated regarding the expression of osteoblastic-related markers, i.e., Runt-related transcription factor 2 (Runx-2), Collagen type I (Col I), alkaline phosphatase (ALP), osteocalcin (OC) and osteoprotegerin (OPG), as observed in figure 5.11.

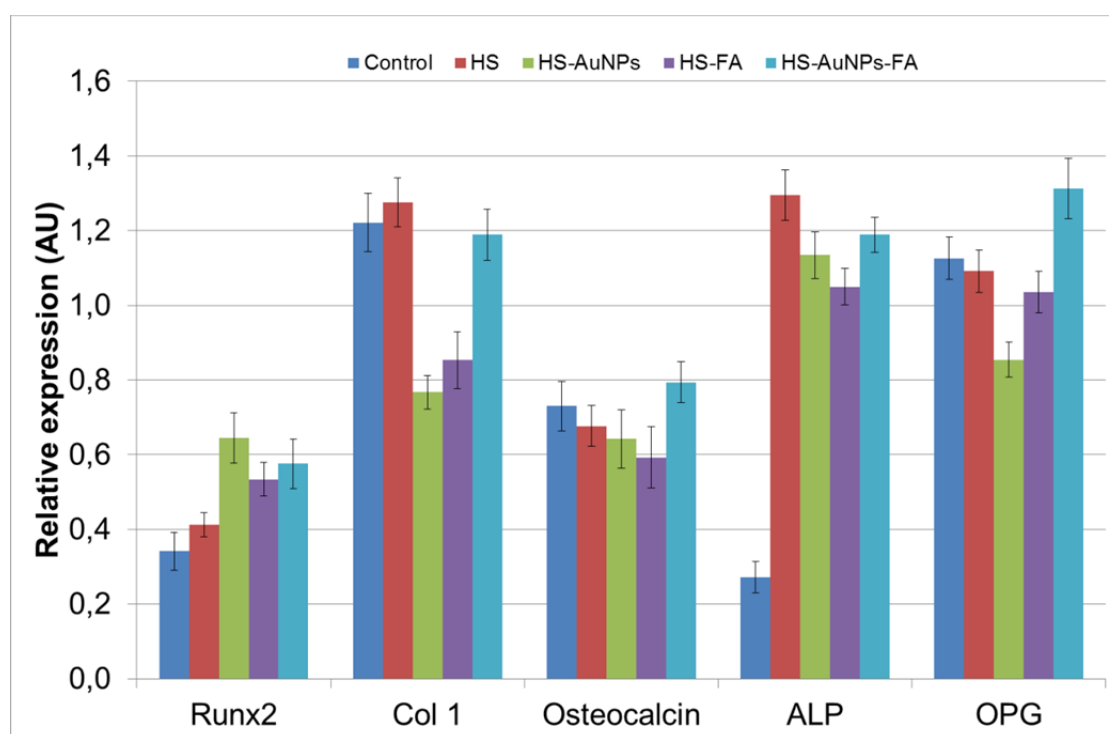


Figure 5.11- Gene expression of RUNX-2, Collagen I, ALP, OC and OPG of MG63 cell cultures exposed to HS, HS-AuNPs and HS-AuNPs-FA nanoparticles, 100 $\mu\text{g/ml}$, during three days. RT-PCR, the PCR products were subjected to a densitometric analysis and normalization to the corresponding GAPDH value.

Analyses of the expression pattern of regulating genes and bone-related proteins revealed three sequential stages during the proliferation and differentiation of human osteoblasts in vitro. These are cell proliferation, extracellular matrix formation and maturation, and extracellular matrix mineralization⁵². There seems to exist two check points to which the cells can progress but cannot develop further without additional signalization: the first

one occurs when proliferation is down-regulated and gene expression associated with the extracellular matrix maturation is induced; and the second when mineralization occurs⁵². Within these stages, actively proliferating Runx-2-expressing osteoblastic cells produce high levels of type I collagen, and a fibronectin- and osteonectin-rich extracellular matrix⁵³. The down-regulation of the proliferation period and the up-regulation of the matrix maturation and mineralization are marked by a temporal sequence of events in which there is an enhanced expression of ALP immediately following the proliferation period, and an increased expression of osteopontin and OC at the onset of mineralization⁵³. It is also suggested that ALP is highly expressed during the early matrix formation and maturation period, followed by a decrease in its activity. During the mineralization period, the expression of OC and the number of mineralization nodules are high^{52,53}.

MG63 human osteoblast-like cells exhibit many osteoblastic behaviors which are characteristic of bone forming cells. Assayed cultures, grown in the presence of 100 µg/ml HS nanoparticles, were shown to enhance the ALP expression, while cultures established in the presence of 100 µg/ml HS-AuNPs nanoparticles induced the expression of both Runx-2 and ALP. No significant differences were found regarding the expression of Col I, OC and OPG, in cultures established with HS particles and control (figure 5.11). However alterations on HS particles surface by the presence of AuNPs have shown major modifications on Col I and OPG expression.

ALP is an enzyme believed to provide inorganic phosphate for osteoblastic-mediated extracellular matrix mineralization process, and its expression is considered a hallmark of osteoblastic differentiation⁵². Both evaluated nanoparticles were shown to enhance the expression of this marker. This observation comes in line with several studies in which the presence of distinct Hap-based nanoparticles, incorporated into the culture microenvironment of osteoblastic and osteoblastic-like cells, seems to enhance the ALP expression in a concentration-dependent way^{54,55}.

Runx-2 is a master regulator of osteogenic gene expression and osteoblast differentiation, being essential for osteoblastic differentiation and bone formation^{52,56}. HS and HS-AuNPs nanoparticles induced the expression of this

transcription factor, substantiating the enhancing role of these nanoparticles in the osteoblastic differentiation process.

According to many reports AuNPs nanoparticles have been found to be “nontoxic”. For example using a human leukemia cell line, gold nanospheres of different sizes (4, 12, and 18 nm in diameter) and capping agents (citrate, cysteine, glucose, biotin, and cetyltrimethylammonium bromide) were found to be nontoxic based on the MTT assay for a concentration up to 25 μM ⁵⁷. Similar results were observed when studying immune system cell line response to AuNPs (spheres, 3.5 nm in diameter) ⁵⁸. In this study, AuNPs entered the cell by (presumably) endocytosis, did not induce any toxicity and reduced the level of reactive oxygen species. Villiers et al. studied the toxicity of citrate-capped AuNPs (spheres, 10 nm in diameter) on dendritic cells (cells of the human immune system that process and present antigens on their surfaces to other cells). They found that gold nanoparticles were not cytotoxic, did not induce cell activation, and did not change the gene and protein expression of the cells ⁵⁹. In contrast to these results, other research groups have found that AuNPs are “toxic”. For example, it was found that cationic quaternary ammonium functionalized gold nanospheres (2 nm in diameter) are toxic (at certain doses) and that the same nanoparticles when having negatively charged surface were not toxic at the same concentration and to the same cell line, i.e (Cos-1) ⁵⁷. This difference was explained by the ability of the cationic nanoparticles to interact with the negatively charged cellular membrane and disrupt the cell membrane ⁵⁷. Pan et al. found that 1.4-nm gold nanospheres triggered necrosis, mitochondrial damage, and induced an oxidative stress on all examined cell lines (HeLa cervix carcinoma epithelial cells) ⁶⁰. However the authors found no evidence of cellular damage for 15-nm gold nanospheres bearing the same surface group, i.e (with triphenylphosphine monosulfonate (TPPMS)) ⁶⁰. This result highlights a possible size-dependent toxicity of AuNPs ⁶⁰. Citrate-capped AuNPs (13 nm in diameter) were found to be toxic to a human carcinoma lung cell line but not to human liver carcinoma cell line at same dosage ⁶¹. These conflicting findings could arise from the variability of the studied cell lines, and nanoparticles chemical/physical properties. Furthermore, the dosing parameters and the exposure time of AuNPs to the cells in these studies vary, making it difficult to compare toxicity assays differently designed.

The promise of gold nanoparticles for many different biological applications has led to a strong interest to expose them to living systems. Studies involving AuNPs coupled with hydroxyapatite and their cellular toxicity are rare or even inexistent. For that reason the cellular toxicity of HS-AuNPs was addressed in this chapter. Though the obtained results allowed to conclude about a non-cytotoxic behavior of the assayed particles, even at a relatively high dose of 500 $\mu\text{g/ml}$, to contrast them truly with published data was unmanageable as studies of MG63 cell line response to similar particles (Hap-AuNPs) or to AuNP were not found so far.

5.5. Hap and Hap-AuNPs nanoparticles functionalized with folic acid, a cell membrane receptor

The focal objective of this section is to discuss the design of a folic acid-conjugated nanoparticle for the specific recognition of the soluble form of the folate receptor expressed at the surface of cells. The adsorption of folic acid (FA) on hydroxyapatite nanoparticles (HS) and hydroxyapatite-gold nanoparticles (HS-AuNPs 5 min) and their biological behaviour folic acid are here addressed.

5.5.1. Synthesis of folic-acid conjugated HS and HS-AuNPs

HS and HS-AuNPs are a convenient target for functionalization because they have a carboxylic acid-enriched surface which may provide a platform for efficient surface immobilization of functional molecules such as DNA, drugs, proteins and fluorescent molecules⁶²⁻⁶⁶. The synthesis of HS and HS-AuNPs nanoparticles was carried out by the hydrothermal method using citric acid as a tailoring agent of particle morphology and simultaneously as a reducing agent of gold ions, as described previously. The ability of HS and HS-AuNPS surfaces enriched with citrate derived species for immobilizing FA is schematically expressed on figure 5.12.

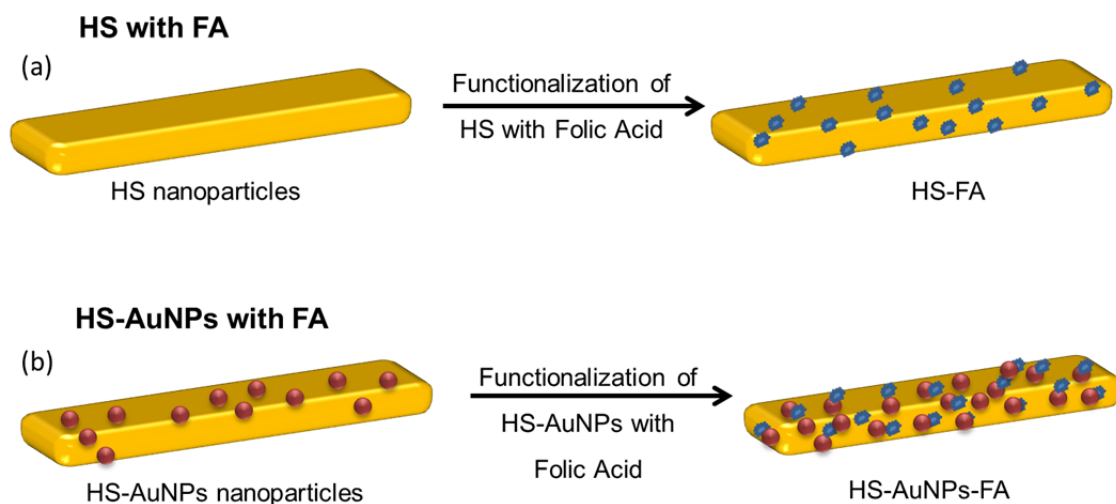


Fig.5.12- Schematic representation of (a) HapNPs (HS) and (b) HapNPs with gold (HS-AuNPs), both functionalized with folic acid (FA).

Figure 5.13 ((a) and (b)) displays TEM micrographs of HS-FA and HS- AuNPs-FA nanoparticles. As evidenced the shape and size of the particles exposed to folic acid were maintained. It is important in drug delivery applications that nanoparticles are individually dispersed, as observed in figure 5.13 ((a) and (b)), because aggregation of nanoparticles makes difficult the transport of drug-loaded nanoparticles to the desired site. Additionally it is observed that gold nanoparticles present in the HS-AuNPs nanoparticles are kept after FA adsorption experiments thus suggesting that gold nanoparticles are strongly bonded to HS particles.

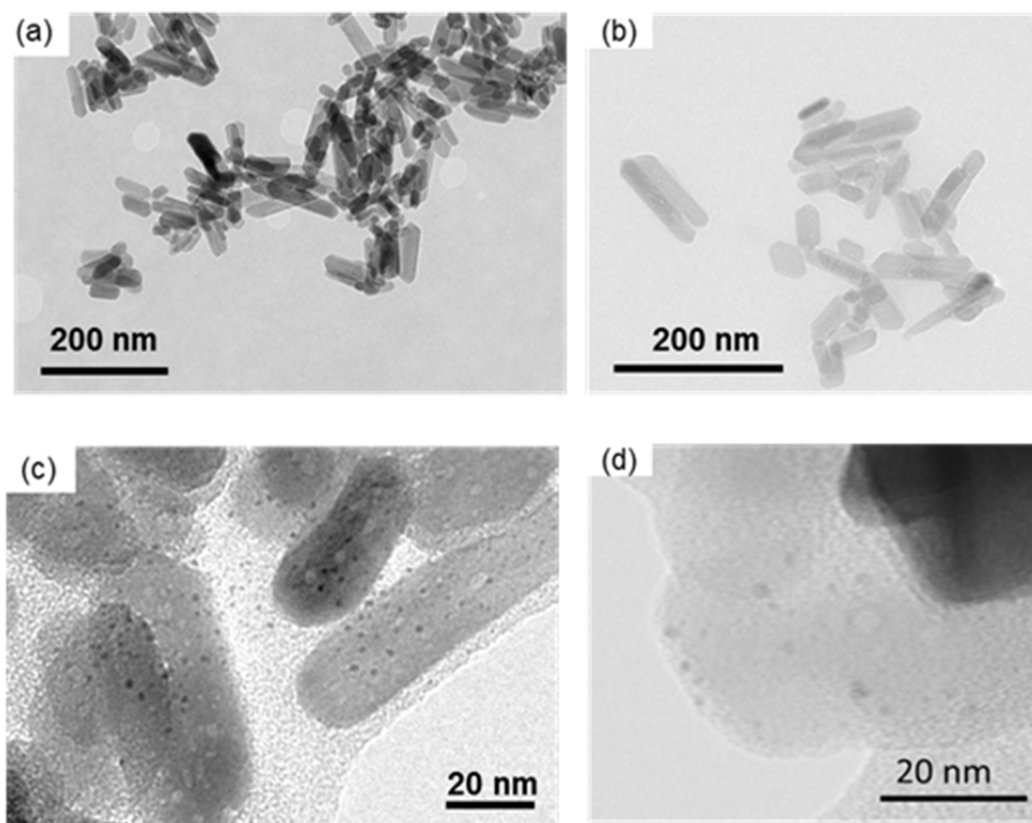


Figure 5.13- TEM micrographs of HS (a); HS-FA (b); HS-AuNPs (c) and HS-AuNPs-FA (d).

The evaluation of drug loaded amounts is an important issue for the sake of engineering drug delivery systems able to supply the required drug dose at the target site. In the present work the maximum FA loaded amount was assessed after the time period required for the loaded particles to display a constant UV absorbance measured at 295 nm. The amount of loaded FA after 2 days was evaluated as 8.5×10^{-5} mol/gram FA for HS nanoparticles and as 1.09×10^{-4} mol/gram FA for HS-AuNPs. As the amounts of FA loaded on HS-AuNPs are higher than on HS, FA binding to Hap particle surface is likely conditioned by the nanoparticles surface chemistry. Comparison of these loaded FA values with literature data is hardly feasible as the published values correspond to FA measurements on supernatant suspension and spectrophotometrically analyzed while in this work Hap particles are dissolved in acid solution in which FA is assayed thus allowing the FA amount effectively loaded on Hap particles to be determined^{15,67,68}. The attachment of FA to HS and HS-AuNPs was further assessed by FTIR analysis.

Figure 5.14 compares the FTIR spectrum of FA to that of unloaded (HS, and HS-AuNPs) and of loaded particles (HS-FA and HS-AuNPs-FA). The FTIR spectrum of pure folic acid displays characteristic bands at 3543, 3416, 3324, 2959, 2924, 2844, 1694, 1640, 1605, 1484 and 1411 cm^{-1} ⁶⁹⁻⁷¹. The bands lying between 3600 and 3000 cm^{-1} are attributed to the hydroxyl (OH) stretching and NH stretching vibrations. Another two bands identified as $\nu(\text{C-H})$ and $\nu_s(\text{C-H})$ of structural unit CH_2 of FA are detected at 2844 cm^{-1} and 2959 cm^{-1} ^{79,80}. The C=O bond stretching vibration of carboxyl group is detected at 1694 cm^{-1} , while the stretching vibration of the C=O bond of $-\text{CONH}_2$ group appears at 1640 cm^{-1} . The band at 1605 cm^{-1} accounts for the bending mode vibration of NH_2 while the stretching vibration (O-H) of OH phenyl skeleton is revealed by the band at 1411 cm^{-1} ⁶⁹⁻⁷¹. Furthermore two other bands at 1346 cm^{-1} and 1450 cm^{-1} are assigned to the aromatic C-H in plane bending¹⁴ and to the stretching vibration of C=C in the backbone of the aromatic ring, respectively⁶⁹.

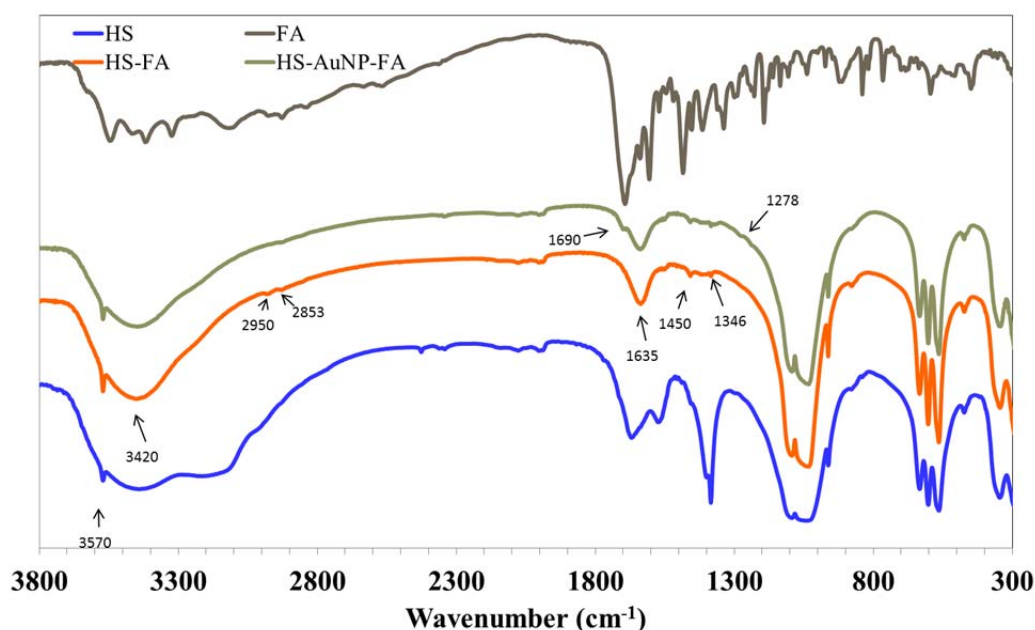


Figure 5.14- FTIR spectra of (—) HS nanoparticles, (—) HS-FA nanoparticles, (—) HS-AuNPs-FA nanoparticles and (—) FA.

As expected the main vibrations assigned to hydroxyapatite are found on all the spectra corresponding to the different types of particles (HS, HS-FA and HS-AuNP-FA) (figure 5.14). The main differences are noticed in the spectral region of 1200-1700 cm^{-1} where the bands detected at 1384, 1402 and 1670 cm^{-1} in

HS FTIR spectrum become absent after exposing HS and HS-AuNPs to the FA solution. Such bands were previously attributed (see discussion in chapter 3), to the vibrations of carboxylic groups differently coordinated to Hap surface. Some of these species seem weakly bound to particles surface and easily desorb during FA loading and/ or get involved in FA conjugation process^{69,71,72}. That is the case of HS-FA and HS-AuNPs-FA that have lost the two intense bands at 1384 cm^{-1} and 1670 cm^{-1} , assigned respectively to $-\text{CH}_2-$ scissoring mode and to C=O stretching of carbonyl containing species.

Looking for evidences of FA conjugation to HS particles, it is noticed that three characteristic bands of FA appearing at 1640 , 1450 and 1346 cm^{-1} are detected on HS-FA and HS-AuNPs-FA spectra. In addition, two small bands in HS-FA nanoparticles at 2959 cm^{-1} and 2844 cm^{-1} , and one a 1694 cm^{-1} in HS-AuNPs, both pertaining to FA are also observed. The presence of these bands is indicative of the successful binding of FA to nanoparticle surface. Nevertheless the chemical binding of FA to both HS and HS-AuNPs surfaces seems to involve different chemical species, probably reflecting the contribution of different pre-adsorbed chemical species on both Hap nanoparticles surface. Several reports on FA conjugation with polymer or metallic nanoparticles, as gold, are found in literature. However in all the reported studies and depending on the nature of the nanoparticles the particles are firstly functionalized with diverse molecules to facilitate FA uptake. In most of the cases the molecules used have an N group in a terminal position allowing the connection of FA to these nanoparticles in an easy way. In our case it was not used any molecule to make the attachment of folic acid to the surface of the HS or HS-AuNPs, although the results seem to indicate that the presence of gold at the surface of the HS particles facilitates the uptake of the FA. Therefore it may be suggested that the precipitation of the gold has resulted in a "reconstruction" or rearrangement of the surface of the HS particles which facilitated the FA attachment. This rearrangement may have been configured by the precipitation of the gold on the surface of HS leaving the surface of the HS particles chemically altered.

5.6. Interaction of HS-FA and HS-AuNPs-FA with osteoblastic cells

Nanotoxicity is a major issue that limits the practical clinical applicability of most nano-contrast agents reported so far. Considering this important matter, the toxicity of different Hap samples on human osteosarcoma-derived MG63 osteoblastic-like cell was tested. As previously shown HS and HS-AuNPs nanoparticles have no significant cytotoxicity. The cytotoxicity of the HS-FA and HS-AuNPs-FA was also evaluated by a MTS assay after incubation with nanoparticles for 1, 3 and 7 days, respectively. Figure 5.7 depicts the comparison of Hap nanoparticles effects on cells viability, for different particles concentrations. No significant cell viability difference is found on HS-FA and HS-AuNPs-FA nanoparticle treated cells as compared to the control (cells without nanoparticles). MG63 cell viability remained high after cell incubation with HS-FA and HS-AuNPs-FA for 7 days, implying that those particles are biocompatible and safe at a concentration below 500 $\mu\text{g/mL}$ and thus can be used for biomedical purposes. Anusha Ashokan et al. studied the toxicity of Hap nanoparticles doped with Eu^{3+} (hexagonal crystals) and functionalized with FA on primary human endothelial cells (HUVEC) and various cell lines including normal mouse lung fibroblast cell line (L929), human nasopharyngeal carcinoma (KB) and human lung cancer cell line (A549). They found that nanoparticles revealed no apparent toxicity even up to relatively high doses of 500 $\mu\text{g/mL}$ and 48 h of incubation⁷³ which is in accordance with the results presented in this thesis.

Following RNA extraction of MG63 cells that had been cultivated without nanoparticles (control) or with HS-FA and HS-AuNPs-FA, expression levels of Runx-2, ALP, Col I, OC, OPG gene were determined via RT-PCR (figure 5.11). Transcription of the housekeeping gene GAPDH was used as reference. The biocompatibility of HS and HS-AuNPs in absence of FA in this cell line had already been demonstrated previously. Comparing the gene expression of HS-FA with the control and HS it is observed that the presence of FA stimulates Runx-2 but reduces the expression of Col I. The other expressed genes remained unchanged. Col I is an essential component of the extracellular matrix, constituting approximately 90% of the total organic matrix in mature

bone. Together with the mineral component, collagen governs the mechanical properties and functional integrity of the osseous tissue. From a number of *in vitro* studies, Col I had been proposed to induce osteoblast differentiation and facilitate mineralization⁷⁴. Additionally as mentioned previously Runx-2 is a master regulator of osteogenic gene expression and osteoblast differentiation, being essential for bone formation. The conjugation of the two opposite effects on genetic transcription seems not to affect the viability of the cells in presence of hydroxyapatite functionalized with folic acid although not contributing to an easy mineralization.

When gold nanoparticles are coupled on HS surface (HS-AuNPs-FA) gene expression results are closer to the control with exception of OPG, as observed in figure 5.11. The presence of FA on HS-AuNPs stimulates the OPG transcription. There are few studies in literature reporting the combination of FA and hydroxyapatite but not its effects on genetic expression. However earlier studies on biosilica led to observe a stimulated OPG transcription⁷⁵. Some studies have shown that mice over-expressing OPG had high bone mass and those without OPG had very low bone mass⁷⁶. OPG has been identified to be one of the most crucial signaling systems that mediate and modulate bone resorption^{75,76}. Hence, the data obtained in the present study suggest that HS-AuNPs functionalized with folic acid result in a strongly enhancement of the expression of genes tested, being this expression similar to or higher than that evidenced by particles HS. These findings point out those nanoparticles (HS-AuNPs-FA) with a considerable biomedical potential for the treatment of osteoporosis disorders.

Moreover, and in order to detail the mechanisms involved in the nanoparticle-mediated osteogenic induction of the established cell cultures, a further step of this research could account for the assessment of the more relevant signalling pathways involved. Thus, the cellular function, in terms of functional activity, could be evaluated in the presence of specific inhibitors of relevant osteogenic signalling pathways, in order to clearly differentiate the most significant ones involved in the induction of the osteogenic process.

Osteoblastogenesis and bone formation are regulated by hormones, growth factors, cytokines, mechanical loading and aging. Osteoblasts can sense these external cues, transduce the signals through various signalling pathways and

regulate the expression of specific genes, to determine cellular fate ⁷⁷. Relevant cellular signalling mechanisms within the osteoblastic cell function are expected to include early electrophysiological signals, possibly associated with integrin receptors and ionic channels, followed by activation of the intracellular signalling pathways ⁷⁸. The most relevant ones seem to be those such as mitogen-activated protein kinase (MAPK), c-Jun N-terminal kinases (JNK), p38, nuclear factor kappa-light-chain-enhancer of activated B cells (NF- κ B), calcium sensing receptor, Wnt/ β -Catenin and protein kinase C ⁷⁹. The activation of these mechanisms can then act to regulate the activity and transcription levels of various transcription factors (e.g., Runx-2) involved in the regulation of the cell survival, commitment and differentiation. The activation of these pathways has been found to broadly mediate the up-regulation of significant osteogenic markers such as collagen type I, alkaline phosphatase, osteocalcin and osteoprotegerin, in a process mediated, at least in part, by Runx-2 induction ⁷⁷⁻⁷⁹.

This mechanistic approach would allow a more complete understanding of the nanoparticle-mediated induction of the osteogenic phenotype and further enhance their potential impact on the development of therapeutic strategies to improve human bone health.

From the obtained results it is worthy emphasizing that HS or HS-AuNPs functionalized with FA have a strong influence on osteogenic signal expression. Additionally the presented studies confirm that HS nanoparticles coupled with gold and functionalized with FA are non-toxic, apparently without adverse effects on the cellular functions, which is an essential pre-requisite for an ideal diagnostic agent.

The present chapter allows concluding that gold (Au) nanoparticles were successful precipitated on HS surface. Spherical Au particles with few nanometers are synthesized after 5 min which size increases with the reaction time though keeping a spherical shape with nanometric dimension.

Carboxylate groups remaining from HS synthesis process play a crucial role in the chemical reaction process involved in AuNPs nanoparticles precipitation.

The study of the biological behaviour of the synthesized nanoparticles has demonstrated that HS and HS-AuNPs do not display severe cytotoxic effects on MG63 cells. Furthermore osteoblastic differentiation was facilitated by the

incorporation of Hap particles on cellular medium since a high proliferation is detected. It was also clearly shown that the presence of HS nanoparticles induce a higher proliferation rate and as well an enhancement of osteogenic parameters of MG63 cells compared to HS-AuNPs nanoparticles, with the exception of Runx-2 gene which is more pronounced in HS-AuNPs than in HS. Finally, a folic acid (FA) based formulation was found based on HS nanoparticles and HS- AuNPs through a facile technique of adsorption. UV and FTIR characterization confirmed the adsorption/functionalization of HS and HS-AuNPs nanoparticles with folic acid. Moreover it was concluded that HS-AuNPs provide better surface conditions for FA conjugation than HS nanoparticles. The functionalization of nanoparticles with FA does not produce significant effects on cell viability even at high particle concentrations. Furthermore, it was established that with exception of Col I all gene expression are enhanced in presence of functionalized nanoparticles. Considering the osteogenic signal expression it can be concluded that depending on the HS functionalization (with gold and/or FA) an enhancement or reduction of the genes expression could be observed, which may condition or be a plus depending on the desired application.

5.7. References

- 1 Lee, Dong-Eun; Koo, Heebeom; Sun, In-Cheol; Ryu, Ju Hee; Kim, Kwangmeyung and Kwon, Ick Chan. "Multifunctional nanoparticles for multimodal imaging and theragnosis". *Chemical Society Reviews* **41**, 2656-2672, (2012).
- 2 Fang, Chen and Zhang, Miqin. "Nanoparticle-based theragnostics: Integrating diagnostic and therapeutic potentials in nanomedicine". *Journal of Controlled Release* **146**, 2-5, (2010).
- 3 Kim, Kwangmeyung; Kim, Jong Ho; Park, Hyungkyu; Kim, Yoo-Shin; Park, Kyeongsoon; Nam, Heayun; Lee, Seulki; Park, Jae Hyung; Park, Rang-Woon; Kim, In-San; Choi, Kuiwon; Kim, Sang Yoon; Park, Kinam and Kwon, Ick Chan. "Tumor-homing multifunctional nanoparticles for cancer theragnosis: Simultaneous diagnosis, drug delivery, and therapeutic monitoring". *Journal of Controlled Release* **146**, 219-227, (2010).
- 4 Min, Kyung Hyun; Kim, Jong-Ho; Bae, Sang Mun; Shin, Hyeri; Kim, Min Sang; Park, Sangjin; Lee, Hyejung; Park, Rang-Woon; Kim, In-San; Kim, Kwangmeyung; Kwon, Ick Chan; Jeong, Seo Young and Lee, Doo Sung. "Tumoral acidic pH-responsive MPEG-poly(β -amino ester) polymeric micelles for cancer targeting therapy". *Journal of Controlled Release* **144**, 259-266, (2010).

- 5 Qian, X. M and Nie, S. M. "Single-molecule and single-nanoparticle SERS: from fundamental mechanisms to biomedical applications". *Chemical Society Reviews* **37**, 912-920, (2008).
- 6 Dreaden, Erik C.; Alkilany, Alaaldin M.; Huang, Xiaohua; Murphy, Catherine J. and El-Sayed, Mostafa A. "The golden age: gold nanoparticles for biomedicine". *Chem. Soc. Rev.* **41**, 2740-2779, (2012).
- 7 Ji, Shun-rong; Liu, Chen; Zhang, Bo; Yang, Feng; Xu, Jin; Long, Jiang; Jin, Chen; Fu, De-liang; Ni, Quan-xing and Yu, Xian-jun. "Carbon nanotubes in cancer diagnosis and therapy". *Biochimica et Biophysica Acta (BBA)-Reviews on Cancer* **1806**, 29-35, (2010).
- 8 Benezra, Miriam; Penate-Medina, Oula; Zanzonico, Pat B.; Schaer, David; Ow, Hooisweng; Burns, Andrew; DeStanchina, Elisa; Longo, Valerie; Herz, Erik; Iyer, Srikant; Wolchok, Jedd; Larson, Steven M.; Wiesner, Ulrich and Bradbury, Michelle S. "Multimodal silica nanoparticles are effective cancer-targeted probes in a model of human melanoma". *J Clin Invest.* **121**, 2768-2780, (2011).
- 9 Matthew, J. Olszta; Xingguo, Cheng; Sang Soo, Jee; Rajendra, Kumar; Yi-Yeoun, Kim; Michael, J. Kaufman; Elliot, P. Douglas and Laurie, B. Gower. "Bone structure and formation: A new perspective". *Materials Science and Engineering R: Reports* **58**, 77-116, (2007).
- 10 Yanjun, Ding; Jia, Liu; Hua, Wang; Guoli, Shen and Ruqin, Yu. "A piezoelectric immunosensor for the detection of α -fetoprotein using an interface of gold/hydroxyapatite hybrid nanomaterial". *Biomaterials* **28**, 2147-2154, (2007).
- 11 Fanhan, Y. i -; Nopphawan, Phothammachai; Kanaparthiramesh; Ziyizhong and Tim, White. "Removing Organic Compounds from Aqueous Medium via Wet Peroxidation by Gold Catalysts". *Environ. Sci. Technol.* **42**, 908-912, (2008).
- 12 Santos, C.; Gomes, P.S.; Duarte, J.A.; Franke, R.P.; Almeida, M. M.; Costa, M. E. V. and Fernandes, M.H. "Relevance of the sterilization-induced effects on the properties of different hydroxyapatite nanoparticles and assessment of the osteoblastic cell response". *Journal of the Royal Society Interface* **accepted**, (2012).
- 13 Liu, DanDan; Zhang, JinChao; Yi, ChangQing and Yang, MengSu. "The effects of gold nanoparticles on the proliferation, differentiation, and mineralization function of MC3T3-E1 cells *in vitro*". *Chinese Science Bulletin* **55**, 1013-1019, (2010).
- 14 Retnakumari, Archana and al., Et. "Molecular-receptor-specific, non-toxic, near-infrared-emitting Au cluster-protein nanoconjugates for targeted cancer imaging". *Nanotechnology* **21**, 055103, (2010).
- 15 Sreeja, Narayanan; Binulal, N. S.; Ullas, Mony; Koyakutty, Manzoor; Shantikumar, Nair and Deepthy Menon. "Folate targeted polymeric 'green' nanotherapy for cancer". *Nanotechnology* **21**, 1-13, (2010).
- 16 Xiaohua, Huang and Mostafa, A. El-Sayed. "Gold nanoparticles: Optical properties and implementations in cancer diagnosis and photothermal therap". *Journal of Advanced Research* **1**, 13-28, (2010).

- 17 Sujatha, K. Arumugam; Rajam, A. Merlin; N.Natarajan; Urmila, Rao; C.Rose and T.P.Sastry. "Formation of gold nanoparticles on Hydroxyapatite surface for enhancement of blood compatibility via a Negative cilia concept". *Journal of Biomedical Nanotechnology* **2**, 46-52, (2006).
- 18 Wissanu, Patungwasa and Jos., H. Hodak. "pH tunable morphology of the gold nanoparticles produced by citrate reduction". *Materials Chemistry and Physics* **108**, 45-54, (2008).
- 19 Hannon, J. B.; Kodambaka, S.; Ross, F. M. and Tromp, R. M. "The influence of the surface migration of gold on the growth of silicon nanowires". *Nature* **440**, 69-71, (2006).
- 20 Beszeda, I; Gontier-Moya, E.G and Imre, Á W. "Surface Ostwald-ripening and evaporation of gold beaded films on sapphire". *Applied Physics A: Materials Science & Processing* **81**, 673-677, (2005).
- 21 Yonglan, Luo. "One-step preparation of gold nanoparticles with different size distribution". *Materials Letters* **61**, 1039-1041, (2007).
- 22 Murphy, Catherine J; Gole, Anand M; Stone, John W; Sisco, Patrick N; Alkilany, Alaaldin M; Goldsmith, Edie C and Baxter, Sarah C. "Gold Nanoparticles in Biology: Beyond Toxicity to Cellular Imaging". *Accounts of Chemical Research* **41**, 1721-1730, (2008).
- 23 Sastry, T. P.; J.Sandaraseelan; K.Swarnalatha; Sobhana, S. S. Liji; Makheswari, M. Uma; Sekar, S. and Mandal, A. B. "Growth of hydroxyapatite on physiologically clotted fibrin capped gold nanoparticles". *Nanotechnology* **19**, 245604-245609, (2008).
- 24 Santosh, Aryal; Remant Bahadur, K. C.; Shanta Raj, Bhattarai; P.Prabu and Hak Yong, Kim. "Immobilization of collagen on gold nanoparticles: preparation, characterization, and hydroxyapatite growth". *J.Mater.Chem* **16**, 4642-4648, (2006).
- 25 Yogita, Gupta; G.N.Mathur and Sandeep, Verma. "Biomimetic synthesis and ultrastructural characterization of a zerovalent gold-hydroxyapatite composite". *Bioorganic & Medicinal Chemistry Letters* **16**, 363-366, (2006).
- 26 Palraj, Kalimuthu and John, S. Abraham. "Studies on ligand exchange reaction of functionalized mercaptothiadiazole compounds onto citrate capped gold nanoparticles". *Materials Chemistry and Physics* **122**, 380-385, (2010).
- 27 Dietmar, Holzmann; Dieter, Holzinger; Guten, Hesser; Thomas, Schmidt and Gunther, Knor. "Hydroxyapatite nanoparticles as novel low-refractive index additives for the long-term UV-photoprotection of transparent composite materials". *Journal of Materials Chemistry* **19**, 8102-8106, (2009).
- 28 Xiaohua, Huang; Prashant, K. Jain; Ivan, H. El-Sayed and Mostafa, A. El-Sayed. "Plasmonic photothermal therapy (PPTT) using gold nanoparticles". *Lasers Med Sci* **23**, 217-228, (2008).
- 29 Prashant, k Jain; Xiaohua, Huang; Ivan, H. El-Sayed and Mostafa, A. El-Sayed. "Review of some interesting surface plasmon resonance-enhanced properties

- of noble metal nanoparticles and their applications to biosystems". *Plasmonics* **2**, 107-118, (2007).
- 30 Masaharu, Tsuji; Nobuhiro, Miyamae; Masayuki, Hashimoto; Michiko, Nishio; Sachie, Hikino; Naoki, Ishigami and Izumi, Tanaka. "Shape and size controlled synthesis of gold nanocrystals using oxidative etching by AuCl⁻¹ and Cl⁻ anions in microwave-polyol process". *Colloids and Surfaces A: Physicochem.Eng.Aspects* **302**, 587-598, (2007).
 - 31 Frank, Caruso; Marina, Spasova; Verónica, Salgueirino-Maceira and Luis, M. Liz-Marzán. "Multilayer Assemblies of Silica-Encapsulated Gold Nanoparticles on Decomposable Colloid Templates". *Advanced Materials* **13**, 1090-1094, (2001).
 - 32 Zhuyuan, Wang; Shenfei, Zong; Jing, Yang; Jin, Li and Yiping, Cui. "Dual-mode probe based on mesoporous silica coated gold nanorods for targeting cancer cells". *Biosensors and Bioelectronics* **26**, 2883-2889, (2011).
 - 33 Melanie, Bradley and Beatriz Sanchez, Garcia-Risueño. "Symmetric and asymmetric adsorption of pH-responsive gold nanoparticles onto microgel particles and dispersion characterisation". *Journal of Colloid and Interface Science* **355**, 321-327, (2011).
 - 34 Weibo, Cai; Ting, Gao; Hao, Hong and Jiangtao, Sun. "Applications of gold nanoparticles in cancer nanotechnology". *Nanotechnology, Science and Applications* **1**, 17-32, (2008).
 - 35 Ross, Ryan D and Roeder, Ryan K. "Binding affinity of surface functionalized gold nanoparticles to hydroxyapatite". *Journal of Biomedical Materials Research Part A* **99A**, 58-66, (2011).
 - 36 Zhenyuan, Zhang; Ryan, D. Ross and Ryan, K. Roeder. "Preparation of functionalized gold nanoparticles as a targeted X-ray contrast agent for damaged bone tissue". *Nanoscale* **2**, 582-586, (2010).
 - 37 Alkilany, Alaaldin M; Lohse, Samuel E and Murphy, Catherine J. "The Gold Standard: Gold Nanoparticle Libraries To Understand the Nano-Bio Interface". *Accounts of Chemical Research*, (2012).
 - 38 Zhu, Aiping; Lu, Yan; Si, Yunfeng and Dai, Sheng. "Fabricating hydroxyapatite nanorods using a biomacromolecule template". *Applied Surface Science* **257**, 3174-3179, (2011).
 - 39 Fleet, Michael E. "Infrared spectra of carbonate apatites: ν_2 - Region bands". *Biomaterials* **30**, 1473-1481, (2009).
 - 40 K. Van, Werde; D. Mondelaers; G. Vanhoyland; D. Nelis; M.K. Van, Bael; J. Mullens and L.C. Van, Poucke. "Thermal decomposition of the ammonium zinc acetate citrate precursor for aqueous chemical solution deposition of ZnO". *Journal of Materials Science* **37**, 81-88, (2002).
 - 41 M.S. Bootharaju and T. Pradeep. "Uptake of Toxic Metal Ions from Water by Naked and Monolayer Protected Silver Nanoparticles: An X-ray Photoelectron Spectroscopic Investigation". *J. Phys. Chem. C* **114**, 8328-8336, (2010).

- 42 Velasquez, J; Pillai, E. D; Carnegie, P. D and Duncan, M. A. "IR Spectroscopy of M+(Acetone) Complexes (M = Mg, Al, Ca): Cation–Carbonyl Binding Interactions". *The Journal of Physical Chemistry A* **110**, 2325-2330, (2006).
- 43 Sanjeev, Kumar; K.S.Gandhi and R.Kumar. "Modeling of formation of gold nanoparticles by citrate reduction". *Ind.Eng.Chem.Res.* **46**, 3128-3136, (2007).
- 44 M.A.Martins; C.Santos; M.M.Almeida and M.E.V.Costa. "Hydroxyapatite micro- and nanoparticles: nucleation and growth mechanisms in the presence of citrate species". *Journal of Colloid and Interface Science* **318**, 210-216, (2008).
- 45 Doostmohammadi, Ali; Monshi, Ahmad; Salehi, Rasoul; Fathi, M. H.; Karbasi, Saeed; Pieleles, Uwe and Daniels, A. U. "Preparation, chemistry and physical properties of bone-derived hydroxyapatite particles having a negative zeta potential". *Materials Chemistry and Physics* **132**, 446-452, (2012).
- 46 Vučinić, Dušica R; Radulović, Dragan S and Deušić, Slaven D. "Electrokinetic properties of hydroxyapatite under flotation conditions". *Journal of Colloid and Interface Science* **343**, 239-245, (2010).
- 47 Chen, Liang; Mccrate, Joseph M; Lee, James C-M and Li, Hao. "The role of surface charge on the uptake and biocompatibility of hydroxyapatite nanoparticles with osteoblast cells". *Nanotechnology* **22**, 105708, (2011).
- 48 Tanyakorn, Muangnapoh; Noriaki, Sano; Shin-Ichi, Yusa; Nawin, Viriya-empikul and Tawatchai, Charinpanitkul. "Facile strategy for stability control of gold nanoparticles synthesized by aqueous reduction method". *Current Applied Physics* **10**, 708-714, (2010).
- 49 Yu-Chin, Lin; Bang-Ying, Yu; Wei-Chun, Lin; Szu-Hsian, Lee; Che-Hung, Kuo and Jing-Jong, Shyue. "Tailoring the Surface Potential of Gold Nanoparticles with Self-Assembled Monolayers with Mixed Functional Groups". *Journal of Colloid and Interface Science* **340**, 126-130, (2009).
- 50 Clover, J. and Gowen, M. "Are MG-63 and HOS TE85 human osteosarcoma cell lines representative models of the osteoblastic phenotype?". *Bone* **15**, 585-591, (1994).
- 51 Pautke, Christoph; Schieker, Matthias; Tischer, Thomas; Kolk, Andreas; Neth, Peter; Mutschler, Wolf and Milz, Stefan. "Characterization of Osteosarcoma Cell Lines MG-63, Saos-2 and U-2 OS in Comparison to Human Osteoblasts". *Anticancer Research* **24**, 3743-3748, (2004).
- 52 Malaval, Luc; Liu, Fina; Roche, Patricia and Aubin, Jane E. "Kinetics of osteoprogenitor proliferation and osteoblast differentiation in vitro". *Journal of Cellular Biochemistry* **74**, 616-627, (1999).
- 53 Mbalaviele, Gabriel; Sheikh, Sharmin; Stains, Joseph P; Salazar, Valerie S; Cheng, Su-Li; Chen, Di and Civitelli, Roberto. "β-Catenin and BMP-2 synergize to promote osteoblast differentiation and new bone formation". *Journal of Cellular Biochemistry* **94**, 403-418, (2005).
- 54 Kim, Kyobum; Dean, David; Lu, Anqi; Mikos, Antonios G and Fisher, John P. "Early osteogenic signal expression of rat bone marrow stromal cells is influenced by both hydroxyapatite nanoparticle content and initial cell seeding

- density in biodegradable nanocomposite scaffolds". *Acta Biomaterialia* **7**, 1249-1264, (2011).
- 55 Patel, Minal; Patel, Ketan J; Caccamese, John F; Coletti, Domenick P; Sauk, John J and Fisher, John P. "Characterization of cyclic acetal hydroxyapatite nanocomposites for craniofacial tissue engineering". *Journal of Biomedical Materials Research Part A* **94A**, 408-418, (2010).
- 56 Yang, Shuying; Wei, Daoyan; Wang, Dian; Phimphilai, Mattabhorn; Krebsbach, Paul H and Franceschi, Renny T. "In Vitro and In Vivo Synergistic Interactions Between the Runx2/Cbfa1 Transcription Factor and Bone Morphogenetic Protein-2 in Stimulating Osteoblast Differentiation". *Journal of Bone and Mineral Research* **18**, 705-715, (2003).
- 57 Alkilany, Alaaldin M. and Murphy, Catherine J. "Toxicity and cellular uptake of gold nanoparticles: what we have learned so far?". *J Nanopart Res.* **12**, 2313-2333, (2010).
- 58 Shukla, Ravi; Bansal, Vipul; Chaudhary, Minakshi; Basu, Atanu; Bhonde, Ramesh R and Sastry, Murali. "Biocompatibility of Gold Nanoparticles and Their Endocytotic Fate Inside the Cellular Compartment: A Microscopic Overview". *Langmuir* **21**, 10644-10654, (2005).
- 59 Villiers, Christian; Freitas, Heidi; Couderc, Rachel; Villiers, Marie-Bernadette and Marche, Patrice. "Analysis of the toxicity of gold nano particles on the immune system: effect on dendritic cell functions". *J Nanopart Res.* **12**, 55-60, (2010).
- 60 Pan, Yu; Leifert, Annika; Ruau, David; Neuss, Sabine; Bornemann, Jörg; Schmid, Günter; Brandau, Wolfgang; Simon, Ulrich and Jahnen-Dechent, Willi. "Gold Nanoparticles of Diameter 1.4 nm Trigger Necrosis by Oxidative Stress and Mitochondrial Damage". *Small* **5**, 2067-2076, (2009).
- 61 Patra, H. K.; Banerjee, S.; Chaudhuri, U.; Lahiri, P. and Dasgupta, A. K. "Cell selective response to gold nanoparticles". *Nanomedicine : nanotechnology, biology, and medicine* **3**, 111-119, (2007).
- 62 C.Santos; C.F.Rovath; Franke, R. P.; M.M.Almeida and M.E.V.Costa. "Spray-dried hydroxyapatite-5-Fluorouracil granules as a chemotherapeutic delivery system". *Ceramics International* **35**, 509-513, (2009).
- 63 Scharnweber, Tim; Santos, Catarina; Franke, Ralf-Peter; Almeida, Maria and Costa, Maria Elisabete. "Influence of Spray-dried Hydroxyapatite-5-Fluorouracil Granules on Cell Lines Derived from Tissues of Mesenchymal Origin". *Molecules* **13**, 2729-2739, (2008).
- 64 Klesing, J.; Chernousova, S.; Kovtun, A.; Neumann, S.; Ruiz, L.; Gonzalez-Calbet, J. M.; Vallet-Regi, M.; Heumann, R. and Eppele, M. "An injectable paste of calcium phosphate nanorods, functionalized with nucleic acids, for cell transfection and gene silencing". *Journal of Materials Chemistry* **20**, 6144-6148, (2010).
- 65 Akahane, Manabu; Ohgushi, Hajime; Kuriyama, Shigeki; Akahane, Takemi and Takakura, Yoshinori. "Hydroxyapatite ceramics as a carrier of gene-transduced bone marrow cells". *Journal of Orthopaedic Science* **7**, 677-682, (2002).

- 66 Roy, Indrajit and, Susmita Mitra, Amarnath Maitra, Subho Mozumdar. "Calcium phosphate nanoparticles as novel non-viral vectors for targeted gene delivery". *International Journal of Pharmaceutics* **250**, 25-33, (2003).
- 67 Stevanovic, Magdalena; Radulovic, Aleksandra; Jordovic, Branka and Uskokovic, and Dragan. "Poly(DL-lactide-co-glycolide) Nanospheres for the Sustained Release of Folic Acid". *Journal of Biomedical Nanotechnology* **4**, 1-10, (2008).
- 68 Zhaowu, Zhang; Jing, Jia; Youqun, Lai; Yanyan, Ma; Jian, Weng and Liping, Sun. "Conjugating folic acid to gold nanoparticles through glutathione for targeting and detecting cancer cells". *Bioorganic & Medicinal Chemistry* **18**, 5528-5534, (2010).
- 69 Yang, Shu-Jyuan; Lin, Feng-Huei; Tsai, Kun-Che; Wei, Ming-Feng; Tsai, Han-Min; Wong, Jau-Min and Shieh, Ming-Jium. "Folic Acid-Conjugated Chitosan Nanoparticles Enhanced Protoporphyrin IX Accumulation in Colorectal Cancer Cells". *Bioconjugate Chemistry* **21**, 679-689, (2010).
- 70 He, Y. Y; Wang, X. C; Jin, P. K; Zhao, Bo and Fan, Xiaoyuan. "Complexation of anthracene with folic acid studied by FTIR and UV spectroscopies". *Spectrochimica Acta Part A: Molecular and Biomolecular Spectroscopy* **72**, 876-879, (2009).
- 71 Bhattacharya, Dipsikha; Das, Manasmita; Mishra, Debashis; Banerjee, Indranil; Sahu, Sumanta K.; Maiti, Tapas K. and Pramanik, Panchanan. "Folate receptor targeted, carboxymethyl chitosan functionalized iron oxide nanoparticles: a novel ultradispersed nanoconjugates for bimodal imaging". *Nanoscale* **3**, 1653-1662, (2011).
- 72 Rutnakornpituk, Metha; Puangsin, Nipaporn; Theamdee, Pawinee; Rutnakornpituk, Boonjira and Wichai, Uthai. "Poly(acrylic acid)-grafted magnetic nanoparticle for conjugation with folic acid". *Polymer* **52**, 987-995, (2011).
- 73 Anusha, Ashokan; Deepthy, Menon; Shantikumar, Nair and Manzoor, Koyakutty. "A molecular receptor targeted, hydroxyapatite nanocrystal based multi-modal contrast agent". *Biomaterials* **31**, 2606-2616, (2010).
- 74 Wei Zhang; Zhi Li and Peng, Bin. "Effects of iRoot SP on Mineralization-related Genes Expression in MG63 Cells". *Journal of Endodontics* **36**, 1978-1982, (2010).
- 75 Wiens, Matthias; Wang, Xiaohong; Schröder, Heinz C; Kolb, Ute; Schloßmacher, Ute; Ushijima, Hiroshi and Müller, Werner E. G. "The role of biosilica in the osteoprotegerin/RANKL ratio in human osteoblast-like cells". *Biomaterials* **31**, 7716-7725, (2010).
- 76 Lane, Nancy and Yao, Wei. "Developments in the scientific understanding of osteoporosis". *Arthritis Research & Therapy* **11**, 228, (2009).
- 77 http://www.waters.com/waters/nav.htm?cid=10049055&locale=en_PT.
- 78 Canalis, E; Deregowski, V; Pereira, RC and Gazzero, E. "Signals that determine the fate of osteoblastic cells". *J Endocrinol Invest.* **28**, 3-7, (2005).

- 79 Chau, JF; Leong, WF and Li, B. "Signaling pathways governing osteoblast proliferation, differentiation and function". *Histol Histopathol.* **24**, 1593-1606, (2009).

General Conclusion and Future Work

It is known that nanoparticle (NP) physical-chemical properties are of paramount importance for the biomedical applications that expose NP to living cells as cellular pathways are prone to be modulated by NP morphological and surface attributes. Thus a pool of knowledge on the biological impacts of particle size, shape, crystallinity and surface properties is required in order to be able to predict both particle fate and elicited cell response. Therefore, the development of successful nano engineered particles and the clarification of NP properties impact on cellular interaction was here envisaged as a valuable contribution for this scientific field.

Framed by this motivation, an important part of this thesis was focused on the synthesis of Hydroxyapatite nanoparticles (Hap NP), and on the modification of its physical-chemical and morphological characteristics by manipulating the synthesis experimental conditions. Moreover, pushed by the recent developments on the field of nanoparticles application as diagnosis and therapeutic tools, the functionalization of Hap NP nanostructures with gold and with folic acid was also carried out in the present work, aiming to impart imaging and therapeutic capacity to NP which could be particularly interesting in applications like cancer treatment. The cellular response to the synthesized nanoscale materials with diverse physico-chemical properties was also addressed.

The main conclusions withdrawn from the results obtained throughout this research can be summarized as follows:

- Two synthesis methods were selected for producing Hap nanoparticles with different characteristics: (i) precipitation from calcium/citrate/phosphate solution at 180°C by an hydrothermal method (HS) under the presence of an organic additive, i.e. citric acid, and (ii) a second wet chemical synthesis method (WCS) at physiological temperature previously reported in the literature ¹.
- The morphology of the precipitated particles by HS has shown a great dependence on the experimental conditions, mainly on the citrate/calcium (Cit:Ca) molar ratio. Nanometric or micrometric Hap particles with different morphologies could be obtained from solution with different Cit:Ca ratios:

crystalline Hap particles with a well-defined prismatic shape and nanometric dimensions may be produced provided the ratio of the organic specie to the calcium ion is maintained close to 3:1. An increase in the Cit:Ca ratio origins hydroxyapatite particles with micrometric size.

- The mechanism of hydroxyapatite growth seems to be controlled by the amount and the configuration of carboxylate groups, derived from citrate ions adsorbed on particles surface.

- As compared to particles obtained by HS, Hap particles synthesized via WCS were seen to be thinner Hap particles, with larger specific surface area but with lower crystallinity, thus confirming previous literature reported results.

- The influence of autoclaving sterilization step, which is required before subsequent *in vivo* application of Hap nanoparticles, revealed that the sterilization modifies markedly the shape, size and aggregation state of WCS nanoparticles which high surface area suffered a severe reduction during autoclaving. These findings pointed out the need of NP characterization after the sterilization step.

- *In vitro* cell culture experiments revealed that both type of Hap nanoparticles (HS and WCS) are biocompatible since no deleterious effects on MG63 cells were observed. Sterilized WCS and HS nanoHap particles were readily internalized by MG63 osteoblastic cells, by an endocytic pathway, and exhibited some differences in the elicited cell response.

- Moreover, the presence of Hap particles in cell culture induces the expression of ALP and BMP-2 genes and potentiates the modulation of the osteoblastic cell response. Low Hap concentrations, did not induce deleterious effects in the cell viability/proliferation, F-actin cytoskeleton organization and apoptosis rate, were furthermore able to increase the expression of ALP and BMP-2.

- Deleterious effects on cell behaviour were observed only at high nanoparticles concentrations, probably because of the vesicular entrapment of the particles and their low degradability.

- Due to the low toxicity and the potential for the modulation of the osteoblastic cell behaviour, WCS and HS nanoHap particles are likely to exhibit an interesting profile for bone tissue applications.
- Spherical gold nanoparticles (AuNPs) were precipitated on HS surface, using a Turkevich related approach. Au particle size increases with reaction time though keeping a spherical shape of nanometric dimension.
- Carboxylate groups remaining from Hap precipitation by HS were found to play a crucial role in the chemical reaction process involved in AuNPs nanoparticles precipitation.
- Biological behaviour of the synthesized nanoparticles has demonstrated that HS and HS with coupled AuNPs (HS-AuNPs) do not have acute cytotoxic effects on MG63 cells. The presence of HS nanoparticles induces highest proliferation rate as well as enhancement of osteogenic parameters of MG63 cells than HS-AuNPs, with the exception for the Runx-2 gene which is more pronounced in HS-AuNPs than in HS. A folic acid (FA) based formulation targeted for theragnosis was prepared using HS-AuNPs via an adsorption technique. The functionalization of Hap or Hap-AuNPs nanoparticles with FA does not produce significant effects on cell viability even at high particle concentrations. Furthermore, it was established that with exception of Col I the remaining genes expressions are enhanced in presence of functionalized nanoparticles.

Future Work

The results obtained in this research provide an input to the engineering of nanoparticles that have a potential to be an added value in the field of diagnosis and treatment of many diseases. However, further information is still required to answer some unsolved questions. Therefore the following topics should be addressed in future work.

- Although synthesised hydroxyapatite particles with complex morphologies were explored and compared several factors related with the citrate effect on crystal growth and final particles morphology require further investigation. Such study is expected to benefit the understanding on Hap crystal growth and particularly, on tailoring the morphology of the particles.
- Only a chelating molecule (citric acid) was tested in the synthesis of Hap particles. However, different chelating molecules, in particular some with biological interest, may be helpful for obtaining particles with different morphologies and sizes.
- Different types (with a different Cit:Ca ratio) of synthesised Hap particles should be sterilized by different methods such as gamma-radiation and tested in cell culture to evaluate the effects of the sterilization method on morphology and therefore on biological response of the particles.
- Although spherical gold nanoparticles were successfully synthesized on Hap surface the obtained SPR band of those particles is not the most adequate for several applications. For that reason the modification on synthesis method and, as consequence, the alterations on gold particles morphology, could help to achieve a better understanding on gold growth mechanism while diversifying the applications of the resulting nanoparticles.
- The method here presented to conjugate folic acid to the Hap particles should be improved. Additionally different concentrations of folic acid

must be tested and the effect of its concentration on cell response evaluated.

- Even though the synthesized particles were mainly envisaged for applications more closely related with bone, the study of the interaction behaviour of these materials with other type of cells seems to be an obvious requirement to improve the potentiality of these Hap particles.

Based on literature reports Hyperthermia ability was suggested for the synthesized HS-AuNPs though not experimentally verified. The confirmation and, if required, the optimization of hyperthermia behaviour is thus mandatory.

6.1. References

- 1 M.A.Martins; C.Santos; M.M.Almeida and M.E.V.Costa. "Hydroxyapatite micro- and nanoparticles: nucleation and growth mechanisms in the presence of citrate species". *Journal of Colloid and Interface Science* **318**, 210-216, (2008).